BRNO UNIVERSITY OF TECHNOLOGY

VYSOKÉ UČENÍ TECHNICKÉ V BRNĚ

CENTRAL EUROPEAN INSTITUTE OF TECHNOLOGY BUT

STŘEDOEVROPSKÝ TECHNOLOGICKÝ INSTITUT VUT

STATIC AND DYNAMIC PROPERTIES OF NANOSTRUCTURED MAGNETIC MATERIALS

STATICKÉ A DYNAMICKÉ VLASTNOSTI NANOSTRUKTUROVANÝCH MAGNETICKÝCH MATERIÁLŮ

DOCTORAL THESIS

DIZERTAČNÍ PRÁCE

AUTHOR

AUTOR PRÁCE

Ing. Marek Vaňatka

SUPERVISOR

ŠKOLITEL

Ing. Michal Urbánek, Ph.D.

BRNO 2020

Abstract

During the last years, magnetic materials and nanostructures have been intensively studied for their applications in recording media and logic circuits. This work follows our ongoing research in this field and mainly focuses on the static and dynamic properties of nanostructured materials, e.g., NiFe, CoFeB, and YIG. The thesis starts with a theoretical introduction showing the basic description of micromagnetic systems, ferromagnetic resonance (FMR), and spin-waves, including the mathematical description of spin-wave dispersion relations. This is followed by the description of experimental methods. Then we present the first experimental part concerning the nucleation process of magnetic vortices, i.e., the transition from the saturated state into the vortex spin configuration while decreasing the magnetic field. Magnetic imaging methods are used, namely Lorentz transmission electron microscopy and magnetic transmission X-ray microscopy. The results are correlated with electrical detection using the anisotropic magnetoresistance effect. The advantage of electrical measurements is their potential integrability into the microprocessor circuitry. In the results, we report that this process in nanometer- and micrometer-sized magnetic disks undergoes several phases with distinct spin configurations called the nucleation states. Moreover, we introduce the analysis of magnetic materials using a vector network analyzer (VNA), which is applied to the measurement of magnetic vortex resonance (evaluation of the gyrotropic frequency and the high-frequency modes as well), the ferromagnetic resonance of thin layers (extraction of basic magnetic material parameters), and propagating spin-wave spectroscopy (PSWS). Spin-wave spectroscopy is further developed to measure the dispersion relations of thin magnetic layers, which can serve as an essential characteristic used in the design of devices. Finally, we show a concept of an antenna device, separating the magnetic excitation from the sample itself, providing no need for electron lithography processes of the antenna fabrication onto the sample. This device has the form of a glass cantilever, on which the excitation antenna is fabricated, a connector, and a coupler. It is then placed on a tilt equipped x-y-z stage, and therefore it provides positionability to any place on the measured sample. The use of glass as the cantilever material enables navigation using a microscope and enables the use of optical detection methods, e.g., Brillouin light scattering (BLS) or Kerr effect.

Keywords

Magnetism, vortex, magnetoresistance, Lorentz microscopy, transmission electron microscope, X-ray microscopy, FMR, spin-wave, dispersion, VNA

Abstrakt

Magnetické materiály a z nich vyrobené nanostruktury jsou v průběhu posledních let studovány pro jejich aplikace v např. záznamových médiích a logických obvodech. Tato práce navazuje na náš předchozí výzkum tohoto oboru s hlavním zaměřením na statické a dynamické vlastnosti nanostrukturovaných magnetických materiálů, jako například NiFe, CoFeB a YIG. Práce začíná teoretickým úvodem s popisem mikromagnetických systémů, dynamiky magnetických vortexů, feromagnetické rezonance (FMR) a spinových vln včetně jejich disperzních vlastností. Následuje popis použitých experimentálních metod a první experimentální část zabývající se nukleačním procesem magnetického vortexu, jinými slovy procesem transformace ze saturovaného stavu do spinové konfigurace magnetického vortexu v průběhu snižování magnetického pole. Jsou použity mikroskopické metody zobrazující magnetickou strukturu materiálu, jmenovitě Lorentzova transmisní elektronová mikroskopie a rentgenová transmisní mikroskopie. Výsledky jsou poté korelovány s měřením elektrické odezvy pomocí jevu anizotropní magnetorezistence. Výhodou elektrických měření je, že plně elektrická detekce dovoluje použití tohoto systému v uzavřených systémech integrovaných obvodů. Výsledky oblasti nukleací magnetických vortexů ukazují, že při tomto procesu prochází magnetizace v nano- a mikrometrových magnetických discích několika fázemi s různými typy spinových konfigurací nazvaných nukleační stavy. Dále je představeno měření magnetických materiálů pomocí vektorového síťového analyzátoru (VNA), což je aplikováno na měření resonance magnetických vortexů (určení gyrotropické frekvence a měření vysokofrekvenčních módů), feromagnetické rezonance tenkých vrstev (získání základních magnetických materiálových parametrů) a spektroskopii spinových vln. Právě spektroskopie spinových vlna je rozvinuta za účelem měření disperzních relací tenkých magnetických vrstev, což je základní charakteristika, jejíž znalost je důležitá v návrhu aplikací. Nakonec je představeno anténní zařízení, díky kterému lze oddělit magnetické buzení od vzorku samotného bez nutnosti absolvovat proces elektronové litorafie, což je zapotřebí v klasickém přístupu antény na vzorku a kontaktování vysokofrekvenční sondou. Toto zařízení se skládá ze skleněného kantilívru, na kterém je vyrobena budící anténa, konektoru a spojovacího prvku v podobě plošného spoje. Celé zařízení je díky umístění na x-y-z stolek s náklonem pozicovatelné a lze tedy měřit v jakémkoliv místě vzorku. Umístění antény na sklo umožňuje navigaci pomocí mikroskopu a optické měření, např. metodou Brillouinova světelného rozptylu (BLS) nebo Kerrova jevu.

Klíčová slova

Magnetismus, vortex, magnetorezistence, Lorentzova mikroskopie, transmisní elektronový mikroskop, rentgenová mikroskopie, FMR, spinové vlny, disperze, VNA

Acknowledgment

I would like to express my gratitude towards my supervisor Dr. Michal Urbánek for providing his valuable expertise during my whole study as well as for numerous bike trips that we took together, discovering the gnarliness of local trails. My sincere gratitude belongs to prof. Jiří Spousta, prof. Tomáš Šikola, and others from the Institute of Physical Engineering and CEITEC, who made our part of the university to be not only historically possible but also a positive, forward-looking place to study and work. I also thank my classmates and colleagues mainly from the magnetism group at CEITEC (Fleš, Kosťa, Igor, Tom, Ondra, Kubina, Jiřina, Vojta, Joni, Kristýna, and others) for friendship, a lot of fun, and numerous foosball games, coffee breaks, and other goodies. If I was to lift one person, it would be Lukáš Flajšman, for our daily cooperation, valuable discussions, partnership during Erasmus, thesis proofreading, and the ubiquitous kindness in his great personality. I thank Jan Michalička not only for the shared bike rides but also for his time that we spend together on working with the transmission electron microscope, where I had the opportunity to learn the Lorentz imaging, which led to a scientific publication. Ondřej Wojewoda deserves my thanks for discussions regarding the theoretical part of this work and BLS measurements. I have to mention Toni Hache and Helmut Schultheiss for their collaboration on the antenna device. I also thank my family for their care and my girlfriend for her unlimited kindness and support.

CzechNanoLab project LM2018110 funded by MEYS CR is gratefully acknowledged for the financial support of the measurements/sample fabrication at CEITEC Nano Research Infrastructure.

I declare that I have written this thesis entitled *Static and dynamic properties of nanostructured magnetic materials* independently, under the guidance of the supervisor, Ing. Michal Urbánek, Ph.D., and using the technical literature and other sources of information, all adequately cited in the thesis, with a detailed list of references provided at the end of the thesis.

Ing. Marek Vaňatka

Contents

Introduction

From the invention of computers in the mid-1900s, computational technology has advanced by immense leaps influencing our everyday lives. Soon after entering the third millennium, small handheld computers (called smartphones) became a reality, placing humanity's knowledge literally into our hands. Magnetic materials have played an essential role in the development of computers, especially in hard drives. The discovery of various forms of magnetoresistance led to massive development in magnetic recording technologies during the 1990s, increasing the storage capacity and shrinking the size dramatically. This gave rise to the new discipline in magnetism called spintronics – a field of electronics considering the spin of an electron as an additional physical degree of freedom, which can be manipulated to obtain unique functionalities given solely by the magnetic origin of the spintronic system [1]. The spin-dependent phenomena in spintronic devices rely on the spin ordering described by micromagnetism[1]. This theory explains, e.g., the formation of domains and various spin structures [2], which is discussed at the beginning of Chapter 1.

For smaller devices, e.g., laptops and smartphones, CMOS-based flash and solid-state drives are prevailing nowadays (2020), primarily because of their lack of moving parts. Magnetic recording is still not beaten for large storage applications, but importantly, magnetic devices will undoubtedly reach a renaissance during the upcoming decades in both data storage and computing [3], motivating further research.

One of the systems studied by numerous scientists, including our research group, is the magnetic vortex in micron-sized disks patterned from soft magnetic materials [4]. Magnetic vortices consist of a magnetization curling in the disk's plane around a vortex core located at the center of the disk, where the magnetization points perpendicular to that plane [2,5,6]. A magnetic vortex can have four energetically equal states given by the four distinct combinations of its circulation, and polarity presents possible applications as multibit non-volatile memory cells [7,8]. Consideration of magnetic vortices in recording media requires precise control over the four states, which has been shown both in dynamic [9–14] and static [15–19] regimes, requiring the vortex annihilation followed by nucleation, where the new state is defined, e.g., by using altered disk geometry [20–22]. Besides the memory applications, vortices have been proposed to be used in data processing as well, including logic circuits [23] or radio-frequency devices [24,25] employing gyrotropic excitation of the vortex core with eigenfrequencies typically on the order of hundreds of MHz.

All of these works have presented many possibilities of vortex state control and manipulation, but one important aspect has been, to some extent, omitted: the mechanism under which the vortex state is formed. This work studies the magnetic vortex nucleation upon the field decrease from saturation, which is dealt with in Chapter 3. We will show that the magnetization evolution between the fully saturated state and the fully nucleated vortex proceeds via different spin configurations called the nucleation states. The nucleation states are described and classified using several probing techniques presented in Chapter 2, e.g., transmission electron microscopy and electrical detection via anisotropic magnetoresistance.

Magnetic vortices have also been reported to function as spin-wave emitters [26], and spin-waves deserve high interest due to their potential in computing [27] alongside

[1] The most fundamental origin of magnetic interactions is, of course, described by quantum mechanics. The micromagnetic theory was developed because it is more suitable for larger (micron sized) structures.

spintronics. One of the exciting characteristics is that they do not move electric charges (like electric waves) and therefore lack the associated energy dissipation in the form of Joule heating. They also have short wavelengths (micro- to nanometer) and high (up to THz [28]) frequency range. Numerous proposals for magnon spintronics and computing were presented, including the most recent ones [27,29]. The later part of this thesis deals with high-frequency magnetic excitation in the forms of ferromagnetic resonance and spin-waves, for which the theoretical basis is provided in the second half of Chapter 1.

The development and availability of modern measurement electronics also enable new ways of research based on electrical measurements. Namely, the vector network analyzer (VNA) is a very powerful tool that, together with Brillouin light scattering (BLS), provides a workbench for a vast number of experiments in the field of magnetism. Because VNA's use is relatively new in our institute, Chapter 4 presents the VNA's measuring principles and its use in relevant experiments in detail. After explaining the VNA's function, we will start with the ferromagnetic resonance (FMR) experiment [30]. The FMR measurement in cavities was available long before introducing VNAs, but the modern VNA-based approach dramatically improves the usability of FMR in the laboratory with no need for the resonant cavity as the excitation source. That is because the VNA-powered FMR experiment is not limited by the cavity's resonant frequency but can work at a broad range of frequencies. For that reason, this method is often referred to as the broadband VNA-FMR. We will provide a comprehensive approach to measuring and interpreting the VNA-FMR data with results on our most common materials (NiFe, CoFeB, YIG).

Then we go beyond FMR by showing dynamic experiments on vortices, exploiting the gyrotropic oscillation of vortex cores and higher frequency modes, and more importantly, we will present experiments regarding spin-waves. Spin-wave propagation can be probed in an experiment called the propagating spin-wave spectroscopy (PSWS), which is purely enabled by a VNA [31]. It uses a pair of microwave antennas to excite and detect the spin-waves, where the VNA records the spin-wave magnitude and phase. Multiple aspects of the PSWS experimental method will be presented in the last section of Chapter 4.

An essential characteristic of spin-waves is the dispersion relation, which connects the wavelength (in terms of the k-vector) of the spin-wave to its frequency. The theoretical description of dispersion relations is provided in Chapter 1 using the dipole only and dipole-exchange models. It is not easy to measure a dispersion in detail, which would typically be done using phase-resolved BLS. This is very time consuming and therefore allows only for several points, while in Chapter 5, we present a relatively fast VNA-based all-electrical approach providing hundreds of measurement points in the dispersion. The dispersion measurement consists of PSWS data acquisition over multiple propagation distances (given by the gap size between the two antennas in the PSWS experiment), where the phase evolution is fitted, and the dispersion is reconstructed. Spin-wave dispersion results are provided for thin layers of NiFe, CoFeB, and YIG. Moreover, the thicker CoFeB layers exhibit mode crossings that result in hybridized dispersions, which are measured and described as well.

Lastly, Chapter 6 will introduce a concept of freestanding antennas, where we attempted to transfer the spin-wave excitation element away from the sample. Our innovative approach allows for skipping the fabrication step of the excitation antennas on each sample and using a positionable device instead, allowing for much more rapid experimental flow.

1 Theoretical introduction on micromagnetic states and spin dynamics

Magnetic properties of matter have been studied for centuries as they have attracted attention ever since humankind crossed the lodestones[2] [32]. Since then, the theory of magnetism has advanced by many substantial leaps leading to well established theoretical background spanning from, e.g., atomistic spin models, the mesoscopic[3] micromagnetic theory, and the effective continuum models for describing the large scale magnetic systems. Description of every aspect of magnetism is far beyond the scope of a single thesis, but this chapter will try to provide a basic understanding of the discussed phenomena to prepare the ground for experiments in the following chapters.

1.1 Basic relations in micromagnetism

The field of micromagnetism studies magnetic matter from the mesoscopic point of view: it does not study the interaction of every pair of spins of which the magnetic material consists, but it is a continuous theory. The first vital quantity to be introduced is magnetization, defined as the density of magnetic moments $\boldsymbol{\mu}$:

$$\boldsymbol{M} = \frac{\mathrm{d}\boldsymbol{\mu}}{\mathrm{d}V}, \tag{1.1}$$

while it is understood as a continuous function of position in space. The maximum value of magnetization is called the saturation magnetization M_s and it takes place when all of the moments are aligned parallel. For later use, we will also define a normalized magnetization vector $\boldsymbol{m}$:

$$\boldsymbol{m} = \frac{\boldsymbol{M}}{M_s}. \tag{1.2}$$

In vacuum, the B-field (magnetic induction) is proportional to H-field by the scalar factor of permeability μ_0. In material, the B-field is defined using the following equation:

$$\boldsymbol{B} = \mu_0 \boldsymbol{H} + \mu_0 \boldsymbol{M}. \tag{1.3}$$

Its basic consequences are illustrated in Fig. 1.1 for a homogeneously magnetized rectangle. The direction of the H-field inside the material opposes the direction of both B-field and magnetization and is often called the demagnetizing field $\boldsymbol{H}_\mathrm{d}$. If we follow the Maxwell's equation

$$\boldsymbol{\nabla} \cdot \boldsymbol{B} = 0, \tag{1.4}$$

and combine it with the equation (1.3), we find that in the absence of magnetization (free space), the H-field is also divergenceless. But there is no reason why the H-field and magnetization could not have sources, which, in analogy with electrostatics, leads to the concept of magnetic charges:

$$\rho_\mathrm{m} = -\mu_0 \boldsymbol{\nabla} \cdot \boldsymbol{M} = \mu_0 \boldsymbol{\nabla} \cdot \boldsymbol{H}. \tag{1.5}$$

[2] Rocks rich in Fe_3O_4.

[3] Mesoscopic stands for the middle ground between atomic level and large scale.

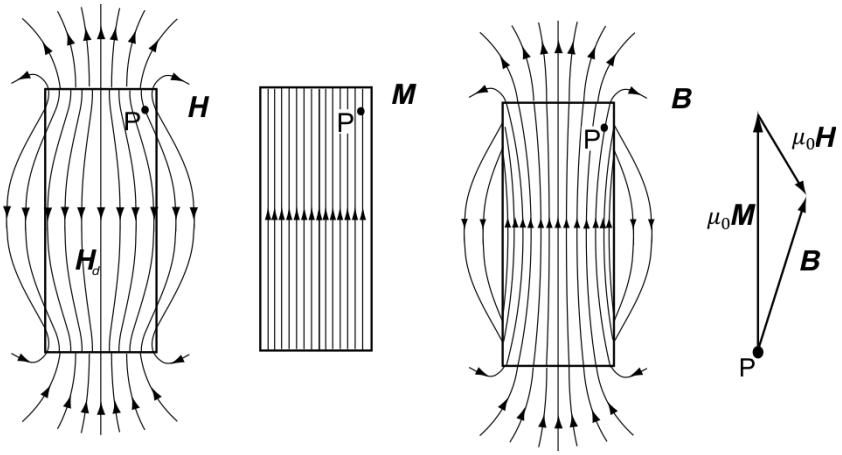

Fig. 1.1: Vectors $\boldsymbol{H}, \boldsymbol{M}$, and $\boldsymbol{B}$ inside of a homogeneously magnetized rectangle must fulfill the equation (1.3). Reprinted from [33].

1.2 Micromagnetic energies

The magnetic states, i.e., the configurations of spins formed in mesoscopic structures, are not random but result from competing magnetic interactions. There are four fundamental interactions present between individual magnetic spins. In the micromagnetic framework, we can represent them with their energy terms.

The interactions are then summarized into the total micromagnetic energy, where the final magnetization state is the result of minimizing it; a stable magnetic state reflects either a local or an absolute energy minimum [33,34]. The total energy is the sum of the four parts:

$$E_{\mathrm{tot}} = E_{\mathrm{ex}} + E_{\mathrm{d}} + E_{\mathrm{Z}} + E_{\mathrm{a}}. \tag{1.6}$$

Each of these contributions is typically represented by a volume integral, which will be defined in the following text. Other energy terms can exist, e.g. the Dzyaloshinskii-Moriya Interaction (DMI) or magnetostriction, but apply only to specific magnetic systems that are not considered in this work.

1.2.1 Energy components

The first component of the total energy E_{tot} is the exchange energy E_{ex}, associated with the exchange interaction, which enables the existence of ferromagnetism and is purely of the quantum mechanical origin [33,34]. Its basic consequence is that the adjacent magnetic moments prefer to be aligned collinearly. Its value is then calculated as the volume integral:

$$E_{\mathrm{ex}} = \iiint A_{\mathrm{ex}} \left[(\nabla m_x)^2 + \left(\nabla m_y\right)^2 + (\nabla m_z)^2 \right] \mathrm{d}V, \tag{1.7}$$

where A_{ex} is called the exchange stiffness constant[4] in units of J/m. Exchange is a short distance interaction, where the quantity describing the length within which the exchange interaction is dominant is called the exchange length:

[4] The typical value for NiFe is $A_{\mathrm{ex}} = 16$ pJ/m.

$$l_{\mathrm{ex}} = \sqrt{\frac{2A_{\mathrm{ex}}}{\mu_0 M_{\mathrm{S}}^2}}. \tag{1.8}$$

Contrary to the exchange interaction, the dipolar energy E_{d} prefers two adjacent spins to align in the opposite direction, and it affects the spins at a more extended scale than exchange. It can be calculated using the H-field inside the material (the demagnetizing field):

$$E_{\mathrm{d}} = -\frac{1}{2}\mu_0 \iiint \boldsymbol{M} \cdot \boldsymbol{H}_{\mathrm{d}}\, \mathrm{d}V, \tag{1.9}$$

where the demagnetizing field $\boldsymbol{H}_d$ opposes the magnetization direction. Minimizing the dipolar energy reduces the volume and surface magnetic charges, which is called the charge avoidance principle. The sample shape plays a crucial role here because the dipolar energy is influenced by the sample's geometry and can create preferred axes of the magnetization orientation. This effect is often referred to as the shape anisotropy [33].

The energy describing the interaction of the magnetization with external magnetic fields is called Zeeman energy E_{Z}. The Zeeman energy represents the energetical penalty for spins not pointing in the external field's ($\boldsymbol{H}_{\mathrm{ext}}$) direction, where it is calculated similarly as the previous dipolar energy:

$$E_{\mathrm{Z}} = -\mu_0 \iiint \boldsymbol{M} \cdot \boldsymbol{H}_{\mathrm{ext}}\, \mathrm{d}V. \tag{1.10}$$

The last energy term considers the crystal (electronic) structure of magnetic material, where the magnetization aligns preferentially along specific crystallographic directions called easy axes. The associated energy of anisotropy can again be calculated in the form of a volume integral. In the simplest case of the uniaxial anisotropy, having only one easy axis, which is found in hexagonal or orthorhombic crystals, the energy term is

$$E_{\mathrm{a}} = \iiint K_{\mathrm{u}} \sin\theta\, \mathrm{d}V, \tag{1.11}$$

where K_{u} is the energy density of the uniaxial anisotropy, and θ is the angle between the easy axis and the vector of magnetization $\boldsymbol{M}$.

1.2.2 Formation of domains and spin structures

The spin structure of magnetic materials in bulk or layers is often broken into domains. This results from competing micromagnetic energies with the total energy E_{tot} being at its minimum when a stable state is reached. Two of the energies, Zeeman energy and anisotropy energy, favor spin alignment along a specific direction given by the effective magnetic field (discussed later) and the easy anisotropy axis respectively. When one of them is dominant, we can expect most of the spins to be aligned with the preferred direction. Those two energies can also be controlled externally. Zeeman energy is given by the external magnetic field, which can be eliminated, and anisotropy can be suppressed by preparing the materials in a way that the magnetic anisotropy strength is negligible, e.g., polycrystalline NiFe[5] or amorphous CoFeB[6].

On the other hand, exchange and dipolar energies are intrinsic and thus are always present. We will use the illustration in Fig. 1.2 to provide an insight into the energy influence

[5] $Ni_{80}Fe_{20}$, often called Permalloy.

[6] $Co_{40}Fe_{40}B_{20}$

on a micron-sized magnetic square structure. (a) shows the resulting spin pattern for the case that we could turn off all of the energy contributions except for the exchange interaction. This interaction favors the spins to be aligned parallel. Therefore, the whole sample consists of a single magnetic domain. Fig. 1.2(b) shows the result of energy competition after introducing the dipolar energy to the system. The dipolar energy favors curling of the spins. This is the opposite to exchange, but it acts at long distances, while the characteristic reach of the exchange interaction is very short and is given by the exchange length l_{ex}. The result then exhibits a magnetic flux closure – a typical feature in the minimization of dipolar energy. The flux closing patterns minimize the surface charges following the charge avoidance principle [33]. This pattern in a magnetic square was first predicted by Landau, and is called the Landau pattern [2]. It consists of four domains with their magnetization circulating around the center point, known as the core, in which the magnetization points out-of-plane. The curling nature of magnetization in this pattern with a core in the middle is what essentially makes it a magnetic vortex.

Fig. 1.2(c,d) illustrates the addition of Zeeman energy and anisotropy energy, where the spin alignment will be influenced by the external magnetic field and the easy axis caused by anisotropy. The magnetic vortex can still exist, but in Fig. 1.2(b), it will be deformed to reflect the added energy terms.

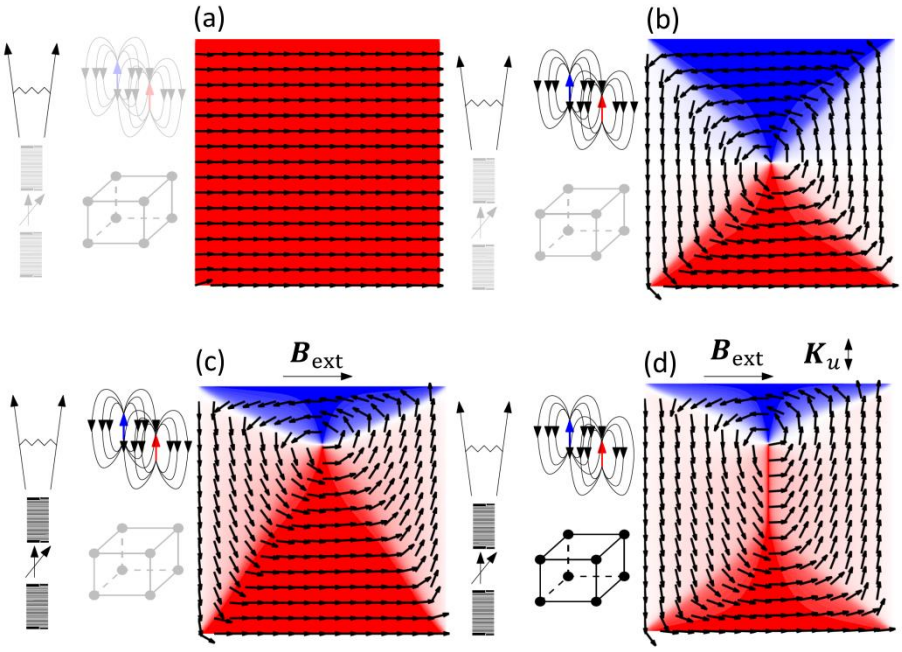

Fig. 1.2: Influence of added energy contributions. (a) Exchange energy only. (b) Competing exchange and dipolar energies lead to the formation of a flux-closing Landau pattern. (c) Added Zeeman energy in the form of the external magnetic field energetically favors the spins oriented along the external magnetic field direction. (d) Bidirectional anisotropy term tries to align the moments to the easy axis. The final spin structure is a result of all four components in competition. Reprinted from [35].

1.3 Magnetic vortices in thin magnetic disks

Now, if we consider a cylindrical geometry with the diameter D of the cylinder much larger than the thickness t (we will call it a disk for simplicity), the magnetic spins will follow the same logic as in the previous section. The ground state will almost always be the magnetic vortex exhibiting the spins' characteristic flux-closing circular pattern. Only now the four

domains will not be formed because the disk has rotational symmetry. Instead, continuous circulation of spins around an out-of-plane core will take place. The exceptions to the vortex creation are disks either too small (both D and t well under 100 nm), in which case the structure will be in a single domain state [36], or too large with respect to the thickness (e.g., $D > 10$ μm and $t \sim 10$ nm), which will result in a multidomain state.

The symmetry of a disk provides four energetically equal (degenerate) vortex states shown in Fig. 1.3. They can be described by two independent parameters: circulation and polarity. The circulation is defined by the sense of the in-plane magnetization curling (clockwise, $c = -1$ or counterclockwise, $c = 1$) while the out-of-plane magnetization direction gives the polarity in the vortex core (pointing up, $p = 1$ or down, $p = -1$). The product cp defines the vortex handedness, either right-handed ($cp = 1$) or left-handed ($cp = -1$). The degeneracy of the vortex states is given by the geometrical symmetry, and it means that none of the four states should be favored upon the vortex nucleation.

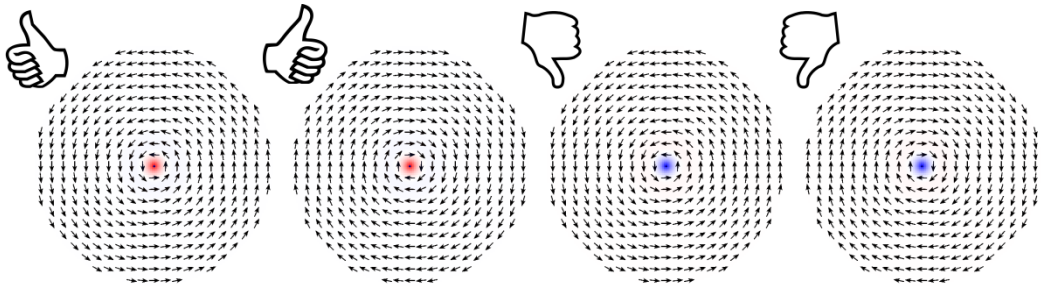

Fig. 1.3: Four vortex states showing all possible combinations of circulation and polarity. The arrows show the direction of magnetization, and the blue-white-red color code represents the out-of-plane magnetization component. The left and right hands indicate the vortex's handedness: the folded fingers show the sense of circulating magnetization, and the thumb points in the direction of the vortex core.

1.3.1 Vortex description by the rigid vortex model

The vortex state in a disk with diameter R and thickness t can be analytically modeled as two regions [16,37] by the well-established rigid vortex model. The vortex core with the radius a and the rest of the disk for $a < r < R$. The core radius can be estimated as [37,38]:

$$a = 0.68(l_{\mathrm{ex}}^2 t)^{1/3}, \tag{1.12}$$

The value a should be understood as the radius, within which there is an out-of-plane magnetization component. The estimation of the core radius is independent of the disk radius and provides somewhat underestimated results. Fig. 1.4 shows the calculation for NiFe parameters ($M_s = 800$ kA/m, $A_{\mathrm{ex}} = 16$ pJ/m)[7] and its comparison with a published experiment [39]. Fitting this experimental data provides that the core radius can be estimated as $a = 0.40t + 1.4 \cdot 10^{-8}$ m, which is in agreement with qualitative MFM[8] observations presented in [40–42].

[7] The corresponding exchange length is $l_{\mathrm{ex}} = 6.3$ nm.

[8] Magnetic force microscopy – a technique imaging magnetic signal using an atomic force microscope equipped with a magnetic probe. Please see the references [40–42] for details.

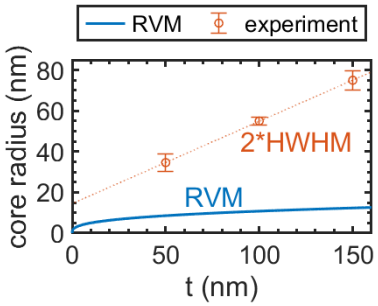

Fig. 1.4: Core diameter comparison for RVM model and experiment [39] *in NiFe disks. The experiment was evaluated for half-width at half maximum (HWHM) of the out-of-plane magnetization signal. The plotted core radius represents the boundary within which the magnetization has an out-of-plane component, as calculated with the RVM. Therefore the experiment is plotted as 2·HWHM. The fit provides the core radius estimation* $a = 0.40t + 1.4 \cdot 10^{-8}$ *m.*

The magnetization within the core diameter has all three spatial components, and the out-of-plane component increases closer to the center. The surrounding area has only in-plane magnetization components (x-y) curling around the center [16]:

$$\text{for } r < a \begin{cases} m_x = \dfrac{-2ar}{a^2 + r^2} \sin\varphi \\ m_y = \dfrac{-2ar}{a^2 + r^2} \cos\varphi \\ m_z = \sqrt{1 - \left(\dfrac{-2ar}{a^2 + r^2}\right)^2} \end{cases} \qquad \text{for } a < r < \begin{cases} m_x = -\sin\varphi \\ m_y = \cos\varphi \\ m_z = 0 \end{cases} \tag{1.13}$$

An example cross-section of magnetization through the disk center is plotted in Fig. 1.5(a). The rigid vortex model also expresses the horizontal core displacement l in the perpendicular direction to the applied magnetic field B:

$$l = \chi(0) \frac{BR}{\mu_0 M_s}, \tag{1.14}$$

where $\chi(0)$ is the initial magnetic susceptibility, calculated as follows [16]:

$$\chi(0) = \frac{2\pi}{\frac{t}{R}\left(\ln\left(\frac{8R}{t}\right) - \frac{1}{2}\right)}. \tag{1.15}$$

Assuming that the susceptibility is independent of the applied magnetic field, we can calculate the vortex annihilation field by substituting the core displacement l with the disk radius R:

$$B_{\text{an}} = \frac{\mu_0 M_s}{\chi(0)}. \tag{1.16}$$

The mean magnetization component along an increasing external magnetic field direction is plotted in Fig. 1.5(b). This model does not cover the nucleation process. Therefore it does not allow to model the whole hysteresis loop of the magnetization reversal process. It is also known that the RVM is accurate only for small disks because larger disks no longer have the susceptibility independent of the magnetic field. Fig. 1.5(b) also shows a comparison to a simulation of a larger disk.

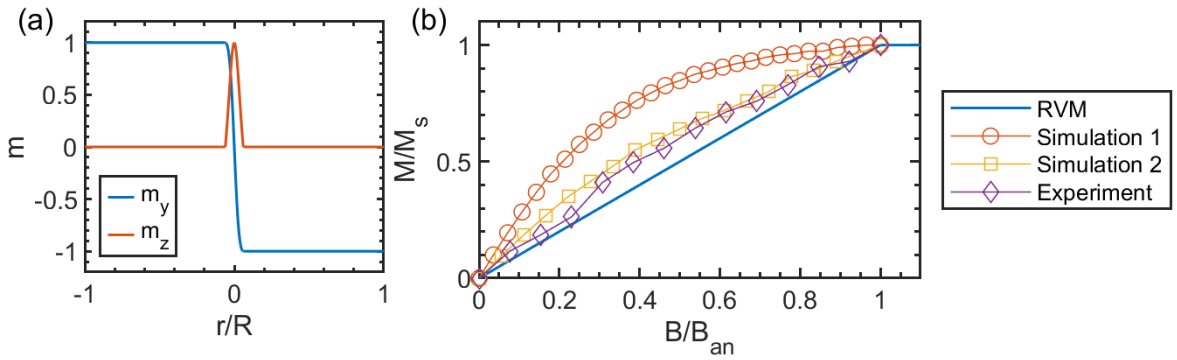

Fig. 1.5: (a) Magnetization components calculated using RVM from Eq. (1.13) for a cross-section of a magnetic disk with NiFe parameters: $M_s = 800$ kA/m, $A_{ex} = 16$ pJ/m, and geometry $R = 0.5$ μm, $t = 40$ nm. The radial component m_x is zero and is not plotted. The core diameter was calculated by using $a = 0.40t + 1.4 \cdot 10^{-8} = 30$ nm. (b) Mean magnetization of a magnetic vortex along an increasing external magnetic field calculated by RVM compared to micromagnetic simulation and experimental data from [13]*: Simulation 1 for $R = 800$ nm, $t = 20$ nm disk, Simulation 2 for the same geometry but decreased edge magnetization which is the best reflection of the experiment.*

1.4 Magnetization dynamics

Even though we have already established that the magnetic configuration will correspond to a minimum of the total energy, we have not described how the minimum is reached. The answer is that magnetic moments will follow an equation of motion which describes a damped precession of each spin to the direction of the local effective magnetic field $\boldsymbol{H}_{\text{eff}}$, calculated from the above mentioned micromagnetic energies as:

$$\boldsymbol{H}_{\text{eff}} = -\frac{1}{\mu_0}\frac{\partial E_{\text{tot}}}{\partial \boldsymbol{M}}. \tag{1.17}$$

The equation of motion is then called the Landau-Lifshitz-Gilbert (LLG) equation [43–45]:

$$\frac{\mathrm{d}\boldsymbol{M}}{\mathrm{d}t} = -\gamma \boldsymbol{M} \times \boldsymbol{H}_{\text{eff}} + \frac{\alpha}{M_s}\boldsymbol{M} \times \frac{\mathrm{d}\boldsymbol{M}}{\mathrm{d}t}, \tag{1.18}$$

where γ is the gyromagnetic ratio[9]. The right part consists of two contributors: the first part is the precessional term and the second part represents the damping term. The precessional term describes the spin's motion in an ideal case of a system with zero damping and is illustrated in Fig. 1.6(a). As every real system has nonzero damping, this needs to be taken into account by the second term proportional to the damping[10] parameter α. The damping term causes the magnetic moment to follow a spiral path until it is aligned to the direction of the effective field $\boldsymbol{H}_{\text{eff}}$ by following a spiral, as shown in Fig. 1.6(b).

The LLG equation is the basis for micromagnetic solvers, which typically use numerical integration to calculate the time evolution of magnetization in defined magnetic structures. The most common solvers are the Object Oriented Micromagnetic Framework (OOMMF [46]) and MuMax3 [47].

---

[9] For a free electron, gyromagnetic ratio is calculated as $\gamma = g|e|/(2m_e)$, where g is a dimmensionless g-factor, e is the electron's charge, and m_e is the electron's mass. Otherwise, gyromagnetic ratio is a material constant, for $\gamma/2\pi$ ranging approx. from 28 to 31 GHz/T.

[10] There are multiple origins of damping, and the parameter α used in the LLG equation should be understood as their sum. The origins are either intrinsic, due to the spin-orbit coupling, or extrinsic, e.g. due the to defects and impurities in the layers. Please see e.g. [105] for further information.

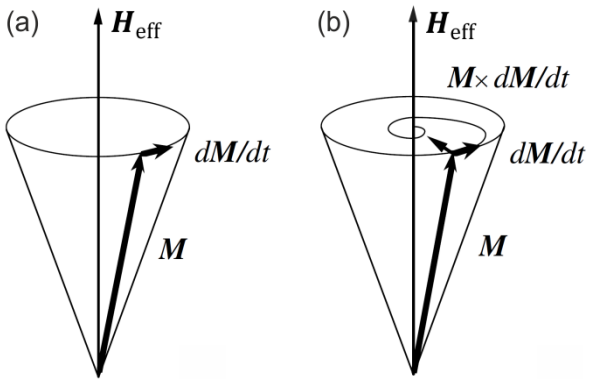

Fig. 1.6: (a) Precession of an undamped magnetic moment. (b) Motion of a damped magnetic spin. Reprinted from [45].

1.5 Magnetic vortex dynamics

Magnetic vortices can be excited by a high-frequency magnetic field or field pulses resulting in the core motion used in, e.g., switching experiments. For each geometry and material, there is an eigenfrequency of the vortex core motion that can be calculated. The core motion in a vortex with a geometry defined in Fig. 1.7 can be described using Thiele's equation [48]:

$$\boldsymbol{G}\times\frac{\mathrm{d}\boldsymbol{C}}{\mathrm{d}t}-\frac{\partial W}{\partial \boldsymbol{C}}=\boldsymbol{F}(t), \tag{1.19}$$

where $\boldsymbol{G}$ is the gyrovector calculated for the vortex core polarity p as [49]

$$\boldsymbol{G}=-\frac{pt\mu_0 M_s}{2\gamma}\hat{\boldsymbol{z}}\,, \tag{1.20}$$

($\hat{\boldsymbol{z}}$ is a unit vector pointing out-of-plane), $\boldsymbol{C}$ is the position vector of the vortex core, W is the potential energy associated with the force restoring the vortex core to the center position, and $\boldsymbol{F}(t)$ is the time-dependent excitation force associated with the excitation magnetic field. The potential W can be calculated as

$$W=\frac{1}{2}\kappa\boldsymbol{C}^2, \tag{1.21}$$

where κ takes the role of a stiffness constant. If no excitation field is applied, then the excitation force is $\boldsymbol{F}(t)=0$, and the equation can be solved, obtaining a set of first-order differential equations:

$$\frac{\mathrm{d}y}{\mathrm{d}t}+\frac{\kappa}{G}x=0,\quad \frac{\mathrm{d}x}{\mathrm{d}t}+\frac{\kappa}{G}y=0. \tag{1.22}$$

This leads to a set of two separated second order differential equations:

$$\frac{\mathrm{d}^2x}{\mathrm{d}t^2}+\left(\frac{\kappa}{G}\right)^2 x=0,\quad \frac{\mathrm{d}^2y}{\mathrm{d}t^2}+\left(\frac{\kappa}{G}\right)^2 y=0, \tag{1.23}$$

and they represent harmonic oscillations of both x and y components of in-plane core position with the eigenfrequency:

$$\omega\equiv\frac{\kappa}{G}. \tag{1.24}$$

In the case of the RVM, the eigenfrequency can be calculated as [49]:

$$f_{\mathrm{RVM}} = \frac{\omega_{\mathrm{RVM}}}{2\pi} = \frac{\gamma}{2\pi}\frac{\mu_0 M_s}{8\pi}\frac{1}{\chi(0)}, \tag{1.25}$$

where $\chi(0)$ is the initial magnetic susceptibility calculated using Eq. (1.15).

Besides the RVM, there is another model, called the two-vortex model [49,50], based on which the stiffness can be calculated as $\kappa = \left(\frac{2}{3}M_s\right)^2 \frac{\pi t}{\chi_0}$, where $\chi_0 = \frac{R}{10t}$ is the susceptibility, and the consequent eigenfrequency is calculated as:

$$f_{2\mathrm{v}} = \frac{\omega_{2\mathrm{v}}}{2\pi} = \frac{5}{9}\frac{\gamma}{2\pi}\frac{\mu_0 M_s t}{\pi R}. \tag{1.26}$$

Calculation of the eigenfrequencies for both models is shown in Fig. 1.7 using NiFe parameters. Fig. 1.7(b) shows the dependence on the disk thickness, and Fig. 1.7(c) shows the dependence on the disk radius. The typical eigenfrequencies for approx. micron-sized disks are in the order of hundreds of MHz. Thicker disks at submicron diameter can reach lower units of GHz.

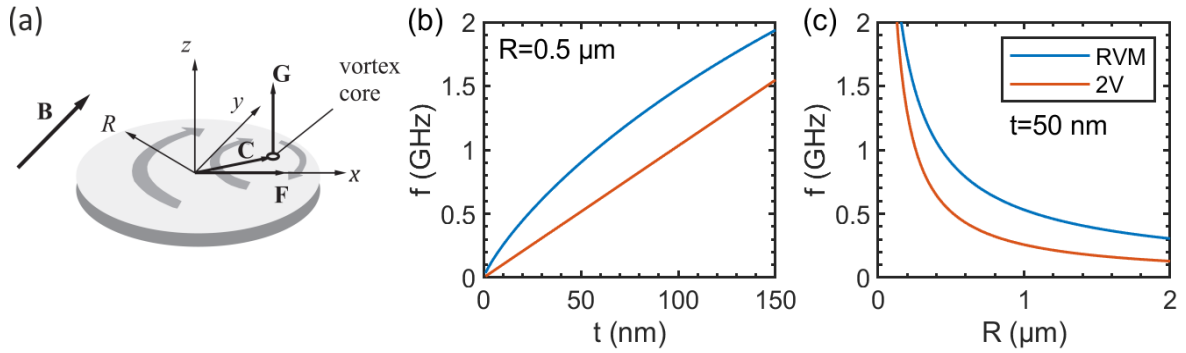

Fig. 1.7: (a) Illustration of the used geometry, reprinted from [13]. *(b,c) Calculated gyrotropic eigenfrequencies of a magnetic vortex with NiFe parameters:* $M_s = 800$ *kA/m, and* $\gamma/2\pi = 29$ *GHz/T for RVM and 2-vortex model predicting the frequencies to be in the range of hundreds of MHz to low units of GHz. The legend is shared for (a,b).*

The vortex dynamics can be utilized towards the core polarity switching. The vortex state under high-frequency excitation creates a dynamic field, so-called gyrofield [51], which has the out-of-plane component in the opposite direction than the magnetization of the vortex core. There is an excitation threshold when the vortex core exceeds a critical vortex core velocity v_c, creating a gyrofield strong enough to flip the core magnetization, i.e., change the polarity. The critical core velocity is proportional to the gyromagnetic ratio and square root of the exchange constant: $v_c \approx \gamma\sqrt{A_{\mathrm{ex}}}$ (approx. 320 m/s for NiFe) [51,52]. Pulsed or sine wave excitation is possible to gain velocity higher than v_c, which was described in simulations [52] and numerous experiments (e.g. [13]).

On the other hand, circulation switching usually requires annihilating the vortex state and controlled nucleation of a new one. The newly nucleated vortex will have the circulation defined by, e.g., altering the disk geometry [20–22] or by symmetry breaking, e.g., arising from the Dzyaloshinskii–Moriya interaction [53].

1.6 Ferromagnetic resonance (FMR)

One important solution of the LLG equation (1.18) is called the ferromagnetic resonance (FMR). It is a spatially uniform collective oscillation, as illustrated in Fig. 1.10(a). The resonant (thickness independent) frequency of a thin film can be calculated from the Kittel formula [54]:

$$f_{\mathrm{FMR}} = \frac{\gamma}{2\pi}\sqrt{B(B+\mu_0 M_S)}, \tag{1.27}$$

where γ is the gyromagnetic ratio, and B is the effective magnetic field where it should be understood as the sum of the external magnetic field B_{ext} with other contributions, e.g., from anisotropy. Because the external magnetic field B_{ext} is the control parameter of the experiment, we will rewrite the equation for $B = B_{\mathrm{ext}} + B_0$ where B_0 will sum all other effective field contributions:

$$f_{\mathrm{FMR}} = \frac{\gamma}{2\pi}\sqrt{(B_{\mathrm{ext}}+B_0)(B_{\mathrm{ext}}+B_0+\mu_0 M_S)}. \tag{1.28}$$

In the case of first-order uniaxial anisotropy, $B_0 = \mu_0 H_{\mathrm{an}}$, and can be calculated as

$$H_{\mathrm{an}} = \frac{2K_u}{M_s}\sin\theta, \tag{1.29}$$

where K_u is the energy density of uniaxial anisotropy, and θ is the angle between the magnetization and the direction of the easy axis. The anisotropy field may be obtained using an angle-dependent FMR experiment but note that it may be difficult to distinguish between the B_0 field contributors. Examples of FMR frequency calculations are shown in Fig. 1.8.

FMR can be used to evaluate the damping parameter α, which will be shown in Section 4.3.4. In order to do so, we can use the FMR peak broadening with frequency [55]:

$$\Delta B = \left(\frac{2\pi}{\gamma}\right) 2\alpha f + \Delta B_0, \tag{1.30}$$

where ΔB is the FMR full width at half minimum and ΔB_0 is called the inhomogeneous broadening constant. The peak broadens linearly with frequency, which is very convenient for analysis. The damping can also be evaluated from the frequency width Δf, while the formula is non-linear and significantly more complicated to fit [55]:

$$\Delta f = (\gamma \Delta B_0 + 4\pi\alpha f_{\mathrm{FMR}})\sqrt{1+\left(\frac{\gamma\mu_0 M_s}{4\pi f_{\mathrm{FMR}}}\right)^2}. \tag{1.31}$$

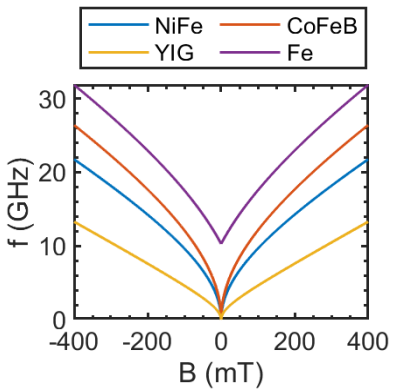

Fig. 1.8: Calculated FMR of materials used in this work: NiFe ($M_s = 800$ kA/m, $\gamma/2\pi = 29$ GHz/T, $B_0 = 0$ mT), CoFeB ($M_s = 1.2$ MA/m, $\gamma/2\pi = 30.2$ GHz/T, $B_0 = 0$ mT), YIG ($M_s = 142$ kA/m, $\gamma/2\pi = 27.6$ GHz/T, $B_0 = 0$ mT), and epitaxial Fe ($M_s = 1.74$ MA/m, $\gamma/2\pi = 29$ GHz/T, $B_0 = 56$ mT) in easy axis.

1.7 Perpendicular standing spin-waves (PSSW)

The perpendicular standing spin-waves (PSSW) are exchange dominated, quantized modes in thin magnetic layers of thickness t. The order of this quantization can be described by the integer parameter n. Their frequency is then described by the Herring-Kittel formula [56]:

$$f_{\mathrm{PSSW}} = \frac{\gamma}{2\pi}\sqrt{\left(B + \frac{2A_{\mathrm{ex}}}{M_S}\left(\frac{n\pi}{t}\right)^2\right)\left(B + \frac{2A_{\mathrm{ex}}}{M_S}\left(\frac{n\pi}{t}\right)^2 + \mu_0 M_S\right)}. \tag{1.32}$$

For $n = 0$, the equation reduces to the Kittel formula (1.27) and calculates the thickness independent FMR. Fig. 1.9 shows example calculations for modes up $n = 3$.

A spin-wave can be confined in the layer along the out-of-plane direction and propagate along the layer's in-plane direction at the same time. The previous equation will not suffice to describe the confined propagating modes, and a more general model, provided in the following Section 1.9, will be necessary.

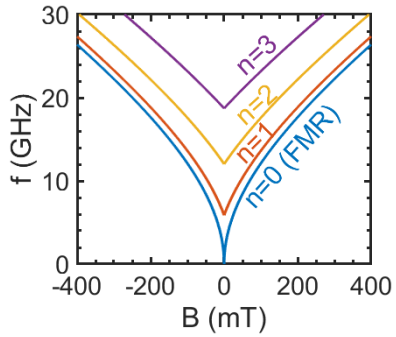

Fig. 1.9: Calculated PSSW modes using the Herring-Kittel equation for CoFeB 100 nm layer: $M_s = 1.2$ MA/m, $\gamma/2\pi = 30.2$ GHz/T, $A_{ex} = 15$ pJ/m, $t = 100$ nm.

1.8 Basic modes of propagating spin-waves

Opposite to the collectively oscillating spins in the FMR experiment, it is possible to create an excitation propagating through space in the form of a wave, as illustrated in Fig. 1.10(b). The length in space over which the spin-wave changes its phase by 2π is called the wavelength λ, using which we can define the k-vector (wave number) as a vector pointing in the direction of propagation and having the size

$$|\boldsymbol{k}| = \frac{2\pi}{\lambda}. \tag{1.33}$$

The k-vector has the unit rad/m, which we emphasize because some works omit to state the radians explicitly, confusing whether the radians are only not stated (as in SI units it is 1) or if there is the factor 2π difference. The k-vectors presented in this work will always be stated in units of rad/µm.

The coupling between the spins enables spin-waves' existence due to its two types: the dipolar interaction and the exchange interaction. The following subsections describe the basic modes of propagating spin-waves and their dispersion relations[11], covering the dipolar interaction dominated regime of propagation parallel and perpendicular to the magnetization.

[11] A dispersion relation connects the k-vector of a wave to its frequency.

Although they do not consider the exchange interaction, they will provide a good and simple approximation for small k-vectors, while medium to high k-vectors, where the exchange interaction has increasing influence, will require a more thorough description that will be provided in Section 1.9. We will also address the spin-wave's group velocity and propagation length, which can be calculated from the dispersion relation.

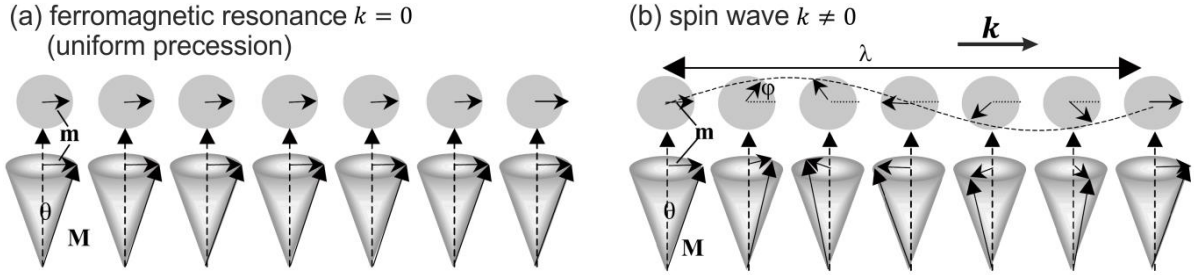

Fig. 1.10: Illustration of (a) ferromagnetic resonance where the spins collectively oscillate and (b) propagating spin-waves. Adapted from [45].

Wave velocity and propagation length

The spin-wave dispersion relations described later can serve to calculate several important parameters of the spin-waves. Firstly we can calculate the phase velocity v_p and the group velocity v_g from the dispersion $f(k)$:

$$v_p = \frac{\omega}{k} = 2\pi\frac{f}{k}, \qquad v_g = \frac{\partial\omega}{\partial k} = 2\pi\frac{\partial f}{\partial k}. \tag{1.34}$$

We can also calculate the time required for the amplitude of the dynamic magnetization to decay by the factor $1/e$ after removal of an excitation, called the spin-wave lifetime [57] as:

$$\tau = \left(\alpha\omega\frac{\partial\omega}{\partial\omega_B}\right)^{-1} = \left(\frac{\alpha 4\pi^2 f}{\gamma}\frac{\partial f}{\partial B}\right)^{-1}, \tag{1.35}$$

where $\omega_B = \gamma B$. By multiplying the equations (1.34) and (1.35), we obtain the propagation length:

$$\Lambda = v_g\tau. \tag{1.36}$$

The propagation length Λ can be a vital judging parameter for every experiment to predict whether it is feasible from the wave attenuation perspective. In metallic films, where the damping α is mostly at the order of 10^{-3}, the propagation lengths are typically only a few micrometers. The propagation length can be very long, even in the cm range, for low damping materials, such as yttrium iron garnet (YIG[12]).

[12] $Y_3Fe_5O_{12}$

1.8.1 Magnetostatic surface waves (MSSW)

When $\boldsymbol{k}$ and $\boldsymbol{M}$ are both in-plane and $\boldsymbol{k} \perp \boldsymbol{M}$, then the propagation mode is called the magnetostatic surface waves (MSSW). It was first derived by Damon and Eshbach, and therefore, it is also known as the Damon-Eshbach (DE) waves [58]. The dispersion can be calculated as follows:

$$f_{\mathrm{DE}} = \frac{\gamma}{2\pi}\sqrt{B(B+\mu_0 M_S) + \frac{(\mu_0 M_S)^2}{4}(1-e^{-2kt})}. \tag{1.37}$$

The DE mode is localized on one of the layer surfaces, and exhibits an exponential decay of the dynamic magnetization through the layer thickness. The localization shifts to the other surface upon the propagation direction reversal, which means that the DE mode is non-reciprocal [59,60].

There is another mode with the $\boldsymbol{k} \perp \boldsymbol{M}$ configuration in perpendicularly magnetized layers, called the forward volume magnetostatic spin-waves[13] (FVMSW). The forward volume geometry is not achievable in our setup due to the absence of an out-of-plane magnetic field and is not presented in any of the experiments covered by this work. Therefore annotating the $\boldsymbol{k} \perp \boldsymbol{M}$ geometry will always refer to MSSW (DE mode).

1.8.2 Backward volume waves (BVMSW)

When $\boldsymbol{k}$ and $\boldsymbol{M}$ are again both in-plane and $\boldsymbol{k} \parallel \boldsymbol{M}$, then the propagation mode is called the backward volume magnetostatic waves (BVMSW) or simply the backward volume (BV) waves. As the name suggests, the waves propagate through the layer's volume, unlike the surface localized MSSW. The dispersion is calculated as follows:

$$f_{\mathrm{BV}} = \frac{\gamma}{2\pi}\sqrt{B\left[B+\mu_0 M_S\left(\frac{1-e^{-2kt}}{kt}\right)\right]}. \tag{1.38}$$

The BV mode exhibits a decreasing frequency in the dispersion, causing the group velocity to have the opposite sign to the phase velocity (antiparallel to the k-vector), thus the name backward waves. A comparison of the MSSW and BVMSW modes is shown in Fig. 1.11 for CoFeB parameters.

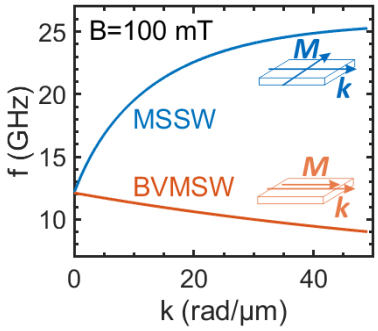

Fig. 1.11: Comparison of the spin-wave dispersion spectra of MSSW and BVMSW modes for a 30 nm CoFeB layer. ($M_S = 1.2$ MA/m, $\gamma/2\pi = 30.2$ GHz/T, $t = 30$ nm)

[13] The forward volume dispersion would be calculated as $f_{\mathrm{FV}} = \frac{\gamma}{2\pi}\sqrt{B\left[B+\mu_0 M_S\left(1-\frac{1-e^{-2kt}}{kt}\right)\right]}$.

1.9 General description of spin-waves by Kalinikos and Slavin

The main limitation of the spin-wave modes presented in Sections 1.8.1 and 1.8.2 is the absence of the exchange interaction; the magnetic interactions were assumed to be dipolar only. The following description takes the exchange interaction into account. Hence it will be referred to as the dipole-exchange model. It will also overcome other limitations of previous expressions, which described only the cases when the k-vector is either parallel or perpendicular to magnetization, and they did not take into account the quantized modes $n > 0$ (PSSW). The dipole-exchange model presented in this section will express the dispersion relation for any angle of propagation, any quantization number (it includes PSSW as the quantized modes can also propagate, i.e., they can have a non-zero in-plane k-vector), it will also allow the use of partially pinned boundary conditions, and lastly, it will allow us to calculate mode hybridizations.

Please note that throughout this work, the symbol[14] k (with no index) will correspond only to the absolute value of the in-plane component of the total k-vector k_{tot} [k_{tot} contains all components, as shown later in Eq. (1.43)]. The quantized part of k_{tot} is sometimes annotated κ and for the most used boundary condition of totally unpinned surface spins, it can be calculated as $\kappa_n = n\pi/t$, where n is the quantization factor. Quantization can also occur for in-plane confined elements (e.g., magnonic waveguides), which is not dealt with in this thesis (see, e.g., [35,61]).

1.9.1 Dipole-exchange dispersion relations of spin-waves

The approximative general description of spin-wave dispersions was provided in the 1980s by Kalinikos and Slavin [62], and is described with the following equations:

$$f = \frac{1}{2\pi}\sqrt{(\omega_B + A\omega_M k_{\mathrm{tot}}^2)(\omega_B + A\omega_M k_{\mathrm{tot}}^2 + \omega_M F_n)}, \tag{1.39}$$

where we can substitute:

$$\omega_B = \gamma B, \tag{1.40}$$

$$\omega_M = \mu_0 \gamma M_s, \tag{1.41}$$

$$A = l_{\mathrm{ex}}^2 = \frac{2A_{\mathrm{ex}}}{\mu_0 M_s^2}, \tag{1.42}$$

and k_{tot} is the total k-vector considering both continuous and quantized wave components:

$$k_{\mathrm{tot}} = \sqrt{k^2 + \kappa_n^2}, \tag{1.43}$$

$$\kappa_n = \frac{n\pi}{t}. \tag{1.44}$$

The number $n = 0,1,2,\ldots$ is the quantization factor for perpendicular standing spin-wave (PSSW) modes, and t is the film thickness. The factor F_n represents the following expression:

[14] The original work [62] uses k_ξ

$$F_n = P_n + \sin^2\vartheta\left(1 - P_n(1+\cos^2\varphi) + \frac{\omega_M P_n(1-P_n)\sin^2\varphi}{\omega_B + A\omega_M k_{\mathrm{tot}}^2}\right), \tag{1.45}$$

where $\varphi = \angle(\boldsymbol{k}, \boldsymbol{M}_{\parallel})$ is the in-plane angle of propagation, $\varphi = 90°$ for the $\boldsymbol{k} \perp \boldsymbol{M}$ geometry and $\varphi = 0°$ for the $\boldsymbol{k} \parallel \boldsymbol{M}$ geometry. The angle ϑ is the out-of-plane angle, $\vartheta = 90°$ for in-plane magnetization and $\vartheta = 0°$ for out-of-plane magnetization.

The factor P_n depends on the surface pinning, which will be discussed later. At the extremes, P_n can be calculated for either totally unpinned or totally pinned surface spins.

$\boldsymbol{P_n}$ for totally <u>unpinned</u> surface spins ($\boldsymbol{n = 0, 1, 2, \ldots}$):

$$P_n = \frac{k^2}{k_{\mathrm{tot}}^2} - \frac{1}{1+\delta_{0n}}\frac{k^4}{k_{\mathrm{tot}}^4}\frac{2}{kt}(1-(-1)^n e^{-kt}), \tag{1.46}$$

where δ is the Kronecker delta. In this case $\delta_{0n} = 1$ for $n = 0$, and $\delta_{0n} = 0$ for $n \neq 0$.

$\boldsymbol{P_n}$ for totally <u>pinned</u> surface spins ($\boldsymbol{n = 1, 2, 3, \ldots}$):

$$P_n = \frac{k^2}{k_{\mathrm{tot}}^2} + \frac{k^2\kappa_n^2}{k_{\mathrm{tot}}^4}\frac{2}{kt}(1-(-1)^n e^{-kt}). \tag{1.47}$$

Note that this expression for totally pinned conditions cannot be used for the zeroth mode[15].

The surface pinning can be more generally expressed with the pinning parameter d having a value of anything between $d = 0$ for totally unpinned surface spins and $d = \infty$ for totally pinned surface spins. This is called partially pinned boundary conditions, that are discussed in 1.9.2.

Fig. 1.12 shows representative plots of the dipole-exchange model calculated for a CoFeB layer. Fig. 1.12(a) compares the data plotted in Fig. 1.11 with the Kalinikos-Slavin model showing the difference at higher k-vector values as this is the exchange dominated region in the dispersion. The $\boldsymbol{k} \parallel \boldsymbol{M}$ geometry now exhibits a nonmonotonic behavior with one minimum because the dispersion in the exchange dominated regime always has a rising character. Fig. 1.12(b) shows the same plot for a higher layer thickness of $t = 100$ nm, where we can observe few attributes. The $\boldsymbol{k} \perp \boldsymbol{M}$ geometry has a minimum as well as the $\boldsymbol{k} \parallel \boldsymbol{M}$ geometry, where the minimum is significantly deeper and at a higher k value. The initial slope of the $\boldsymbol{k} \perp \boldsymbol{M}$ geometry dispersion is also much steeper.

Although we plotted the spectra up to $k = 150$ rad/μm, we have to keep in mind that most experiments are limited to work only up to a few tens of rad/μm at most. The experiments presented in this work mostly did not overcome 10 rad/μm.

An interesting feature is the mode crossing of $n = 0$ mode with $n > 0$ modes, which is observable at higher thicknesses. Fig. 1.12(a) shows plots of CoFeB 100 nm layer for modes from $n = 0$ to $n = 3$, where we can see the crossings. This can potentially lead to mode hybridization as the degenerate states are prohibited, which will be discussed in the following subsection. In Fig. 1.12(b), we can also notice the minimum in the $\boldsymbol{k} \perp \boldsymbol{M}$ dispersion at approx. 50 rad/μm. This would mean that the group velocity will become negative. This was previously shown to be an inaccuracy of this model, and it is not physically valid [63].

[15] Also often called the fundamental mode.

A mathematically simplified version of the dipole-exchange model expressed from Eq. (1.39)-(1.46) for the case of in-plane magnetized sample, totally unpinned surface spins, and only for $n = 0$ is provided with the following equation [61]:

$$f = \frac{\gamma}{2\pi}\sqrt{\left(B + \mu_0 M_s P \sin^2\varphi + \frac{2A_{\text{ex}}}{M_S}\,k^2\right)\left(B + \mu_0 M_S(1-P) + \frac{2A_{\text{ex}}}{M_S}\,k^2\right)}, \tag{1.48}$$

where $\varphi = \angle(\boldsymbol{k}, \boldsymbol{M})$ is the in-plane angle of propagation, $\varphi = 90°$ for the $\boldsymbol{k} \perp \boldsymbol{M}$ geometry and $\varphi = 0°$ for the $\boldsymbol{k} \parallel \boldsymbol{M}$ geometry. The parameter P is expressed as

$$P = 1 - \frac{(1 - e^{-kt})}{kt}. \tag{1.49}$$

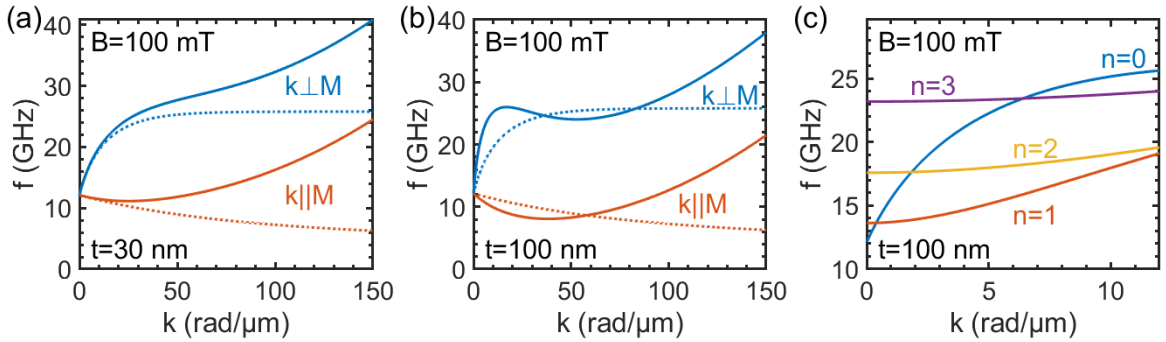

Fig. 1.12: Kalinikos-Slavin dipole-exchange model (for totally unpinned surface spins) plotted for CoFeB layer with parameters: $M_s = 1.2$ MA/m, $\gamma/2\pi = 30.2$ GHz/T, $A_{ex} = 15$ pJ/m, and thickness (a) $t = 30$ nm, (c,d) $t = 100$ nm. Dotted lines represent the dipolar-only dispersions calculated by Eq. (1.37) and (1.38). (a,b) shows the zeroth mode only, (c) shows the zeroth and the first three PSSW modes.

1.9.2 Partially pinned boundary conditions

The previous section showed calculations of the dipole-exchange dispersion spectra but was limited to the boundary conditions with either totally unpinned or totally pinned surface spins. This section introduces general surface pinning based on [62], using the parameter d to express the pinning strength. While the theory was developed using pinning parameters for each surface of the layer separately (d_1 and d_2), we will consider only the scenario of symmetrical pinning, with parameters $d_1 = d_2 = d$. We also consider equal pinning strength for all components of dynamic magnetization. The parameter d ranges from $d = 0$ for totally unpinned surface spins and $d = \infty$ for totally pinned surface spins. For our most interesting thickness $t = 100$ nm, the most significant change takes place between $d = 1 \cdot 10^7$ and $1 \cdot 10^8$, everything smaller is very close to totally unpinned, and anything higher is very close to totally pinned surface spins.

The previously presented math in Eq. (1.39)-(1.45) will remain unchanged. The difference will project only into the parameter P_n. This P parameter will also serve in the next section regarding mode hybridizations, for which we will need the full definition of the P parameter as a combination of two quantization numbers n and n'. The pinning dependent $P_{nn'}$ parameter is calculated as follows:

$$
\begin{aligned}
P_{nn'} = \frac{k^2}{k_{\mathrm{tot},n}^2}\delta_{nn'} \\
&+ \frac{kA_nA_{n'}}{2tk_{\mathrm{tot},n}^2k_{\mathrm{tot},n'}^2}\Bigg[(k^2-d^2)e^{-kt}(\cos\kappa_n t + \cos\kappa_{n'} t) \\
&+ (k-d)e^{-kt}\Bigg((dk-\kappa_n^2)\frac{\sin\kappa_n t}{\kappa_n} \\
&+ \left(dk-\kappa_{n'}^2\right)\frac{\sin\kappa_{n'} t}{\kappa_{n'}}\Bigg) \\
&- (k^2-d^2)(1+\cos\kappa_n t\cos\kappa_{n'} t) \\
&+ \left(\kappa_n^2\kappa_{n'}^2 - d^2k^2\right)\frac{\sin\kappa_n t}{\kappa_n}\frac{\sin\kappa_{n'} t}{\kappa_{n'}} \\
&- d\Bigg(k_{\mathrm{tot},n}^2\cos\kappa_{n'} t\frac{\sin\kappa_n t}{\kappa_n} \\
&+ k_{\mathrm{tot},n'}^2\cos\kappa_n t\frac{\sin\kappa_{n'} t}{\kappa_{n'}}\Bigg)\Bigg],
\end{aligned}
\tag{1.50}
$$

where we can substitute:

$$
A_n^2 = 2\left[\frac{\kappa_n^2+d^2}{\kappa_n^2} + \frac{\sin\kappa_n t}{\kappa_n t}\left(\frac{\kappa_n^2-d^2}{\kappa_n^2}\cos\kappa_n t + \frac{2d}{\kappa_n}\sin\kappa_n t\right)\right]^{-1}, \tag{1.51}
$$

$$
k_{\mathrm{tot,n}} = \sqrt{k^2+\kappa_n^2}, \tag{1.52}
$$

For n', the Eq. (1.51) and (1.52) will remain the same, but $n = n'$ will be substituted. The coefficient κ_n can no longer be expressed as $n\pi/t$ (which works only in the limit cases for $d = 0$ and $d = \infty$) but it has to be calculated as a solution of the following transverse equation:

$$
(\kappa_n^2 - d^2)\tan(\kappa_n t) = 2\kappa_n d. \tag{1.53}
$$

This equation has one trivial solution for $\kappa_n = 0$, which will not be considered, and an infinite number of non-trivial solutions. Fig. 1.13 shows the left and right parts of the transverse equation plotted for a range of κ values (using $d = 1 \cdot 1.2^7$, and $t = 100$ nm), where the solutions are intersections of the two lines, marked in red circles.

When considering the partial pinning and no longer using the Eq. (1.44), we have to define the meaning of an n^{th} mode. For the zeroth mode $n = 0$ we will use the first non-trivial solution of the transverse equation, marked κ_0. Then the first mode $n = 1$ will be the second non-trivial solution κ_1, etc. Hence the κ_n will be the $(n+1)^{\mathrm{th}}$ solution of the transverse equation. For the case of totally unpinned surface spins, where the pinning parameter approaches zero ($d \to 0$), the first solution converges to zero ($\kappa_0 \to 0$), and $\kappa_n = n\pi/t$. For the case of totally pinned surface spins, where the pinning parameter goes to infinity ($d \to \infty$), the first solution converges $\kappa_0 \to \pi/t$, and the solutions will be $\kappa_n = (n+1)\pi/t$. For this definition of the n^{th} mode, we have to keep in mind, that it is inconsistent with Eq. (1.47) from [62], calculating the totally pinned surface spins. Totally pinned surface spins will not allow the existence of unconfined modes, and for that reason, the authors of [62] expressed the Eq. (1.47) for $n \geq 1$, where n marks the confinement order, while we will rather keep the

definition for $n = 0$ being the lowest, fundamental mode because it will hold consistency when plotting the dispersions for different pinning parameters (Fig. 1.14).

Example calculations are provided in Fig. 1.14 showing the results for a variety of different pinning parameters from $d = 0$ for totally unpinned (also previously shown in Fig. 1.12) to $d = 1 \cdot 10^{10}$ which is effectively equal to totally pinned surface spins. All calculations are shown for 100 mT because it is a typical field level in our experiments. We show the dispersions for two thicknesses $t = 30$ nm (a,c) and $t = 100$ nm (b,d), and two geometries for $\boldsymbol{k} \perp \boldsymbol{M}$ (a,b), and for $\boldsymbol{k} \parallel \boldsymbol{M}$ (c,d).

Each of the graphs also shows two modes for $n = 0$ and $n = 2$, for the reason of ground preparation for the calculation of mode hybridizations, because there we will mostly be interested in the hybridization of the zeroth and second modes. For the modes to hybridize, they have to be crossing, which out of the four plotted cases happens only in Fig. 1.14(b). The zeroth and second modes are plotted in the same color for a given pinning parameter. Therefore we can observe the changing crossing's position, going up in frequency and k-vector. There is also a second crossing in k-vector range approx. 18 to 32 rad/µm, but the second crossing is well beyond our experimental capability and will be less interesting. Because the κ values now have to be calculated numerically, Table 1.1 states their values for each spectrum plotted in Fig. 1.14.

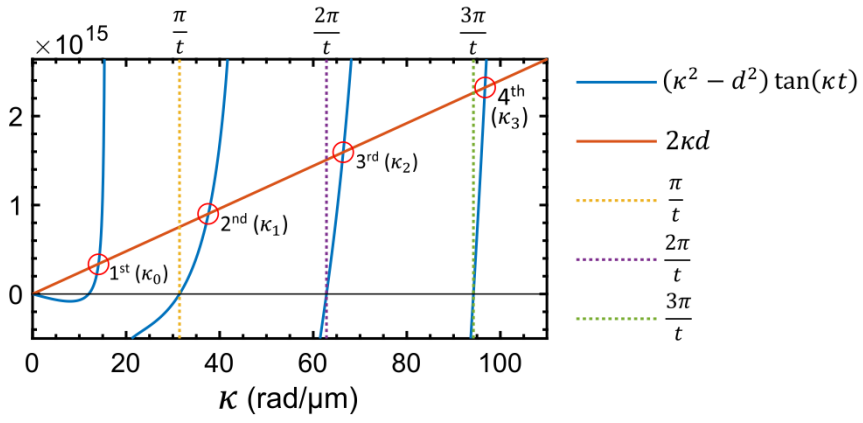

Fig. 1.13: Left and right sides of the transverse equation plotted for a pinning parameter $d = 1 \cdot 1.2^7$, and thickness $t = 100$ nm. The solutions are marked with red circles. Values $n\pi/t$ are marked for reference.

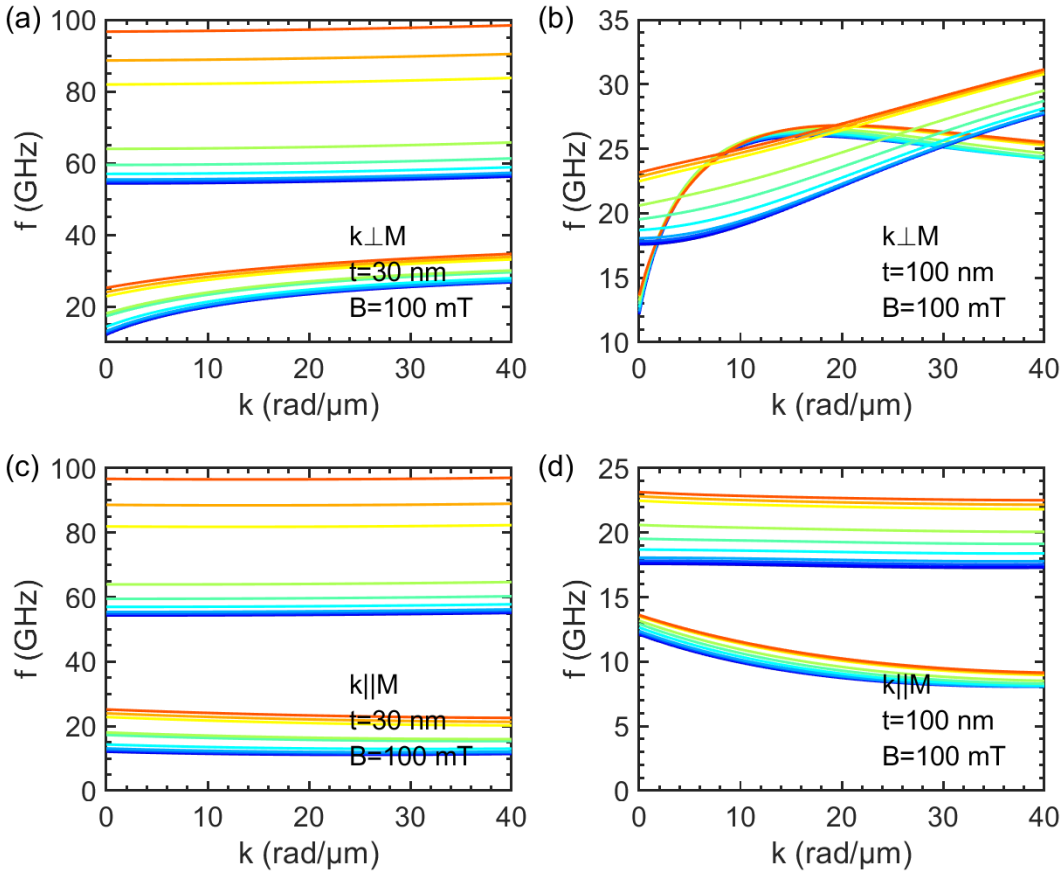

Fig. 1.14: Dipole-exchange spectrum using the general surface pinning parameter d plotted for the first and third κ solutions ($n = 0 \rightarrow \kappa_0$ is the first non-trivial solution, and $n = 2 \rightarrow \kappa_2$ is the third non-trivial solution). Legend is provided in Table 1.1. The used material parameters for CoFeB are: $M_s = 1.2$ MA/m, $\gamma/2\pi = 30.2$ GHz/T, $A_{ex} = 15$ pJ/m, and thicknesses: (a,c) $t = 30$ nm, (b,d) $t = 100$ nm. Configurations: (a,b) $\boldsymbol{k} \perp \boldsymbol{B}$ geometry, (c,d) $\boldsymbol{k} \parallel \boldsymbol{B}$ geometry. The dispersion for $d = 0$ represent totally unpinned surface spins, and for $d = 1 \cdot 10^{10}$ represent the surface spins that are effectively totally pinned (increasing has negligible difference).

Table 1.1: Legend for Fig. 1.14. The κ values are solutions of the Eq. (1.53), and they are depend on the pinning parameter and thickness only (independent of material parameters).

d	color	$t = 30$ nm		$t = 100$ nm	
		κ_0 (rad/μm)	κ_2 (rad/μm)	κ_0 (rad/μm)	κ_2 (rad/μm)
0		0	209.4	0	62.8
$1.0 \cdot 10^6$		8.1	209.8	4.4	63.1
$5.0 \cdot 10^6$		18.0	211.0	9.6	64.4
$1.0 \cdot 10^7$		25.2	212.6	13.1	65.8
$2.5 \cdot 10^7$		38.4	217.1	18.6	69.7
$5.0 \cdot 10^7$		60.9	224.1	22.8	74.6
$1.0 \cdot 10^8$		65.9	236.1	26.3	80.7
$5.0 \cdot 10^8$		92.5	280.1	30.2	90.7
$1.0 \cdot 10^9$		98.2	295.0	30.8	92.4
$1.0 \cdot 10^{10}$		104.0	312.1	31.4	94.1

1.9.3 Hybridization of $n = 0$ and $n' > 0$ modes

This section will deal with the mode crossings, where the dispersion modes hybridize. The hybridized modes were also described in [62], which will provide the basis for the presented equations. We will be interested mainly in the crossings of the zeroth mode $n = 0$, with the PSSW modes, for which we will use $n' > 0$. Each of them have a dispersion spectrum $f_n = \omega_n/2\pi$ and $f_{n'} = \omega_{n'}/2\pi$ calculated using the Eq. (1.39). The hybridized modes will then be calculated as first-order perturbation for previously calculated degenerative state. For in-plane magnetized sample we can then calculate frequencies near the point of degeneracy from the following characteristic equation [64]:

$$\begin{aligned}(\omega_{nn'}^2 - \omega_n^2)(\omega_{nn'}^2 - \omega_{n'}^2) &\\ = \omega_M^2\left[\left(\Omega_n + \frac{\omega_M}{2}\right)\left(\Omega_{n'} + \frac{\omega_M}{2}\right) - \omega_{nn'}\right] 2\left(P_{nn'}^2 + 4Q_{nn'}^2\right) &\\ + \omega_M^4\left(P_{nn} - \frac{1}{2}\right)\left(P_{n'n'} - \frac{1}{2}\right) 2\left(P_{nn'}^2 - 4Q_{nn'}^2\right) &\\ - \omega_M^4\left(P_{nn'}^2 - 4Q_{nn'}^2\right)^2,&\end{aligned} \tag{1.54}$$

where $P_{nn'}$ is calculated using Eq. (1.50), the factor $Q_{nn'}$ is expressed as

$$\begin{aligned}Q_{nn'} = \frac{kA_nA_{n'}}{2tk_{\mathrm{tot},n}^2k_{\mathrm{tot},n'}^2}\Bigg[&(k^2 - d^2)e^{-kt}(\cos\kappa_n t - \cos\kappa_{n'}t)\\ &+ (k-d)e^{-kt}\left((dk - \kappa_n^2)\frac{\sin\kappa_n t}{\kappa_n} - \left(dk - \kappa_{n'}^2\right)\frac{\sin\kappa_{n'}t}{\kappa_{n'}}\right)\\ &+ (k-d)\left(\left(dk - \kappa_{n'}^2\right)\cos\kappa_n t\frac{\sin\kappa_{n'}t}{\kappa_{n'}}\right.\\ &\left.- (dk - \kappa_n^2)\cos\kappa_{n'}t\frac{\sin\kappa_n t}{\kappa_n}\right)\\ &+ (1 - \cos\kappa_n t\cos\kappa_{n'}t)\frac{2\left[d^2k^2 + \kappa_n^2\kappa_{n'}^2 + \left(\kappa_n^2+\kappa_{n'}^2\right)(k^2+d^2)\right]}{\kappa_{n'}^2 - \kappa_n^2}\\ &- \frac{\sin\kappa_n t\sin\kappa_{n'}t}{\kappa_n\kappa_{n'}\left(\kappa_{n'}^2 - \kappa_n^2\right)}\left(dk\left(\kappa_n^4+\kappa_{n'}^4\right) + \left(d^2k^2 - \kappa_n^2\kappa_{n'}^2\right)\left(\kappa_n^2+\kappa_{n'}^2\right)\right.\\ &\left.- 2\kappa_n^2\kappa_{n'}^2[d^2 + k^2 - dk]\right)\Bigg].\end{aligned} \tag{1.55}$$

The coefficients A_n and $A_{n'}$ are calculated using Eq. (1.51), and finally, the coefficient Ω_n is calculated as

$$\Omega_n = \omega_B + \omega_M A(\kappa_n^2 + k^2). \tag{1.56}$$

The characteristic equation (1.54) can be solved as:

$$\omega_{nn'} = \sqrt{\frac{\omega_n^2 + \omega_{n'}^2 - 2P_{nn'}^2\omega_M^2 \pm \sqrt{\Gamma}}{2}}, \tag{1.57}$$

where Γ is a factor depending on both the dipolar (P and Q factors), and exchange interaction (Ω factors) which will be substituted with:

$$\begin{aligned}\Gamma = \omega_n^2 + \omega_{n'}^2 - 4P_{nn'}^2\omega_{n'}^2\omega_M^2 - 2\omega_n^2\left(\omega_{n'}^2 + 2P_{nn'}^2\omega_M^2\right) \\ + 4P_{nn'}^2\omega_M^2\left[\Omega_n(2\Omega_{n'} + \omega_M) + \omega_M\Omega_{n'}\right. \\ \left. + \omega_M^2\left(1 - P_{n'n'} - P_{nn} + 2P_{n'n'}P_{nn} + 2P_{nn'}^2\right)\right].\end{aligned} \tag{1.58}$$

Now we can use the presented method to calculate hybridized dispersions. We will be focusing on 100 nm thick CoFeB in the $\mathbf{k} \perp \mathbf{B}$ geometry because it is also a measured type of sample, with experimental results presented in Chapter 5. Fig. 1.15(a) shows the dipole-exchange dispersion relations for zero pinning to show a reference of the crossing points. Fig. 1.15(b-d) shows the calculated hybridized modes for $d = 0$, $\mathrm{d} = 1.2 \cdot 10^7$, and $\mathrm{d} = 3.0 \cdot 10^7$ respectively, where we can observe the influence of the pinning parameter on the dispersion openings. Modes $n = 0$ and $n = 1$ do not hybridize, but modes $n = 0$ and $n = 2$ show an increasing opening at the crossing. Therefore, the experimentally detected opening can be used to estimate the pinning parameter.

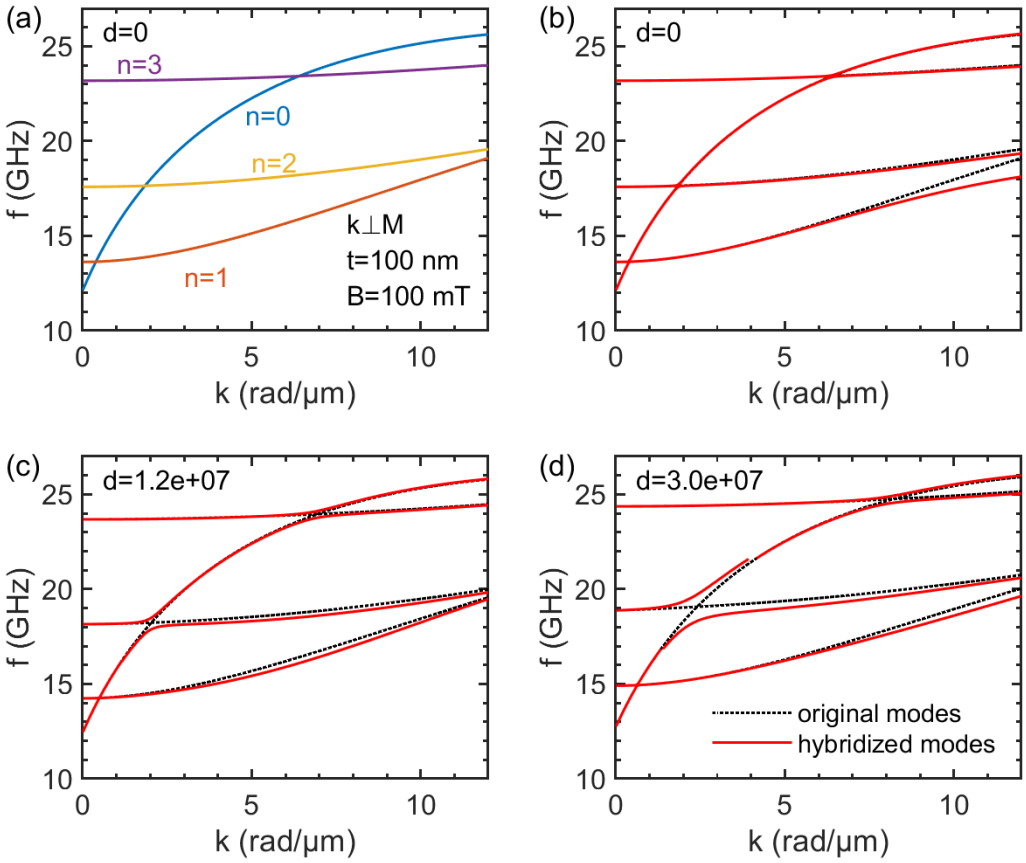

Fig. 1.15: Dispersion calculation for thickness $t = 100$ nm, and CoFeB parameters: $M_s = 1.2$ MA/m, $\gamma/2\pi = 30.2$ GHz/T, $A_{ex} = 15$ pJ/m. (a) Dispersion modes without the calculated hybridizations showing the mode crossings for pinning $d = 0$. (b) Hybridized dispersions for $d = 0$ calculated using Eq. (1.54), and (c) $d = 1.2 \cdot 10^7$, (d) $d = 3.0 \cdot 10^7$. The dashed lines are showing the positions of the original modes. The opening for $n = 0$ and $n = 1$ stays minimal, while increasing of the pinning parameter opens the dispersion crossings for $n = 0$ and $n = 2$ modes.

2 Used experimental methods with examples

This chapter intends to describe the experimental methods used throughout this work. An exception is the vector network analyzer, to which Chapter 4 is devoted. A larger part of this chapter consists of microscopy techniques with magnetic contrast imaging capability because they are beneficial for understanding the micromagnetic behavior of studied structures. Even though the imaging comes at a very high cost of the instrumentation (electron microscopes or even synchrotron), it is still very important because the direct observation of the studied processes cannot be entirely replaced by indirect methods based on, e.g., electric charge transport. Nevertheless, if we consider a functional on-chip device, the focus logically moves towards the electrical excitation/detection of all necessary physical processes. This includes magnetic properties, e.g., during memory cells' readout (traditionally in hard disk drives and nowadays even in magnetic RAMs). We probe the magnetization in disks using the anisotropic magnetoresistance effect, where the main advantage is in its relative simplicity. The disadvantage lies in higher sample preparation effort as it usually requires multiple step lithography with precise alignment.

2.1 Lorentz Transmission Electron Microscopy (LTEM)

Since the first electron microscope invention in the early 1930s, the field of transmission electron microscopy (TEM) has developed into one of the most useful tools in structural analysis. Materialists use it for electron diffraction and also for its high-resolution imaging, nowadays reaching subångström resolution. Besides standard imaging and electron diffraction, many other detection techniques were also developed, including tomography, secondary and backscatter electron imaging, electron holography, cathodoluminescence, and magnetic imaging [65]. This section refers to the last-mentioned - magnetic imaging - where the method’s full name is Lorentz transmission electron microscopy (LTEM) or Lorentz microscopy.

Before describing the principles of magnetic imaging function in TEM, we must discuss the optics used in these microscopes. They can use either an electric or magnetic field to focus or transform the electron beam. Much lower aberrations of the magnetic type of lenses give them superiority over electrostatic lenses, and they are used almost exclusively. Furthermore, the most important lens in the microscope – the objective lens – is always the immersion type, i.e., there is a strong leak of its magnetic field to the sample space. From here originates the evident conflict of the objective’s magnetic field (typical values over 2 T) with the studied samples because the field is high enough to saturate the vast majority of the magnetic specimen. This problem is solved by equipping the microscope with an extra lens taking over the objective’s purpose and by turning the objective lens off. This extra lens is placed further away from the sample to leave the sample space free of the magnetic field, and it is usually referred to as the Lorentz lens. The tradeoff is the loss of resolution (due to much higher

aberrations), going down to about 1 nm for imaging and it is (in some of the techniques) even further reduced for acquiring the magnetic contrast.

During the TEM imaging, a thin sample is illuminated with a parallel electron beam. If the sample is magnetic, then its interaction with the electron beam can be understood in terms of the Lorentz force, of which the magnetic part is:

$$\boldsymbol{F} = -e(\boldsymbol{v} \times \mathbf{B}). \tag{2.1}$$

Considering a specimen of thickness t with in-plane magnetic domains, and with the saturation induction of the magnetic material B, the magnitude of the Lorentz deflection angle β is given by

$$\beta = \frac{eB\lambda t}{h}, \tag{2.2}$$

where e is the positive elementary charge, h is the Planck's constant, and λ is the electron wavelength [66–68]. This angle β is typically in order of μrad, which is about three orders of magnitude lower than the typical angles in Bragg diffraction [69]. The consequences of the electron deflection in the magnetic field of the sample can be used for the two basic imaging modes in Lorentz microscopy: the Fresnel mode and Foucault mode that are both schematically illustrated in Fig. 2.1. Further use can be implemented in the scanning mode of TEM for acquiring the so-called differential phase contrast. These three methods will be described in the following subsections.

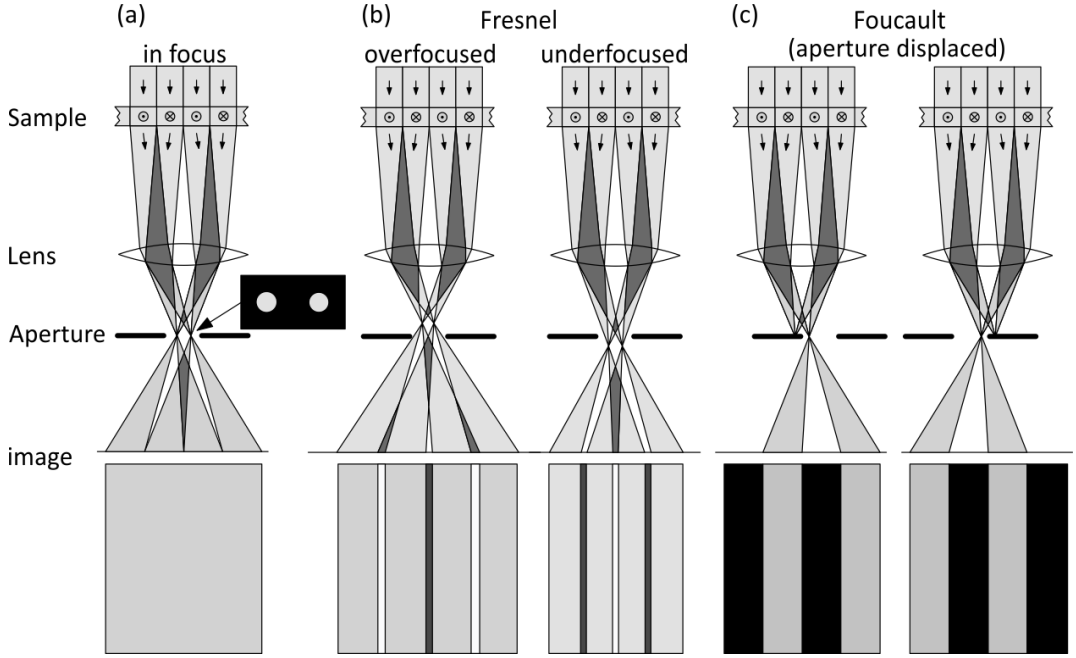

Fig. 2.1: Schematics of the basic LTEM function. (a) When the specimen is in focus, there is no magnetic contrast. (b) Defocusing leads to the Fresnel contrast highlighting the domain walls. (c) The Foucault contrast is introduced by inserting an aperture to the diffraction plane of the Lorentz lens (in the sense of dark-field imaging), highlighting only a certain range of the in-plane magnetization directions. Adapted from [70].

Fresnel mode

When a magnetic sample is imaged with the microscope's optics correctly focused, there is no observable magnetic contrast [Fig. 2.1(a)]. The Fresnel mode is the easiest method of achieving magnetic contrast because it only uses defocusing of the Lorentz lens. Under these conditions, the magnetic domain walls are imaged as alternate bright (convergent) and dark

(divergent) lines [Fig. 2.1(b)]. The bright lines occur when the domain walls are positioned such that the magnetization on either side deflects the electrons towards the domain wall. The vectorial product nature of the Lorentz force yields no contrast related to the out-of-plane magnetization component. This is unfortunate for imaging the magnetic vortex cores. Images of the magnetic vortex show a white/black spot at the vortex core position, but the contrast gives the circulation, not polarity. Determination of the vortex polarity was also presented, but it was based only on the small displacement of the intensity spot to the opposite directions for opposite polarities when the sample was tilted [71]. The Fresnel mode is useful for real-time studies of magnetization reversal, as it is relatively easy to implement and can provide a frame rate up to approx. 1 Hz, depending on the camera settings. However, this mode does not provide any direct information about the magnetization direction within the sample. In case we want to match the Fresnel images to magnetization maps, we must calculate the magnetic contrast. This can be done with the Micromagnetic Analysis to Lorentz TEM Simulation (MALTS [72]), which is an open-source toolbox using magnetization vector files, typically calculated by micromagnetic simulators (e.g., OOMMF), as inputs.

It should be noted that the spatial resolution is not high (typically around 50 nm) because the images must be recorded at a relatively high value of objective lens defocus (in the mm range) to provide sufficient contrast [70]. Changing the defocus sign (i.e., going between underfocusing and overfocusing) reverses the contrast. The images presented in this work were acquired on FEI Titan Themis TEM at the acceleration voltage of 300 kV using underfocus. Example images acquired from NiFe rectangles and disks using the Fresnel mode are presented in Fig. 2.2.

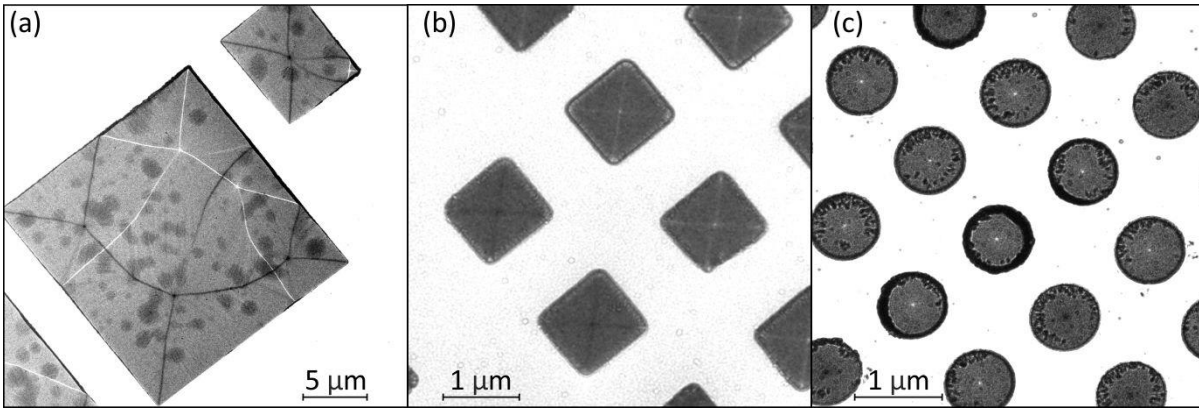

Fig. 2.2: Examples of Fresnel LTEM imaging performed on FEI Titan: (a) domain structure in larger patterns, (b) Landau patterns in 1 µm squares, (c) vortex states in 500 nm disks. The contrast does not provide any direct information about the local direction of magnetization but rather highlights the domain walls' positions. In the case of the disks, white/black dots at the center provide the position of the vortex core (but not its polarity), and the color depends on the circulation being opposite for white and black.

Foucault mode

This mode uses the fact that the diffraction pattern splits while imaging a magnetic sample [schematically shown at the aperture plane of Fig. 2.1(a)]. To image magnetic domains using the Foucault mode, the Lorentz lens is kept in focus (contrary to defocusing in the Fresnel mode), but a portion of the diffraction pattern is blocked by displacing an aperture located in the same plane as the diffraction pattern. Under normal TEM conditions, this aperture would be the so-called objective aperture because it is located in the objective lens'

back-focal plane. However, when using the Lorentz lens for imaging, this lens's back-focal plane is not at the position of the objective aperture, but it is very close to the so-called selected area aperture.

The contrast results from the magnetization direction within the magnetic domains. Bright areas correspond to domains where the magnetization orientation is such that electrons are allowed to pass through the aperture, and dark areas to those where magnetization orientation is in the directions of which the aperture blocks the electrons. By knowing the relative direction of the aperture and image, the direction of magnetization within the various domains can be qualitatively determined [70]. A useful tip on how to distinguish the in-plane magnetization spread represented by the white contrast during acquisition is to take an image of a magnetic disk in the vortex state that is few micrometers wide because it continuously contains all directions of the in-plane magnetization.

An example of Foucault imaging is presented in Fig. 2.3. In the case of our microscope, the difficult part of this mode rests in imaging of the diffraction pattern, which is not the same procedure as in normal TEM mode (in normal TEM imaging, the projection system readjusts to image the diffraction pattern on the fluorescent screen). In the Lorentz mode, the diffraction image is achieved by lowering the Lorentz lens excitation by a large factor in the imaging mode until the diffraction pattern appears (while considering the spot splitting due to magnetic samples to be very small, in many cases even hidden in the central spot). Then the aperture is placed to the desired place, and the projection system is switched to its diffraction mode, in which we find the image by changing the diffraction focus. Even after the image is successfully found, the limiting factor might be the camera length[16] of the diffraction mode limiting the magnification (in theory not the resolution, but in the end, this is connected to the pixel size of the used camera), making it unusable for structures smaller than 500 nm.

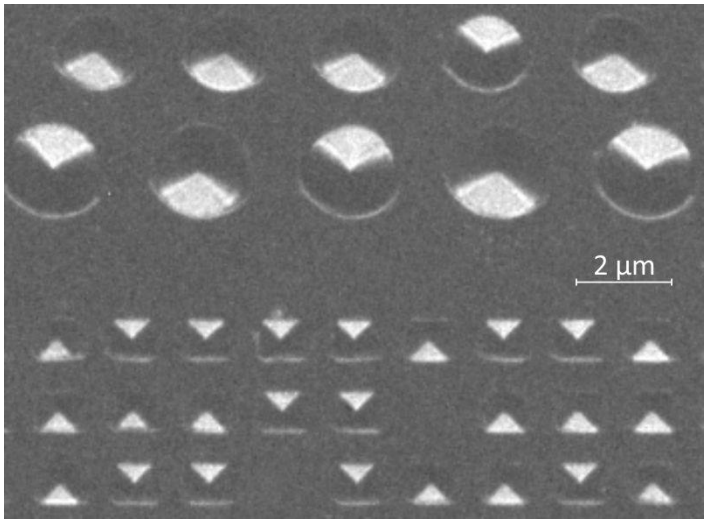

Fig. 2.3: Example of Foucault LTEM imaging performed on FEI Titan. The aperture was placed into the diffraction spot in a way that only one direction of the magnetization along the x-axis is visible (the white contrast). The top of the image shows 2 µm and 2.5 µm wide disks with vortex states of opposite circulations when the bright part of the disk is at the upper/lower side. A similar contrast is visible on 1 µm sized squares at the bottom part of the image. The bright parts of the squares at the upper/lower side correspond to the opposite circulations of the Landau patterns in the squares.

[16] Camera length is a parameter used in transmission electron microscopes, which effectively changes the magnification of the diffraction pattern.

Structures with lateral size at least 1 μm, e.g., the squares in Fig. 2.3, are still imaged with sufficient resolution.

In general, we can say that both Fresnel and Foucault microscopy are fairly simple to implement, provide a clear picture of the overall domain geometry, and they are a useful indication of the directions of magnetization in (at least) the larger domains. However, a significant drawback of the Fresnel mode is that no information is directly available about the direction of magnetization within any single domain, whilst reproducible positioning of the contrast-forming aperture in the Foucault mode is difficult [70].

Differential phase contrast

Unlike the Fresnel and Foucault imaging modes that are performed in the widefield TEM mode, the Differential Phase Contrast (DPC) uses the scanning TEM (STEM) mode to probe the magnetization of the studied sample. The main idea behind it remains the same – the transmitted electron beam is deflected due to the Lorentz forces originating at the sample. The implementation is different because the image is not acquired on a camera or fluorescent screen. Instead, the transmitted intensity is recorded on a detector, which is split into segments (typically four), and they are read separately (schematics of the DPC function is shown in Fig. 2.4). As the beam is deflected to the direction perpendicular to the in-plane magnetization of the studied sample, the magnetic contrast can be acquired by calculating the difference of pairs of the segments and by normalizing it by the sum of segment signals. If we mark the segments with A, B, C and D, then we can produce two orthogonal maps, where the signals are [69]:

$$\mathrm{signal}_1 \approx \frac{(A+B)-(C+D)}{A+B+C+D}, \tag{2.3}$$

$$\mathrm{signal}_2 \approx \frac{(A+D)-(B+C)}{A+B+C+D}. \tag{2.4}$$

An example image of the orthogonal magnetization maps is shown in Fig. 2.5, and the in-plane magnetic contrast is clearly superior to the Foucault images. The magnetic resolution in DPC imaging is mostly defined by the size of the electron probe, which is typically around 10 nm in the field free mode. It was recently further enhanced in an aberration-corrected field-free microscope to achieve the magnetic resolution of 1 nm [73]. Further achievements were also made by employing a pixelated detector (instead of a four-segment detector) in order to gain more information [74] about the sample, especially about its structure.

The DPC method's downside is the limited usability of the objective lens as the magnetic field source. The objective lens can be controlled, but the image distortion is significantly higher than in the Fresnel mode. The DPC signal is crucially dependent on the beam position on the segmented detector, and the extra objective excitation not only damages the resolution, while even more importantly, but also causes beam shifts on the detector. Therefore, even small fields ~ 10 mT require a realignment of the microscope. Larger fields will even require full column realignment, which is a lengthy service procedure not allowed to regular users during microscope operation.

Besides imaging of ferromagnetic structures, DPC can also be used for mapping electric fields in the sample [75] or, most recently, for imaging of antiferromagnetic domains [76]. In both cases, those samples are typically not sensitive to the magnetic field. Therefore, standard STEM imaging using the objective lens may be used with down to subnanometer resolution.

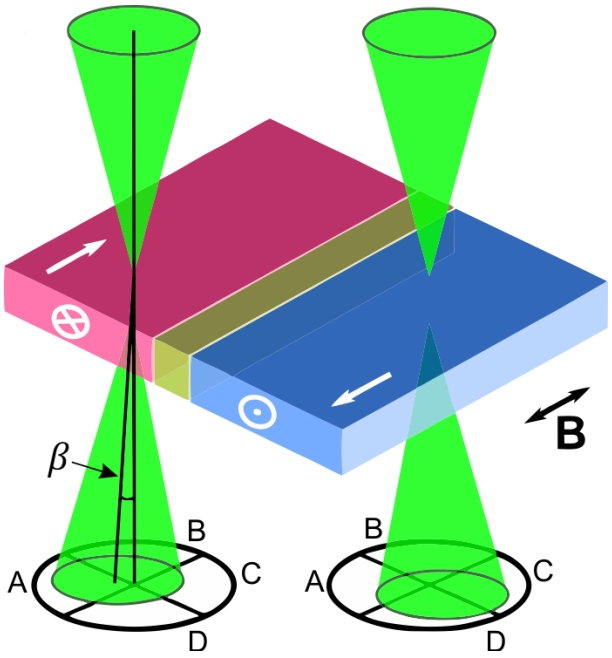

Fig. 2.4: Schematics of DPC in STEM. The electron beam transmitting the sample is deflected in the direction perpendicular to the magnetization direction. Two orthogonal images of magnetization can be calculated by differentiating the segments (marked A-B-C-D) of the detector, as was shown in Eq. (2.3) and (2.4). Reprinted from [74].

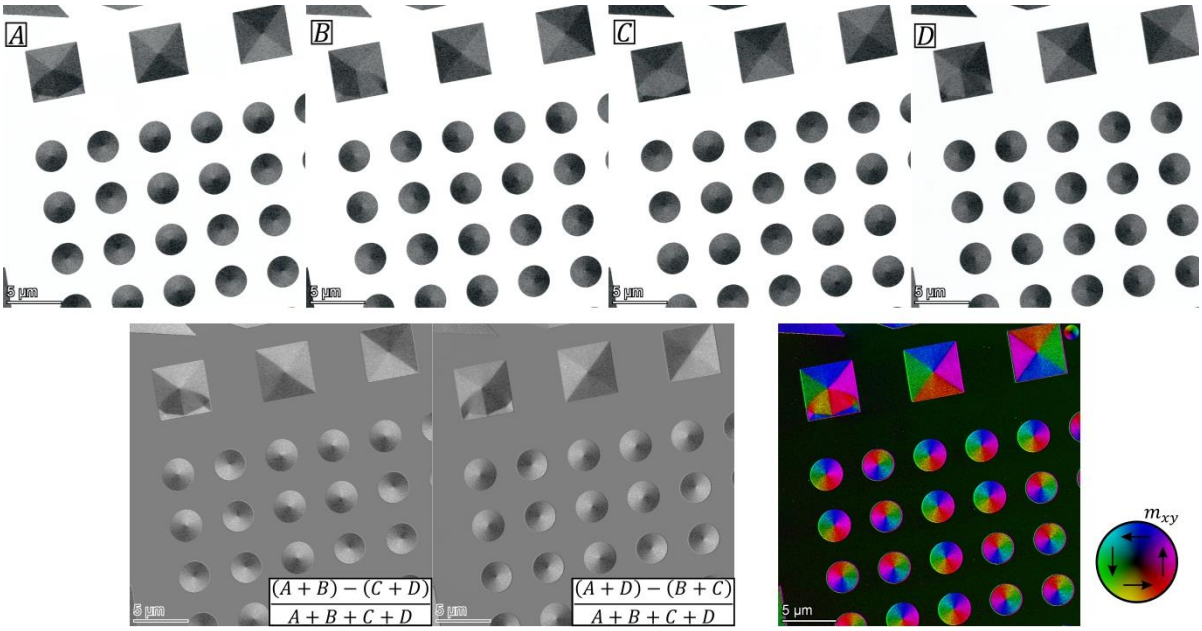

Fig. 2.5: Example of DPC imaging in magnetic rectangles and disk showing the vortex states. The four A-B-C-D images in the top row represent the signals from individual detector segments. The bottom row images show the processed signals using the representation from Eq. (2.3)-(2.4), and the color representation.

2.2 Magnetic Transmission X-ray Microscopy (MTXM)

Magnetic Transmission X-ray Microscopy (MTXM) is one of the types of X-ray microscopy techniques used for magnetic imaging of nanostructures. The contrast is provided by the X-ray Magnetic Circular Dichroism (XMCD), which is the X-ray absorption cross section's dependence on the relative orientation between the helicity of the photon beam and the projection of the magnetization in a ferromagnetic specimen onto the photon propagation direction [77,78]. Its physical origin is closely related to the polar magneto-optical Kerr effect. However, because for the XMCD, the initial state is a well-defined core level state, XMCD features an element-sensitivity, and according to dipole selection rules, also a symmetry-selectivity [79].

The sources of the circularly polarized X-ray radiation, which is essential to observe XMCD contrast, are usually synchrotron storage rings, either at helical undulators or at bending magnets [77]. Our measurements were done at beamline 6.1.2 (XM-1) of the Advanced Light Source (ALS) in Berkeley, California. The system at the ALS is schematically shown in Fig. 2.6. The X-rays emitted from a bending magnet enter the microscope that has an optical design similar to a conventional microscope using visible light – there is a source, a condenser, an objective lens, and a detector. However, because soft X-rays' refractive index is close to one, conventional lenses or mirrors cannot be used. Instead, Fresnel zone plates (circular gratings with a radially increasing line density, see [80] for details) are used to focus the X-ray radiation [77]. Our imaging was carried out with a spatial resolution of 25 nm at Fe L3 absorption edge (707 eV). In contrast to the full field microscope at the ALS beamline 6.1.2, there are also scanning transmission X-ray microscopes used at other beamlines or at other synchrotrons (e.g., BESSY at Helmholtz Zentrum Berlin).

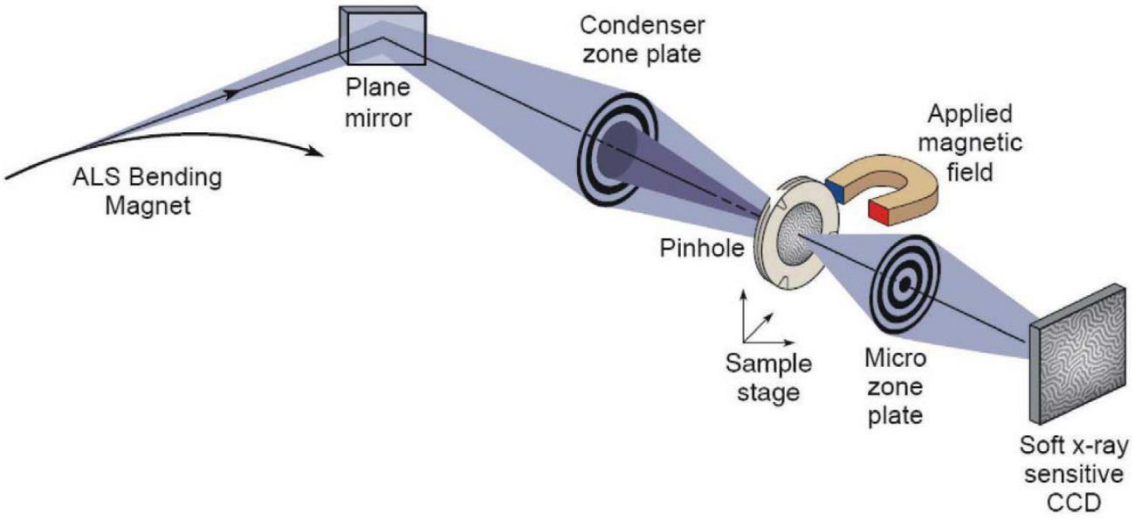

Fig. 2.6: Schematics of MTXM imaging. X-ray radiation from the bending magnet enters the microscope using Fresnel zone plates as the condenser and objective lenses. The image is then acquired on the CCD camera. Reprinted from [77].

Even though this method was used only for static imaging in this work, the pulsed nature of the synchrotron radiation also provides a good temporal resolution in stroboscopic experiments. The resolution is given by the length of the electron bunches circulating in the storage ring. For ALS, it is about 70 ps. While the normal operation mode of the storage ring runs at a repetition frequency of 500 MHz (multi-bunch), it can also be operated in a so-called two-bunch mode with only two electron bunches circulating in the ring. The resulting

repetition rate of 3.05 MHz is much lower as it is more suitable for time-resolved experiments [77]. The results achieved in stroboscopic pump-probe experiments performed at ALS by our group were shown in publications [12,13].

The two-bunch mode sacrifices a lot of intensity to achieve time resolution, so the multi-bunch mode is favored for the static experiments. Example images are shown in Fig. 2.7, wherein case of (a), the vortex cores have out-of-plane magnetization yielding the black/white contrast for opposite vortex polarities. The other example in Fig. 2.7(b) shows the magnetic contrast on a NiFe wire with a propagating domain that is pinned on a notch.

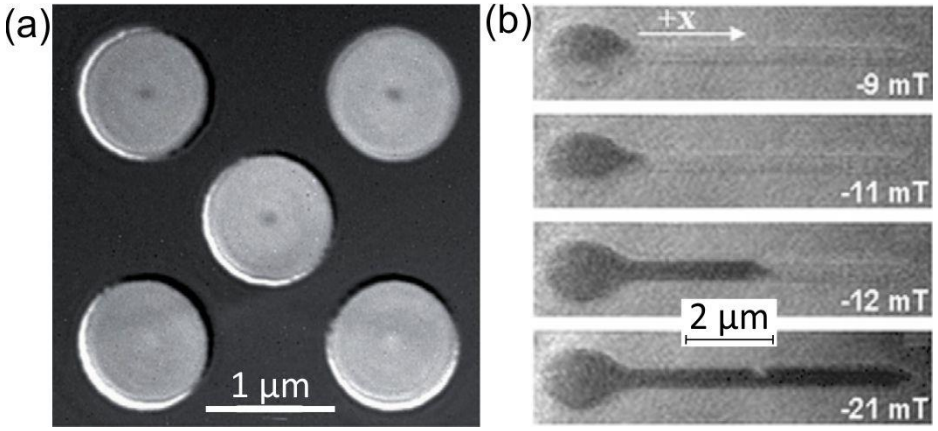

Fig. 2.7: Examples of MTXM images: (a) magnetic vortices, the black/white dots at the disk center represent the opposite vortex polarities. Reprinted from [78]*. (b) MTXM images of a notch-patterned NiFe nanowire in different magnetic fields. The elliptical head and triangular notch serve as a DW nucleation pad and artificial pinning site. Reprinted from* [81]*.*

2.3 Electrical detection by anisotropic magnetoresistance (AMR)

The electrical detection techniques are here to accompany the magnetic imaging. It is a less demanding group of methods in terms of the necessary equipment, although the sample fabrication process is often more difficult. When the electrical properties are dependent on the sample's magnetization state, we talk about magnetoresistance, i.e., a change of electrical resistance with changing the spin configuration inside magnetic structures. There are several types of magnetoresistance effects, of which the simplest one is the anisotropic magnetoresistance (AMR). It was discovered already in the 19th century by William Thomson (honored as Lord Kelvin) [82], but it is a useful detection technique even nowadays. It has rather small amplitude (about 1%) when compared to the other two most common types of magnetoresistance – giant [83] and tunneling [84] – which both exhibit changes in the order of tens to hundreds of percent. On the other hand, the giant or tunneling magnetoresistances are measured in heterostructures while AMR is always present as its resistivity only depends on the angle φ between the vectors of current density $\boldsymbol{j}$ and magnetization $\boldsymbol{m}$. If we suppose resistance $\varrho_{\parallel}$ for $\varphi = 0°$ and $\varrho_{\perp}$ for $\varphi = 90°$, it can be shown, that the resistivity depends on φ as the following function [82,85]:

$$\varrho(\varphi) = \varrho_{\perp} + (\varrho_{\parallel} - \varrho_{\perp}) \cos^2 \varphi. \tag{2.5}$$

The AMR phenomenon is schematically shown in Fig. 2.8 for a magnetic stripe with electrical connections on two sides. The constants $\varrho_{\parallel}$ and $\varrho_{\perp}$ can be measured for each material, the values for NiFe were previously determined in our experiments [85] to be:

$$\varrho_{\parallel} = 7.50 \cdot 10^{-7}\,\Omega\mathrm{m},$$
$$\varrho_{\perp} = 7.40 \cdot 10^{-7}\,\Omega\mathrm{m}. \tag{2.6}$$

Magnetoresistance, being a change in resistance, is often expressed as a percentage of the value at saturation. We can calculate its value from the measured resistance as

$$\mathrm{MR} = \frac{R - R_{\mathrm{sat}}}{R_{\mathrm{sat}}} \cdot 100\%. \tag{2.7}$$

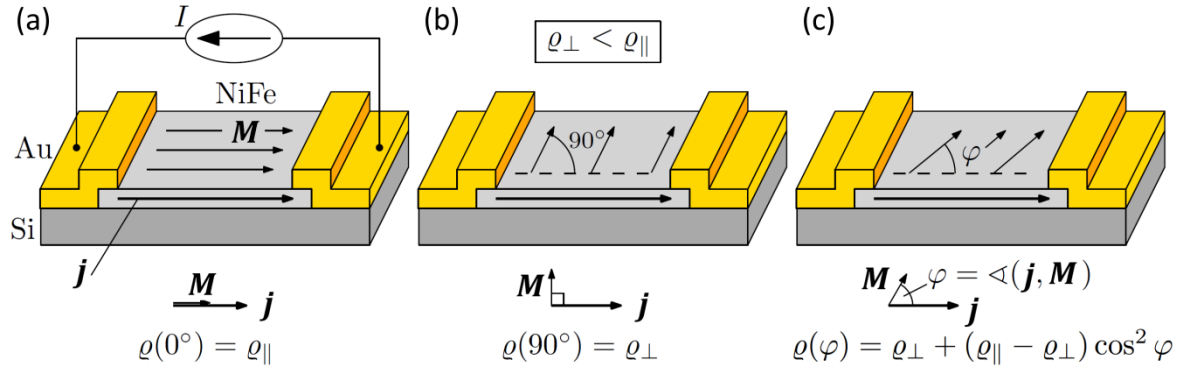

Fig. 2.8: Principles of anisotropic magnetoresistance demonstrated on a magnetic stripe. The resistivity of the layer varies with the angle φ, with its maximum and minimum at $0°$ and $90°$ respectively. Reprinted from [42].

2.4 Brillouin light scattering (BLS)

An essential method for probing dynamic magnetization in thin layers and nanostructures is Brillouin light scattering [86]. It probes the inelastic scattering of light from spin-waves (or their quanta, called magnons). In this process, the incident light (ω_i, $\boldsymbol{k}_i$) either gains energy during the annihilation of a magnon (so-called anti-Stokes process) or loses energy during the creation of a magnon (so-called Stokes process). Therefore, the scattered photon changes the frequency and k-vector (ω_f, $\boldsymbol{k}_f$). Both are schematically shown in Fig. 2.9. Due to the symmetry arguments, the in-plane component of the total system k-vector must be conserved. Thus, the maximal k-vector of spin-waves can be probed in so-called backscattering geometry and is computed as

$$k_{\mathrm{max}} = 2\frac{2\pi}{\lambda_{\mathrm{light}}}, \tag{2.8}$$

where λ_{light} is the wavelength of used light. The typical BLS experiment uses laser light with $\lambda_{\mathrm{light}} = 532$ nm, and the maximal wavenumber is therefore limited to 23.6 rad/um.

The signal may be focused using a microscope objective lens to achieve a spatial resolution. The instrument is then often called a µBLS. The combination of nano-positioning and focusing of the light enables 2D mapping of the spin-wave intensity. Another variant inbuilds an electro-optical modulator (EOM) to the beam path, which allows adding a reference signal with a constant phase to the laser light, enabling measurement of the spin-wave phase. A phase-resolved setup has been developed in our laboratory [35], also allowing us to measure standard µBLS (by disabling the EOM), its schematics is shown in Fig. 2.10.

BLS is used as a support measurement method for experiments presented in Chapters 4 and 5. A more detailed description of the BLS method is beyond the scope of this thesis. Please see references [35,86] for further details.

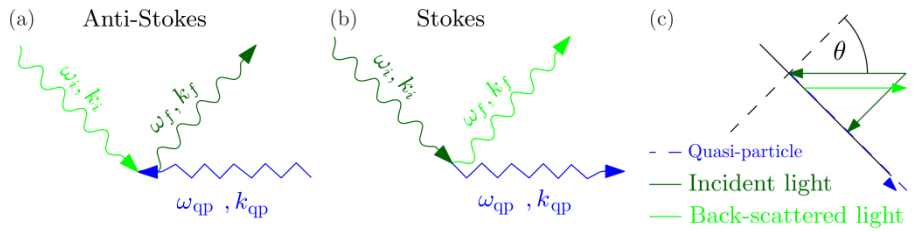

Fig. 2.9: Schematics of the (a) Anti-Stokes and (b) Stokes process of a photon with a quasi-particle magnon. (c) Schematics of the backscattering geometry. Reprinted from [35].

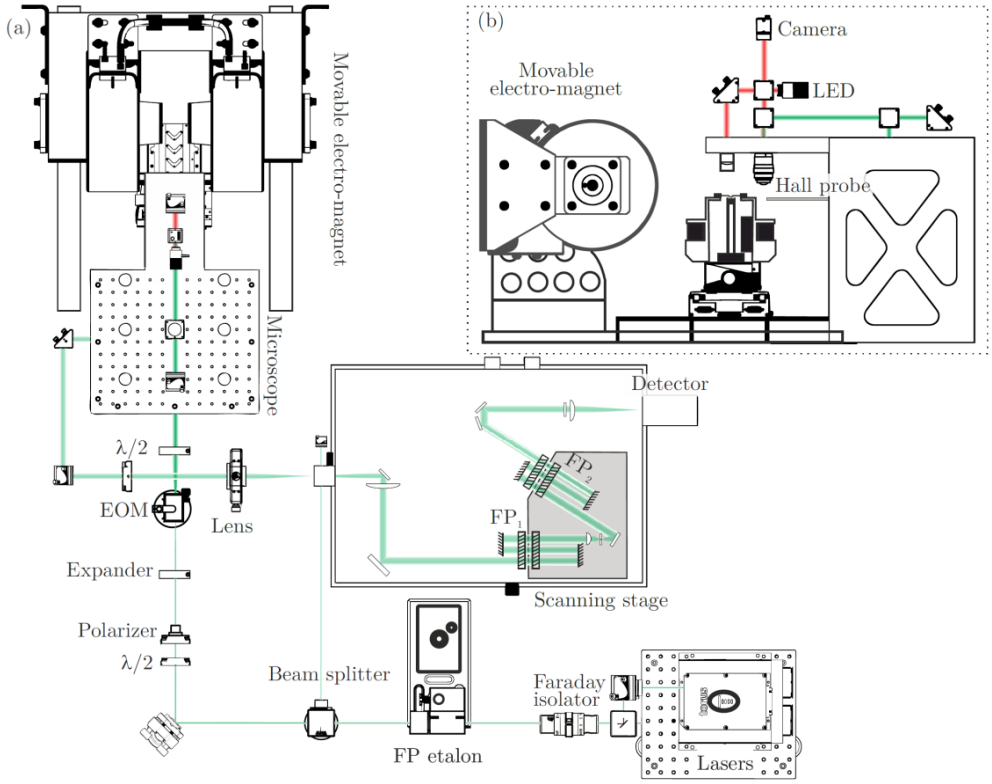

Fig. 2.10: Schematics of the BLS setup. (a) Top view of the whole setup. (b) Side view of the microscope module and electro-magnet. Reprinted from [35].

2.5 Sample fabrication methods

All of the previously described experimental methods study micro- or nanostructured material that can be prepared in many ways. Within the focus of this thesis, we fabricate our samples almost exclusively by the combination of e-beam lithography (EBL) and deposition of metals by sputtering or evaporation. E-beam and UV lithography use the same steps to transfer the patterns from a design to a sample: a sensitive resist layer is spin-coated onto a substrate, and the sample is consecutively exposed by either electrons or UV light (see the process schematics in Fig. 2.11). EBL is a serial process as the machine converts the sample design to beam paths that are scanned point by point. The advantage is a very good resolution (down to several nanometers) and versatility, while it is slow when large areas need to be exposed. The UV lithography uses masks over which the whole sample is exposed at once. This is very quick, but the necessity of a glass mask makes it useful mainly for large production

facilities - any change in the design requires manufacturing a new mask that is lengthy and expensive. The limiting factor for our fabrication would also be the method's resolution, as submicron structures are hard to expose by optical means in a research facility. As lithography techniques are immensely used in semiconductor production and many research facilities, this topic is covered in more detail in various books, e.g., [87,88].

The metal deposition is typically carried out by sputtering or evaporation, and both are available in our laboratory. Sputtering uses ions of an inert gas (typically argon) produced in plasma discharge and accelerated against the target material. The target atoms are released by the energy and momentum of the bombarding ions, and when the sample is placed in a suitable position, the sputtered atoms condensate on the sample surface, forming the deposited layer. The advantage is that it is not limited to conductive materials as RF plasma if often used to sputter insulators (e.g., SiO_2 or Al_2O_3). The disadvantage is that sputtering is far from being unidirectional deposition, i.e., the material lands on the sample under a wide range of angles, which complicates the metallization of a substrate previously masked by EBL (this topic is discussed in [42]).

The second important method of metal deposition is evaporation. In this method, an intense electron beam is generated from a filament and steered by magnetic fields to strike the source material until it melts and starts to evaporate. During evaporation, the atoms usually land onto the sample under a very narrow-angle spread, making it preferable for the lift-off process. This method has the disadvantage of different suitability of various materials for melting by the e-beam in a crucible. Evaporation of some materials may be difficult or impossible because the heated metal can, e.g., develop stress during cooling, causing the crucible to break. Evaporation of nonconductive materials may be problematic as well, but not impossible, because, e.g., SiO_2 is evaporated routinely. The advantage of evaporation is that the deposition rate can be very high, even tens of nanometers per second, making it suitable for thick film coatings.

An overview of sample types used in this work is provided in Table 2.1. Some details relevant to each sample type are given in the table, while otherwise, the recipes are standard (e.g., dose) and should be provided in your laboratory or in datasheets of used materials (especially resists).

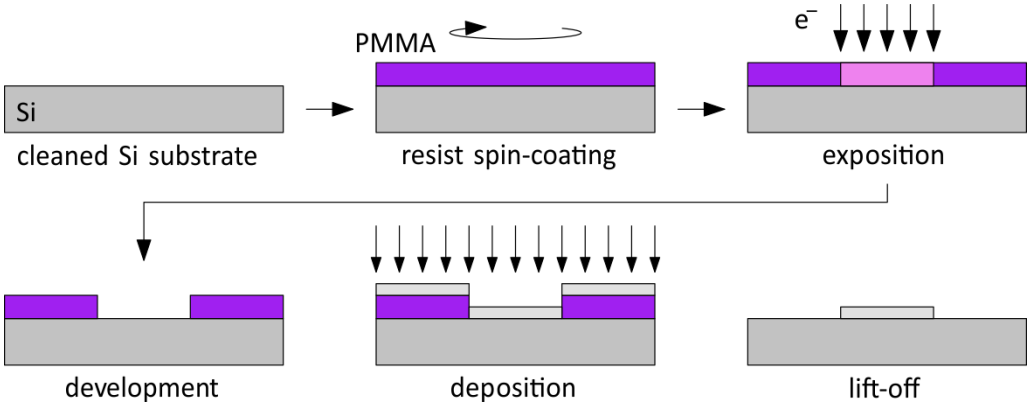

Fig. 2.11: Schematics of positive process e-beam lithography. The resist layer is spin-coated onto a clean substrate. The e-beam writer then exposes the resist, followed by development that selectively dissolves the exposed parts of the resist (not exposed parts in the negative process). The sample is then covered in metal by sputtering or evaporation, and the parts of the substrate covered by resist are consecutively lifted off. Only the areas without resist are left covered with the deposited layer.

Table 2.1: Sample type overview providing details related to the fabrication process used in each experimental chapter of this work. The details that are not provided may be considered standard techniques, also dependent on your actual equipment. For those, please consult your nanolab staff. The GDS designs used in this work may be shared upon request, please contact the author of this work.

Ch. Num.	Sample use	Notable process details
3	LTEM experiment	See [89] for extensive details. Substrate: prefabricated SiN membrane in TEM format, purchased from Silson Ltd. Resist: 4% PMMA was used without problems, other resists (e.g., CSAR) are known to suffer from low adhesion on SiN. Spin coating: the membrane must be fixed off-center by taping or by using an adapter (no vacuum). The resist layer does not thin down when rotating at the center of the coater. Lift off: no sonication may be used, only spraying
	MTXM experiment	Substrate: prefabricated SiN membrane in format compatible with the ALS microscope, purchased from Silson Ltd. Spin coating: taping must be used (no vacuum) Lift-off: no sonication may be used, only spraying
	AMR experiment	Two step lithography requiring alignment structures in the design must be used to precisely connect the electrodes Substrate: undoped Si
4, 5	PSWS and Dispersion measurement	One step lithography of antennas, standard procedures are used Substrate: undoped GaAs (low RF losses)
6	Glass cantilever with antenna	Substrate: microscope cover glass, thickness #0 Resist: 8% PMMA, providing ~ 1 µm resist layer. A conductive layer was applied (Allresist AR-PC 5090.02) because the substrate is a non-conductor. Spin coating: vacuum is allowed, the glass does not crack; otherwi se standard Lift-off: sonication is allowed

3 Magnetic vortex nucleation states under static conditions

This chapter presents an experiment using various methods introduced in Chapter 2 to probe the magnetic behavior of NiFe disks undergoing magnetic field decrease from saturation to zero. Our main goal was to detect and compare the magnetic states during this field transition using magnetic imaging and all-electrical detection, focusing on the stage just before the vortex state is nucleated, so-called nucleation states.

Experimental measurements of the nucleation states were carried out for NiFe disks with diameters ranging from 500 nm to 4 μm and thicknesses ranging from 20 nm to 100 nm. The disks were fabricated by electron beam lithography, evaporation, and lift-off process on 30 nm and 200 nm thick SiN membranes suitable for the Lorentz Transmission Electron Microscopy (LTEM), and the Magnetic Transmission X-ray Microscopy (MTXM), respectively. For the Anisotropic Magnetoresistance (AMR) measurements, we used undoped Si (100) as a substrate, and the disk fabrication was followed by a second lithography step in which a pair of Au contacts was fabricated in order to establish electrical connections to the disk with the contact geometry that is schematically shown later in this chapter in Fig. 3.10.

3.1 Classification of magnetic vortex nucleation states

The nucleation states are the transition spin configurations in magnetic disks through which the magnetization proceeds between the fully saturated state and the fully nucleated vortex state. Before we provide any results about the nucleation of magnetic vortices, we have to classify the nucleation possibilities. For this purpose, we performed micromagnetic simulations of disks with varying diameters and thicknesses. We used OOMMF with the following parameters: cell size of $(4 \times 4 \times 4)$ nm^3, saturation magnetization $M_s = 800$ kA/m, and exchange constant $A = 13$ pJ/m. Our simulation data show that three distinct nucleation pathways are possible, and Fig. 3.1 shows the three corresponding nucleation states. The first nucleation state, the **C-state** [15], is shown in Fig. 3.1(a). It consists of spins following the C letter's shape to decrease the dipolar energy compared to the disk in saturation. This state is common for small disks (approximately for diameters $D < 400$ nm and thicknesses $t < 20$ nm). The C-states are not so interesting to observe for their low complexity, and because of their size, they are hard to probe because the disk sizes below 1 μm are usually on the limit of our imaging methods. In our work, we focus on two other nucleation states that can be found in larger disks: the **vortex-pair state** [90] and the **buckling state** [18,19,91] that are shown in Fig. 3.1(b), and Fig. 3.1 (c), respectively. So far, the evidence for these states was based on micro-Hall magnetometry [18] or AMR [19,91] measurements combined with micromagnetic simulations, but direct observation by magnetic microscopy methods was missing.

The vortex-pair state [Fig. 3.1(b)] is favored in intermediate disks with diameters $D > 400$ nm and thicknesses $t < 120{,}000$ nm$^2/D$ (the constant $120{,}000$ nm^2 was deduced from our analysis of LTEM images of arrays of different sized disks). However, the crossover between the vortex-pair state and the buckling state is continuous, and for each disk geometry in this work, we found both states with an increasing probability of finding the buckling state in large disks (see LTEM imaging in Fig. 3.5). The vortex-pair state consists of two vortex cores around which the magnetization is curling in the opposite sense (opposite circulations).

Micromagnetic simulations show that the two cores of the vortex-pair state always have opposite polarities (giving the same handedness for both vortices of the pair). Upon the field decrease, the cores move towards each other, decreasing the net magnetization along the field direction until they annihilate, and a single vortex core is formed in the disk. As the polarity and circulation of the two competing vortices are opposite, the final vortex state will be random for symmetry reasons. However, this is difficult to realize in real samples because the geometrical symmetry can be broken due to lithographic imperfections and surface roughness of the substrate.

The buckling state [Fig. 3.1(c)] is favored in large disks. The buckling state's characteristic features are the three Bloch domain walls with in-plane magnetization curling around them. When the applied field is decreased, those three domain walls move towards each other until a vortex state is formed. The buckling state has a lower symmetry than the vortex-pair state, and the in-plane magnetization shape indicates the final circulation of the vortex – in the case of Fig. 3.1(c), the circulation will become counterclockwise. Even though the situation is less evident for the final polarity state, the simulations show that the m_z components at the disk edge will become dominant over those at the disk center – in the case of Fig. 3.1 (c), the vortex core polarity will be defined by the m_z component of the red domains.

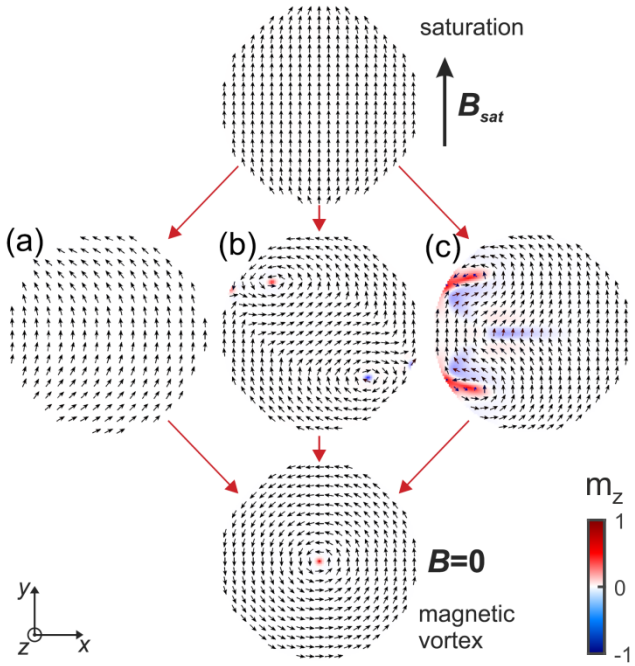

Fig. 3.1: Magnetic vortex nucleates upon the field decrease from saturation while undergoing one of the nucleation states visualized by micromagnetic simulations: (a) C-state, (b) vortex-pair state, and (c) buckling state. The blue-white-red color scale represents the perpendicular component of magnetization. Reprinted from [92].

3.2 Lorentz microscopy of the vortex nucleation states

Imaging of the magnetic vortex nucleation process was done on arrays of NiFe disks prepared by EBL on TEM compatible SiN membranes. The TEM compatibility means that the chip size must fit a 3 mm diameter circle, and the studied region must be transparent for electrons. Thus, the chosen membrane type was only 30 nm thick with a window size 250 µm, fabricated by Silson Ltd. The difficult part during lithography is the membrane spin-coating because the typical machines are adjusted to coat whole wafers and not for such small samples. Fixing of the membrane in spin-coater was handled using 3D printed holders, and because of the trial and error testing, the membrane was placed off-axis. On-axis coating had unsatisfactory results as this approach did not lead to thinning of the resist to thicknesses in order of hundreds of nanometers. Off-axis coating produces inhomogeneous but sufficient

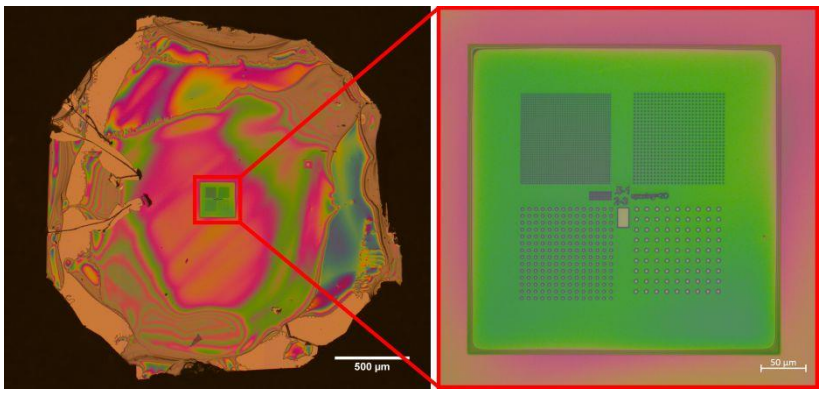

Fig. 3.2: TEM compatible SiN membrane manufactured by Silson Ltd. with the window size 250 µm coated in resist. The detail on right shows exposed and developed patterns (disk arrays) for LTEM imaging.

layers of resist considering the window being reasonably small. The typical spin-coating and exposure results are shown in 3.2, and the procedure is shown in more detail in [89].

The LTEM images (Fresnel imaging by defocusing) of the nucleation states were acquired using FEI Titan TEM at the accelerating voltage of 300 kV. As it was described in Section 2.1, this method does not image the magnetization inside of the sample directly, but it only reveals the domain wall structure as the images of neighboring domains shift towards each other or apart from each other due to the Lorentz forces, thus creating positive or negative overlap yielding white or black contrast respectively. The external magnetic field needed for vortex annihilation and subsequent gradual nucleation is applied by the TEM objective lens (which is normally turned off in the Lorentz mode). As this field is oriented along the microscope optical axis, the sample was tilted by 30 degrees to gain an in-plane magnetic field component. The tilt results in elliptical projections of the disks, and the necessary defocus causes further distortions that are observable in the images.

Example sequences for the vortex nucleations undergoing the transitions through the vortex-pair state and the buckling state are shown in Fig. 3.3. During the sequence, the objective lens was excited to produce enough field to saturate the disks, and then it was gradually turned off while capturing the magnetization states in the Fresnel mode. As it was introduced, the images do not directly tell us the magnetization distributions, but we can see the positions of the domain walls or the position of vortex cores, and thus we can observe how the mechanism works. In the top row of Fig. 3.3, we can see that the vortex-pair state nucleation process has two critical stages: the first one is demonstrated at the snapshots taken at 35.2 mT and 30.4 mT, showing several black and white lines that after a further decrease of the magnetic field form a half-black and half-white ellipse inside of the disk – snapshots taken at 27.2 mT and 22.4 mT. When the field was reduced further, the magnetic vortex nucleated with the circulation represented by the low contrast black dot in the disk (snapshots taken at 12.8 mT and 0 mT).

The bottom row of Fig. 3.3 shows the vortex nucleation undergoing the transition through the buckling state. When the saturation is broken, the first stage of the buckling state is characteristic with the small domain walls at the disk boundary, which is observable in the snapshot taken at 32.0 mT. Then when the field is being decreased, the buckling gradually transforms to the state corresponding with the snapshot taken at 20.8 mT, after which the vortex nucleates. The buckling state nucleation mode typically leads to the vortex formation at a relatively high field, causing significant displacement of the vortex core right after

nucleation. This is visible as the displaced and expanded vortex core, represented by the white line in the snapshot taken at 19.2 mT. After the field is completely switched off, the core moves to the center of the disk, represented by the dot in the middle of the disk, in our case having the white contrast – the final vortex circulation is opposite to the one shown at the vortex-pair nucleation sequence in the first row.

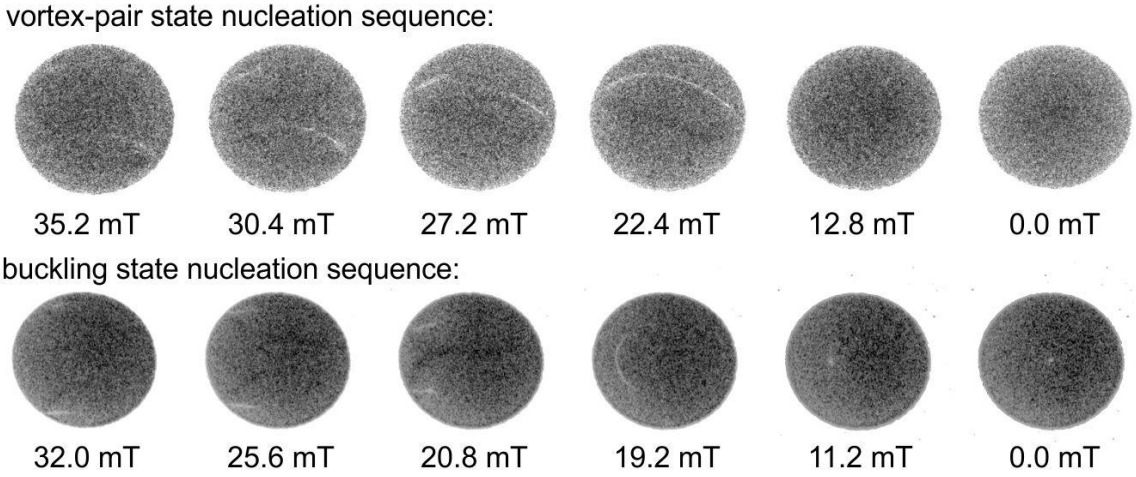

Fig. 3.3: LTEM sequences of magnetic vortices going through the vortex-pair state (top row) and buckling state nucleation process in $t = 2$ μm, $t = 100$ nm disk in the top row and $t = 3$ μm, $t = 100$ nm disk in the bottom row. Magnetic fields (pointing in the vertical direction) were estimated using the calibration curve of the microscope's objective lens provided by the manufacturer.

The ambiguity of indirect magnetization observation can be overcome by performing micromagnetic simulations of the corresponding magnetization states and comparing the calculated LTEM contrast to the measured data. We used Micromagnetic Analysis to Lorentz TEM Simulation (MALTS [72]) to compare the acquired images with micromagnetic simulations. Fig. 3.4 shows the important stages of the vortex nucleation modes in the top row, compared to the LTEM contrast images calculated by MALTS in the middle row. The source magnetization distributions simulated by OOMMF, from which the LTEM contrast was calculated, are shown in the bottom row of Fig. 3.4. LTEM images show a good agreement between the simulated and measured magnetic contrast for both the vortex-pair state stages [Fig. 3.4(a,b)] and the buckling state [Fig. 3.4(c,d)]. The C-state has no magnetic contrast in LTEM [Fig. 3.4(e)]. A reference vortex state at zero magnetic field is shown in Fig. 3.4(f).

The vortex-pair state nucleation process consists of two steps indicated in Fig. 3.4(a) and Fig. 3.4(b). The LTEM image in Fig. 3.4(a) is characterized by two lines, one with black and one with white contrast (in-plane domain walls) separating the three main domains containing the in-plane magnetization in the disk. Additionally, we can observe two intense spots at the disk boundary, where one of them is lighter and the other one darker than the background. They represent Bloch domain walls featuring a larger magnetization curl (i.e., higher contrast). Upon decreasing the field, the white and black lines move closer to each other until the Bloch domain walls unpin from the disk boundary into two standalone vortex cores yielding the spin configuration of the vortex-pair state in Fig. 3.4(b). Further field decrease leads to the formation of a single vortex. In case of the buckling state [Fig. 3.4(c,d)], the nucleation process is different. When the field decreases from saturation, the first step is forming Bloch domain walls at the disk boundary yielding bright LTEM contrast in these positions. From this state, the buckling state is formed by moving the two domain walls towards each other, which is accompanied by the gradual formation of a third domain wall at the disk center. The LTEM

contrast then consists of a typical line passing through the disk center splitting towards the edge where the line bounces off the edge with reversed contrast [from black to white in case of Fig. 3.4(d)]. Further field decrease leads to the formation of a single vortex with polarity defined by the m_z component of the Bloch walls nucleated at the disk boundary.

The LTEM also shows two other aspects of the vortex nucleation. The first one is the pinning of magnetization present in a large portion of studied disks, leading to deformed nucleation states. However, after their study, we concluded that the number of nucleation modes is only seemingly higher than the three presented modes, but they all are only variations of the vortex-pair state or the buckling state which were caused by the pinning.

The other aspect was the observation of more than one nucleation mode presented in an array of identical elements, only the probability of each varies with the disk's geometry. This is shown in the example presented in Fig. 3.5, where the neighboring $d = 2$ µm, $t = 100$ nm disks have two different nucleation states - the vortex-pair state (left) and the buckling state (right).

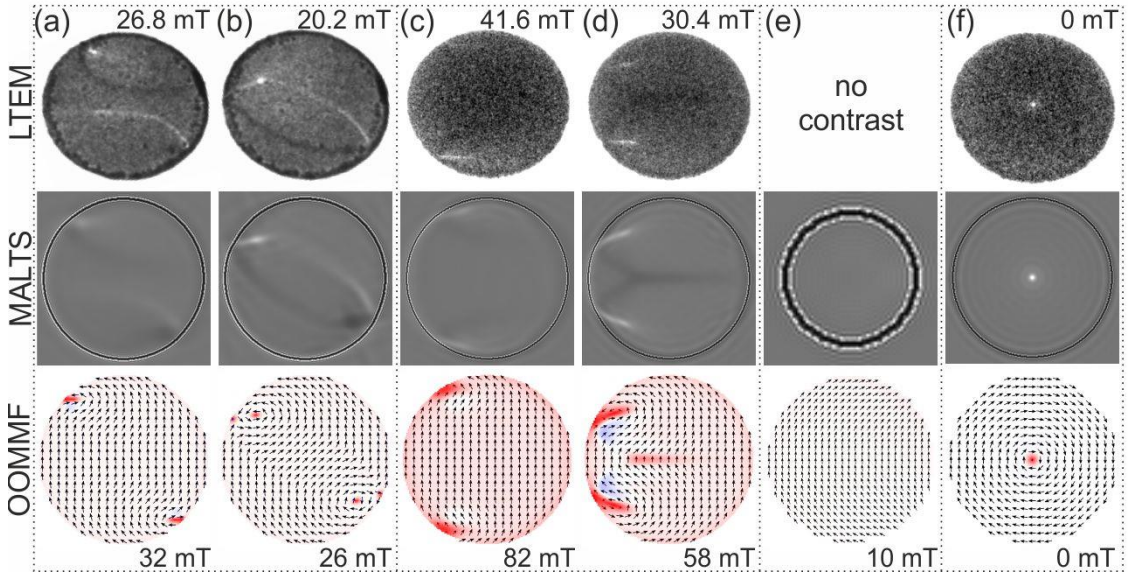

Fig. 3.4: Simulation and LTEM imaging of vortex nucleation states in magnetic field. The sample was tilted by 30°, and the indicated field values are the in-plane field components. Top row: LTEM observation; middle row: LTEM contrast simulated from the spin configurations shown in the bottom row: OOMMF micromagnetic simulations. The blue-white-red color scale represents the perpendicular component of magnetization. Columns: (a,b) Two consecutive configurations forming the vortex-pair state in a $D = 2$ µm, $t = 40$ nm disk. (c,d) formation of the buckling state in a $D = 2$ µm, $t = 100$ nm disk . (e) Simulations of the C-state in a $D = 200$ nm, $t = 16$ nm disk which does not show magnetic contrast in LTEM. (f) vortex state for reference. Reprinted from [92].

Fig. 3.5: Both the vortex-pair state (left) and the buckling state (right) captured in two $D = 2$ μm, $t = 100$ nm disks neighboring in the same array. Although the geometry of both disks is identical, their shapes in the images are different because of the high defocus. Note that the magnetic field is pointing in the horizontal direction and that the vortex-pair state is at the stage corresponding to Fig. 3.4(a).

3.3 Electrical detection of the vortex nucleation states

Alongside magnetic imaging, the nucleation processes were further studied by measuring the associated resistance changes due to AMR. This was performed by both numeric calculations and experimental measurements. We considered the symmetrical contact geometry presented in Fig. 3.6(a) with the magnetic field oriented along the *y*-axis. In this configuration, the highest resistance is measured at saturation, where the spins are aligned along both the applied field and the current density $\boldsymbol{j}$ (we neglide the current deviation from the y-asis for symmetrical contacts). Then each of the states comes with a lower level of electrical resistance following the AMR law for resistivity (AMR was also discussed in Section 2.3): $\rho(\varphi) = \rho_{\perp} + (\rho_{\parallel} - \rho_{\perp}) \cos^2 \varphi$, where φ is the angle between the vector of current density $\boldsymbol{j}$ and the vector of magnetization $\boldsymbol{m}$.

The OOMMF output files were used to calculate each state's resistance along the hysteresis loop to predict the shape and specific features of the measured data for the different nucleation processes going through the vortex-pair state or the buckling state. In the resistance calculation, we consider the direction of magnetization provided by the OOMMF magnetization map. The simulation gives the direction of magnetization at each point (cell) of the disk, but the problem arises from the current density direction. This can be calculated for constant resistivity materials (e.g., using COMSOL Multiphysics), but for non-constant resistivity caused by AMR, it presents a problem: the current density direction is dependable on the local resistivity and vice versa, which is much more difficult to solve. Our approach is considering that the resistance change is small, and thus we assume constant direction of current (homogenous current density in the whole volume for the simplest case of symmetrically placed contacts). Then we use each simulation cell's magnetization direction to calculate its resistivity and consecutively the resistance. Finally, we connect all of the cells as a resistor network (cells connected in parallels and series) to obtain the total resistance value at each magnetic field.

Fig. 3.6(c,d) shows the simulated and experimental AMR data for vortex nucleation through the vortex-pair state. The magnetic field was swept in the direction from positive to negative field values. The simulated data in Fig. 3.6(c) show an abrupt resistance drop at 24 mT, where the vortex-pair state is formed in the disk, and then the resistance decreases linearly upon further lowering of the field. This is associated with the motion of the two cores of the vortex-pair state towards each other until the two cores annihilate into a single vortex state at 12 mT, leading to an abrupt increase of the resistance. The following curve represents

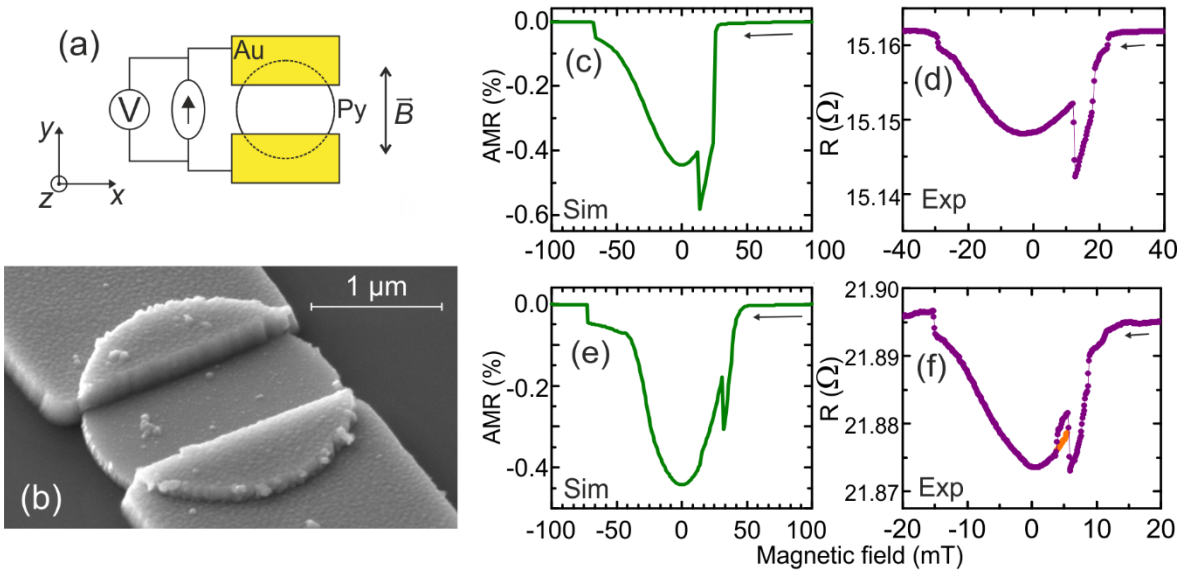

Fig. 3.6: Modeling and measurement of AMR data probing the magnetic vortex nucleation mechanisms. (a) schematics of the sample geometry with the electrical connection. (b) SEM image of a NiFe disk with gold contacts prepared by a two-step lithography process. (c-f) simulated and experimental AMR data of magnetic disks with nucleation via (c,d) the vortex-pair state ($D = 2$ μm, $t = 75$ nm disk) and (e,f) the buckling state ($D = 4$ μm, $t = 50$ nm disk).

the reversible displacement of the vortex core in a magnetic field. After reversing the field orientation, the annihilation occurs at -68 mT, where the resistance jumps up to the saturation level. The experimental data in Fig. 3.6(d) show the same features as those predicted by the simulation. The only difference is the nucleation part, where the resistance drops in several steps due to the pinning of magnetization (also observed during the LTEM imaging), which delays the formation of the vortex-pair state. The experimental values of the nucleation and annihilation fields are lower than the simulated values as the simulations are performed for 0 K.

The AMR data in Fig. 3.6(e,f) show similar general behavior compared to the data in Fig. 3.6(c,d), but several differences allow us to associate it with the buckling state nucleation process. One difference is in the first part of the nucleation process, where the resistance decreases gradually, without the abrupt drop all the way from saturation, where the buckling state is gradually formed. The other difference is in the larger depth of the resistance dip with respect to the resistance of the vortex state at zero field, in contrast to the shallower dip in the AMR data of the vortex-pair state. The nucleation occurs at 32 mT, where the resistance suddenly increases. A significant point of interest is at 15 mT, where a small drop in the resistance is present. When inspecting the simulated states at each point around this drop, we found that the nucleated vortex state does not have a single vortex core but instead, there are two vortex cores with an antivortex in between them. This is called the vortex-antivortex-vortex (VAV) triplet, and its simulation is shown in Fig. 3.7. The VAV triplet is stable in a range of a few mT, and after further field decrease, it annihilates into a single vortex core resulting in a small drop in the AMR data. This state was electrically detected with a typical peak shown in the purple curve shown in Fig. 3.6(f) between 4-6 mT. However, when the measurement was repeated multiple times, this peak was present only in about 30% of all field sweeps, while

the other field sweeps in this range followed the green trace in Fig. 3.6(f). This is attributed to the VAV triplet's lower stability compared to the vortex state with a single core at the same magnetic field.

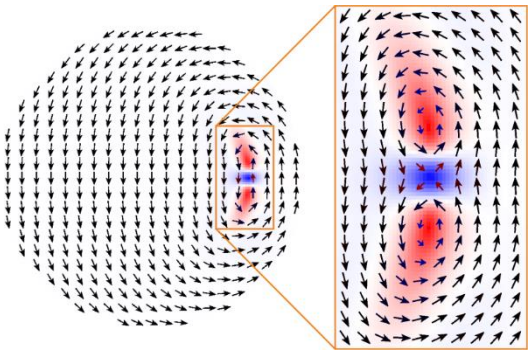

Fig. 3.7: Simulation of the vortex-antivortex-vortex (VAV) triplet with detail on the right side. The blue-white-red color scale represents the perpendicular component of magnetization.

3.4 VAV triplet imaging by MTXM

The VAV triplet, explored in the previous section using AMR measurements and simulations, was not observed during the LTEM imaging. This is expected because LTEM has no contrast connected to the out-of-plane magnetization, and thus it is impossible to distinguish between the vortex core and the VAV triplet at the same magnetic field. For imaging of the out-of-plane magnetization details, we must use a different method sensitive to this component. In our case, we used MTXM (see Section 2.2). In this method, the magnetic contrast due to XMCD is dependent on the out-of-plane component, and the resolution is down to 25 nm. Thus this method is very suitable for our purposes. In Fig. 3.8, we present snapshots taken during a magnetic field sweep, and we compare the images with a simulation. Both the magnetic vortex nucleation and annihilation processes were captured in the sequence. In (a,b), we can see two stages of the buckling state, from which the VAV triplet is nucleated in (c,d), marked by the red rectangle. After further field reduction, the VAV triplet transforms into a single vortex core. When the field direction is reversed, the core moves to the direction perpendicular to the applied field until it annihilates (full saturation is not shown).

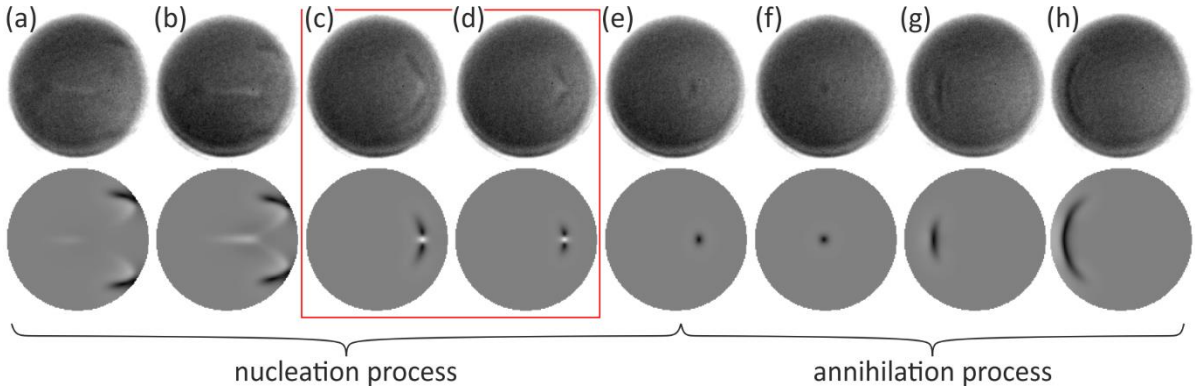

Fig. 3.8: MTXM imaging (top row) of the vortex nucleation and annihilation processes in a $D = 2$ µm, $t = 100$ nm disk compared to OOMMF simulations (bottom row). The red rectangle marks snapshots of the VAV triplet. The grayscale represents the perpendicular component of magnetization in both the experiment and the simulation.

Moreover, Fig. 3.9 shows an MTXM comparison of the magnetic vortex nucleation from a buckling state with and without the VAV triplet as an intermediate stage. The measurement was taken on the same disk during two magnetic field sweeps.

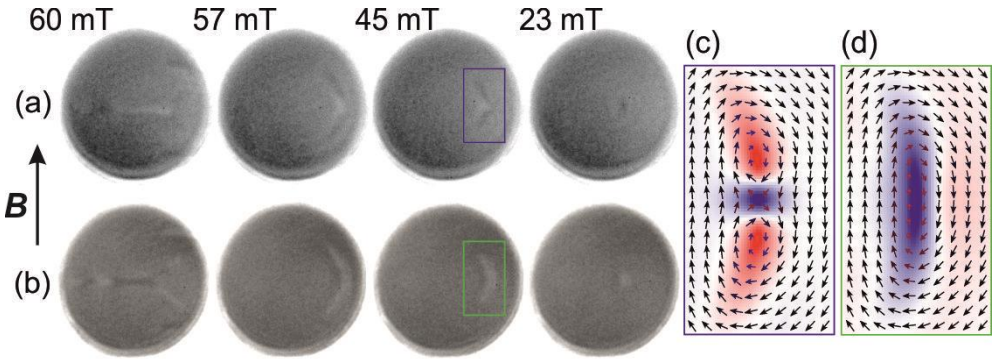

Fig. 3.9: MTXM images showing nucleation sequences from two variations of the buckling state in a $D = 2$ μm, $t = 100$ nm disk . (a) Nucleation leading to the VAV triplet. (b) Nucleation leading to a single vortex core. (c) Detail of the VAV triplet (OOMMF simulation). (d) Detail of the vortex core at the same magnetic field as the VAV triplet in (c). Reprinted from [92].

3.5 Detection of the vortex circulation by AMR

The anisotropic magnetoresistance on magnetic vortices can yield more than the information about the nucleation states. If we introduce an asymmetry to the electrical contacts by moving it to the side, leaving half of the disk uncovered, we can detect the vortex circulation. Fig. 3.10 shows calculated AMR data for magnetic field sweeps of disks nucleating through the vortex-pair state (top) and the buckling state (bottom). The figure also shows both calculations for the symmetrically placed contacts (green curves) and asymmetrically placed contacts (red and blue curves). When we introduce the asymmetry, the curves are different for the opposite circulations (graphs follow the given legend), and the main difference is around the zero field. That is because after the vortex nucleates, its core moves in the perpendicular direction to the applied field, i.e., it moves towards the contact gap or away from it. The resistance decrease compared to the saturation is given by the net magnetization perpendicular to the current density in the area where most of the current is flowing. As most of the current go directly through the gap, the lowest resistance is measured when the vortex core is displaced to the effective contact center. For opposite circulations, this occurs in opposite magnetic fields leading to the resistance minima at the left/right side with respect to zero field for clockwise/anticlockwise circulations.

Measurement of the vortex polarity is not possible because there is no suitable contact geometry that would allow it. But the measurement of the vortex polarity is possible to be implemented in the dynamic measurement mode by acquiring frequency spectra of the induced voltage. This was explained in, e.g., [14,93].

The AMR with asymmetrical contacts was also experimentally detected. Fig. 3.11 shows an example of field sweeps from both positive and negative directions, and the four curves show measurements for both circulations following the color code. From the details of the resistance drop just before the nucleation, we can also determine the nucleation mode of this particular disk, which is the vortex-pair state, as its shape corresponds to Fig. 3.6(c,d).

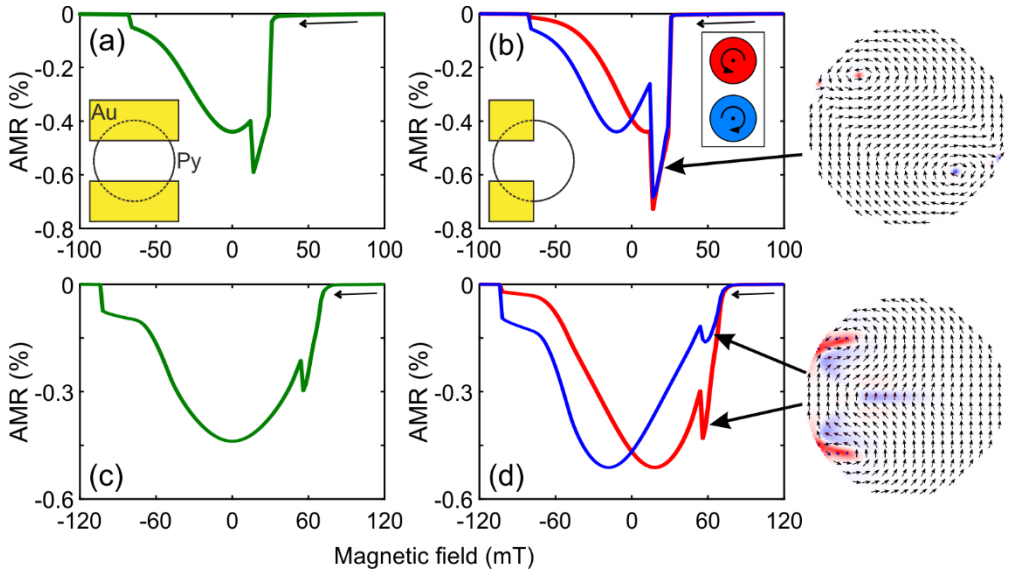

Fig. 3.10: Calculated AMR using OOMMF micromagnetic simulation of a NiFe disk nucleating through the vortex-pair state [(a,b) at the top row] and the buckling state [(c,d) at the bottom row]. The calculation was performed considering two contact geometries: symmetrical contacts with a gap of one disk radius [green curves at (a,c)] and asymmetrical contacts covering only half of the disk [red and blue curves (b,d)]. Asymmetrical contacts provide different curves for opposite vortex circulations.

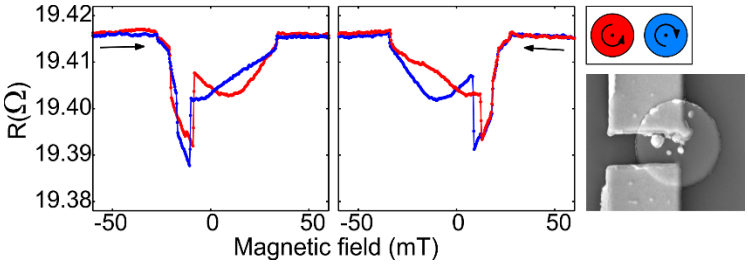

Fig. 3.11: Example of measured AMR with asymmetrical contacts on a $D = 1.5$ μm, $t = 75$ nm disk. The data corresponds to the vortex-pair state nucleation, and the colors follow the same color code for circulations as in the simulations in Fig. 3.10.

3.6 Summary of the magnetic vortex nucleation states

The vortex nucleation is an interesting process influenced by the disk's geometry and material. The nucleation states were classified into the C-state, the vortex pair state, and the buckling state using magnetic imaging and electrical detection. The magnetic imaging sequences revealed details of how the nucleation states evolve with the magnetic field. The VAV triplet was an intriguing feature that we observed in both simulations, imaging, and electrical measurement. Although the VAV triplet measurements are convincing, it proved difficult to repeat in newly fabricated samples, focused solely on its stabilization. The fact that it requires a significant amount of luck to stabilize disqualifies its usage in applications.

4 Vector network analysis in magnetization dynamics experiments

In this chapter, we will introduce the measurement device crucial for the following experimental chapter: **the vector network analyzer (VNA)**. It generates and detects high-frequency signals with the maximum possible operating frequency exceeding 100 GHz. VNA consists of ports to which a sample, commonly called a device under test (DUT), is connected using high-frequency cables, or high-frequency probes.

In general, VNAs can have multiple ports, but there are typically only two ports necessary for carrying most of the experiments in the field of magnetism. Therefore, the following description will be limited to a 2-port VNA, but can be extended to a multi-port VNA if needed. Fig. 4.1 shows an image of the setup established in our laboratory – VNA (Rohde & Schwarz ZVA50) is connected to a probe station using microwave probes to connect the samples. The sample is placed in the gap of a rotatable electromagnet providing up to 400 mT of the in-plane magnetic field (no available option for out-of-plane field).

VNA, in contrast to an oscilloscope, works directly in the frequency domain. Instead of the signal's time dependence, it measures the signal amplitude and its phase shift with respect to the excitation signal. However, these two quantities (amplitude and phase) can carry the

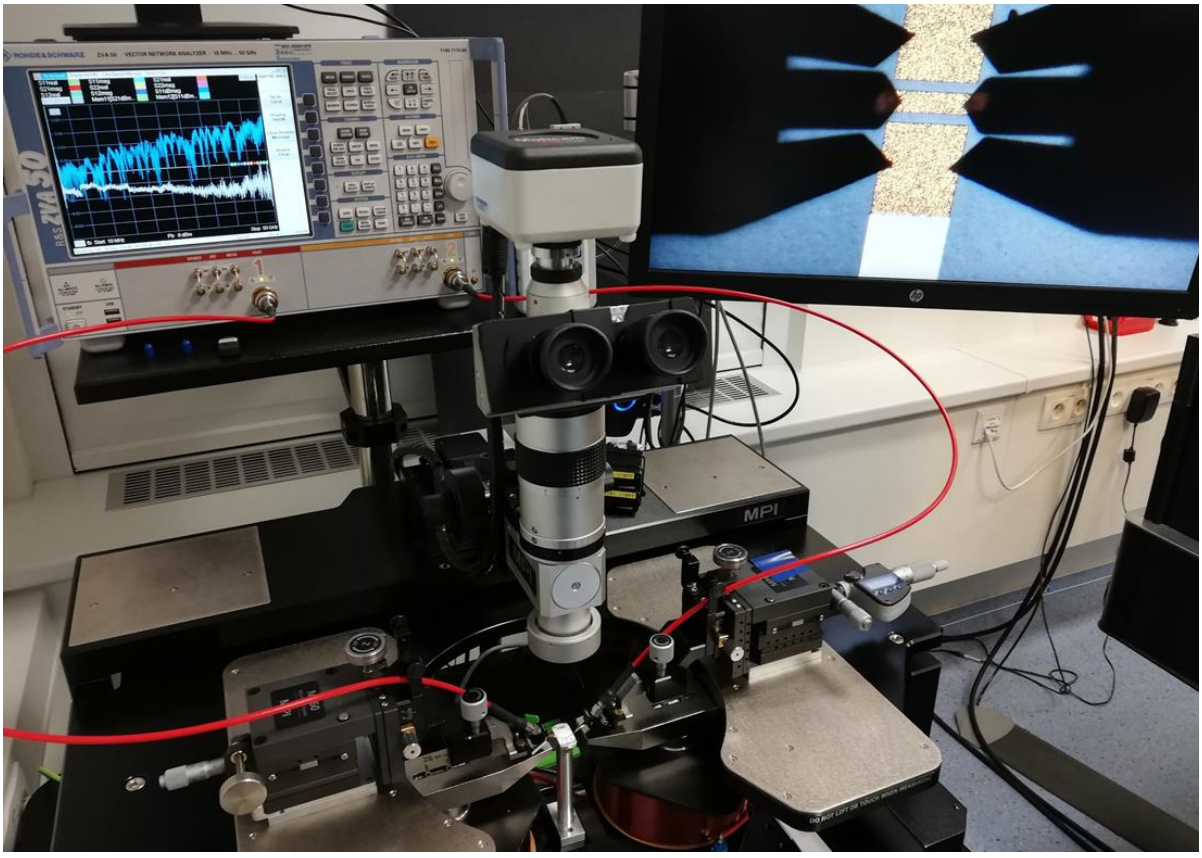

Fig. 4.1: VNA measurement station. The Rohde & Schwarz ZVA50 instrument (top left) is connected to microwave probes that can establish electrical contact with the sample mounted in the gap of the electro-magnet. Navigation is provided with a microscope.

desired information from the sample with the advantage of a much higher reachable frequency than any oscilloscope can reach. VNA can also test the sample's response for a wide frequency range in a very short time, typically testing hundreds of frequency measurements per second, depending on the detectors' bandwidth settings.

4.1 The function of a vector network analyzer

4.1.1 Wave quantities and S-parameters

VNA generates a sinusoidal test signal a_j, often called stimulus, which is applied to the DUT. The signal at the DUT undergoes three basic processes: reflection, absorption, and transmission resulting in a signal b_i, which will be (at least in the case of a linear DUT) sinusoidal as well. Here, the subscripts i, j stand for port numbers 1 and 2. An example of the wave quantities is shown in Fig. 4.2. Both signals a_j and b_i are measured using receivers described later in this chapter. As we do not use active devices, the received signals b_i will always be smaller than test signals a_j, and generally may be phase shifted with respect to each other. In the measurement, the quantities are usually represented using the complex scattering parameters – S_{ij}-parameters. They provide transition from the generated signals represented by an a-vector to the detected b-vector using the following matrix multiplication:

$$\begin{pmatrix} b_1 \\ b_2 \end{pmatrix} = \begin{pmatrix} S_{11} & S_{12} \\ S_{21} & S_{22} \end{pmatrix} \begin{pmatrix} a_1 \\ a_2 \end{pmatrix} \tag{4.1}$$

Here, it is apparent that S-parameters with the same indices (S_{11} and S_{22}) connect wave quantities from the same port, and therefore they represent the reflection of microwaves from the DUT back to the same port. On the other hand, the remaining S_{21} and S_{12} parameters connect wave quantities from both ports and represent microwave transmission from one port to the other. The parameter S_{21} represents the transmission from Port 1 to Port 2 and is called the forward transmission, while S_{12} represents the opposite direction and is called the reverse transmission. During the measurement, there is always only one active output at the time, i.e., a_1 and a_2 are not active at the same time.

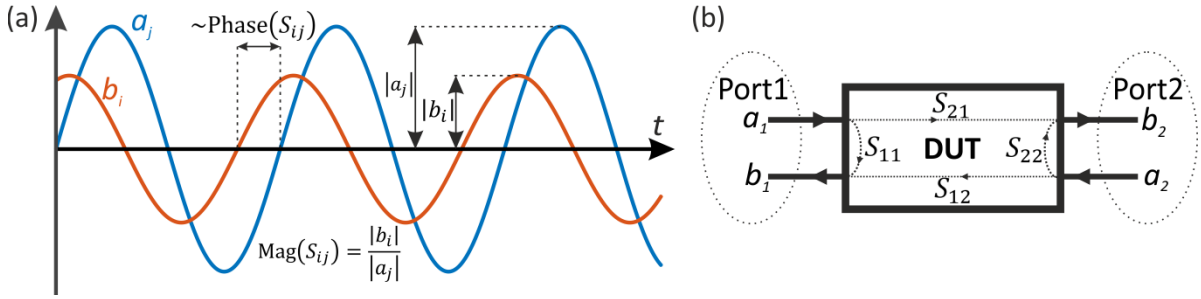

Fig. 4.2: (a) Illustration of the generated and detected wave quantities. (b) Schematics of S-parameters using wave quantities on a 2-port VNA. S_{21} represents the forward transmission from Port 1 to Port 2 and S_{12} represents the reverse transmission from Port 2 to Port 1.

The S-parameters are complex numbers; the absolute value of the complex number represents the magnitude, and the argument (angle of the vector representing the complex number in the Gauss plane) represents the phase:

$$|S_{ij}| = \frac{|b_i|}{|a_j|} \equiv \text{magnitude}, \tag{4.2}$$

$$\arg(S_{ij}) = 2\pi f \Delta t \equiv \text{phase}. \tag{4.3}$$

It is important to note that because the S-parameters are ratios of two signals, they are unitless. For the sake of readability, we will rewrite the representation of magnitude and phase as follows:

$$\mathrm{Mag}(S_{ij}) = |S_{ij}|, \tag{4.4}$$

$$\mathrm{Phase}(S_{ij}) = \arg(S_{ij}). \tag{4.5}$$

Modern VNAs have a very wide dynamic range of measurement. For that reason, it usually measures the magnitude in the logarithmic scale expressed in decibels. The conversion into the decibel scale can be done as:

$$S_{ij}(\mathrm{dB}) = 10\log\frac{P_{\mathrm{VNA-in}}}{P_{\mathrm{VNA-out}}} = 10\log\frac{|b_i|^2}{|a_j|^2} = 20\log\frac{|b_i|}{|a_j|} = 20\log|S_{ij}| \tag{4.6}$$

The results expressed in decibels are then always negative because the received signals b_i are always smaller than the output signal a_j. Therefore 0 dB equals to $S_{ij} = 1$ in the linear scale, and for each -10 dB, the power drops by a factor of 10 times (e.g., -20 dB equals 1/100 of the original output power, which corresponds to 1/10 of the original signal size).

From the physicist's perspective, the VNA can be (to some extend) perceived as a black box, but it is still useful to understand the VNA receiver's essential operation, which recovers the measured waves' magnitude and phase. Therefore, the receiver will be of primary interest in the following sections, where the main receiver components' function will be described.

4.1.2 VNA receiver operation

A typical 2-port VNA instrument is represented with the schematics shown in Fig. 4.3. Firstly, one microwave generator is shared for both ports using microwave switches, and then there are two receivers per port: one measures the generated wave as a reference while the second one measures the scattered signals coming back to the port from a DUT. These two signals are selected in a directional element represented with the yellow boxes in the schematics (Fig. 4.3).

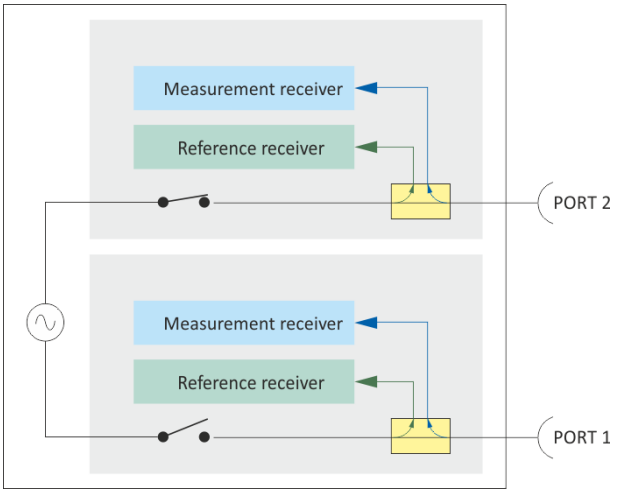

Fig. 4.3: Schematics of a 2-port VNA. The two ports share the same microwave generator. Each port then has its own reference and measurement receivers tracking the signals directed by the directional element (yellow box). Reprinted from [94].

Now we will describe the receiver's function, which recovers the magnitude and phase of the measured signals. The receiver function is represented with the schematics shown in Fig. 4.4. The first receiver stage is analog (no digital device can process the VNA's frequency range), and its purpose is to downshift the frequency carrying the measured signal. This is done by taking the incoming signals $a(t)$ and $b(t)$, that are noted as RF signals, and mixing (multiplying) them with a local oscillator (LO) signal at the f_{LO} frequency creating an intermediate frequency (IF) signal with the frequency $f_{\mathrm{IF}} = |f_{\mathrm{RF}} - f_{\mathrm{LO}}|$ and amplitude A_{IF}:

$$x_{\mathrm{IF}}(t) = A_{\mathrm{IF}} \cos(2\pi f_{\mathrm{IF}} t + \varphi_{\mathrm{IF}}). \tag{4.7}$$

There is also another carrier frequency $f_{\mathrm{RF}} + f_{\mathrm{LO}}$, but it will not be used. The reason of this process is to downshift the carrier frequency to make the analog-digital conversion possible, and we will be interested only in the IF signal at the frequency $f_{\mathrm{IF}} = |f_{\mathrm{RF}} - f_{\mathrm{LO}}|$. Therefore, a low pass filter can be used after this mixing stage to reduce the measurement noise carried at frequencies above f_{IF}. The signal frequency then becomes sufficiently low for an analog-digital converter allowing the receiver to do the rest of the procedure digitally.

After the conversion, the signal is filtered again by a digital bandpass filter. This filter's width is called the **measurement bandwidth** (typically in the range of 10 Hz to 10 kHz) and defines the balance between the signal and noise levels. Larger bandwidth allows for faster measurement but with a higher noise level. This is because narrower filters (smaller bandwidth) filter out not only noise but also lower the desired signal amplitude, resulting in longer acquisition times. The selection of the measurement bandwidth is made based on the experimental requirements, where we try to achieve a compromise between the acquisition time and signal quality. Long acquisition times also have other negative side effects like long-term drifts induced by, e.g., variations in the room temperature.

Consequently, we would like to obtain the desired quantities, which is done by the procedure known as I/Q demodulation (I stands for in-phase and Q for quadrature). This process mixes the signals down to the DC frequency $f = 0$ Hz by taking our filtered IF signal and multiplying it with the signal generated by the so-called numerically controlled oscillator (NCO). The NCO signal has two parts where one of them is phase shifted by 90°:

$$x_{\mathrm{NCO}}^{0^\circ}(t) = A_{\mathrm{NCO}} \cos(2\pi f_{\mathrm{NCO}} t), \tag{4.8}$$

$$x_{\mathrm{NCO}}^{90^\circ}(t) = A_{\mathrm{NCO}} \sin(2\pi f_{\mathrm{NCO}} t). \tag{4.9}$$

Provided that we selected the frequency $f_{\mathrm{NCO}} = f_{\mathrm{IF}}$ we can use the trigonometrical identities:

$$\cos\alpha \cos\beta = \frac{1}{2}[\cos(\alpha - \beta) + \cos(\alpha + \beta)], \tag{4.10}$$

$$\cos\alpha \sin -\beta = \frac{1}{2}[\sin(\alpha - \beta) - \sin(\alpha + \beta)]. \tag{4.11}$$

In order to calculate two signals representing real and imaginary parts of a complex number:

$$\begin{aligned} \mathrm{Re}(x) &= x_{\mathrm{IF}}(t) x_{\mathrm{NCO}}^{0^\circ}(t) \\ &= \frac{1}{2} A_{\mathrm{IF}} A_{\mathrm{NCO}} [\mathbf{cos}(\boldsymbol{\varphi}_{\mathbf{IF}}) + \cos(4\pi f_{\mathrm{NCO}} t + \varphi_{\mathrm{IF}})], \end{aligned} \tag{4.12}$$

$$\begin{aligned} \mathrm{Im}(x) &= x_{\mathrm{IF}}(t) x_{\mathrm{NCO}}^{90^\circ}(t) \\ &= \frac{1}{2} A_{\mathrm{IF}} A_{\mathrm{NCO}} [\mathbf{sin}(\boldsymbol{\varphi}_{\mathbf{IF}}) - \sin(4\pi f_{\mathrm{NCO}} t + \varphi_{\mathrm{IF}})]. \end{aligned} \tag{4.13}$$

Now we can apply a low pass filter to both components because we are interested only in the DC component:

$$x = A_x[\cos(\varphi_{\mathrm{IF}}) + i\sin(\varphi_{\mathrm{IF}})], \tag{4.14}$$

where the quantity $A_x = \frac{1}{2}A_{\mathrm{IF}}A_{\mathrm{NCO}}$ is proportional to the original wave amplitude of a or b and the angle φ_{IF} is the phase difference of a or b shifted by a constant. As the S-parameters are dependent on both a and b, it is not an issue that we do not measure the amplitude and phase directly because we are interested only in the ratio of signal amplitudes (multiplying both by the same constants cancels out) and the phase difference, where the phase shift of the x signal is subtracted.

This type of receiver is often called a heterodyne receiver (based on the Latin word hetero = different) because it involves two analog signals in the process chain – the VNA output from its internal generator and the other coming back to the VNA as reflection or transmission from the DUT.

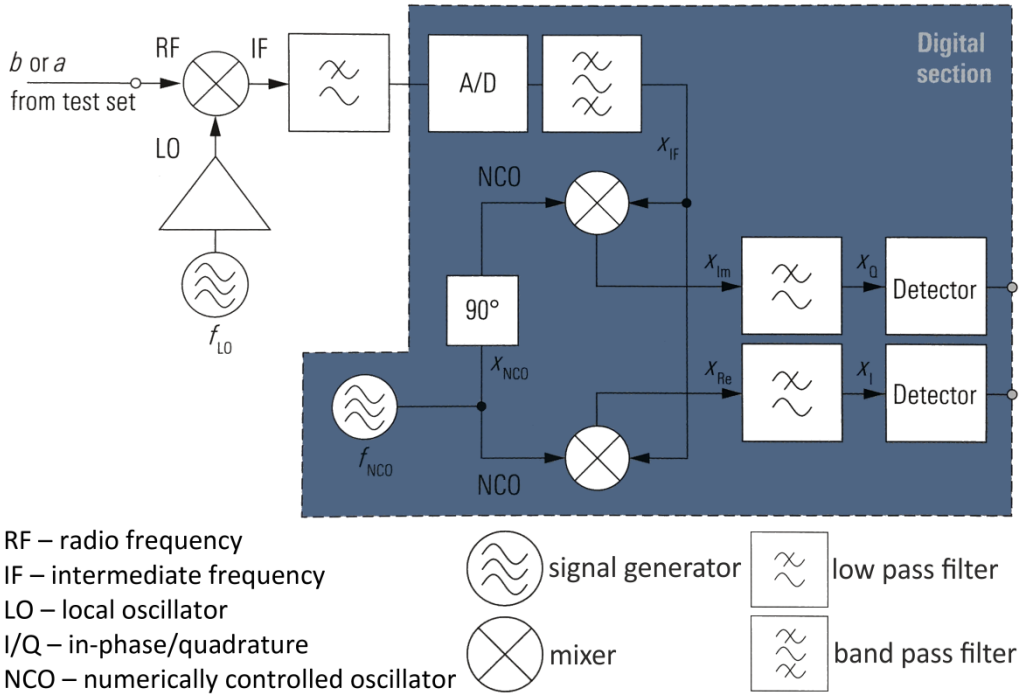

Fig. 4.4: Schematics of the heterodyne receiver. The input RF signal (from wave a or b) is mixed (multiplied) with LO signal and filtered, creating an intermediate frequency (IF) signal at the frequency $f_{IF} = |f_{RF} - f_{LO}|$. The IF signal is then converted to digital and bandpass filtered around the f_{IF} frequency which carries the magnitude and phase information from the original wave. The signal is then further processed by the I/Q demodulation method [Eq. (4.8)-(4.14)] in order to recover the signal magnitude and phase. Reprinted from [94].

4.1.3 VNA-DUT connection

Previously, we examined the VNA's internal operation, but we have not discussed how the DUT is connected into it. Each port of a VNA is equipped with a high-frequency connector to which compatible cables are mounted. There are different connector types because higher frequencies require different geometry of both the connectors and the coaxial cables (in general, both get smaller at higher frequencies to keep a single-mode operation of the connector/cable with low-wavelength radiation). Connectors, cables, and the devices themselves (VNAs, microwave generators, etc.) with higher frequency specifications also mean a significantly higher price. Therefore, the cables are matched to the corresponding

connectors. Conversions between the connectors are possible, but the chain's weakest component will limit the maximum frequency.

The oldest, simplest, and also the cheapest is the BNC connector. It is a bayonet-style connector often used on low-end oscilloscopes and frequency generators, but it is not very suitable for the spin-waves' gigahertz regime, where it can get overwhelmed easily. The most used alternative is the SMA connector, which has the maximum frequency of 18 GHz and uses a threaded interface, requiring to be torqued for proper use. It has a low price and beats the BNC frequency limit by a factor of 4.5. The next great option is the PC 2.92 mm connector, where the maximum frequency of 40 GHz is sufficient to cover the vast majority of magnetism related experiments. It is also mechanically compatible with SMA. A photo comparison of BNC, SMA, and PC 2.92 mm connectors is shown in Fig. 4.5. A variety of relevant connectors is summarized in Table 4.1.

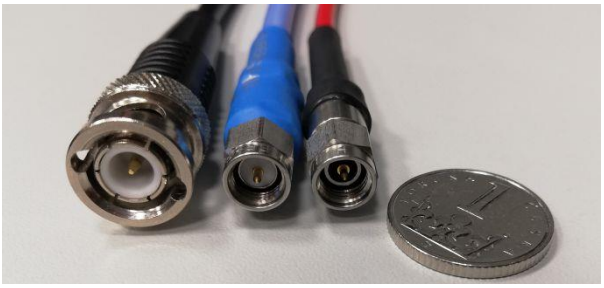

Fig. 4.5: Photo comparison of the most common connectors. From left: BNC, SMA, PC 2.92 mm connectors, and 1 CZK coin ($D = 2$ cm). All connectors are the male type.

Table 4.1: Selection of the most used high-frequency connectors.

Connector	Maximum frequency	SMA mechanical compatibility	note
BNC	4 GHz	No	Older connector
Type N	11 GHz	No	Robust industrial connector
SMA	18 GHz	Yes	Widely used, cheap
PC 3.5 mm	26.5 GHz	Yes	Similar to SMA, with a higher max. f
PC 2.92 mm	40 GHz	Yes	Great value compromise
PC 2.4 mm	50 GHz	No	
PC 1.85 mm	67 GHz	No	
PC 1 mm	110 GHz	No	

The cables can be directly connected to a DUT if it is equipped with a compatible connector. However, this is not the case often used in scientific experiments. The sample usually needs to be contacted by another suitable high-frequency interface. The samples presented herein mostly consist of a flat semiconductor substrate (Si, GaAs), where a high-frequency spin-wave excitation antenna is fabricated on the sample surface (this topic will be discussed in Section 4.2). For this purpose, we use microwave probes that provide interconnection between coaxial cables on the instrument side (by a compatible connector) and planar structures on the sample side. A typical microwave probe is shown in Fig. 4.6. They consist of legs where one is always connected to the signal line, and one or two legs are connected to the ground around the signal leg.

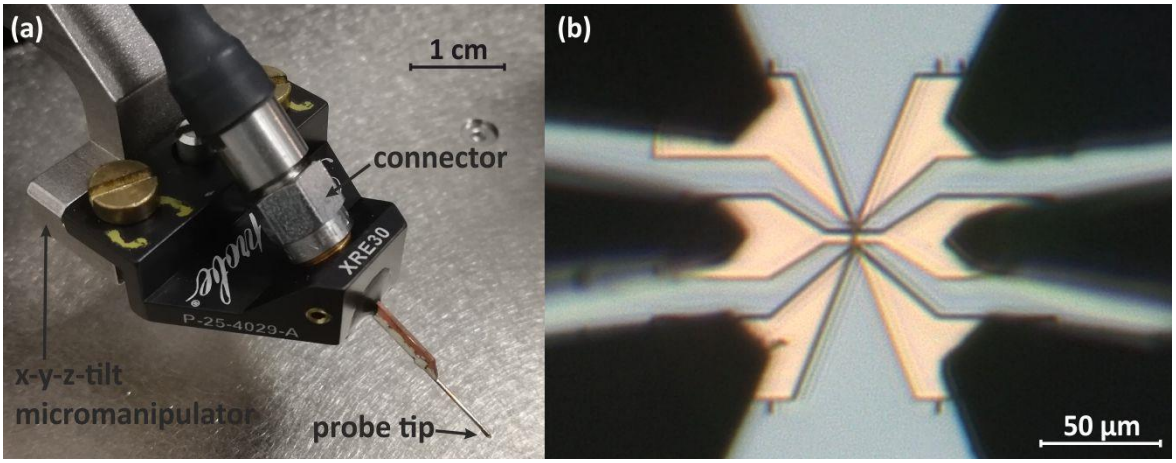

Fig. 4.6: (a) Photo of a microwave probe by GGB industries. (b) Navigation microscope view of landed GGB probes onto a sample.

4.1.4 VNA calibration

The VNA is designed to characterize a device's behavior by evaluating the magnitude and phase of the incident and reflected waves. However, systematic errors contribute to the measurement coming from the VNA's internal structure and connecting cables. For the calibrated VNA, we can talk about the reference plane of a port. That is the place from which the signal change is effectively measured.

There are various calibration methods, but we will limit the description in this setup to the Through-Open-Short-Match (TOSM) method, which has the highest number of correction factors applied to the measurement. As the name suggests, the calibration kit then consists of four calibration standards providing ideally perfect: 1) connection between the two ports (Through), 2) opened circuit, where the signal is not connected anywhere (Open), 3) short circuit, where the signal contact is directly connected into the ground (Short) and lastly 4) matching standard, where the signal contact is loaded through the VNA's matching impedance[17] into the ground (Match). To perform a new calibration, each of the standards is connected to the cable or microwave probe (based on the used VNA-DUT interface) and measured. The correction parameters are then calculated and applied directly to the VNA instrument.

When the connection to the DUT is made directly with the cables, we use a suitable (mechanically compatible) calibration kit, where the standards are three permanent single port fixtures (Open, Short, Match) and one two-port fixture (Through) that are mounted to the cables, and measured one by one. Then the instrument calculates the correction parameters based on the measurement. Cables with connected calibration standards are shown in Fig. 4.7.

If the sample is connected using microwave probes, then a calibration substrate needs to be used. The calibration substrate is a high-quality sample with fabricated standards of all required measurements (in our case Open, Short, Match, and Through) that are one by one contacted with the probes and measured in order to collect data for the calibration correction.

[17] Most instruments have sources and loads matched to $50\,\Omega$ characteristic impedance. If you are unfamiliar with the concept of characteristic impedance then please consider studying high frequency transmission lines, for example [95].

Schematics of the calibration standards used with microwave probes is shown in Fig. 4.8. In the calculation, it is not enough to acquire the data of each standard, but also several parameters of the probes and the calibration substrate are necessary, and for this reason, we would always use the combination of probes and substrate from one supplier.

Calibration should be performed regularly, approximately once a week, or whenever there is a change in the connecting cables or probes. Ideally, the VNA could be calibrated before each measurement, but this is often not the case as the process is labor-intensive.

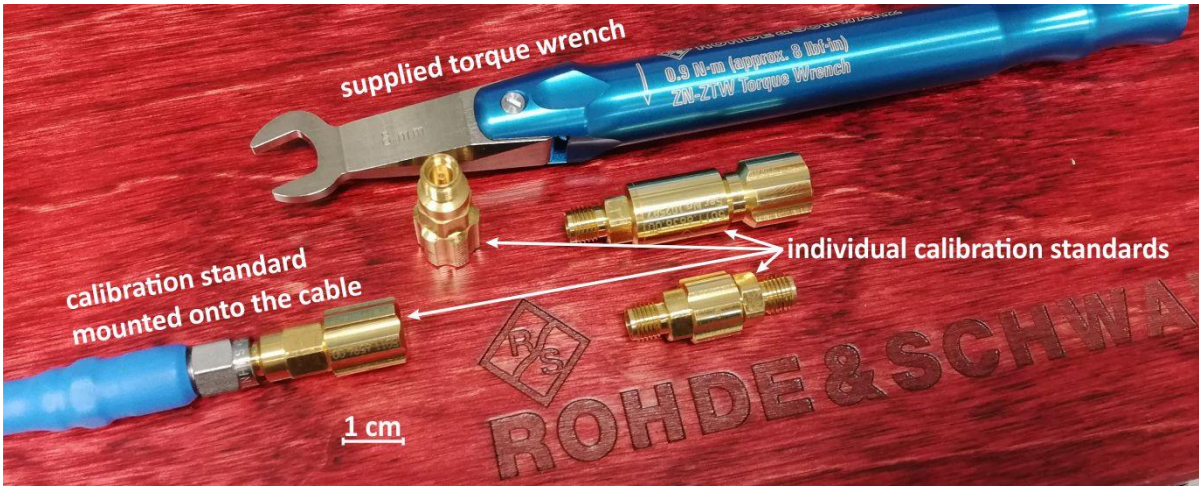

Fig. 4.7: Rohde & Schwarz ZV-Z235 calibration kit for PC 3.5 mm compatible connectors.

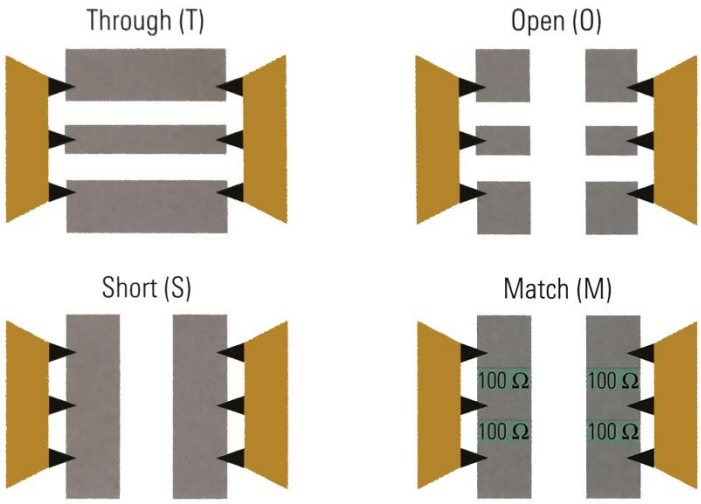

Fig. 4.8: Schematics of TOSM calibration coplanar standards for use with microwave probes. Reprinted from [94].

4.2 Excitation structures (antennas) in magnetic experiments

The VNA based methods conventionally rely on driven (coherent) excitation of magnetization dynamics by a microwave magnetic field. Electromagnets are not useful tools for this job as they have high inductance limiting the maximum operating frequency. Therefore, we need to use a simpler device with minimal inductance that can be powered by the VNA's generator. The desired capability is the high-frequency operation and microwave field localization allowing us to excite also non-zero k-vectors (spin-waves). Together we will call these structures antennas even though it does not fulfill the standard definition being a transmission device used to broadcast signals between locations. The three basic types used in this work are striplines, coplanar waveguides, and ground-signal (GS) antennas, all of which are described in the following paragraphs.

When designing the excitation antennas, we should keep in mind the characteristic impedance of the VNA's ports ($50\ \Omega$) to which the geometry needs to be matched to suppress unwanted reflections. For this purpose, we use the freeware TX line software [96], providing calculation tools for standard microwave structures based on the geometry and substrate material's permittivity. In the case of more complicated designs, it would be necessary to perform a finite element analysis or simply take a qualified guess based on previous experience.

When exciting spin waves, the source of excitation must match both the temporal and spatial frequency of the spin-wave mode. The spatial profile of the magnetic field created by the antenna dictates the ensemble of k-vectors, that the structure can excite. Thus, for all of the antenna types, we will be interested in their excitation spectra, represented by the excitation efficiency J_{exc}, which provides the degree of excitation for every k-vector. The spectrum can be calculated as a Fourier transform of the magnetic field's spatial distribution produced by the antenna's conductive lines. Therefore, it is essential to know the magnetic field distribution first, which typically requires finite element analysis. However, very good estimations were presented in the appendix of [97]. Despite the crude simplification relying only on the distribution of the current density $\boldsymbol{j}$, it provides very accurate results. The spectra shown below were calculated from the current density distributions (for striplines, CPWs, and GS antennas).

Striplines (microstrips)

Stripline is the most basic structure consisting only of a (rectangular) wire, as shown in Fig. 4.9. Then the magnetic field lines around the wire have an approximately elliptical shape. The excitation spectrum can be calculated as:

$$J_{\mathrm{exc}}^{\mathrm{strip}}(k) = \left(\frac{\sin \frac{k l_s}{2}}{\frac{k l_s}{2}} \right)^2, \tag{4.15}$$

where l_s is the width of the stripline. The advantages (or possibly disadvantages) are that striplines can also excite FMR ($k = 0$), then the excitation efficiency gradually decreases with increasing k, and that the excitation spectrum is continuous.

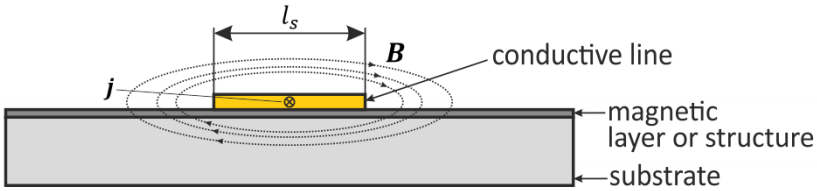

Fig. 4.9: Cross-section of a stripline excitation antenna.

Coplanar waveguides (CPW)

Another widespread planar excitation structure is the coplanar waveguide (CPW). It consists of three parallel conductive lines where the middle one is connected to the signal source, and the surrounding lines are grounded, as shown in Fig. 4.10.

The passing electric waves generate magnetic fields that have an opposite direction for each neighboring line, which forbids excitation of certain k-vectors, most importantly $k = 0$, which is the FMR. Contrary to this statement, CPWs are often used for FMR experiments because of their excellent transmission properties, and this can be possible when the signal line is very wide, at least in the order of tens of microns (for thin metallic layers). Ideally, the CPW is designed as a transmission line, i.e., connecting to two VNA ports. Minimal attenuation can be achieved if the characteristic impedance is well matched. CPWs can also form meanders where there is an even higher selection of excited k-vectors, creating almost a discrete excitation spectrum. The spectrum consists of multiple excitation peaks with quickly decaying amplitude. It can be calculated as follows:

$$J_{\mathrm{exc}}^{\mathrm{CPW}}(k) = \left(\frac{\sin\frac{kl_s}{2}}{\frac{kl_s}{2}} - \frac{\sin\frac{kl_{\mathrm{GND}}}{2}}{\frac{kl_{\mathrm{GND}}}{2}} \cos\left[k\left(\frac{l_s}{2} + \frac{l_{\mathrm{GND}}}{2} + l_{\mathrm{gap}} \right) \right] \right)^2, \tag{4.16}$$

where l_s is the width of the signal line, l_{GND} is the width of the ground line, and l_{gap} is the width of the gap between the signal and ground lines.

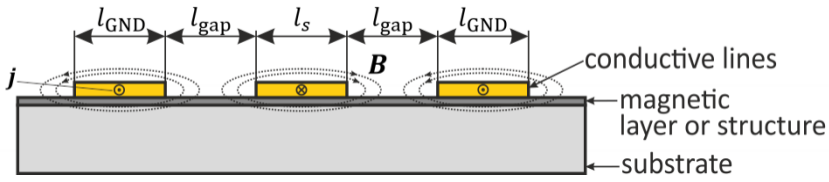

Fig. 4.10: Cross-section of a coplanar waveguide (CPW).

Ground-signal (GS) antennas

A very similar antenna type to the CPW is a GS antenna. It is essentially a CPW, but one of the grounds is missing, as shown in Fig. 4.11. It has similar excitation properties to a CPW. Compared to the CPW spectrum, the GS antenna has slightly broader peaks in the excitation spectrum (smaller selectivity). Also, the ratio of the excitation efficiency of the first side band with the primary peak is slightly higher in case of GS than in the case of CPW. The excitation spectrum can be calculated as:

$$J_{\mathrm{exc}}^{\mathrm{GS}} = \left| \frac{1}{il_s k} \left(e^{-ikl_s} - 1 \right) \left(e^{-ik(l_s + l_{\mathrm{gap}})} - 1 \right) \right|^2, \tag{4.17}$$

where l_s is the width of both the signal and ground lines, and l_{gap} is the width of the gap between the signal and ground lines.

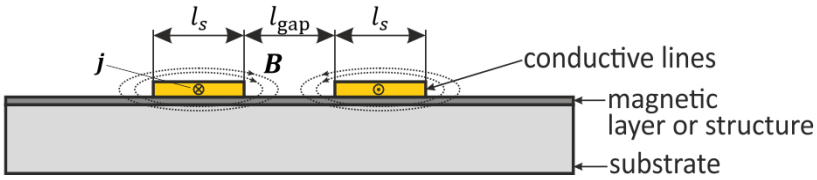

Fig. 4.11: Cross-section of a GS antenna.

Comparison of the excitation spectra

Here we will compare the excitation spectra of the mentioned antenna types. The excitation spectrum of each of them is plotted in Fig. 4.12. One of the differences is that striplines can excite FMR ($k = 0$) whereas CPW and GS cannot. The graph shows that CPW's and GS's excitation spectra are very similar. The GS antenna has slightly broader peaks. Striplines are more often chosen when there is a need for a continuum of excited k-vectors. On the other hand, if we require very high k-vector numbers, we have to shrink the stripline width, which brings higher lithography requirements, and it is also less effective because of its resistance increase. The excitation of high k-vectors is easier with CPW or GS antenna, where the spectrum depends on all geometrical parameters, but it is more difficult to fabricate for minimal dimensions, especially with small gaps in the order of 100 nm or less.

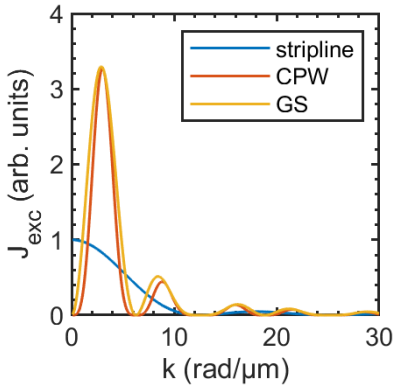

Fig. 4.12: Comparison of the excitation spectra J_{exc} for stripline antenna, coplanar waveguide and GS antenna. All calculation dimensions are 500 nm ($l_s = l_{gap} = l_{GND} = 500$ nm).

Other antenna types: ladders, meanders, and others

There are also different antenna designs being developed for specific purposes. The two main types are ladders [98] and meanders [97,99]. Both use a set of striplines, wherein the ladders' case, they are connected in parallel (neighboring striplines have the current flow in the same direction), or in the case of meanders, the striplines are connected in series (neighboring striplines have the current flow in the opposite direction). Meander antennas can also be formed from CPWs [97]. Both approaches allow for very selective excitation (narrow peaks in the excitation spectrum) and allow for more effective excitation of very high k-vectors when compared to striplines, CPWs, or GS antennas.

4.3 Ferromagnetic resonance measured on VNA

Ferromagnetic resonance (FMR), being the collective oscillations of magnetic spins, is the simplest case of high-frequency excitation. Historically, the first FMR experiments used a microwave resonant cavity placed in the gap of an electromagnet [30]. The incident microwaves drive the cavity to resonance, and the microwave photons then excite the magnetic sample. The observed quantity is the reflected microwave power at a given magnetic field. Although such resonant systems are very sensitive, the main disadvantage lies in the cavity's very narrow frequency band of operation. The only variable parameters in the experiment are the external magnetic field and the respective angle of the sample to the external magnetic field direction.

Modern FMR experiments often use a VNA and planar excitation structures like the before mentioned striplines and CPWs. Here both the frequency and magnetic field can be swept in an extensive range providing much more data for detailed analysis. The method is usually called the broadband VNA-FMR. The main principle remains the same: a microwave source excites the sample, this time using the high-frequency field of a stripline or CPW, and then the microwave transmission through the CPW is detected on the second VNA port. There is also no need for complicated sample installation as it is simply placed over the waveguide with the studied layer facing down (so-called flip-chip method).

There is a variety of fixtures providing an interface for the VNA-FMR experiment. In our lab, we use a CPW fabricated onto a GaAs substrate utilizing electron beam lithography and electron beam evaporation. The parameters of the CPW were calculated using the TX line (freeware) software to match the impedance of the VNA. The CPW is interfaced to the VNA using microwave probes, which is schematically shown in Fig. 4.13.

An alternative is to the flip-chip method is to fabricate a permanent fixture with a waveguide contacted to RF connectors. Therefore, there would be no need for microwave probes. This approach can be superior because such a fixture with metalized vias and a well-defined ground plane can exhibit an almost flat frequency response. Nevertheless, it is far more challenging to design and fabricate it because employing more advanced RF system knowledge is required. On the other hand, the microwave probes are supplied with a complete calibration method, and even if the fabrication of self-developed CPW fixtures was not possible, every calibration substrate is equipped with a long CPW transmission line of very high quality that can be used precisely for this purpose with no need for in-house lithography.

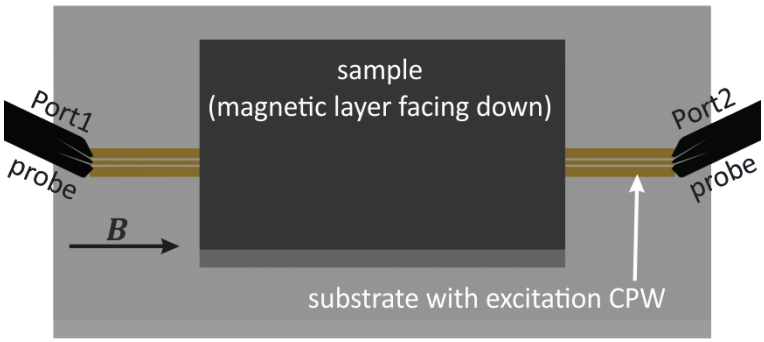

Fig. 4.13: Schematics of the VNA-FMR experiment. The coplanar waveguide is connected to the VNA using a pair of microprobes. The external magnetic field is aligned with the CPW, onto which the sample is placed with the magnetic layer facing down.

4.3.1 Data processing

The ferromagnetic resonance is observed as a dip in the frequency spectrum of the transmission signal magnitude $\mathrm{Mag}(S_{21})$. This dip represents an energy loss because the power is used to excite the ferromagnetic resonance. There are also other sources of frequency-dependent energy dissipation; thus, the measured FMR signal is modulated onto a non-even background. An example of an unprocessed FMR signal for a 30 nm thick CoFeB layer is shown in Fig. 4.14(a,c). It is profitable to use a suitable data processing method to suppress the non-magnetic background, which is constant over the magnetic field. The simplest method by far is to divide the measured transmission magnitude by a reference. The most straightforward reference acquisition can be made by increasing the magnetic field high enough that the FMR peak goes out of the measured frequency range. This is often hardly possible in our case of the 380 mT maximum field and a 50 GHz VNA. A useful alternative is to calculate the reference as the median value of the measured signal magnitude for all magnetic fields at every single frequency because the median well reflects the background value:

$$\div \mathrm{Mag}(S_{ij}) = \frac{\mathrm{Mag}(S_{ij})}{S_{ij}^{\mathrm{ref}}}, \quad S_{ij}^{\mathrm{ref}} = \mathrm{median}_B\left[\mathrm{Mag}(S_{ij})\right]. \tag{4.18}$$

We will use the division symbol ÷ to annotate this kind of processing (opposite to signal subtraction, annotated Δ, which is used in the data processing of PSWS, Section 4.5). After applying this procedure, the signal value is relative to the background, which now has a value of 1. An example of processed data is shown in Fig. 4.14(b,d).

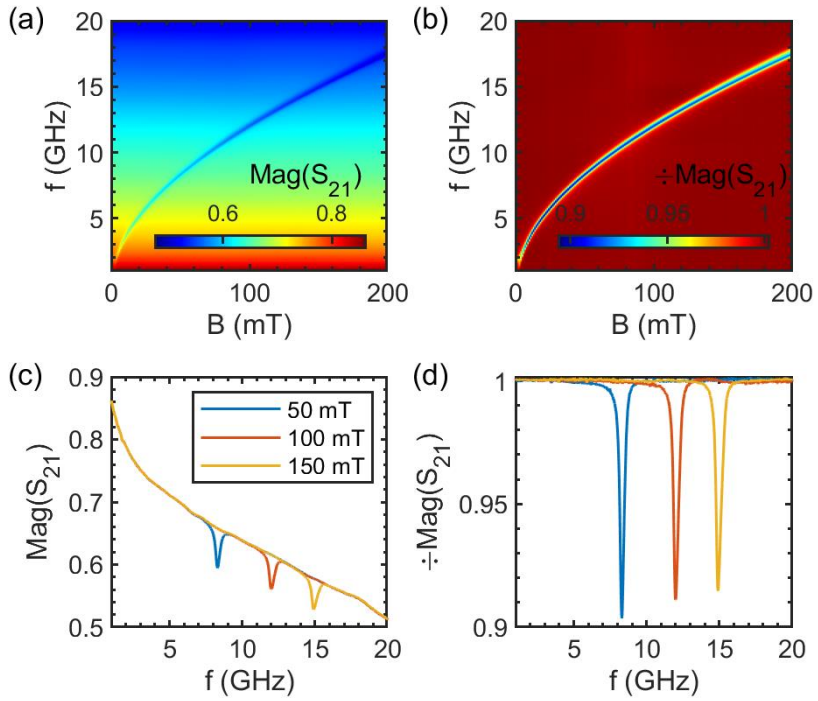

Fig. 4.14: Processing of VNA-FMR data. (a) Example of raw S_{21} data magnitude acquired from CoFeB 30 nm layer for a wide range of magnetic fields and frequencies. (c,d) Single scans for magnetic fields 50, 100, and 150 mT. (b,d) Each point is then divided by the median value over all measured fields suppressing the background, which now has a value of 1. This data can be used for further evaluation of material parameters.

The disadvantage of the previous approach is that the value $\div \mathrm{Mag}(S_{21})$ has no real physical meaning, but it usually does not limit this method's purpose when quantitative evaluation of the signal is not of interest. It clears the data into very sharp dips on a very flat background [Fig. 4.14(d)], and it does not change the peak positions. Thus, it does not affect the fit using the Kittel formula, presented in the following section.

On the other hand, there is a sophisticated model calculating the dynamic susceptibility χ (or rather a variable that is proportional to it). The dynamic susceptibility χ is a complex variable which is very well mathematically described and can be fitted not only for the peak

positions but also for its whole shape, including the damping parameter α. The great disadvantage is much higher acquisition time because the method requires measuring a reference in the perpendicular magnetic field and a reference of the excitation CPW without the sample, while this processing approach is more often unnecessary. It was previously dealt with within our group [100], and a full description is also given in [30,101], which I recommend for further reading.

4.3.2 Extraction of saturation magnetization and gyromagnetic ratio

The main goal of FMR measurement is usually extraction of the basic material parameters: Saturation magnetization M_s and gyromagnetic ratio γ. This can be done by fitting the peak positions f_{FMR} by the Kittel formula (also previously presented in Section 1.5):

$$f_{\mathrm{FMR}} = \frac{\gamma}{2\pi}\sqrt{(B_{\mathrm{ext}} + B_0)(B_{\mathrm{ext}} + B_0 + \mu_0 M_S)}. \tag{4.19}$$

The field offset B_0 is typically non-zero even for non-anisotropic materials like NiFe or CoFeB because there usually is a small residual magnetocrystalline anisotropy. Another contributing factor to B_0 is the shape anisotropy. Therefore it should not be omitted in the fit. Fig. 4.15 shows the processed VNA-FMR data and their fits using Eq. (4.19) for our three most used materials: NiFe, CoFeB, and YIG, all fitted for M_s, γ, and B_0. The fits reproduce the data with remarkable agreement, and the resulting fit coefficients are reasonable and non-deviating from the known values. However, we should be cautious when using unconstrained fits because the constants M_s, and γ are highly dependent on each other, and the fit may yield

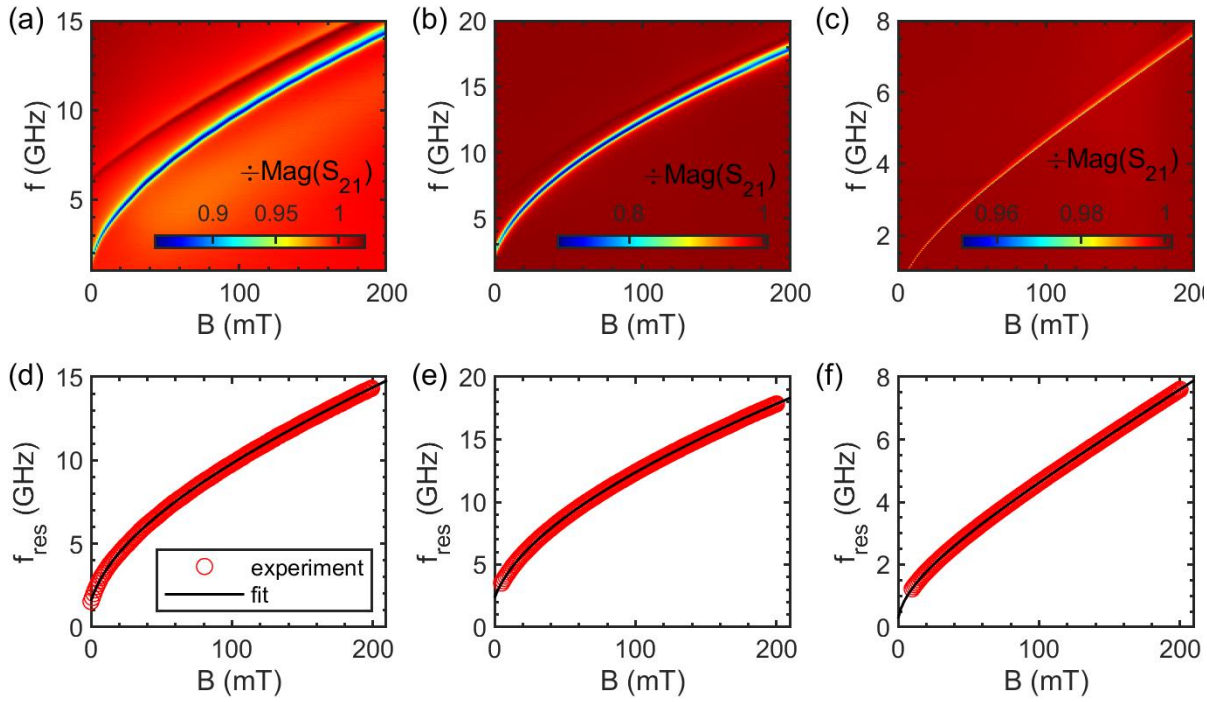

Fig. 4.15: VNA-FMR scans fitted with the Kittel formula Eq. (4.19) for (a) NiFe 100 nm, (b) CoFeB 100 nm, (c) YIG 100 nm. (a,b) have visible PSSW bands above the FMR band. Measurements were performed in a decreasing magnetic field.

Fit parameters:

(d) NiFe 100 nm: $M_s = 801$ kA/m ($\mu_0 M_s = 1.01$ T), $\gamma/2\pi = 29.0$ GHz/T, $B_0 = 2.85$ mT

(e) CoFeB 100 nm: $M_s = 1.20$ MA/m ($\mu_0 M_s = 1.51$ T), $\gamma/2\pi = 30.2$ GHz/T, $B_0 = 4.00$ mT

(f) YIG 100 nm: $M_s = 142$ kA/m ($\mu_0 M_s = 0.178$ T), $\gamma/2\pi = 27.6$ GHz/T, $B_0 = 0.55$ mT

inaccurate results for some samples even when the fit exhibits a very low deviation from the experimental data. This problem can be solved by fixing either M_s or γ at a known level and fitting only the remaining one together with the field offset B_0.

The first two materials presented in Fig. 4.15 also have a second visible magnetic field dependent signal above the FMR. This mode belongs to perpendicular standing spin-waves (PSSW) and can be used for extraction of the exchange constant A_{ex}, which will be discussed in the next Section 4.3.3.

Another measured sample was a layer of epitaxial Fe (001) on a MgO (001) single crystal substrate. The sample was grown by magnetron sputtering at an elevated temperature. The epitaxial growth facilitated a high magnetocrystalline anisotropy, which is reflected in terms of the field offset B_0. Fig. 4.16 shows the processed measurements of this sample at both (a) the easy axis along the [100] direction, and (b) the hard axis along the [110] direction. At the easy axis, the FMR spectrum for positive and negative fields meets at the frequency axis, while at the hard axis, the spectrum has two dips. When decreasing the field towards zero, the magnetic moments will align into the easy axis, and the resonant frequency should be the same as in (a). When raising the field from zero, we are overcoming the anisotropy strength, and the direction of magnetization within the sample is not well defined, and we exclude it from the analysis. Beyond the dip, the whole sample should be aligned into the hard axis and follow the Kittel formula, only the field offset B_0 will be negative, while at the easy axis, it will have the same size but positive sign. Therefore, we can use both measurements in one fit; only the field offset's sign must change for each part. The fitting results are shown in Fig. 4.16(c). The small jump in approx. zero-field suggests the magnetization flip into the other direction of the easy axes due to slight misalignment of the magnetic field and the sample's hard axis.

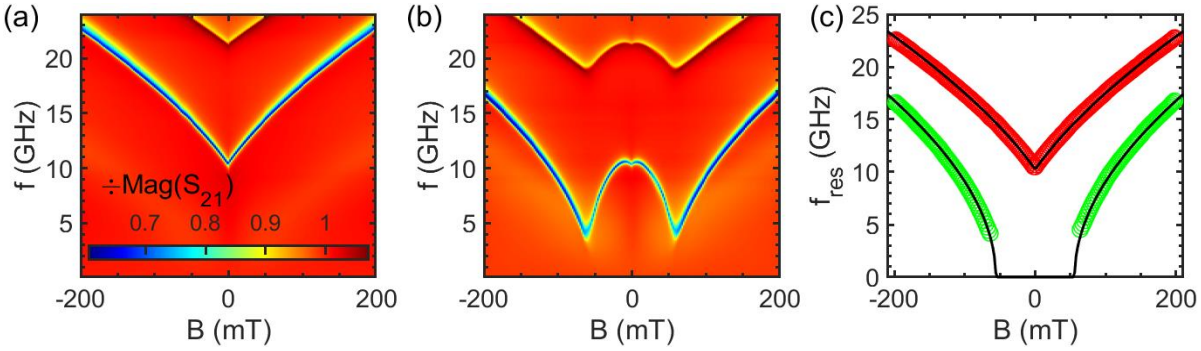

Fig. 4.16: VNA-FMR scans of a sample with high anisotropy - epitaxial Fe 30 nm. (a) easy axis scan along the [100] direction. (b) hard axis scan along the [110] direction. The color scale is shared for (a,b). (c) Kittel fit for both the easy axis (red circles) and the hard axis (green circles) sharing the field offset B_0 which is positive in case of easy axis and negative in the case of the hard axis. Signal bands in upper parts of (a,b) belong to PSSW.
Fit parameters: $M_s = 1.74$ MA/m ($\mu_0 M_s = 2.18$ T), $B_0 = 55.8$ mT; fixed $\gamma/2\pi = 29.0$ GHz/T.

4.3.3 Extraction of the exchange constant from PSSW

The VNA-FMR experimental setup can also excite the perpendicular standing spin-waves (PSSW), which will be visible in the signal as an extra band above the FMR band. FMR always has a higher signal and a different shape. The FMR data is measured in the form of a dip in the

signal $\div \mathrm{Mag}(S_{21})$, while the PSSW signal looks like a dip derivative, making it more challenging to locate automatically with software. In case we have access to the full dynamic susceptibility χ, we can use the real part $\mathrm{Re}(\chi)$ to locate the PSSW position, because it shows a dip [while the shape of $\mathrm{Im}(\chi)$ looks similar to $\div \mathrm{Mag}(S_{21})$]. The PSSW band follows the Herring-Kittel formula (also presented in Section 1.7):

$$f_{\mathrm{PSSW}} = \frac{\gamma}{2\pi}\sqrt{\left(B + B_0 + \frac{2A_{\mathrm{ex}}}{M_S}\left(\frac{n\pi}{t}\right)^2\right)\left(B + B_0 + \frac{2A_{\mathrm{ex}}}{M_S}\left(\frac{n\pi}{t}\right)^2 + \mu_0 M_S\right)}. \qquad (4.20)$$

It has the same form as the Kittel formula, but there is an extra term $\frac{2A_{\mathrm{ex}}}{M_S}\left(\frac{n\pi}{t}\right)^2$. Here, A_{ex} is the exchange constant, which can be extracted by fitting the experimental data. Additionally, it is also dependent on M_s and on the sample thickness t. The positive integer parameter n is the standing wave order (the formula reduces into the Kittel formula for $n = 0$). Although higher orders than one can exist and can be detected, e.g., by BLS, we have never observed any other PSSW band than for $n = 1$ in the VNA-FMR experiment. Some materials show very strong PSSW signal [epitaxial Fe in Fig. 4.16 or NiFe in Fig. 4.15(a)], some materials show a weak but detectable signal [CoFeB in Fig. 4.15(b)], and some materials show no measurable PSSW signal whatsoever [YIG in Fig. 4.15(c) or thinner layers of CoFeB, e.g., 30 nm in Fig. 4.14]. The PSSW bands were evaluated in Fig. 4.17 by fitting A_{ex} and fixing all of the remaining constants. The constants B_0 and t cannot be fitted because they are correlated to A_{ex}, while M_s is possible to fit. However, it is not recommended because it is a good practice to extract the M_s parameter from the Kittel fit or from a vibrating sample magnetometer (VSM) measurement. The quality of the fit will be dependent on the accuracy of the obtained constants prior to the fitting of PSSW. We should always be cautious about the obtained values when using unconstrained fits with multiple dependent parameters.

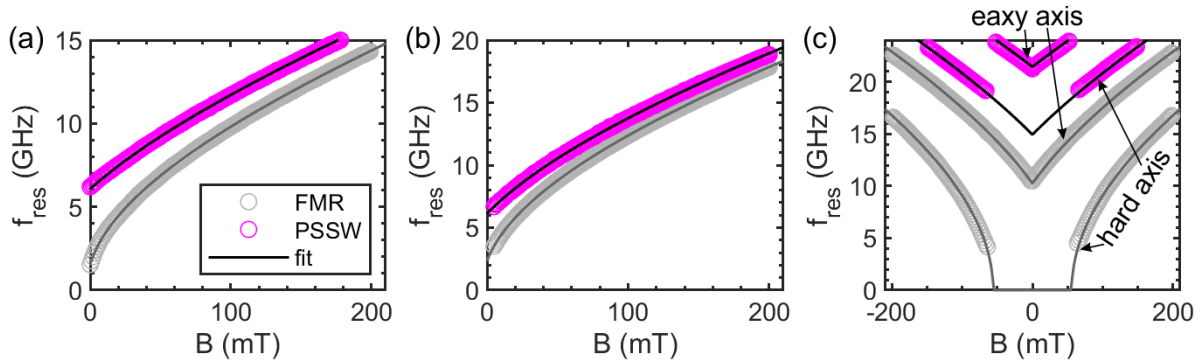

Fig. 4.17: Fitting of the exchange constant A_{ex} using the data from Fig. 4.15 for (a) NiFe 100 nm, (b) CoFeB 100 nm, (c) epitaxial Fe 30 nm in both easy and hard axes. The YIG measurement in Fig. 4.15(c) did not show a PSSW band that could be processed. The FMR frequency is replotted in gray points for reference, in the case of (c) for both the easy and hard axes. All parameters (M_s, γ, B_0) were fixed at the values given in Fig. 4.15. The layer thickness was not measured but was fixed at the nominal deposition value. The PSSW bands were considered to be of the first order, i.e., $n = 1$ in all cases. Fitting was performed only for A_{ex}:

(a) NiFe 100 nm: $A_{ex} = 16.9$ pJ/m,

(b) CoFeB 100 nm: $A_{ex} = 16.3$ pJ/m,

(c) epitaxial Fe 30 nm: $A_{ex} = 13.5$ pJ/m.

4.3.4 Extraction of the damping parameter

The last material constant that is possible to extract from the FMR spectrum is the damping parameter α. This can be achieved using two approaches. Either by fitting the dynamic susceptibility when it is available or by evaluating the FMR peak broadening. The dynamic susceptibility fitting was extensively dealt with in [100]. In the following text we will show the second approach. The FMR peak's width shows a linear increase with increasing frequency. This frequency-dependent broadening can be described with the following equation [55]:

$$\Delta B = \left(\frac{2\pi}{\gamma}\right) 2\alpha f + \Delta B_0, \tag{4.21}$$

where ΔB is the FMR dip's full width at half minimum and ΔB_0 is called the inhomogeneous broadening constant.

The dip width needs to be evaluated, and one of the options is fitting it with a suitable peak function. In order to achieve good results, the magnetic field step must be small enough to have a sufficient number of points in the dip. A good way of evaluating an FMR dip is by fitting it with the asymmetric Lorentzian function $L(B)$ [102]:

$$L(B) = C_{\mathrm{sym}} \frac{\left(\frac{\Delta B}{2}\right)^2}{\left(\frac{\Delta B}{2}\right)^2 + (B - B_{\mathrm{res}})^2} + C_{\mathrm{asym}} \frac{\frac{\Delta B}{2}(B - B_{\mathrm{res}})}{\left(\frac{\Delta B}{2}\right)^2 + (B - B_{\mathrm{res}})^2} + C_0, \tag{4.22}$$

where ΔB is the dip's full width at half maximum (minimum), B_{res} is the resonant magnetic field, and constants $C_{\mathrm{sym}}, C_{\mathrm{asym}}, C_0$ are the amplitudes of the symmetric part, asymmetric part, and constant offset, respectively. For fitting of $\div \mathrm{Mag}(S_{21})$ data, the constant offset can be fixed at the value 1. Fig. 4.18(a) shows the effect of each part of the symmetric and asymmetric $L(B)$ parts with an example fit in (b).

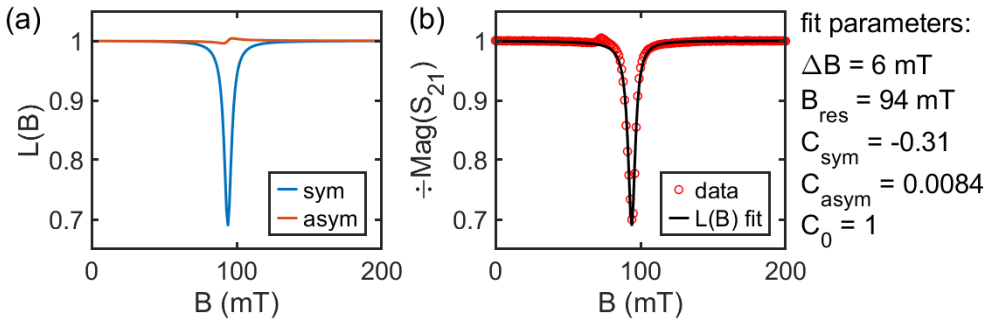

Fig. 4.18: (a) symmetric and asymmetric parts of $L(B)$ plotted for parameters fitted from CoFeB 100 nm FMR measurement at $f = 12$ GHz demonstrating the shape of each $L(B)$ part. (b) Data with the $L(B)$ fit combining the parts plotted in (a).

Now we can plot the peak width ΔB against frequency and extract the damping from the linear fit. Fig. 4.19 shows the fits for (a) NiFe, (b) CoFeB, and (c) epitaxial Fe layers. We should note that the change in width is small, and we need to be cautious with this analysis. In the case of the NiFe layer in Fig. 4.19(a), the dependence shows oscillations, which were not explained even after careful examination of the fits, but the overall dependence is linear, and the extracted $\alpha = 0.0074$ is reasonably comparable to the value $\alpha = 0.007$ found in

literature [103]. Results for the CoFeB layer in Fig. 4.19(b) look reasonable; only the extracted $\alpha = 0.0089$ is high when compared to the expected value around 0.004 [103]. The dependence for epitaxial Fe in Fig. 4.19(c) also exhibits certain anomalies at approx. 14, 17.5, and 20 GHz, but the overall dependence is linear, yielding $\alpha = 0.010$.

The intriguing thing about this fit is the inhomogeneous broadening constant ΔB_0, for which our fits yielded negative values in two out of our three cases. If we consider only intrinsic Gilbert damping caused by the spin-orbit coupling, then the broadening constant should be positive, suggesting that there are other contributors to the damping. Previous reports have shown that the negative broadening can be caused by two magnon scattering due to the presence of defects in the film [104,105]. We should note that the extracted damping is the total damping, consisting of all contributions.

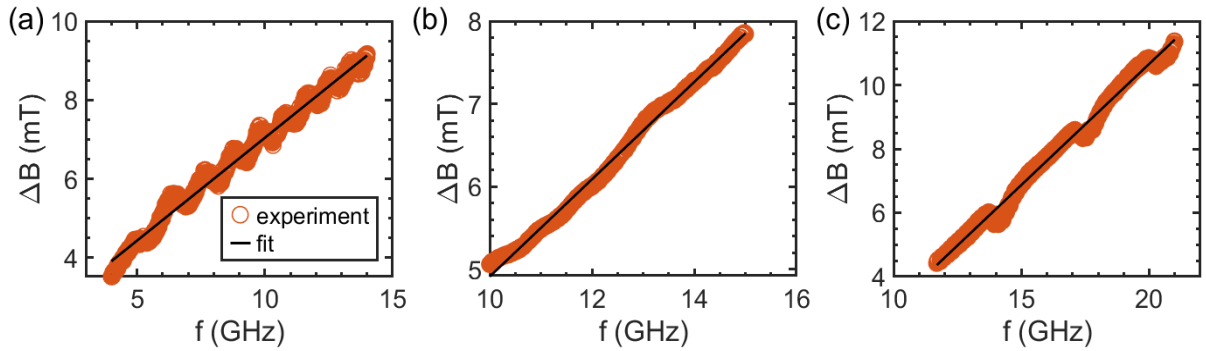

Fig. 4.19: Evaluation of the damping parameter α for (a) NiFe 100 nm, (b) CoFeB 100 nm, (c) epitaxial Fe 30 nm. The YIG data was not fitted because of the narrow character of its peaks, where the width cannot be reliably evaluated without decreasing the field step size drastically.
Fitting was performed only for α:

(a) NiFe 100 nm: $\alpha = 0.0074$, $\Delta B_0 = 1.8$ mT,
(b) CoFeB 100 nm: $\alpha = 0.0089$, $\Delta B_0 = -0.1$ mT,
(c) epiFe 30 nm: $\alpha = 0.0101$, $\Delta B_0 = -4.5$ mT.

4.3.5 Recommended approach to material analysis by VNA-FMR

In the following recipe, we summarize our recommended practice for material evaluation by VNA-FMR. Please consider the actual experimental expectations and adjust the procedure.

1. Measure VNA-FMR sweep.
   Be aware of setting the VNA frequency range to capture all the required data. Perform a power sweep if unsure what power to use (typically less than 0 dBm). Data from standard materials usually have very high signals. Therefore there is no need for small measurement bandwidth; 1 or 10 kHz is typically used.
2. Fit the VNA-FMR peaks using the Kittel formula.
   Fitting parameters will be M_s, γ and B_0. Because fitting of all three may not be reliable, we can fix either M_s or γ to a known value. We are usually interested in the M_s value, therefore fixing γ is more desirable when the constant is known for the given material. On the other hand, γ is not easily measured by other experiments. Therefore when γ cannot be reliably obtained (e.g., an unknown material lacking literature), we can fit M_s, because it is measurable by VSM, while fitting γ.
3. AFM[18] or XRR[19] measurement of layer thickness.
4. If possible, fit the PSSW spectrum.
   All parameters will be fixed except for A_{ex} requiring precise knowledge of M_s and t because their uncertainties will directly project into the A_{ex} error. B_0 cannot be fitted here because it is directly related to A_{ex}.
5. Evaluate α by a linear fit of the peak broadening.
   Beware that γ is the weighting parameter for α, and its uncertainty will project to the result.

4.3.6 Summary of VNA-FMR fitting results

The previously presented FMR data provided a guideline to the acquisition and evaluation of the VNA-FMR measurement. The following Table 4.2 summarizes all the material parameters that were evaluated in this subchapter. Thicknesses were not measured, and the nominal values are stated.

Table 4.2: Summary of the fitting results obtained from the FMR analysis.

	t (nm)	M_s (kA/m)	M_s (T)	$\gamma/2\pi$ (GHz/T)	B_0 (mT)	A_{ex} (pJ/m)	α ()	ΔB_0 (mT)
	(nominal)	(Kittel fit)				(PSSW)	(broadening)	
NiFe	100	801	1.01	29	2.85	16.9	0.0074	1.8
CoFeB	100	1200	1.51	30.2	4	16.3	0.0089	-0.1
Epi. Fe	30	1740	2.18	29	55.8	*N/A*	*N/A*	*N/A*
YIG	100	142	0.178	27.6	0.55	13.5	0.0101	-4.5

[18] Atomic force microscope
[19] X-ray reflectometry

4.4 Magnetic vortices under high-frequency excitation

Chapter 3 was devoted to the static nucleation processes of magnetic vortices, and even though vortex dynamics go beyond the goals of this thesis, two basic experiments regarding high-frequency vortex excitation were tested using the VNA. Various experiments using VNA measurement of vortices were also presented in the literature, e.g. [106–108].

As opposed to the electrical detection using the AMR effect, where individual disks are probed, the VNA cannot detect a single unit's signal. Hence the samples have to consist of a larger number (hundreds) of disks, for which a collective response is measured. For experiments where this does not present a problem, the experiment is relatively straightforward. The sample can have the form of a CPW, where the disks are fabricated onto the signal line in a second lithography step, as shown in Fig. 4.20(a). The RF probes then contact both sides of the CPW, measuring the vortex signal.

4.4.1 Measurement of the vortex gyrotropic precession

A typical experiment that can be detected on magnetic vortices is the gyrotropic precession of the vortex cores. The calculation of the gyrotropic eigenfrequency was presented in Section 1.5. The frequency of this mode is usually in the order of hundreds of MHz. For the used dimensions (diameter $D = 1$ μm, and thickness $t = 50$ nm) and NiFe parameters, the eigenfrequency was calculated to be 901 MHz (RVM) and 516 MHz (two-vortex model). The measurement in Fig. 4.20(b) shows the microwave absorption in the CPW due to exciting the gyrotropic resonance at the frequency be approx. 370 MHz in zero field. Therefore we can conclude that the models overestimate the eigenfrequencies, while the two-vortex model is closer to reality.

The magnetic field was swept from negative values to positive, and we can observe the nucleation taking place in approx. -10 mT, and the annihilation in approx. 14 mT. The data is also blurred due to the high number of measured disks, which can have slightly different nucleation and annihilation fields. The frequency slightly increases with the magnetic field, which is expected [14].

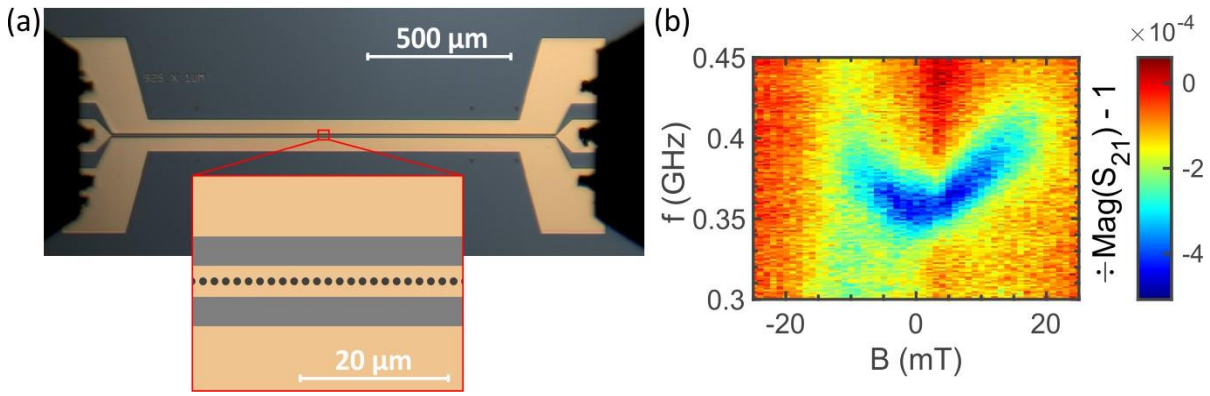

Fig. 4.20: VNA measurement of the magnetic vortex resonance. (a) Navigation microscope micrograph of CPW with magnetic discs on top of the signal line (~1000 units of NiFe disks, $D = 1$ μm, $t = 50$ nm). The detail shows the layout of the disks on the signal line. (b) S_{21} transmission measurement showing the vortex resonance.

4.4.2 Excitation of vortices in the GHz regime

Magnetic vortices also have a detectable high-frequency response measured with the same experimental layout as in Fig. 4.20(a). When the disks are saturated, the measured signal corresponds to FMR, which can be observed in Fig. 4.21 for magnetic fields larger than approx. 25 mT. When the field is lowered below this level, the magnetic vortices nucleate in the disks, and their high-frequency response will be measured. There are several visible branches between -25 and 25 mT in both the transmission parameter in Fig. 4.21(a) and the reflection parameter in Fig. 4.21(b).

According to the simulations in [109], the branches visible in Fig. 4.21(a,b) at approx. 6.5 GHz and 7.5 GHz in zero field should be azimuthal spin-wave modes, and the branch at 9 GHz should be a radial spin-wave mode.

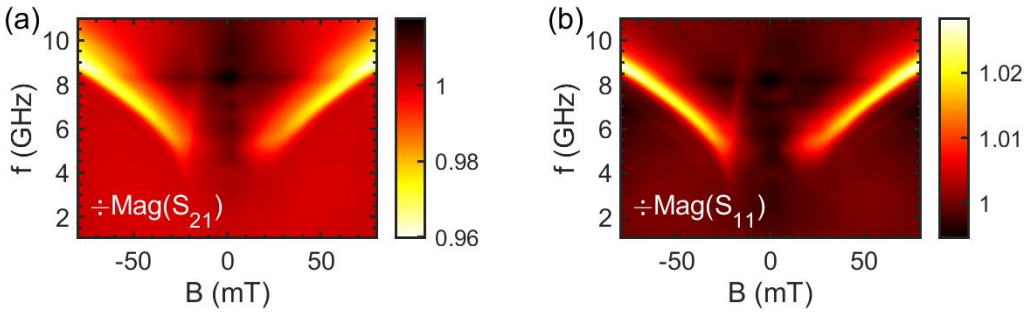

Fig. 4.21: VNA measurement of high-frequency magnetic vortex excitation for ~1000 units of NiFe disks, $D = 2\ \mu m$, $t = 80\ nm$. The bright bands reaching to high magnetic fields are the FMR response of the disks in saturation. Spin-wave excitation modes are visible within the -25 to 25 mT field range.

4.5 Propagating spin-wave spectroscopy (PSWS)

The propagating spin-wave spectroscopy (PSWS) is a VNA-based technique utilizing a pair of microwave antennas (stripline, GS, CPW) to study spin-wave propagation. One of the antennas is powered by the VNA's microwave source and excites spin-waves, propagating over the gap. The second antenna serves as an induction pick-up detected by the VNA's second port, as shown in Fig. 4.22. The first experimental demonstration was performed on YIG in the 1970s [110]. In metallic layers, it was first measured by Bailleul et al. in 2001 [31].

The excited spin-waves have the properties given by the dispersion relation of the given material, which connects the temporal frequency to the k-vector, but it also dictates other properties like the group velocity v_g and propagation length Λ. The dispersion properties were previously described in Chapter 1.

The antenna type will determine the excitation properties and can be designed for the needs of the experiment. Striplines (rectangular wires) provide a continuous spectrum of k-vectors, where the maximum excited k-vector is limited by the stripline width. Ciubotaru et al. [111] showed scalability of the antennas, where 125 nm wide striplines provided a wide continuous k-vector band. Good alternatives are GS antennas, e.g. [31,112,113], or coplanar waveguides, e.g. [97,114,115], both providing a filtering capability for the k-vector spectrum allowing only specific ranges to exist. PSWS can be measured on both nanostructured materials (stripes) [97,111–114,116,117] as well as layers [115,118]. It was previously shown that the PSWS signal could be negligibly different for continuous layers and stripes [115], which is true for wider stripes where the in-plane quantization does not play a role. PSWS signals can also be modeled [97,115,119].

We mainly focus on measuring magnetic layers using striplines due to the simplicity of fabrication (no extra patterning of the magnetic layer, as it is unnecessary unless the waveguide modes need to be probed) and the continuous k-vector spectrum. This serves as the basis for the dispersion measurement because the VNA can measure both the magnitude and phase of the detected microwaves. Therefore, it measures the spin-waves phase, which is useful for further analysis. The phase then serves in the process of dispersion extraction, which will be described in Chapter 5.

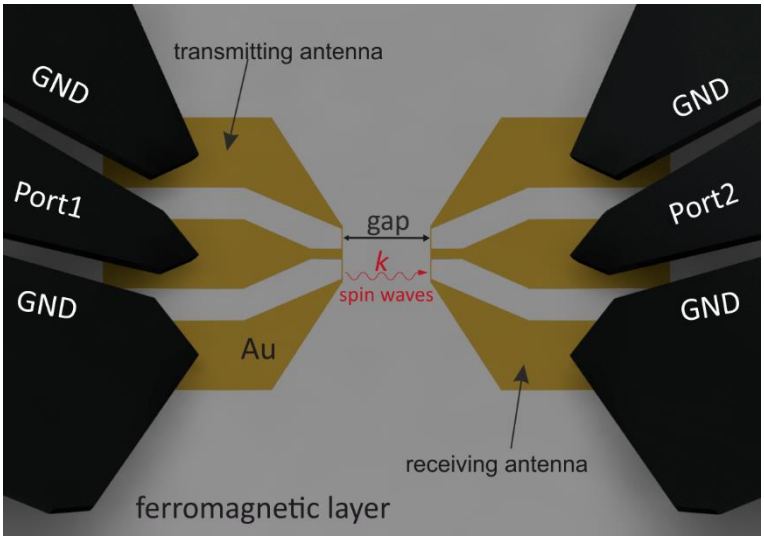

Fig. 4.22: Schematics of the PSWS experiment. A pair of microwave antennas is connected to a VNA using microwave probes. One antenna excites spin-waves in the magnetic layer underneath in which the waves propagate over the gap distance and are detected using the induction pick-up of the second antenna.

4.5.1 Data Processing

The raw S-parameters, as they are measured by the VNA, carry the PSWS signal that is modulated onto a non-magnetic background. The background is always present in the experiment due to the crosstalk between the antennas. It should be constant over the magnetic field and therefore can be subtracted by a reference signal S_{ij}^{ref}. The reference can be either measured as a high magnetic field sweep (signals are out of the frequency range) or calculated as the median value of the real and imaginary S_{ij} components over all measured magnetic fields (the median value well reflects the background level), providing the processed signal ΔS_{ij}:

$$\Delta S_{ij} = S_{ij} - S_{ij}^{\mathrm{ref}}, \quad S_{ij}^{\mathrm{ref}} = \mathrm{median}_B\left[\mathrm{Re}(S_{ij})\right] + i \cdot \mathrm{median}_B\left[\mathrm{Im}(S_{ij})\right]. \tag{4.23}$$

Example results of the S_{21} signal measured on a 30 nm thick CoFeB layer over the gap distance 1.8 µm using the $\boldsymbol{k} \perp \boldsymbol{M}$ geometry and 500 nm wide striplines is shown in Fig. 4.23(a,b,c). Processed ΔS_{21} data is then shown in Fig. 4.23(d,e,f). The signal is stronger in the $+B$ part of the spectrum because this geometry is known to be non-reciprocal, which will be discussed later.

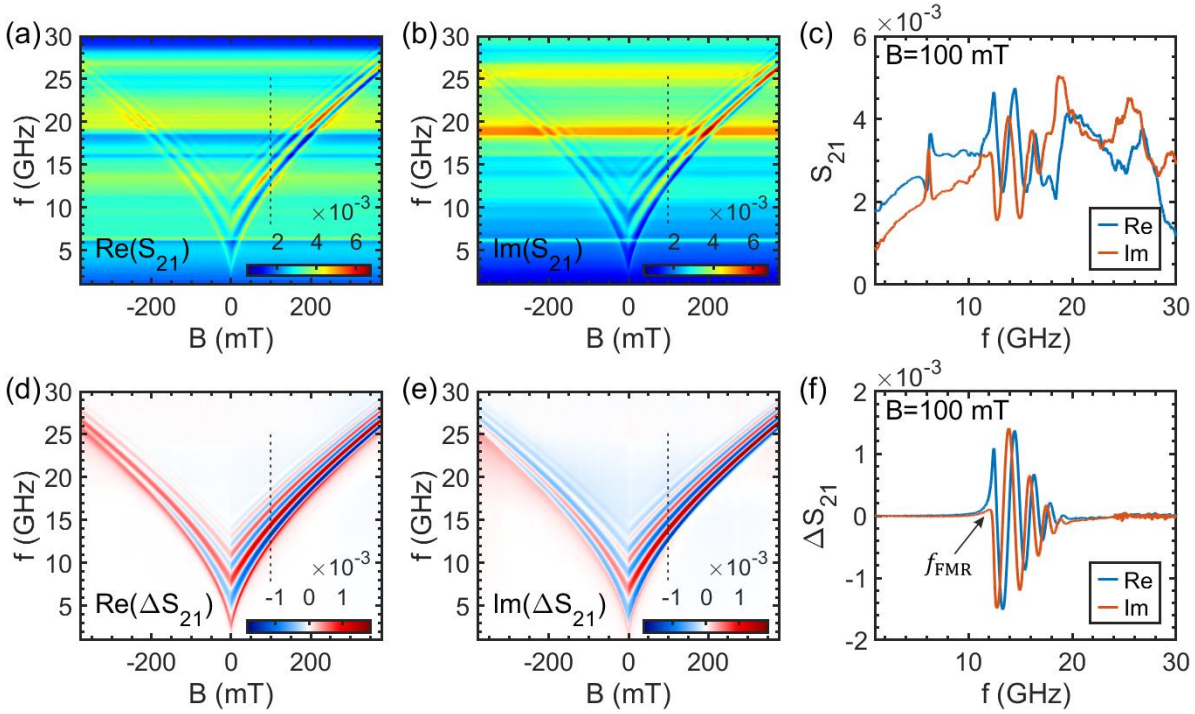

Fig. 4.23: PSWS data processing. The measurement was performed at $\boldsymbol{k} \perp \boldsymbol{M}$ geometry showing the spin-wave non-reciprocity – the signal is stronger for the positive magnetic field than the negative magnetic fields. (a,b) real and imaginary parts of raw S_{21}, (c) an example S_{21} sweep at magnetic field $B = 100$ mT. The magnetic signal is modulated onto a background signal, which is constant over all magnetic fields. (d,e) real and imaginary parts of processed (subtracted) ΔS_{21}, (f) ΔS_{21} sweep at magnetic field $B = 100$ mT. Background of the processed signal is zero, and the spin-wave signal is expressed in the form of oscillations in the real and imaginary parts of ΔS_{21}, showing the changing phase.

4.5.2 Effect of microwave power in the PSWS experiment

PSWS measurement relies on a reasonable selection of VNA's settings. A very elementary precaution is to keep the microwave power low enough to stay in the spin-wave linear regime. An increase of power above a certain value will cause non-linear spin-wave

excitation. The non-linear effects are then observed in the experiment as frequency shifting for each spin-wave band and by lowering the overall signal. This is undesirable, and therefore a power sweep should be performed before each experiment (every combination of material, external magnetic field, and antenna) when unsure what power is safe to use.

Fig. 4.24 shows this behavior for layers of (a) NiFe and (b) YIG. We can also note that those two materials show the extremes regarding the appropriate power as NiFe enters the non-linear regime at approx. 0 dBm and YIG at approx. -16 dBm [remember that the power uses a logarithmic scale, and changes by a factor of 10 for every 10 dBm, see Eq. (4.6)].

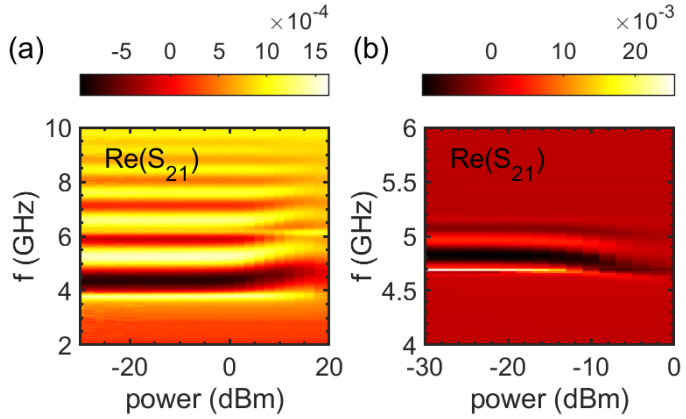

Fig. 4.24: Examples of PSWS power sweeps in $\boldsymbol{k} \perp \boldsymbol{M}$ geometry. The plotted signal is the real part of S_{21} without proccesing. (a) NiFe 40 nm at 20 mT. (b) YIG 100 nm at 100 mT. Both measurements were done using 500 nm wide stripline antennas.

4.5.3 Measurement aspects of PSWS

This subsection will present several characteristics of the PSWS experiment providing an experimentalist's insight into the measurement. We will demonstrate each presented aspect in a separate subsection to describe the main characteristics of the measurement.

Choice of the microwave antenna

Before starting a PSWS experiment, we must design and fabricate microwave antennas to excite and detect spin-waves. The design has to reflect the experimental expectation of the excited k-vectors. We have used the three basic types, previously described in Section 4.2 on page 56: striplines, CPWs, and GS antennas. For the use of PSWS experiments, they are fabricated in pairs, as shown in Fig. 4.25.

The most common antenna type in this work is the stripline. It has several advantages: It has a continuous spectrum starting from $k = 0$ up to a cut off based on the stripline width and the detection sensitivity. The experiments show that 8 rad/µm is reachable for 500 nm wide striplines. A quick conservative estimate of the stripline's cut off k-vector can be calculated as $k_{\max} = \pi / l_s$. The striplines also have high-k side peaks in the excitation spectrum, similar to CPW or GS antennas, but their amplitude (excitation strength) is too small and not usable in PSWS experiments, at least in the case of metallic layers with considerable damping. On the other hand, the overall excitation efficiency is the lowest among all the other types.

Besides choosing the antenna's excitation part, we also have to design the connecting lines to the probes. They usually consist of a coplanar waveguide (three thicker parallel planar lines with the same pitch as the used probes have, in our case 50 µm), and its characteristic impedance needs to be matched to the VNA's 50 Ω generator. It is less critical than in the FMR experiment, but it can still play a role. In an ideal world, the excitation part short-circuiting the signal line to the grounds would be a perfect 50 Ω impedance, but this is not achievable with simple wires because a fully matching circuit cannot be created.

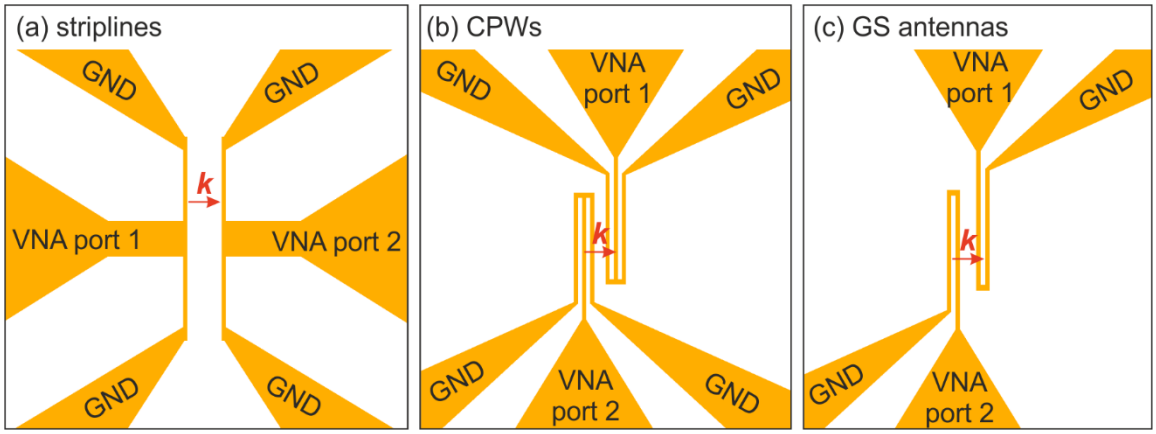

Fig. 4.25: Microwave antennas in the PSWS experiment.

We should also be mindful of the designed stripline length with respect to the maximum gap size in the experiment. It was previously reported [120,121] that the excited spin-waves can create a spatial pattern dominated by spin-wave beams traveling at different specific angles. This scenario is possible in materials where the dispersion is strongly anisotropic, which in-plane magnetized layers are (the in-plane MSSW and BVMSW modes). We spatially probed the spin-wave intensity around the striplines using BLS, showing this "caustics" in a 100 nm thick CoFeB layer shown in Fig. 4.26. We have to be careful in the design process of the gaps between the antennas for the PSWS experiment because the described effect can influence the measurement, and we recommend to use gap sizes smaller than the stripline length.

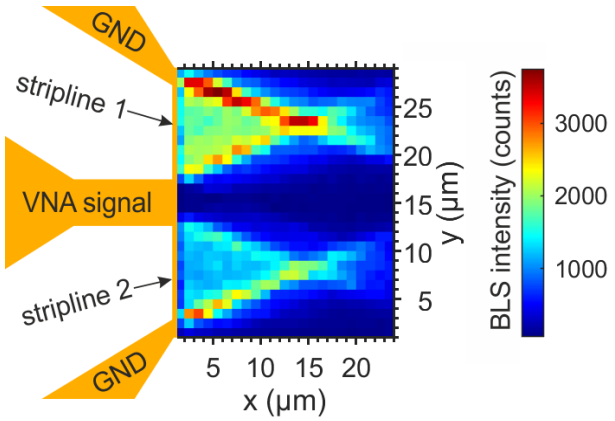

Fig. 4.26: 2D map of BLS intensity around the striplines measured on a 100 nm thick CoFeB layer. Excitation was facilitated by a 0.5 μm x 10 μm striplines. The experiment shows that the excited spin-waves form caustics. The used excitation frequency was set to 11 GHz.

The stripline antenna usually uses a pair of individual striplines on each unit, as shown in Fig. 4.25(a) and Fig. 4.26. The microwave probes used for contacting have three legs: ground, signal, and ground again (GSG). Therefore the striplines are the short-circuiting wires from the middle signal contact into each ground, turning by plus and minus 90-degree angles. When the antenna is powered, the magnetic fields created by the striplines have opposite directions with respect to each other, causing the excitation of each stripline having a shifted spin-wave phase. This effect was measured using phase-resolved BLS [35], confirming the spin-wave excitation phase shift π between the antennas, which is shown in Fig. 4.27. When the signals are detected by the induction pick up on the second antenna, the process is reciprocal, and therefore the signals from both arms are added together, not subtracted. Thus, it is highly recommended to keep both the excitation and detection antennas with the same geometry.

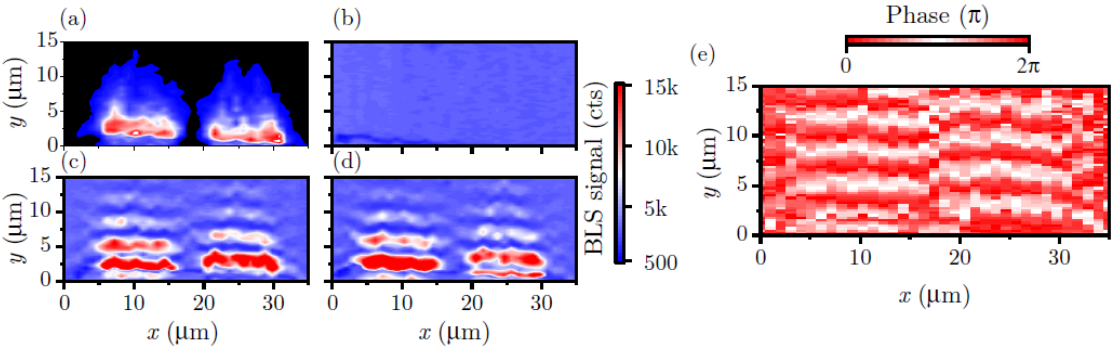

Fig. 4.27: (a-d) Four BLS measurements needed for full phase reconstruction: (a) intensity measurement with no modulation, (b) electrically modulated light with no spin-wave excitation (c-d) interference between spin-waves and the electro-optical modulator (EOM) signal for two phases shifted by $\pi/2$. (e) reconstructed phase from (a-d). Reprinted from [35].

Influence of the propagation distance (gap)

We usually use two antennas of the same type in the PSWS experiment, but we can vary the gap size between them. Therefore, the distance over which the spin-waves must propagate before reaching the receiving antenna is a part of the experimental design. The real and imaginary components of the transmission parameters oscillate in the frequency spectrum because of the frequency-dependent k-vector (given by the dispersion relation). This means that there is a different wavelength λ at each frequency, and therefore the phase change is also different for each frequency. The rate of the oscillations increases with the gap size, as shown in Fig. 4.28(a,b). Now we use this data to calculate the phase, and we can also unwrap it. The process of unwrapping is connecting the phase into a continuously changing line because the phase of the complex number is first expressed in the $-\pi$ to $+\pi$ interval, creating a saw-like profile. Fig. 4.28(c) shows a plot of unwrapped phases calculated from the real and imaginary ΔS_{21} data in (a,b). We can see that it is rising more rapidly for larger gaps. This will be an essential characteristic for the process of the dispersion extraction described in Chapter 5.

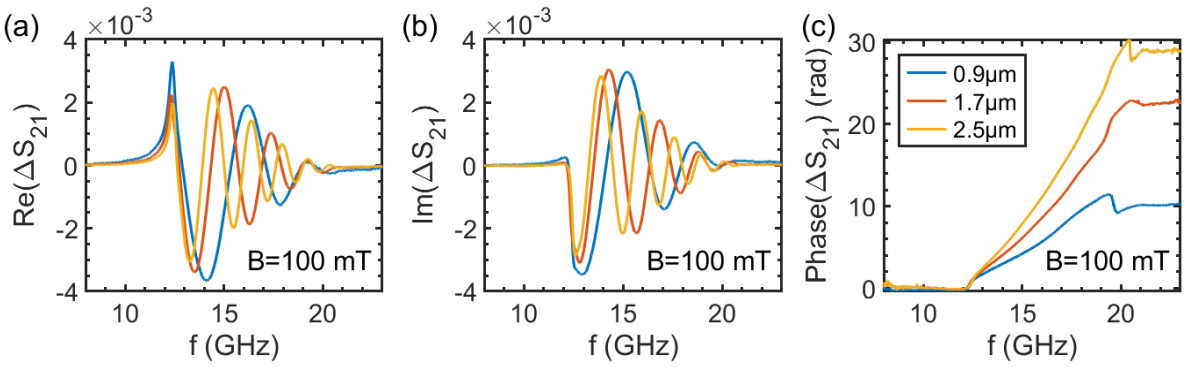

Fig. 4.28: (a) Real part, (b) imaginary part, and (c) unwrapped phase of the ΔS_{21} transmission parameter of a spin-wave propagation over variable distance detected in the PSWS experiment. The legend states the gap size between the antennas and is shared for (a-c).

Non-reciprocity of magnetostatic surface waves

The most studied spin-wave propagation mode is the $\boldsymbol{k} \perp \boldsymbol{M}$ geometry (MSSW), also called the DE mode. The DE mode is localized onto one of the layer surfaces with an exponential distribution of the dynamic magnetization along the layer's thickness, contrary to the volume character of the $\boldsymbol{k} \parallel \boldsymbol{M}$ geometry (MSBVW). When the direction of propagation is reversed, the maximum of the dynamic magnetization shifts from one surface to the other one. Therefore the surface waves are non-reciprocal [59,60].

The non-reciprocity provides that one of the transmission parameters S_{21} and S_{12} is stronger due to both the stronger excitation, and to the larger induction pick up from the nearer surface. In Fig. 4.29, we demonstrate this effect, wherein (a,b) the field is positive, and the signal S_{21} is stronger than S_{12}. After the field reversal to the opposite direction in (c,d), the signal strengths are swapped. They are identical in shape, but only the signal amplitude differs.

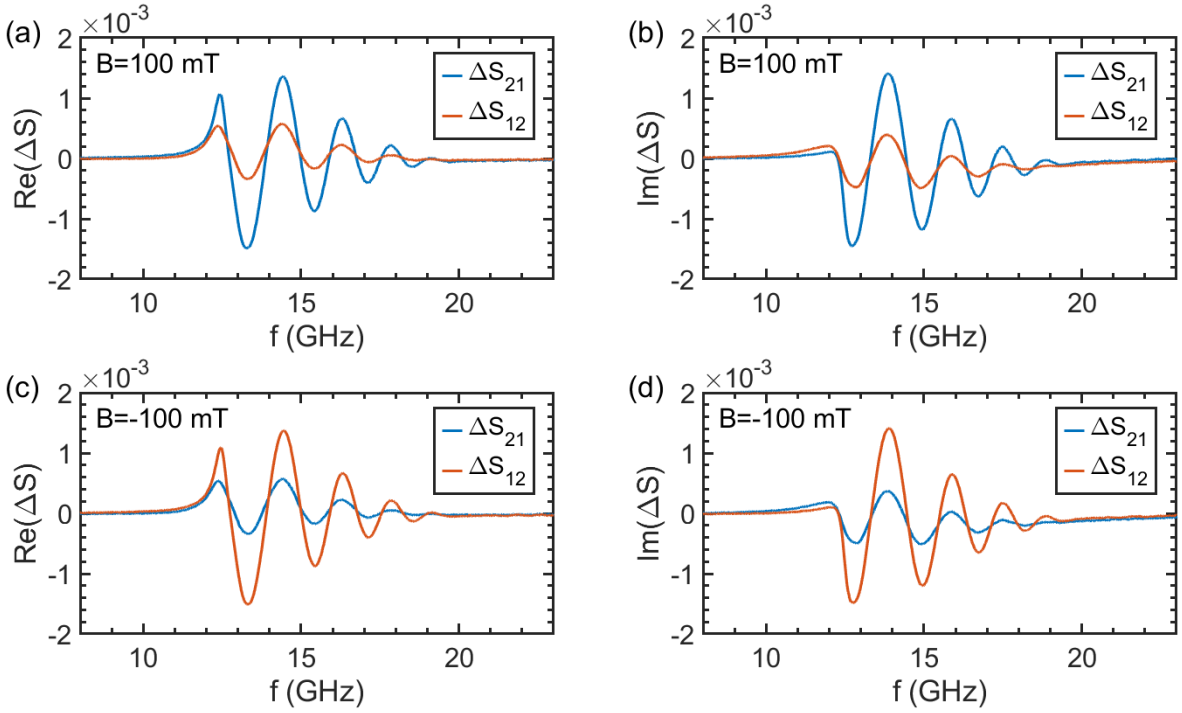

Fig. 4.29: Non-reciprocity of magnetostatic surface waves demonstrated on CoFeB 30 nm layer measured by 500 nm striplines. (a,b) S_{21} and S_{12} signals measured over 1.8 µm gap between the antennas at $B = 100$ mT, where the forward transmission S_{21} is stronger than the reverse transmission S_{12}. (c,d) The same measurement at $B = -100$ mT, showing the opposite scenario – the reverse transmission S_{12} is stronger than the forward transmission S_{21}.

Probe contacting problems

The quality of the probe contact onto the sample can have a crucial influence on the acquisition. The GGB picoprobes model 40A used in our setup are recommended to use from 25 to 75 µm of vertical overtravel after first touching the sample surface. The vertical travel is translated to the horizontal overtravel of 10 to 15 µm across the sample surface (probe moves forward), which is observable in the navigation microscope. After removing the probe, there should be three scrub marks on the pads. Seeing only one or two marks suggests a wrong

probe tilt that has to be corrected before the measurement on every sample individually (due to slightly different mounting errors for each sample). The tilt is corrected using the micromanipulator, and it will have a crucial influence on the performance. A correct tilt will also prevent us from using too much pressure providing an optimal lifetime of the probe.

A common problem is an inconsistent contact during the measurement resulting in a fluctuating measurement. The VNA performs scanning over frequencies, and we usually also scan over the magnetic fields. The inconsistent contacting will result in vertical stripes in the measurement, which will not be possible to remove in the data subtraction process (see Fig. 4.30). When observing this kind of difficulty, the experiment should be stopped and restarted after recontacting. Although the stripes are often visible in the transmission spectra (S_{21} and S_{12}), the reflection parameters S_{11} and S_{22} are even more sensitive and will respond to any contact inconsistency.

Even though our probes are fully non-magnetic (a necessary condition for every magnetic experiment), we can also observe some slight skating over the surface upon field changes, which adds to the contacting inconsistency. This suggests magnetic parts somewhere in the system (the motion is relative; it may be located elsewhere than the probes themselves), and it is difficult to eliminate it entirely.

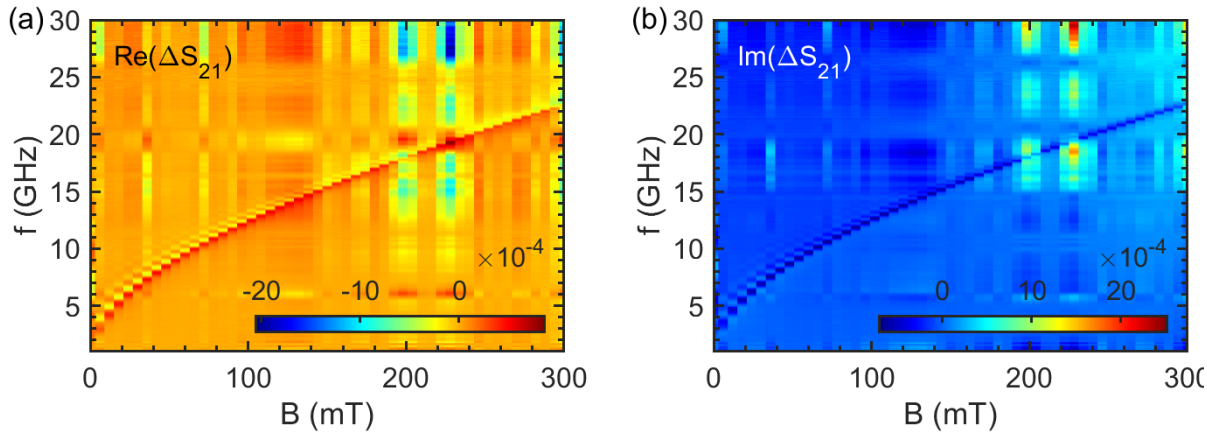

Fig. 4.30: Effect of incorrect sample contacting: vertical stripes in the VNA spectrum during a PSWS measurement of CoFeB 30 nm layer in $\boldsymbol{k} \perp \boldsymbol{M}$ geometry.

Temperature drift

The instability of the room temperature also affects the measurement showing vertical stripes in the spectrum. This time, the stripes have the same time period as the temperature changes, typically due to the air conditioning cycles. Most of the laboratories are air-conditioned, and its controls may be limited (impossible to fully control the AC regulation). Thus this effect may be hard to eliminate. A partial way is to decrease the acquisition time by lowering the number of measured points and by using faster VNA settings when possible.

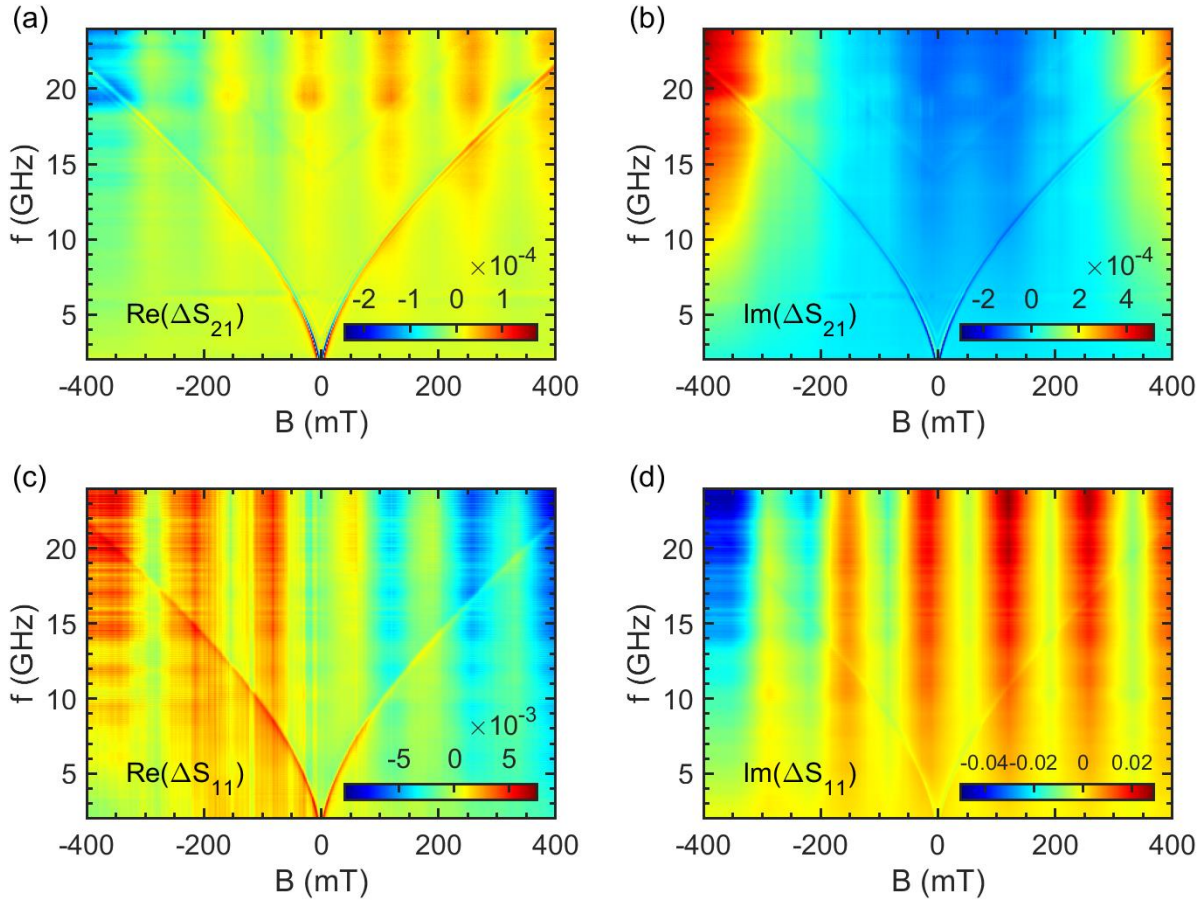

Fig. 4.31: Effect of the temperature drift: time-periodic vertical stripes in the VNA spectrum during a PSWS measurement of CoFeB 30 nm layer in $\boldsymbol{k} \parallel \boldsymbol{M}$ geometry. The $\boldsymbol{k} \parallel \boldsymbol{M}$ geometry has a significantly lower signal than $\boldsymbol{k} \parallel \boldsymbol{M}$ geometry emphasizing the stripes. The reflection spectrum has a lower signal to background ratio, and therefore the vertical stripes are more apparent in S_{11}.

4.5.4 Practical notes for the PSWS measurement

The PSWS experiment can be sensitive to many factors. The following list summarizes the primary points of focus in the efforts of the best possible data acquisition.

1. Set the magnet correctly
   Use the right calibration, or use a hall probe to verify it. Alternatively, measure the magnetic field during the experiment, if possible.
2. Fix the sample well by gluing or taping
3. Make sure the sample is not touching the magnet poles
   Using small magnet gaps may cause proximity of the sample to the poles. Touching will project onto the probe placement, potentially damaging both the sample and the probes.
4. Make sure the VNA is calibrated and optimize its settings
   E.g., when the temperature changes are a concern, optimize the experimental settings (VNA bandwidth, number of measured points) to minimize the acquisition time.
5. Set the correct power!
   Microwave power is easily overlooked, but it plays a significant role in the measurement. If unsure, then perform a power sweep measurement. The correct power can be different for every material-antenna combination. It should be in the -10 to 5 dBm range for metallic materials (NiFe, CoFeB) and -30 to -20 dBm for YIG.
6. Set the measurement range on the VNA.
   Note that when the starting or ending frequency is changed, the instrument holds the number of measured points. When a specific frequency step is required, now it has to be changed again. Beware of undersampling when the measured features are small. Calculate estimates to predict this. Reasonable parameters for PSWS on metallic materials are frequency step 10 to 20 MHz and bandwidth 1 kHz.
7. Measure as many magnetic fields as timely possible
   When the data subtraction process is necessary [using Eq. (4.23)], measure for as many magnetic fields as possible because it will allow for better background evaluation.
8. Check all of the measured signals
   After starting a measurement, check all of the measured signals, and restart when observing difficulties with the probe contacting, similar to Fig. 4.30.

5 Spin-wave dispersion relations measured by VNA

The previous chapter presented the PSWS experiment (Section 4.5), which will be the basis for evaluating the spin-wave dispersion relations presented in the following sections. All of the fitted dispersions use the dipole-exchange model presented in Section 1.9 with totally unpinned surface spins (except for the hybridized modes).

5.1 Spin-wave dispersion extraction using the PSWS experiment

In previous reports, the spin-wave dispersion was extracted from YIG by using the CPW excitation. As the CPWs excitation spectrum exhibits distinct peaks, it allows extracting one point in spin-wave dispersion for each of the CPWs excitation spectrum peaks. The central k-vector of each excitation spectrum peak is then assigned to a frequency from either the envelope of the S_{21} sweep [116,122] or by fitting the S_{21} spectrum [115]. This approach is limited to only several extracted points, and is not easily transferable to metallic materials because of the low signal amplitude when compared to YIG due to large damping in metallic layers, making it impossible to use more than two peaks from the excitation spectrum. There was also an attempt to evaluate the dispersion from a single VNA sweep [123,124] by applying the equation:

$$k(f) = \frac{\Delta\varphi_{\mathrm{SW}}(f)}{L}, \tag{5.1}$$

where φ_{SW} is the spin-wave phase and L is the distance over which the phase is measured. This approach requires to know the precise distance over which the spin-wave changes its phase, which is challenging to evaluate because the measured phase difference can be offsetted by a measurement-related and frequency-dependent phase offset. We can write the phase difference as

$$\mathrm{Phase}(\Delta S_{21}) = \varphi_{\mathrm{SW}} + \varphi_0, \tag{5.2}$$

where ΔS_{21} is the VNA transmission signal with subtracted background using Eq. (4.23). The offset φ_0 is not needed in the routine described below, where only a relative phase change is necessary to know. Another limitation hides in the maximum measurable k-vector, which will be $k_{\mathrm{max}} = \pi/L$ because the phase is measured in the $-\pi$ to $+\pi$ interval and the real phase change over the distance L will not be possible to determine correctly from the measurement for larger $k > k_{\mathrm{max}}$ (at least for excitation antennas with non-continuous excitation spectrum, e.g., CPWs or even ladder antennas, where the phase cannot be unwrapped in the frequency spectrum, see the discussion below).

Our approach uses multiple measurements of the spin-wave phase over several gap sizes g between the antennas. Subsequently, we assume a single plane wave propagating in the layer, and that the measured phase difference at each frequency evolves linearly with the relative change of the gap size, which is reflected in Eq. 5.1. Because the relative change of the gap size g is a controlled parameter (in the design used for lithography) and the phase difference $\mathrm{Phase}(\Delta S_{21})$ is extracted from the VNA measurement, we can fit the following equation, where the slope of the fit is identified as the spin-wave k-vector:

$$\mathrm{Phase}(\Delta S_{21}[g, f]) = k(f)g + \varphi_0(f), \tag{5.3}$$

The phase offset φ_0 is the fit intercept. Therefore, for executing this method, we need to fabricate multiple antenna pairs with varying gap g. The magnetic entity for which we want to evaluate the spin-wave dispersion needs to be as identical as possible for each pair of antennas. This is easily achievable for the continuous magnetic layers at which we focus, yet it can be problematic when applying this approach to magnetic nanostructures. The phase is calculated from the subtracted transmission data; an example of phases measured over multiple gap distances on CoFeB 30 nm thin film is shown in Fig. 5.1(a). Correct data subtraction is critical because it affects the quality of the calculated phase of the spin-wave, and both the random and systematic errors can create artifacts in the dispersions. Therefore, the data must be acquired carefully, minimizing undesirable effects of, e.g., probe contacting or temperature (mentioned in Section 4.5).

The example phase measurements $\mathrm{Phase}(\Delta S_{21})$, plotted in Fig. 5.1(a), start changing after the frequency reaches the FMR frequency at approx. 12 GHz, and the slope of the curve is higher for larger gaps. I.e., the lowest measured phase corresponds to the smallest gap and the uppermost to the largest measured gap size. Then we plot all the measured phases for each frequency against the gap sizes g between the antennas [representative frequencies are plotted in Fig. 5.1(b)]. It shows linear phase dependencies that can be easily fitted, as was explained, with the slopes of the lines equal to the k-vector. Now we can finally plot the extracted k-vectors against their respective frequencies, showing the resulting dispersion relation in Fig. 5.1(c).

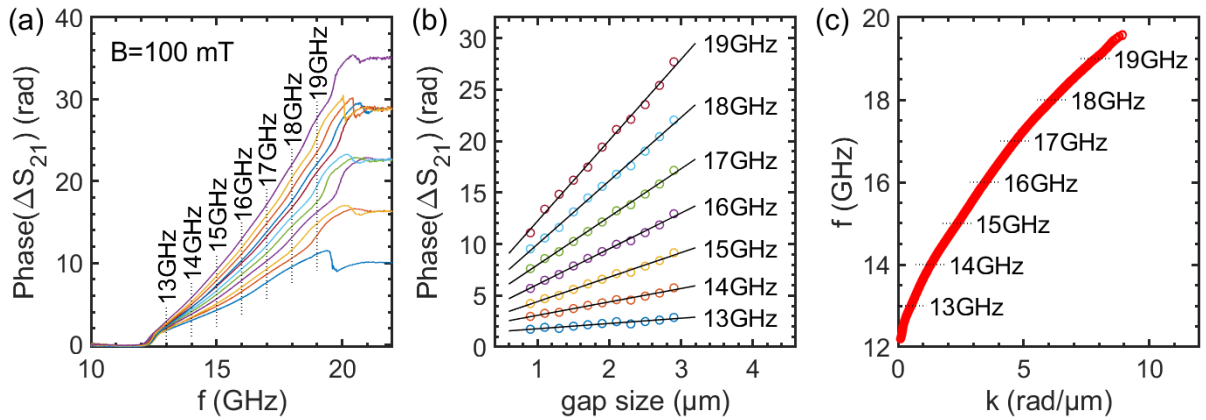

Fig. 5.1: Extraction of the dispersion from the PSWS experiment on CoFeB 30 nm layer. (a) unwrapped ΔS_{21} phases measured over several gap distances from 0.9 μm (the lowest line) to 2.9 μm (the steepest line) with the step of 200 nm. (b) representative fits of the phase where the fit's slope yields the desired k-vector at that frequency. (c) dispersion relation extracted for all frequencies within the range with sufficient PSWS signal.

The gap sizes have to be designed to respect the following limitations. The largest gap needs to be small enough that the wave does not significantly attenuate before reaching the detection antenna. From our experimental observation, no larger than double the propagation length Λ for the given material, magnetic field, and k-vector. We need to fabricate multiple pairs of antennas with a step in between the gap distances that needs to reflect the maximum expected phase change between neighboring gap sizes (maximum excited k-vector can be calculated based on the antenna's geometry, as shown in Section 4.2). This phase change has to be smaller than π, except for certain cases discussed later. Small k-vectors may have a phase change that is too small, which increases the relative error. If we

require accurate fitting for small k-vectors, the maximum gap should be large enough to provide a phase change of at least 1 radian while respecting the propagation length condition.

Before fitting the data as plotted in Fig. 5.1(b), we have to unwrap the phase correctly. That means adding or subtracting multiples of 2π to each point to eliminate the saw-like profile [Fig. 5.2(a)], caused by the limited measured phase range between $-\pi$ and $+\pi$, to achieve a continuous line [Fig. 5.2(b)]. By unwrapping, we eliminate possible steps in the phase evolution when plotted against the gap size, and now the dependence should be linear[20]. A comparison of the original and unwrapped phase is shown in Fig. 5.2(c).

There is a degree of freedom for achieving correct unwrapping, and we can use any approach as long as the unwrapped phase is extracted correctly. In the case of the data plotted in Fig. 5.1(a), the phases are unwrapped in the frequency spectra, and no extra unwrapping is necessary in Fig. 5.1(b). This is possible because the used stripline has a continuous excitation efficiency spectrum starting from the FMR frequency up to a certain width-dependent cutoff. As the frequency step size set on the VNA is usually small, the phase shift of the neighboring points is always smaller than π, and we can achieve correct unwrap even when the phases for neighboring gap distances at the same frequency are higher than π. The safest approach is to unwrap the phases when plotted against the gap size [Fig. 5.1(b) or Fig. 5.2(c)], but in this case, the phase change of neighboring points must be smaller than π. This would be necessary for antennas with extremely discrete excitation spectrum (e.g., ladders or meanders) because in such cases, we can never unwrap the data in the frequency spectrum, and the gap distance step has to be small enough to reflect it.

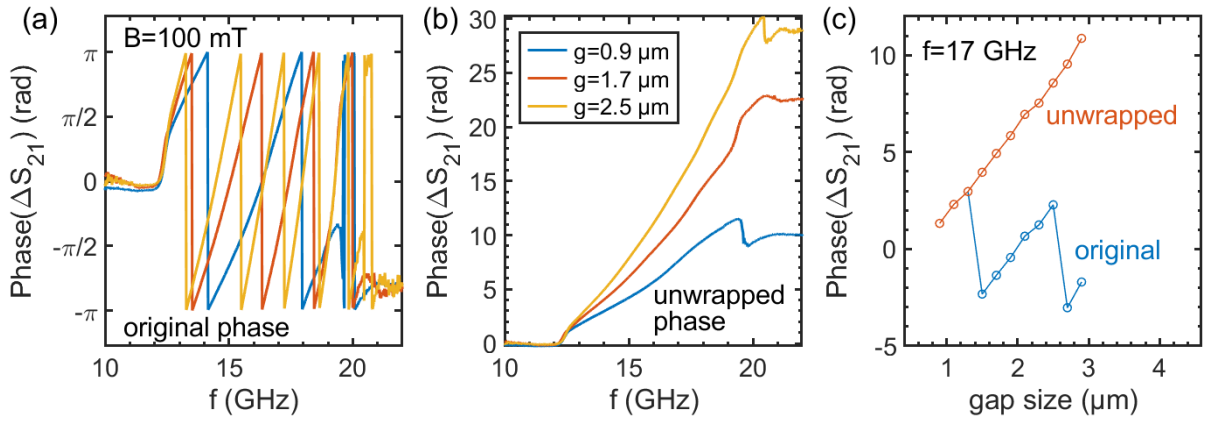

Fig. 5.2: Phase treatment from the PSWS experiment demonstrated on CoFeB 30 nm layer. (a) Phase of the ΔS_{21} transmission signal (b) Unwrapped phase using the data from (a). (c) Representative comparison of the original and unwrapped phase plotted against the gap size at $f = 17$ GHz.

The extraction process of the dispersion relation was also cross-checked using phase-resolved BLS. Fig. 5.3(a) shows dispersions measured by VNA (red circles) and by BLS (blue squares). Fig. 5.3(b) compares VNA and BLS phase measurements versus the distance for a selected frequency of 11.5 GHz. Both graphs show good agreement between the VNA and BLS experiments.

[20] Here we consider only the existence of a single k-vector at each frequency. The dependance can also be non-linear in e.g. magnonic crystals, where we can expect multiple k-vectors as solutions for each frequency.

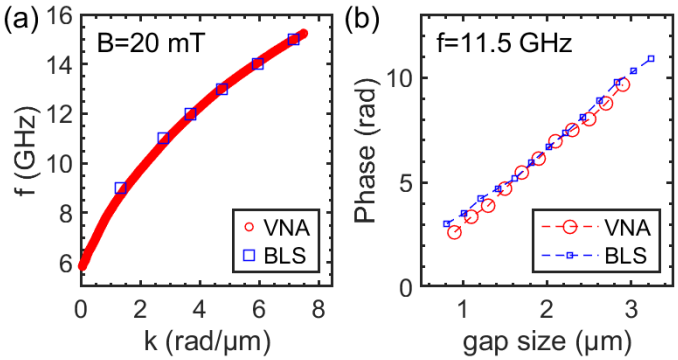

Fig. 5.3: (a) Comparison of measured spin-wave dispersion for CoFeB 30 nm layer using VNA (red circles) and phase-resolved BLS (blue squares). (b) comparison of the phase measurement at $f = 11.5$ GHz obtained by VNA and phase-resolved BLS. The magnetic fields could slightly vary for each experiment because it was acquired in separate setups.

5.2 Spin-wave dispersion of NiFe layer

The first material on which we tested the spin-wave dispersion measurement was a NiFe layer. The material is known for its relatively short spin-wave propagation lengths (due to relatively small magnetization and high damping), but measuring it in the PSWS experiment was non-problematic. Fig. 5.4(a,b) shows representative data in the $\boldsymbol{k} \perp \boldsymbol{M}$ geometry. The background has a slight magnetic field dependence, which is visible in the lightly red-colored ($\sim 10^{-5}$ signal level) top right corner in Fig. 5.4(a,b). It was identified as an experimental setup-related issue. Fig. 5.4(c) shows the experimentally evaluated dispersion relations for the magnetic field from 20 mT to 200 mT. The evaluated dispersions were fitted using the dipole-exchange model with reasonable agreement. The maximum detected k-vector was slightly below 10 rad/μm but the 200 nm wide stripline should theoretically excite k-vectors up to approx. 20 rad/μm. We attribute this to the high attenuation in NiFe and the decreasing propagation length for higher k-vectors in the $\boldsymbol{k} \perp \boldsymbol{M}$ geometry.

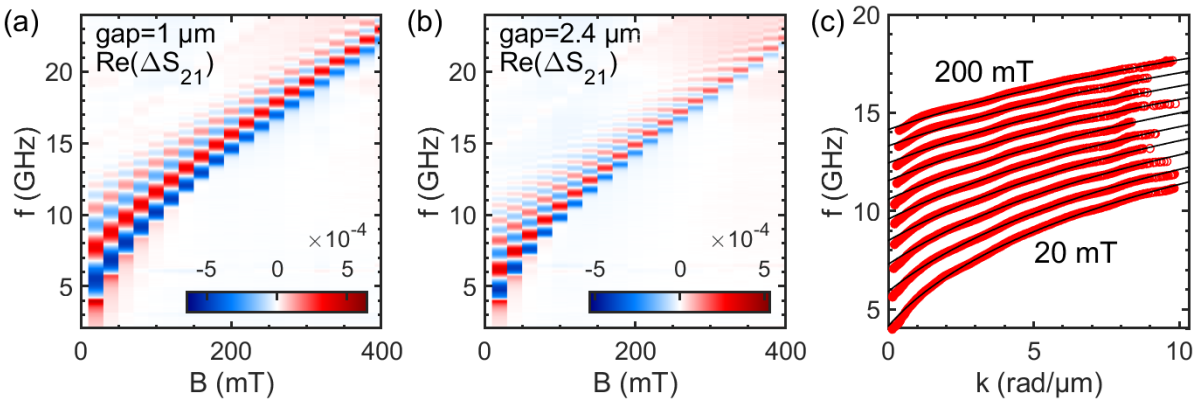

*Fig. 5.4: PSWS experimental data in $\boldsymbol{k} \perp \boldsymbol{M}$ geometry. **Material: NiFe 40 nm layer**, used antenna type: $l_s = 200$ nm striplines, used power: 5 dBm. (a,b) representative data. (c) extracted dispersion relations for fields from 20 to 200 mT with 20 mT step with fit using the dipole-exchange model. Measured gaps: 1.00, 1.11 1.24, 1.38, 1.55, 1.73, 1.93, 2.15, 2.40, and 2.68 μm. Fit parameters: $\gamma/2\pi = 28.8$ GHz/T, $t = 34.1$ nm; fixed parameters: $M_s = 800$ kA/m ($\mu_0 M_s = 1.0$T), $A_{ex} = 16$ pJ/m.*

The influence of the gap size on the measurement is clearly visible in Fig. 5.4(a,b), where the oscillations of $\mathrm{Re}(\Delta S_{21})$ get denser for larger gaps because the phase change is larger (one oscillation period corresponds to 2π phase change). It is even more apparent when the ΔS_{21} frequency sweeps are plotted against the gap size, as shown in Fig. 5.5(a,b). The transmission data should also decay exponentially as the spin-wave attenuates, following the equation:

$$\mathrm{Mag}(\Delta S_{21}) = I e^{-g/\delta}, \tag{5.4}$$

where I is the spin-wave related signal amplitude, g is the gap size, and δ is the propagation length (δ will be used as the experimental propagation length, and $\Lambda = v_g\tau$ [Eq. (1.36)] as the theoretical one). We fitted the experimental data, with representative fits shown in Fig. 5.5(c). The acquired propagation lengths are around 2 µm. The fitting was done by applying the natural logarithm on the data and fitting it with a line $px + q$, ensuring that all of the fitting points have equal weights. Then the propagation length is obtained as $\delta = -1/p$, and $I = e^q$.

In Fig. 5.5(a,b), we can also notice a slight vertical shift of each VNA sweep, which will be even more apparent below in CoFeB data plotted in Fig. 5.8(a,b), meaning that the FMR frequency is shifted in each measurement, and we attribute it to the magnetic field being inhomogeneous due to the small magnet gap. This is undesirable because it will project to the dispersions, where we use the magnetic field as a control parameter. It is necessary to consider this during the sample design process, where we should keep the individual pairs of antennas as close as possible to minimize the field differences.

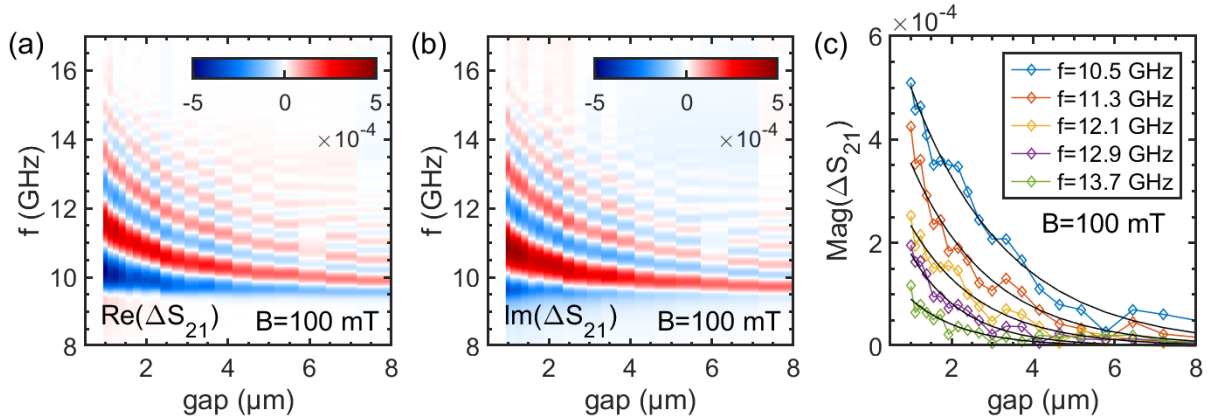

Fig. 5.5: (a,b) PSWS experimental data in $\boldsymbol{k} \perp \boldsymbol{M}$ geometry plotted against the gap size. ***Material: NiFe 40 nm layer****, used antenna type: $l_s = 200$ nm striplines. (c) Magnitude plots at selected frequencies show exponential decay with fits: $\delta_{10.5GHz} = 2.35$ µm (1.28 rad/µm), $\delta_{11.3GHz} = 1.95$ µm (2.77 rad/µm), $\delta_{12.1GHz} = 1.71$ µm (4.17 rad/µm), $\delta_{12.9GHz} = 1.30$ µm (5.93 rad/µm), and $\delta_{13.7GHz} = 1.31$ µm (8.19 rad/µm). The k-vectors were assigned using the dispersion measurement from Fig. 5.4.*

More detailed data on the propagation lengths are shown in Fig. 5.6 for magnetic fields 20, 100, and 200 mT. The data is plotted with the k-vectors on the horizontal axis, where the previously extracted dispersion relations [Fig. 5.4(c)] provided the conversion from frequencies in the VNA measurement. The error bars correspond to fit's 95% confidence interval. Orange curves provide theoretical comparison calculated from the theoretical propagation length using Eq. (1.36) and material parameters obtained from the dispersion fit, except for the damping $\alpha = 0.0074$, obtained from FMR measurement (Fig. 4.19). The measured propagation lengths are smaller by approx. a factor of 2 when compared to the calculation, suggesting even higher damping, and this demonstrates rather bad propagation properties of NiFe, which could be caused by the polycrystalline nature of the layers. That is also why NiFe is not a prospective candidate for usage in future spin-wave devices, where the spin-wave attenuation is a crucial parameter.

We should note that the probes must be re-landed on each separate pair of antennas, causing different contact resistance, which creates an error in the signal magnitude. A certain precaution is therefore required when drawing conclusions from the propagation lengths δ extracted from the PSWS experiment, as shown here.

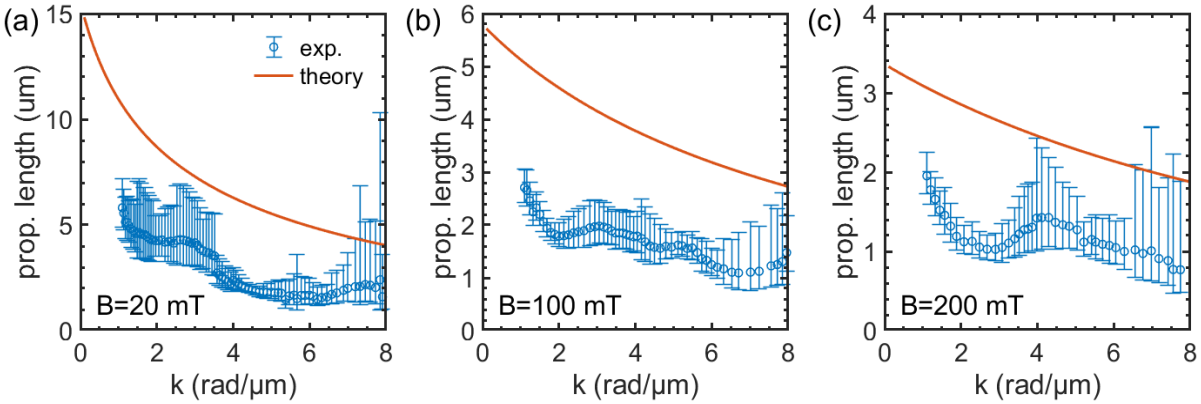

*Fig. 5.6: Experimental fits from the previously shown data and theoretical calculations of the propagation length for **NiFe 40 nm layer** for (a) $B = 20$ mT, (b) $B = 100$ mT, (c) $B = 200$ mT. The calculation uses the constants from the dispersion fit (Fig. 5.4), and $\alpha = 0.0074$ obtained from FMR (Fig. 4.19). The experiment shows lower propagation lengths than the calculation.*

5.3 Spin-wave dispersion of CoFeB layers

The thin 30 nm layers of CoFeB exhibit similar qualitative behavior to the previously measured NiFe. CoFeB has higher M_s and γ values, therefore the overall frequency range is above the one of NiFe, and importantly, the maximum measured signal is approx. 3x higher at comparable gap size (approx. $4 \cdot 10^{-3}$ for 30 nm CoFeB vs. approx. $5 \cdot 10^{-4}$ for 40 nm NiFe). Fig. 5.7(a,b) show representative experimental data in the $\boldsymbol{k} \perp \boldsymbol{M}$ geometry, and Fig. 5.7(c) shows the extracted dispersion relations fitted with the dipole-exchange model displaying good agreement. The maximum extracted k-vector is comparable to the NiFe measurement in Fig. 5.4(c) while the used stripline is wider ($l_s = 500$), which is because the signal is higher by one order of magnitude and therefore, lower excitation efficiency is required.

CoFeB 30 nm was also evaluated for the propagation lengths similar to NiFe. Representative data plotted against the gap distance with representative exponential fits are shown in Fig. 5.8. In Fig. 5.8(a,b) we can observe the mentioned effect of shifted VNA sweeps,

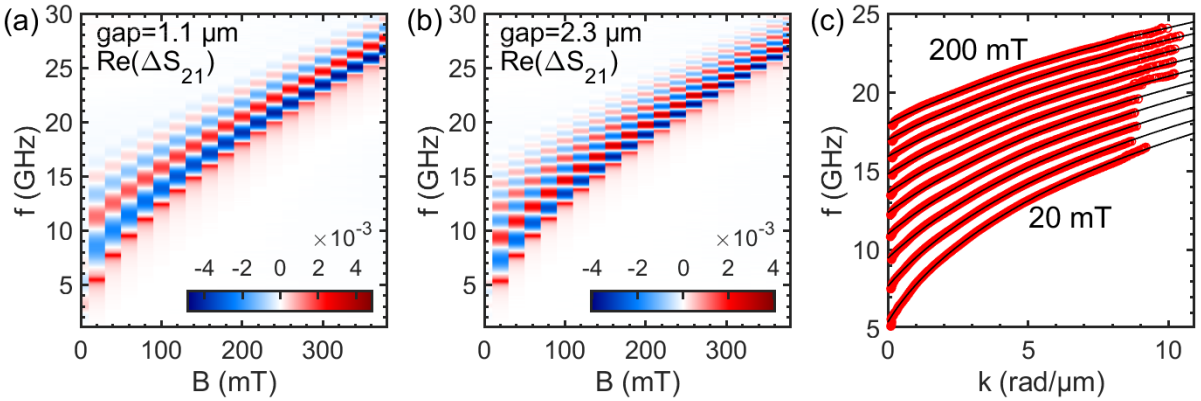

*Fig. 5.7: PSWS experimental data in $\boldsymbol{k} \perp \boldsymbol{M}$ geometry. **Material: CoFeB 30 nm layer**, used antenna type: $l_s = 500$ nm striplines, used power: 0 dBm. (a,b) representative data. (c) extracted dispersion relations for fields from 20 to 200 mT with 20 mT step with fit using the dipole-exchange model. Measured gaps: 0.9 to 2.9 μm with 0.2 μm step.*
Fit parameters: $M_s = 1.20$ MA/m ($\mu_0 M_s = 1.51$ T, $t = 29.6$ nm; fixed parameters: $\gamma/2\pi = 30.8$ GHz/T, $A_{ex} = 15$ pJ/m.

more pronounced here than in the NiFe measurement, as was shown in Fig. 5.5(a,b). We assume that the magnetic field differences from structure to structure were larger on the CoFeB sample because a different layout was used.

The propagation lengths are plotted in Fig. 5.9 for both the experiment and calculation. The material parameters used in the calculation were again obtained from the dispersion fit, and the damping $\alpha = 0.0089$ was obtained from FMR (Fig. 4.19). The experimental propagation lengths are noticeably higher than those measured on the previously presented NiFe, having values around 4 µm for CoFeB vs. 2 µm on NiFe at 100 mT. But the experimental values are slightly higher than the theoretical calculation, suggesting that the real damping is lower than what was measured in the FMR experiment. Moreover, lower values would be consistent with the literature, even as small as $\alpha = 0.004$ [103].

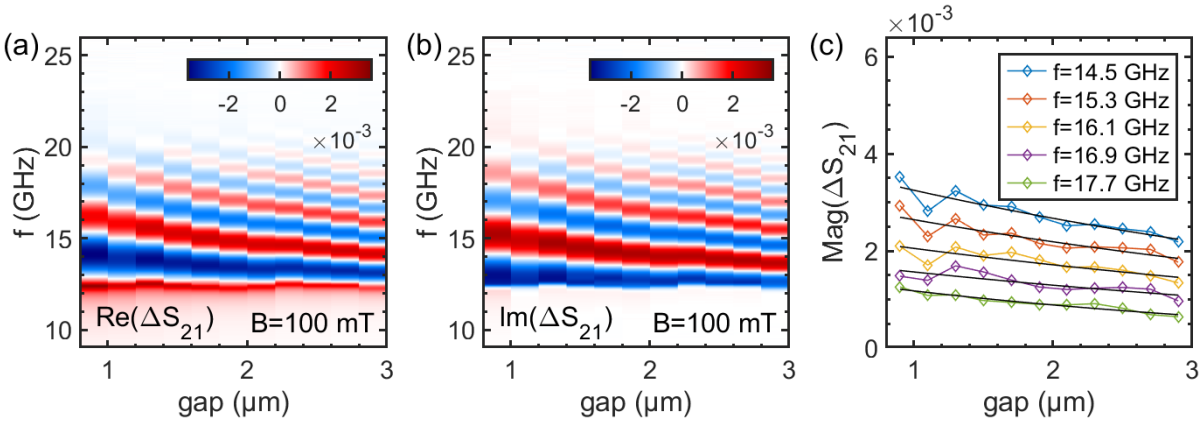

Fig. 5.8: (a,b) PSWS experimental data in $\boldsymbol{k} \perp \boldsymbol{M}$ *geometry plotted against the gap size.* ***Material: CoFeB 30 nm layer****, used antenna type:* $l_s = 500$ *nm striplines. (c) Magnitude plots at selected frequencies show exponential decay with fits:* $\delta_{14.5GHz} = 5.12$ *µm (1.81 rad/µm),* $\delta_{15.3GHz} = 5.3$ *µm (2.69 rad/µm),* $\delta_{16.1GHz} = 5.55$ *µm (3.58 rad/µm),* $\delta_{16.9GHz} = 5.23$ *µm (4.54 rad/µm), and* $\delta_{17.7GHz} = 3.54$ *µm (5.56 rad/µm). The* k*-vectors were assigned using the dispersion measurement from Fig. 5.7.*

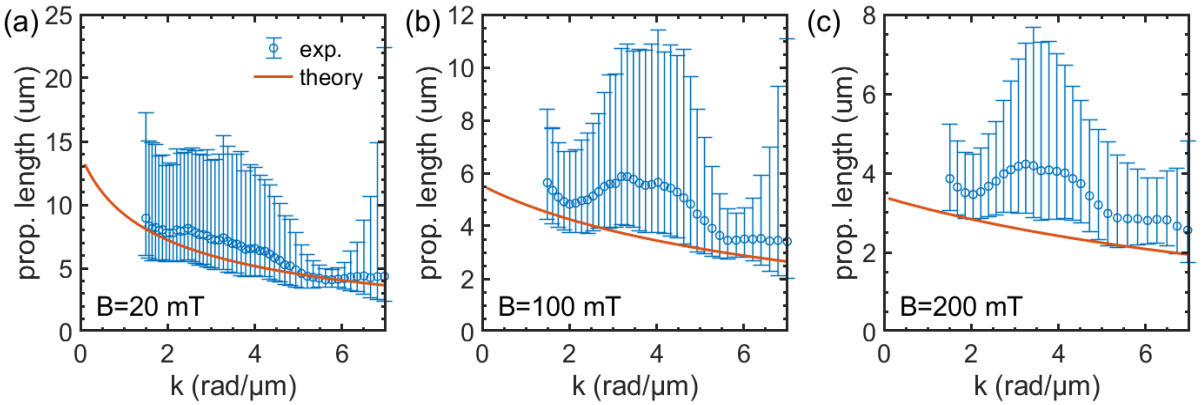

Fig. 5.9: Experimental fits from the previously shown data and theoretical calculations of the propagation length for ***CoFeB 30 nm layer*** *for (a)* $B = 20$ *mT, (b)* $B = 100$ *mT, (c)* $B = 200$ *mT. The calculation uses the constants from the dispersion fit (Fig. 5.7), and* $\alpha = 0.0089$ *obtained from FMR (Fig. 4.19). The experiment shows lower propagation lengths than the calculation.*

CoFeB 30 nm was the first sample where we tested the $\boldsymbol{k} \parallel \boldsymbol{M}$ geometry by rotating the in-plane electromagnet. Despite the effort, we had no success of acquiring any data whatsoever, even on the shortest measured gap size of 1 µm. It was later revealed using the propagation length estimations [based on Eq. (1.36)] that the BV waves could not reach the detection antenna due to the attenuation, and thus could not be detected. However, the propagation length increases noticeably with the film thickness, and for this reason, we measured a 100 nm thick CoFeB layer. Within the range of our electromagnet, the propagation distance for the $\boldsymbol{k} \parallel \boldsymbol{M}$ geometry is between 1 and 2 µm, which should be detectable. Measurement using $l_s = 500$ nm striplines proved it possible, while the signal was too low to process the dispersions reliably. A dramatic improvement was observed by using CPWs (with parameters $l_s = l_{\mathrm{gap}} = l_{\mathrm{GND}} = 500$ nm), which should have approx. 3x the excitation efficiency (see Fig. 4.12) with the disadvantage of a non-continuous spectrum of excited k-vectors. The measured data was sufficient to evaluate the spin-wave dispersions, with results plotted in Fig. 5.10 (please note that the $\boldsymbol{k} \parallel \boldsymbol{M}$ geometry is plotted as negative k-vectors to prevent overlapping and increase clarity of the plotted points).

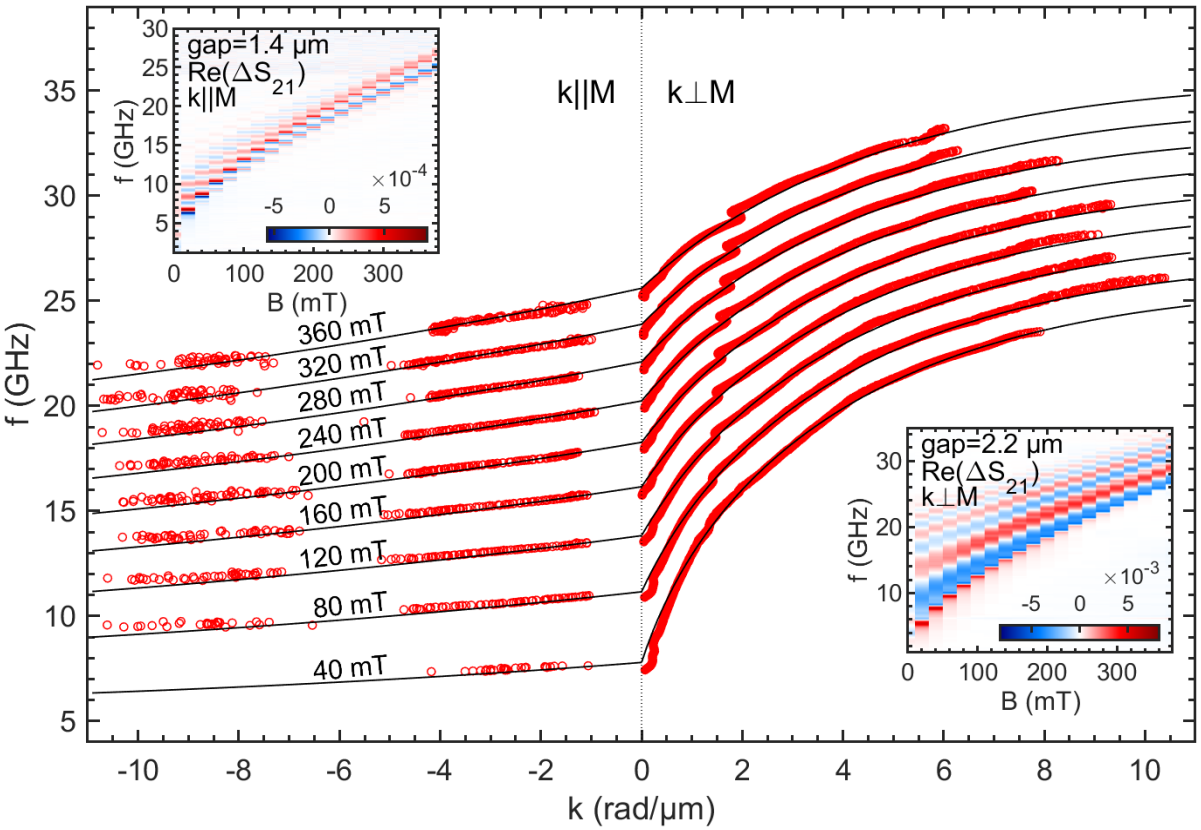

Fig. 5.10: PSWS experimental data in $\boldsymbol{k} \perp \boldsymbol{M}$ and $\boldsymbol{k} \parallel \boldsymbol{M}$ geometries with extracted dispersion relations for fields from 40 to 360 mT with 40 mT step. Black lines show the fit using the dipole-exchange model. ***Material: CoFeB 100 nm layer****, used antenna type for $\boldsymbol{k} \perp \boldsymbol{M}$: $l_s = 500$ nm striplines, for $\boldsymbol{k} \parallel \boldsymbol{M}$: $l_s = l_{gap} = l_{GND} = 500$ nm CPWs, used power: 0 dBm. Insets show representative data. Measured gaps for $\boldsymbol{k} \perp \boldsymbol{M}$: 1.0 to 3.4 µm with 0.4 µm step. Measured gaps for $\boldsymbol{k} \parallel \boldsymbol{M}$: 1.0, 1.4, and 1.8 µm.*
Fit parameters: $M_s = 1.24$ MA/m ($\mu_0 M_s = 1.51$ T), $t = 100$ nm; fixed parameters: $\gamma/2\pi = 30.8$ GHz/T, $A_{ex} = 15$ pJ/m.

The $\boldsymbol{k} \perp \boldsymbol{M}$ geometry was also measured with the processed dispersions plotted in the right half of Fig. 5.10. Most of the points follow the dipole-exchange model with distortions between $k = 1$ and 2 rad/µm. It was found that those frequencies belong to $n = 2$ mode of PSSW and therefore the observed features should be the hybridization of the two participating modes ($n = 0$ and $n = 2$), which will be discussed below in subsection 0. The previously shown measurements show undisturbed dispersions in agreement with the model because the thicknesses were low, and the modes cross above the detected k-vector range. Thus were not detected.

The propagation lengths were measured and calculated for CoFeB 100 nm layer with results shown in Fig. 5.11 for the $\boldsymbol{k} \perp \boldsymbol{M}$ geometry, and in Fig. 5.12 for the $\boldsymbol{k} \parallel \boldsymbol{M}$ geometry. The propagation lengths can be affected by the PSSW hybridization for k-vectors between 1 and 2 rad/µm for the $\boldsymbol{k} \perp \boldsymbol{M}$ geometry, but the rest of the measured range shows values comparable to the calculation. The propagation lengths in the $\boldsymbol{k} \parallel \boldsymbol{M}$ geometry is only in 1-2 µm range, and the overall signal size is low. The points were evaluated from three gap sizes. Thus, the measurement error is significant, but the data in Fig. 5.12 shows an agreement with the calculation.

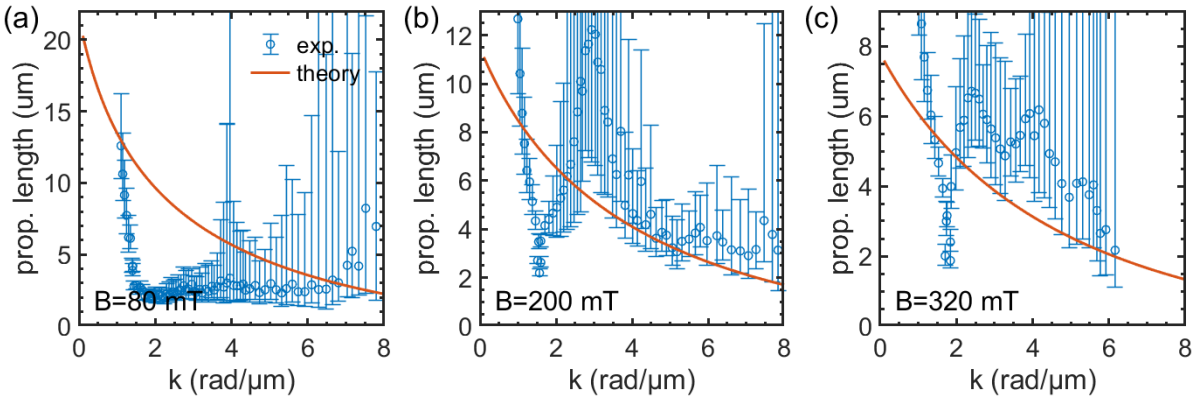

*Fig. 5.11: Experimental fits from the previously shown data and theoretical calculations of the propagation length for **CoFeB 100 nm layer** in $\boldsymbol{k} \perp \boldsymbol{M}$ geometry for (a) $B = 80$ mT, (b) $B = 200$ mT, (c) $B = 320$ mT. The calculation uses the constants obtained from the dispersion fit (Fig. 5.10), and $\alpha = 0.0089$ obtained from FMR (Fig. 4.19). The experiment shows comparable propagation lengths.*

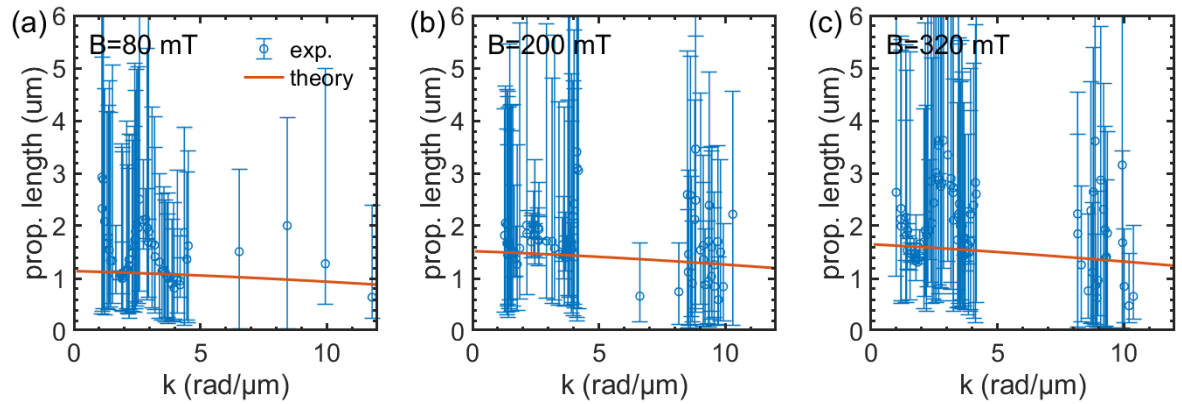

*Fig. 5.12: Experimental fits from the previously shown data and theoretical calculations of the propagation length for **CoFeB 100 nm layer** in $\boldsymbol{k} \parallel \boldsymbol{M}$ geometry for (a) $B = 80$ mT, (b) $B = 200$ mT, (c) $B = 320$ mT. The calculation uses the constants obtained from the dispersion fit (Fig. 5.10), and $\alpha = 0.0089$ obtained from FMR (Fig. 4.19).*

5.3.1 Dispersion hybridization with PSSW

The measured data on CoFeB 100 nm layer (Fig. 5.10) showed distortions at frequencies estimated to be the $n = 2$ dispersion mode (PSSW). The modes $n = 1$ and $n = 3$ also cross the dispersion relations within the measured k-vector range but odd modes should not hybridize with the even $n = 0$ mode because they do not have the same symmetry. Therefore, the dispersion can show slight distortions at the crossings due to both modes' existence, but the shape should remain unchanged, showing no hybridization. To verify the cause of distortions to be PSSW, a control thermal BLS was taken on the CoFeB 100 nm layer to reveal the PSSW positions. It is shown in Fig. 5.13, with the theoretical PSSW positions plotted using the Herring-Kittel formula. The parameters were used the same as in Fig. 5.14. There is a slight mismatch, most likely due to the different magnet in the BLS setup.

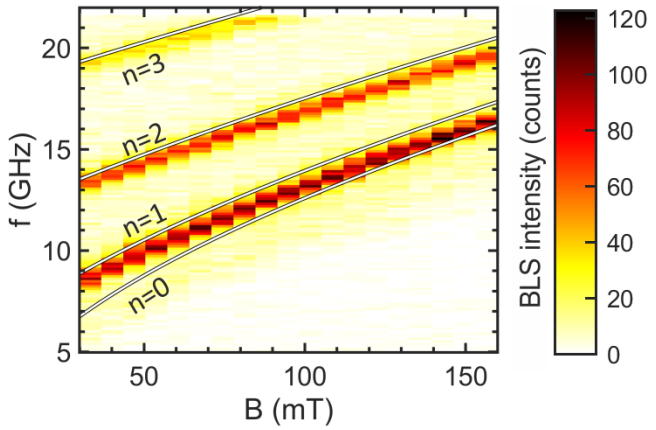

Fig. 5.13: Thermal BLS scan probing the spin-wave modes in CoFeB 100 nm layer. The lines show the calculation of the Herring-Kittel model [Eq. (1.32)] for $n = 0$ to 3 to show approximative positions of the FMR and PSSW modes. The parameters used for the calculation were the same as in Fig. 5.14. The slight mismatch is understandable due to the different magnets used in each experiment.

Modes $n = 0$ and $n = 2$ are both even and thus hybridize. The hybridization was noticeable in Fig. 5.10 in the k-vector range between $k = 1$ to 2 rad/µm increasingly with the magnetic field where the top and bottom branches have a larger opening. This portion of the dispersion cannot be fitted with the basic dipole-exchange model because the hybridization needs to be considered, but the rest of the dispersions follow the model well.

The calculation of hybridizations using the dipole-exchange model was provided in Section 1.9, where we also demonstrated that the pinning parameter d playes a significant role. That is because the mode hybridizations have a very small opening in order of MHz in systems with totally unpinned surface spins [$d = 0$, calculation shown in Fig. 1.15(b)], not reflecting the reality. However, the hybridization opening increases with the pinning parameter, which can be observed in Fig. 1.15(c,d), and the pinning value can be obtained by fitting the measured data.

The comparison of the measured data with the calculated hybridizations based on the beforementioned model is shown in Fig. 5.14 for a variety of magnetic fields. The method of k-vector extraction presented in this chapter provided values within the opening, but those were deemed physically invalid, and are plotted as light gray instead of red points in Fig. 5.14. The pinning parameter was estimated to be $d = 1.2 \cdot 10^7$, reflecting the experimentally found openings. This measurement proved non-zero surface pinning, while most literature uses the totally unpinned surface spins for the dispersion calculations. This can be justified by the large number of parameters playing a role in the calculation (M_s, γ, A_{ex}, t, B, φ, ϑ), making it impossible to observe the influence of another one parameter in experiments, where only a small part of the dispersion is used (within units to tens of rad/µm). From this point of view, the measured hybridizations provide a reasonable way to estimate the surface pinning.

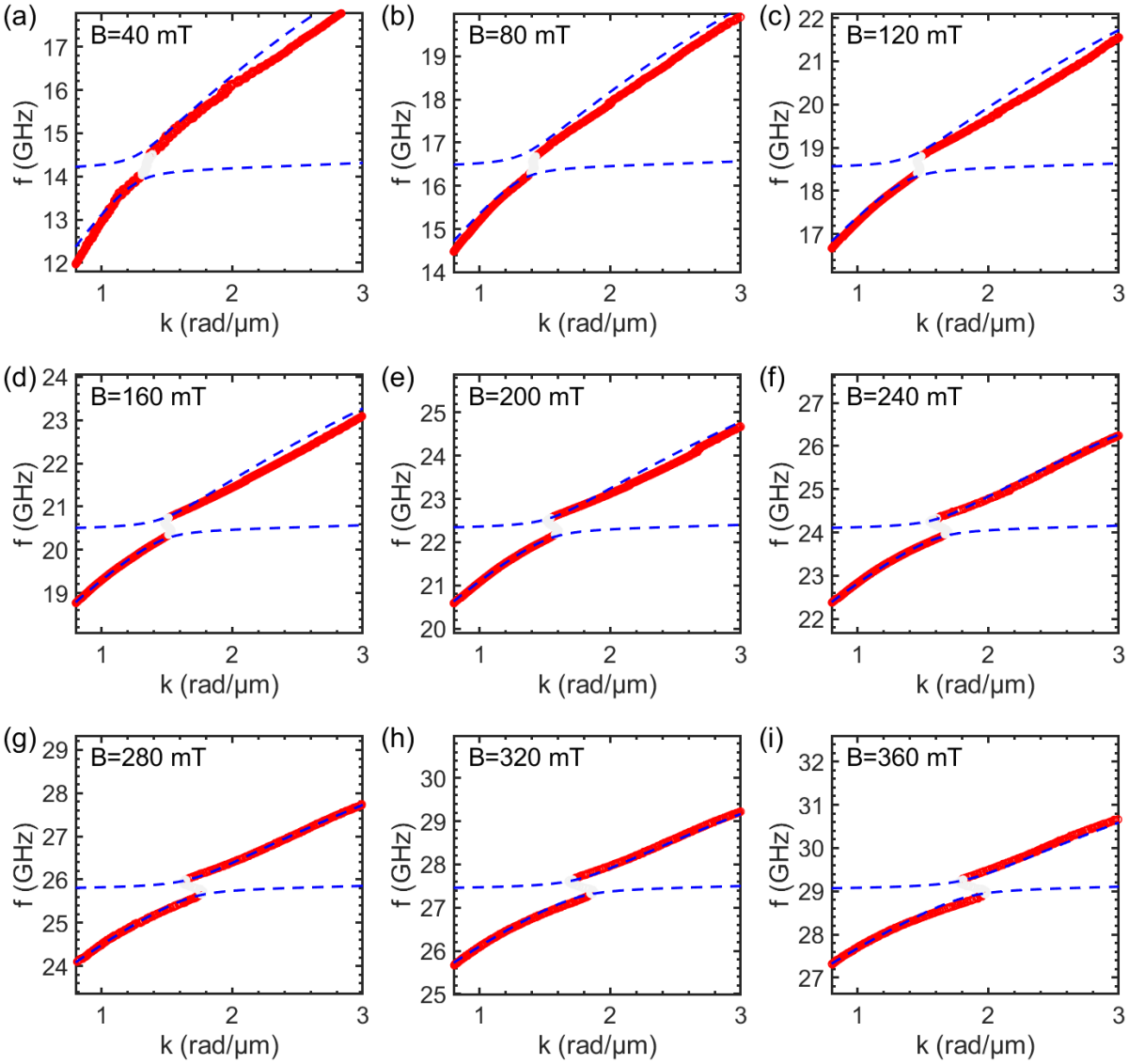

*Fig. 5.14: Hybridization of $n = 0$ ($\kappa_0 = 13.8$ rad/μm) with $n = 2$ ($\kappa_2 = 64.0$ rad/μm) modes measured on **CoFeB 100 nm layer**. Model parameters: $M_s = 1.23$ MA/m ($\mu_0 M_s = 1.55$ T), $\gamma/2\pi = 30.8$ GHz/T, $t = 104$ nm, $A_{ex} = 13$ pJ/m, $d = 1.2 \cdot 10^7$. The horizontal axis is identical for all graphs. The length of the vertical axis is 6 GHz in all graphs. The dashed blue lines represent the calculated hybridized modes based on Eq. (1.54). The points evaluated within the hybridization's frequency range are plotted in light grey as they are not valid.*

5.4 Spin-wave dispersion of YIG layers

The material that we are going to present last is yttrium iron garnet (YIG), and it is perhaps the easiest to measure due to its extremely low damping $\alpha \approx 10^{-4}$ to 10^{-5} (based on the layer quality and thickness). YIG is also the most difficult to prepare out of our studied materials. It is typically grown either by liquid phase epitaxy (micrometer thick films) or by pulsed laser deposition (submicron thick films) [125]. The low damping translates into the signal magnitude. The maximum signals were around $\mathrm{Mag}(S_{21})_{\max} \approx 5 \cdot 10^{-2}$, which is by far the strongest measured signal in any of our PSWS experiments. The small saturation magnetization causes the overall frequencies to be at relatively low at levels below or around 10 GHz. The spin-wave frequency bandwidth for the k-vector range up to 8 rad/μm is very

narrow, covering less than 1 GHz at each field, which is visible in the representative data shown in Fig. 5.15(a,b). This makes the data look visually different than the previous NiFe or CoFeB, but the overall behavior remains the same.

Fig. 5.15(c) presents the extracted dispersions for both $\boldsymbol{k} \perp \boldsymbol{M}$ and $\boldsymbol{k} \parallel \boldsymbol{M}$ geometries measured by pairs of $l_s = 500$ nm striplines. The data shows very good quality with one exception – both parts belonging to each geometry should meet at $k = 0$ but there is an offset, more pronounced at higher fields. We assign this to the magnetic field's inhomogeneity within the 16 mm magnet gap because the measured structures cover around 3x3 mm^2 area on the sample. At 200 mT, the frequency difference at $k = 0$ corresponds to approx 8 mT of magnetic field difference, which is realistic in our electromagnet with 16 mm gap between the poles.

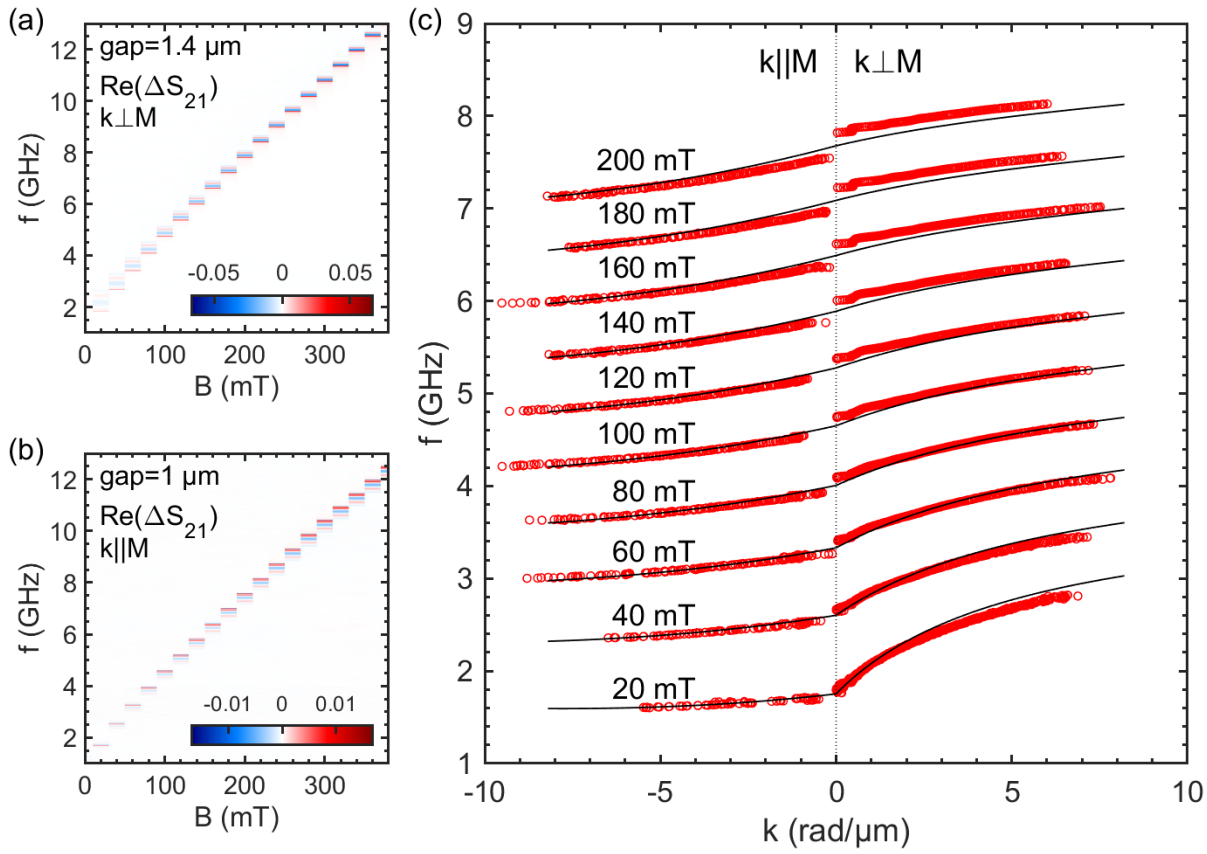

Fig. 5.15: PSWS experimental data in $\boldsymbol{k} \perp \boldsymbol{M}$ and $\boldsymbol{k} \parallel \boldsymbol{M}$ geometries with extracted dispersion relations for fields from 20 to 200 mT with 20 mT step with fit using the dipole-exchange model. ***Material: YIG 100 nm layer****, used antenna type:* $\boldsymbol{l_s = 500}$ ***nm striplines****, used power:* -30 *dBm. Measured gaps: 1.0 to 3.0 μm with 0.4 μm step.*
Fit parameters: $M_s = 140$ *kA/m (*$\mu_0 M_s = 0.176$ *T),* $t = 113$ *nm; fixed parameters:* $\gamma/2\pi = 28$ *GHz/T,* $A_{ex} = 3.6$ *pJ/m.*

Fig. 5.16 shows the data plotted vs. the gap size, while this time, we did not fit the propagation distance. The maximum measured gap was 3.4 µm, which proved to be a good choice for dispersion extraction. But due to YIG's exceptionally small damping, there is almost no detectable signal decay over this distance, and thus the exponential fit is not possible.

Fig. 5.17 presents theoretical propagation lengths for both $\boldsymbol{k} \perp \boldsymbol{M}$ and $\boldsymbol{k} \parallel \boldsymbol{M}$ geometries, showing that the DE propagation lengths in smaller magnetic fields and for smaller k-vectors even overcome 100 µm (the used damping was $\alpha = 3.5 \cdot 10^{-4}$ [115]). For thicker films, the damping would be even smaller, and the propagation lengths can be even in the mm range [103]. The $\boldsymbol{k} \parallel \boldsymbol{M}$ calculation at $B = 20$ mT shows the propagation decreasing down to zero at approx. $k = 7$ rad/µm, where the dispersion has a minimum (extremes in the dispersion lead to the group velocity $v_g = 0$). This explains the lack of measured points in the dispersions shown in Fig. 5.15 around this k-vector and field.

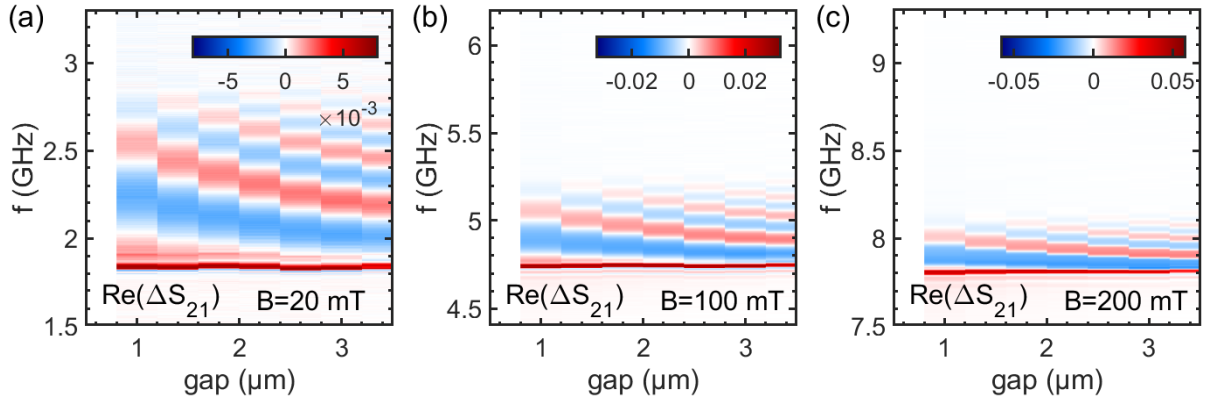

Fig. 5.16: PSWS experimental data in $\boldsymbol{k} \perp \boldsymbol{M}$ geometry plotted against the gap size. ***Material: YIG 100 nm layer****, used antenna type* $\boldsymbol{l_s = 500}$ ***nm striplines.***

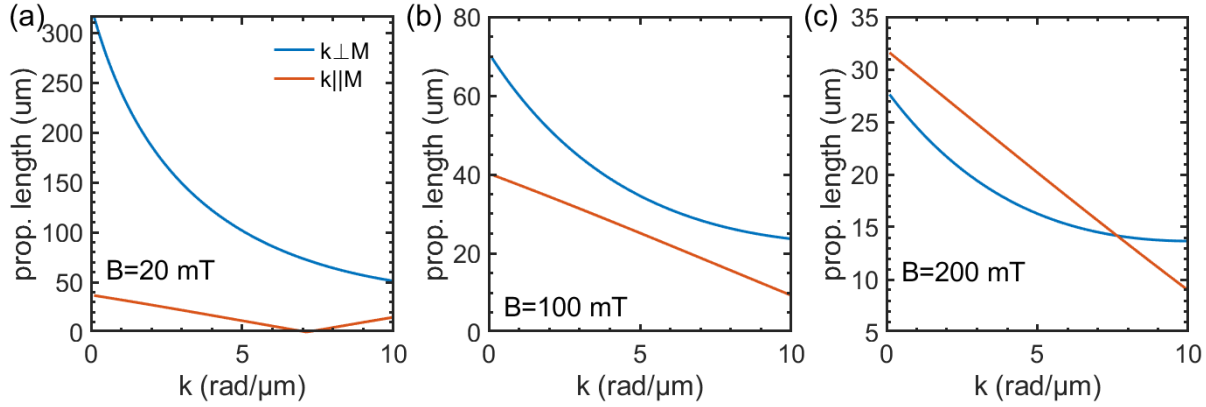

Fig. 5.17: Theoretical calculations of the propagation length for ***YIG 100 nm layer*** *for (a) $B = 20$ mT, (b) $B = 100$ mT, (c) $B = 200$ mT. The calculation uses the constants from the dispersion fit (Fig. 5.18), and $\alpha = 3.5 \cdot 10^{-4}$ [115].*

To have a comparison of sample measurement for two different antenna types, the YIG layer was also measured using GS antennas with $l_s = l_{\text{gap}} = 500$ nm, and in both $\boldsymbol{k} \perp \boldsymbol{M}$ and $\boldsymbol{k} \parallel \boldsymbol{M}$ geometries. The extracted dispersions are presented in Fig. 5.18, showing good agreement with the dipole exchange model, also with smaller mismatch around $k = 0$, because the structures used in this measurement were placed closer to each other on the sample, maintaining better magnetic field homogeneity within the used area.

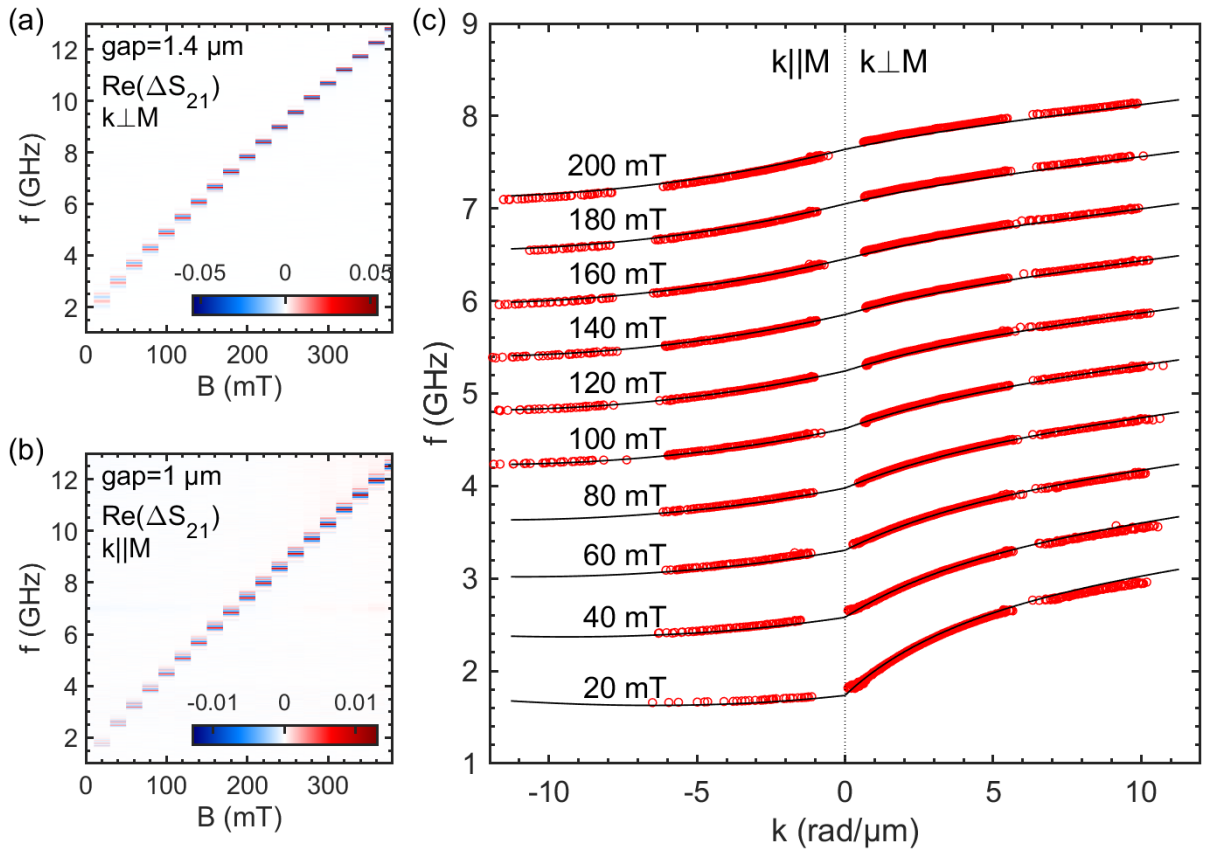

Fig. 5.18: PSWS experimental data in $\boldsymbol{k} \perp \boldsymbol{M}$ and $\boldsymbol{k} \parallel \boldsymbol{M}$ geometries with extracted dispersion relations for fields from 20 to 200 mT with 20 mT step with fit using the dipole-exchange model. ***Material: YIG 100 nm layer****, used antenna type:* $\boldsymbol{l_s = l_{gap} = 500}$ ***nm GS antennas****, used power:* -30 *dBm. Measured gaps: 1.0 to 3.0 μm with 0.4 μm step.*
Fit parameters: $M_s = 140$ *kA/m* ($\mu_0 M_s = 0.176$ *T*), $t = 113$ *nm; fixed parameters:* $\gamma/2\pi = 28$ *GHz/T,* $A_{ex} = 3.6$ *pJ/m.*

5.5 PSWS measurement on a magnonic crystal

The PSWS experiment with the dispersion extraction was also considered for magnonic crystals as they show a potential path in data processing [103]. They are artificial magnetic materials with properties periodically varied in space, which creates a complex spin-wave dispersion spectrum. One of the magnonic crystals' typical features is the formation of bandgaps in the spin-wave dispersion. The bandgap is a range of frequencies at which the spin-wave propagation is prohibited.

The simplest magnonic crystals can be produced by spatially varying the layer thickness and/or magnetization [103]. We attempted the PSWS measurement by modifying an already existing NiFe sample using a focused ion beam (FIB) patterning. The fabricated structure [shown in Fig. 5.19(a)] consisted of FIB-written stripes, where the layer is slightly milled (decreasing the thickness), and the used gallium ions also implant into the layer, causing a slight decrease of the saturation magnetization.

The Fig. 5.19(b,c) shows 2D transmission scans plotting $\mathrm{Re}(\Delta S_{21})$ and $\mathrm{Mag}(\Delta S_{21})$ signals, where the bandgap is visible. Fig. 5.19(d-f) shows line scans at representative magnetic fields, showing the existence of a bandgap in the data. The measured data was acquired for

the gap between the antennas of 4 µm, and the signal size was very small, peaking at only $\mathrm{Mag}(\Delta S_{21}) = 1.8 \cdot 10^{-4}$.

The dispersions were not evaluated because only one structure was modified. Moreover, a different material than NiFe would be recommended to attempt the dispersion measurement because the signal was too low, making the phase unreliable. Even more so because the resulting phase evolution in space would no longer be linear, and a more complex function would have to be used due to the existence of multiple k-vectors at the same frequency. Even though magnonic crystals' fabrication and characterization is beyond our current goals, our measurement shows a promising research direction.

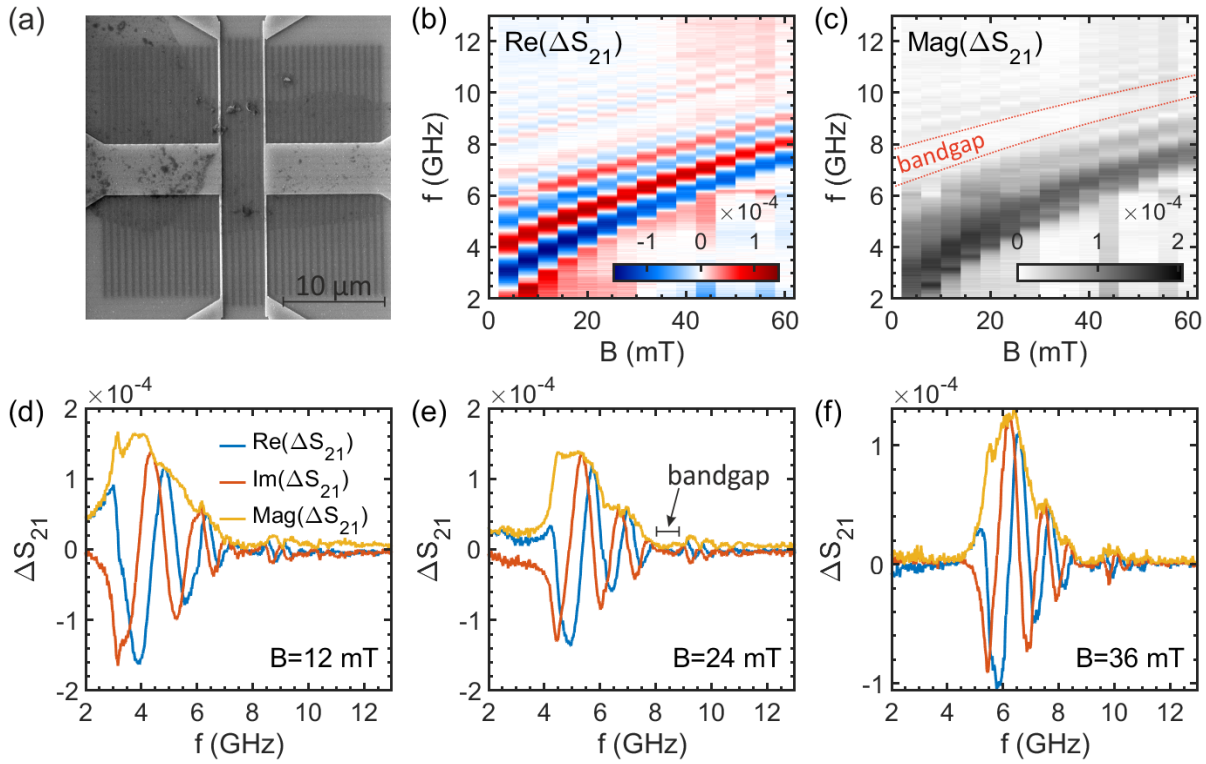

Fig. 5.19: (a) SEM image of NiFe layer with FIB-patterned stripes creating a magnonic crystal from a NiFe 40 nm layer with a pair of $l_s = 200$ nm stripline antennas. (b-f) ΔS_{21} data plots showing a visible band gap (e.g., around 8 GHz for 24 mT).

5.6 Summary of the spin-wave dispersion measurements

This chapter presented data on spin-wave dispersions that were measured by a VNA using the PSWS experiment. It proved to be a very powerful technique for characterizing magnetic layers' dynamic properties, which was demonstrated on NiFe, CoFeB, and YIG thin layers. Alongside the dispersions, data on propagation lengths were also presented.

Probing of advanced features, like the mode hybridizations in 100 nm CoFeB layers or the bandgap in FIB-modified NiFe layer creating a magnonic crystal, was also demonstrated. The hybridized dispersion modes proved to be a useful tool for evaluating the layers for the surface pinning parameter because the opening of hybridized modes is strongly dependent on the pinning. The pinning parameter is also not easy to obtain by other conventional methods.

6 Freestanding and positionable microwave antenna device

Previous chapters dealt with spin-wave excitation and detection, where the antennas (one antenna in case of BLS detection) had to be patterned on the sample. The fabrication of antennas directly on the sample can be a complex and time-consuming process requiring the availability of a nanofabrication facility. Moreover, some samples present extra challenges in the process of antenna fabrication, e.g., samples using single-crystal copper substrates used in [127,128], where the antenna parts can be easily short-circuited through the substate disabling it from spin-wave excitation. Another disadvantage of the classical approach is that the antenna is no longer repositionable after fabrication. This led to the idea of separating the excitation antenna from the sample itself by designing and fabricating an antenna device that would be freestanding with the ability to land to any position on the sample. Simultaneously, this device would have to allow optical detection by BLS or other techniques and navigation on the sample. Therefore the first design choice was to fabricate it on a transparent substrate. The main concept idea of this approach is shown in Fig. 6.1. The following paragraphs will describe its full design and use in optically and electrically detected experiments.

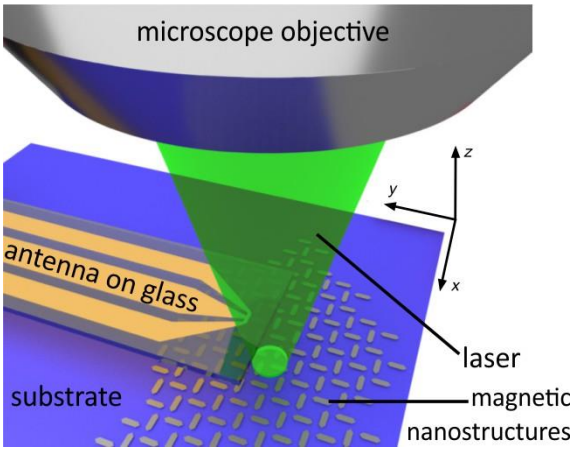

Fig. 6.1: Positionable antenna device with excitation part fabricated on a glass cantilever landed on a sample with magnetic nanostructures. Reprinted from [126].

6.1 Design and fabrication of the antenna device

Fig. 6.2(a,b) shows a side and top views of an antenna device model, where the device was designed to consist of three main parts:

1. thin glass cantilever with the excitation part,
2. printed circuit board (PCB) coupler,
3. SMA connector (Rosenberger 32K243-40ML5).

The glass cantilever is a 100 µm thick glass plate with a fabricated antenna. The antenna itself consists of the excitation part, which is either a stripline or another excitation structure (see Section 4.2), and a connecting CPW of matched characteristic impedance (calculated using the TX Line software [96]). The design is then patterned by e-beam lithography into a 1 µm thick PMMA resist coating covered with a conducting layer (Allresist AR-PC 5090), followed by e-beam evaporation of Ti 5 nm/Cu 500 nm/Au 10 nm multilayer, and lift-off. Consequently, the cantilever is covered with a 50 nm thick SiO_2 layer to avoid short-circuiting to the sample. The relatively thick copper layer is used to minimize the ohmic losses due to the approx. 2 cm long connecting CPW length. The fabrication is usually done in batches either on a glass wafer [Fig. 6.2(c)] or on cover glass plates that are consecutively cut into individual units [Fig. 6.2(d)] by a diamond saw dicer.

The second part is a printed circuit board with a CPW providing the interconnection between the SMA connector and the glass cantilever. The glass is glued onto the PCB, and the electrical connection is accomplished by wirebonding, using 25 µm thick and 250 µm wide ribbon wires. The connector is attached to the PCB and soldered, completing the antenna device unit.

This assembly is then fixed onto a manipulator, which besides x-y-z translational motions should favorably have a two-way tilt as well. The tilt manipulator will allow the cantilever to point down against the sample, which can then be lowered into the contact and start flexing. The 100 µm thick glass is conveniently flexible and will withstand bending by at least 2 mm for the 2 cm cantilever length. After the touchdown, we can observe an interference pattern [stripes, demonstrated in Fig. 6.2(e)] that will hint us about a glass tilt present, which can be eliminated by adjusting the tilt angles. Full elimination of the interference pattern is a good indicator that the antenna is in the best achievable contact.

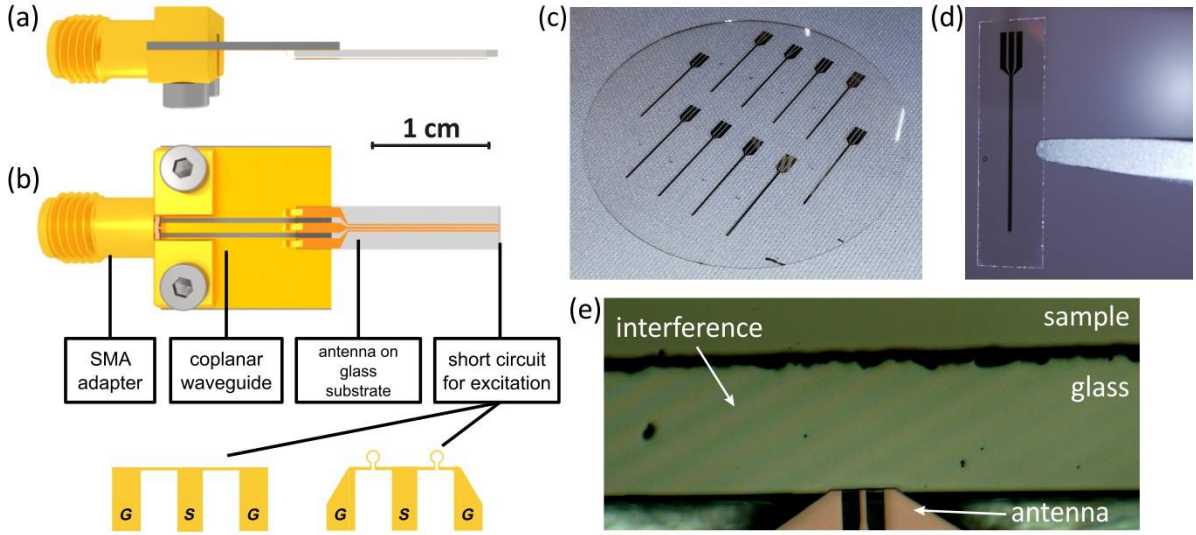

Fig. 6.2: (a) side view and (b) top view of the antenna device with a description of its components. The short-circuiting antenna ending can be modified based on the experimental requirements. The details show the stripline for in-plane excitation and omega-shaped antennas for out-of-plane excitation. Other variants are possible, e.g., a CPW. Reprinted from [126]*. (c) Glass wafer (2") with fabricated antennas. (d) One antenna unit diced from the wafer. (e) Interference pattern of an imperfect antenna landing onto the sample surface. Elimination of the stripes by tilting the stage will result in better contact between the glass cantilever and the sample.*

6.2 Excitation characteristics

Most of our tests were performed with $l_s = 1$ µm striplines used as the excitation endings on the antenna device. Fig. 6.3(a) presents the calculated magnetic field induced by the current flow in the stripline. Because the antenna on glass does not always have to be in perfect contact with the sample surface, we can estimate the influence of different distances between the stripline and the sample. Fig. 6.3(b,c) shows the calculated out-of-plane and in-plane components of the induced magnetic field for different antenna-sample distances. The simulation was performed with an assumption of a homogeneous current flow of $I = 63$ mA confined to the stripline geometry. We can observe that the magnetic field is decreasing with the distance, to about one half at 500 nm distance compared with the stripline's surface (distance 0 nm). This will also influence the antenna's excitation spectrum as the field's spatial

confinement decreases with the distance. The excitation spectrum was calculated as a Fourier transform of the field distribution and is shown in Fig. 6.3(c). The decaying excitation strength is anticipated with increasing distance to the sample, emphasizing the importance of good contact of the antenna to the measured sample.

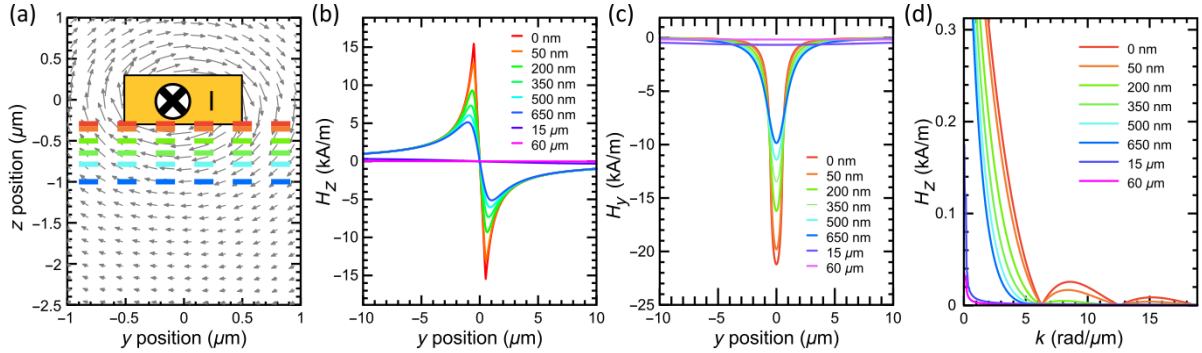

Fig. 6.3: Distance dependent excitation properties. (a) Cross-section of the used 1 µm x 0.5 µm wire with the calculated magnetic field distribution. The colored dashed lines indicate the z-positions, where the field distribution is analyzed (b,c) Calculated components of the excitation magnetic field in several distances from the wire. (d) Calculated excitation spectra for different distances from the stripline. Reprinted from [126].

As a proof of concept for the antenna device's functionality, we show in Fig. 6.4 the direct comparison of the measured BLS signal intensity of thermally excited spin-waves (red curve) in a Pt(4.5 nm)/Cu(0.87 nm)/NiFe(5 nm)/Al(3.5 nm) thin film at an applied in-plane magnetic field of 51 mT. The antenna was then connected to a signal generator outputting 6 GHz at a nominal power of 30 dBm. The significant increase of the measured signal (blue curve) clearly shows the selective excitation of the NiFe layer by the nearby suspended antenna. Both BLS measurements were performed through the glass cantilever to maintain comparable measurement conditions. Additionally, an RF sweep was performed to detect the peak intensity for different microwave frequencies to demonstrate that dynamics can be driven over a wide frequency range [Fig. 6.4 green curve]. Even though the largest intensity is reached around the ferromagnetic resonance, we observe a significant increase of signal for higher frequencies up to 6.6 GHz, which corresponds to a k-vector of 7 rad/µm.

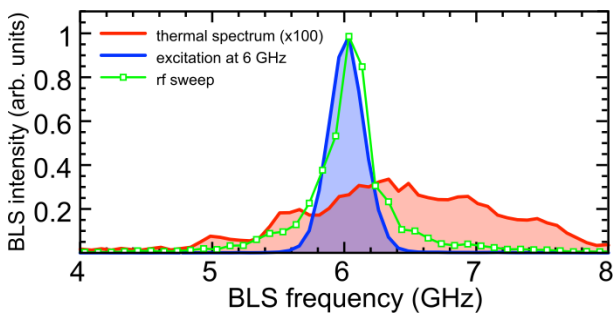

Fig. 6.4: Proof of concept for the antenna device using BLS detection. The red curve shows a magnified thermal spectrum measured on a Pt(4.5 nm)/Cu(0.87 nm)/NiFe(5 nm)/Al(3.5 nm) film. Blue and green curves show the BLS spectra under excitation at 6 GHz and for an RF sweep respectively, showing a signal increase by approx. 400 times. Reprinted from [126].

6.3 Use of the antenna device in BLS experiments

Brillouin light scattering is the typical experimental environment to benefit from the antenna device usage for sample excitation. The sample then needs no modifications and can be directly mounted into the BLS setup and measured. There is one case (the measurements of thermal magnons) when the sample does not need any modifications anyway. It is a measurement during which no excitation is used, and the signal is generated purely by

thermally activated excitations of the sample. Even though this is a standard approach measurable by BLS, it can be difficult or impossible on some sample types. A typical example is the commonly studied YIG, which is transparent for the commonly used 532 nm light and the backscattering due to thermal spin waves has a very small cross-section.

When the antenna device is used on YIG, the signal is enhanced by the antenna's excitation. This readily allows us to perform, e.g., optically detected FMR experiment on YIG with incomparably shorter measurement times compared against pure thermal excitation. The FMR measurement was performed in a way that the sample is excited with the antenna device, and the BLS signal is detected while sweeping the magnetic field. The peak signal for each frequency, plotted in Fig. 6.5(a), corresponds to the FMR magnetic field. Fitting the resonant frequency to magnetic field dependence by the Kittel formula allows for the extraction of material parameters, shown in Fig. 6.5(b). A direct comparison of the measured BLS intensity with and without the antenna device excitation active is shown in Fig. 6.5(c), where no thermal signal is detected. This confirms the technique's utility because it allowed basic characterization of the sample by FMR in a short time, while otherwise, the YIG sample is not possible to measure by thermal excitation in a reasonable time.

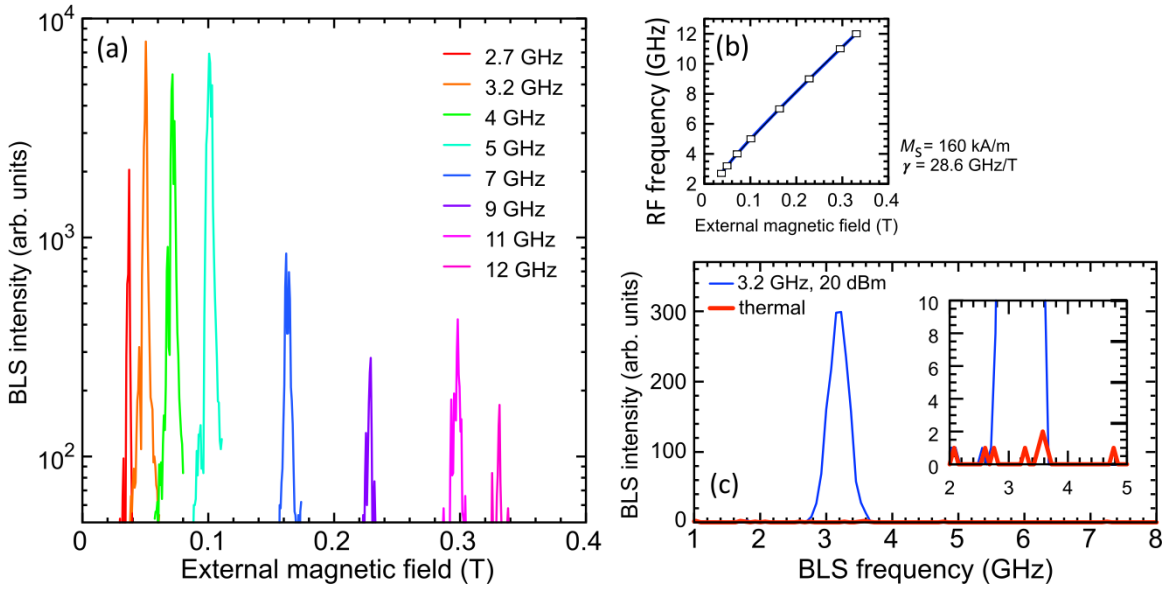

Fig. 6.5: (a) BLS-detected FMR peaks of a YIG film excited by the antenna devices at eight different RF-frequencies (b) Kittel formula fit of the peak positions. (c) comparison of the signal with and without the excitation by the antenna device active. Inset is the detailed signal for the frequency range of the expected FMR of the YIG. Reprinted from [126].

The antenna device is suitable not only for the FMR experiment, but it can also excite propagating spin-waves when carefully landed on the sample minimizing the antenna-sample distance. We have performed a BLS study of the antenna spatial excitation profile on a 240 nm thick CoFeB layer. Fig. 6.6(a,c) shows two graphs mapping the BLS intensity around the stripline ending of the antenna device landed on the layer. The maps show the spin waves propagating in two beams with a significant drop in between them. The intensity drop can be attributed to the excitation phase shift of π between the striplines and thus to the destructive interference of the spin waves between the two antennas.

Fig. 6.6(b,d) shows the intensity dependence in the logarithmic scale along the dotted white lines in (a,c). An exponential fit for the higher field measurement shows a close to linear behavior and allows to determine the decay length of 22.3 µm for the BLS intensity, indicating

a propagating spin-wave mode. For the smaller field, the extraction shows a deviation from a clear linear behavior, indicating a localized, directly excited mode in the antenna's close vicinity. We fit only the points close to the antenna to obtain a decay length for comparison. A value of 11.0 µm is obtained. From the fits, it can be confirmed that the excited mode at 86.3 mT extends further. The different propagation range of both modes can be explained by the spin-wave dispersion relation.

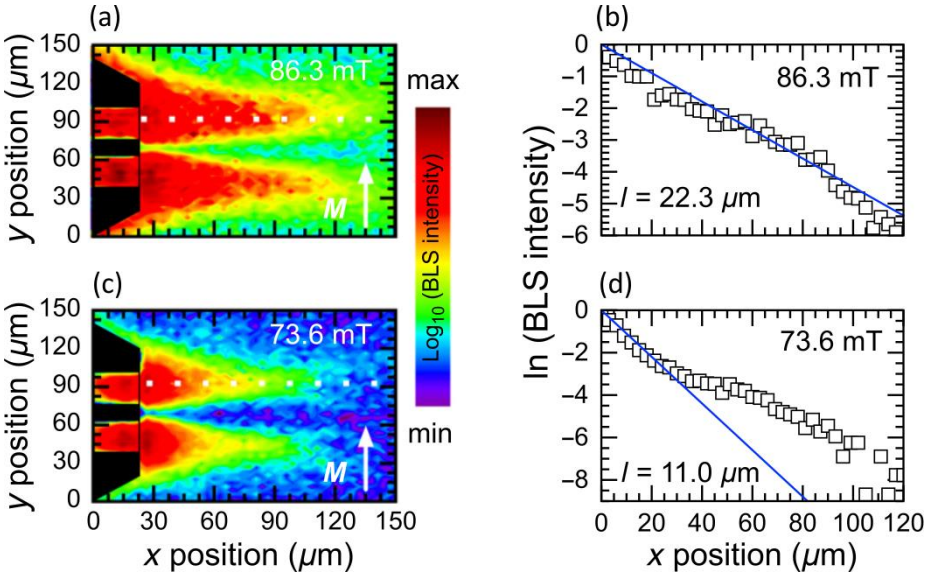

Fig. 6.6: (a,c) 2D maps of BLS intensity at (a) $B = 86.3$ mT and (d) $B = 73.6$ mT. (b,d) shows the BLS intensity plotted along the white dotted lines in (a,c), showing exponential decay. Reprinted from [126].

The next experiment demonstrates the possibility of using the antenna device to perform an injection-locking experiment with a spin Hall nano-oscillator (SHNO), a topic recently studied by multiple groups [129,130]. The SHNO is a device that can exhibit magnetic auto-oscillations after introducing current into its junction. The micrograph in Fig. 6.7(a) shows the SHNO junction patterned by e-beam lithography from a Ta(2 nm)/Pt(7 nm)/CoFeB(5 nm)/Ta(2 nm) stack.

The current applied to the SHNO mostly flows through the Pt and generates a pure spin current via the spin Hall effect [131–133]. This pure spin current enters through the interface into the magnetic CoFeB layer. This layer's magnetization is aligned perpendicular to the DC current by an external magnetic field, which is a necessary condition to obtain auto-oscillations of the magnetization.

Since magnetization and DC current are exactly perpendicular, we work at the point of maximized spin-transfer torque. The auto-oscillations are localized in the 630 nm wide constriction, where the highest current density is reached [37]. Fig. 6.7(b) shows the intensity of the auto-oscillations measured by BLS in dependence of the applied current at an external magnetic field of 34.5 mT. The auto-oscillations occur only for one direction of the electric current, whereas increased damping of the magnetization is enforced in the opposite current direction. Please note the negative nonlinear frequency shift of the auto-oscillations during the increase of current and the onset of the auto-oscillations, a typical property for SHNO with in-plane magnetization.

After demonstrating auto-oscillations in the SHNO, the antenna is positioned close to the constriction and connected to a signal generator. The microwave frequency through the

antenna is swept between 3.5 and 5 GHz in 25-MHz steps at a nominal power of 16 dBm, and a dynamic Oersted field is generated, affecting the magnetic layer of the SHNO. A DC current of 3.5 mA is applied to the SHNO at an external magnetic field of 34.5 mT. In Fig. 6(c), it is demonstrated that the auto-oscillations can synchronize to the dynamic Oersted field in a certain locking range. We separate the locking process into five segments. If the difference between the frequency of the external stimulus and the auto-oscillations is too large, then there is no synchronization possible, and the auto-oscillation frequency stays constant (segments I and V). However, if the difference between microwave and auto-oscillation frequency is reduced, frequency pulling sets in. The auto-oscillation frequency is stepwise shifted to the external stimulus's frequency (segments II and IV). Within segment III the auto-oscillations are synchronized to the dynamic antenna field. This is indicated by the linear correlation between the externally driven microwave frequency through the antenna and the auto-oscillation frequency in this segment. The included circles are obtained by fitting the measured spectra by Lorentz functions. Fig. 6.7(d) shows the antenna's excitation without auto-oscillations, meaning that the DC current is switched off during this measurement. It can be clearly seen that the direct spin-wave excitation within the locking range is much weaker than the auto-oscillation intensity. Please note that both plots are normalized to each other. Fig. 6.7(e-h) compares the properties of the excited spin-wave modes within the SHNO.

Further description is beyond the scope of this Chapter, focusing on presenting the antenna device functionality. Please see [126] for further details.

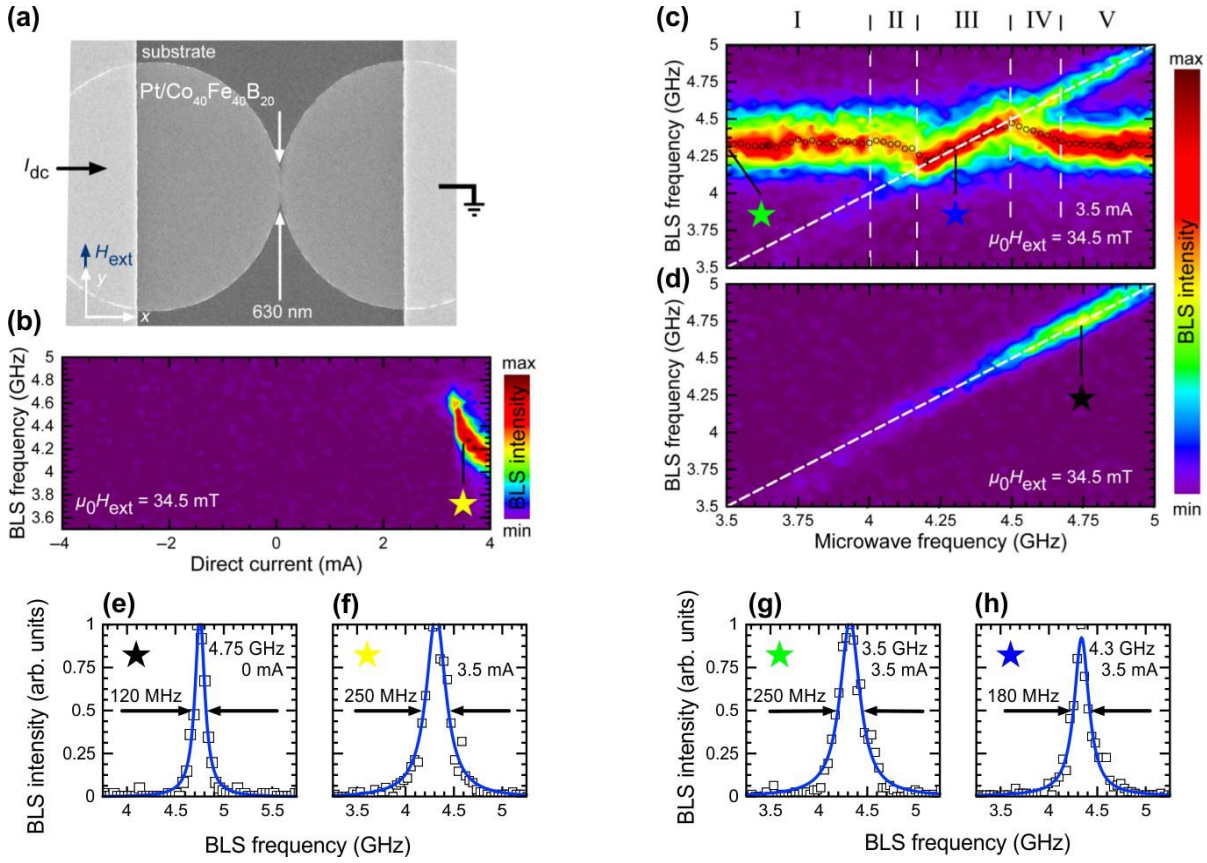

Fig. 6.7: (a) SEM micrograph of SHNO. (b) Intensity of the SHNO auto-oscillations measured by BLS. (c) Locking characteristics of the SHNO measured as a function of applied microwave frequency for a fixed DC current. (d) excitation from the antenna without auto-oscillations (no DC current applied). (e-h) comparison of the excited modes within the SHNO. Reprinted from [126].

6.4 Use of the antenna device in FMR and PSWS experiments

We have attempted to use the antenna device for electrical measurements using the VNA in FMR and PSWS experiments. While in the case of the BLS experiments, where the antenna served as the excitation source only with the detection technique completely separated, the VNA experiments use both electrical excitation and detection. There are challenges associated with this because, contrary to the excitation use only, VNA depends on the system's calibration to place the measurement reference planes as close to the device as possible. However, calibration with a non-standard connection would require the development and execution of a calibration kit with a calibration software specifically for this purpose, e.g., a set consisting of devices of the same design but with calibration standards manufactured at its endings instead of the excitation antennas.

The idea of the FMR experiment using the antenna device is the localization of the detected signal for use in, e.g., inhomogeneous samples, where the properties could be probed with a certain spatial resolution. In a standard VNA-FMR experiment, described in Section 4.3, a large area of the sample is excited, and the signal is measured in the microwave transmission signal. This approach has no spatial resolution, but the main advantage is that the connection of a well-matched excitation waveguide to a calibrated VNA means that most of the signal comes from the sample.

The constraint of the antenna device used in the FMR experiment is that we are limited to use the reflection S_{11} parameter only. On top of this, the thin striplines used here excite not only FMR but also spin-waves, which is not desirable in this case, because it influences the FMR peak. It can be limited by choosing a wider stripline. Confinement of the FMR means it is no longer a collective oscillation of all moments in the sample, influencing the measurement. Another downside of this approach is that the signal line guiding the RF excitation to the striplines can excite the sample and can potentially produce an even higher signal than the stripline endings. The described unwanted excitation can be suppressed in the case of nanostructured samples containing multiple individual elements, where the antenna device would excite and detect them one by one with no need for the excitation antenna fabricated on every studied element on the sample (e.g. [134]).

The VNA-FMR experiment was tested by landing the stripline ending on a 40 nm thick NiFe layer close to the substrate edge, as shown in the navigation photo in Fig. 6.8(a). In this way, we were able to assure that the signal comes only from the stripline ending. The measured signal, shown in Fig. 6.8(b) for $\div \mathrm{Mag}(S_{11})$, exhibits a visible FMR band, but its magnitude is less than 1 % when compared to the background. While this signal is detectable, it is also too small for detailed analysis, and we cannot expect more than a rough fit using the Kittel formula if we needed it.

Another tested experiment using the VNA was PSWS, which was introduced in Section 4.5. As the main objective is to measure spin-wave propagation in magnetic layers, the antenna device could introduce a breaking improvement of the on-run changeable propagation distance because the traditional approach (also used for the dispersion extraction presented in Chapter 5) relies on antennas fabricated onto the sample. Measurement of multiple propagation distances requires the fabrication of multiple instances of the antennas, where each pair has a different gap between the antennas.

This approach was tested, and Fig. 6.9(a) shows an image acquired by the navigation camera showing two CPW antennas, with the antennas' excitation parts placed over a NiFe stripe on the GaAs substrate. One antenna (on the left) is fixed on the sample and contacted with a microwave probe, and the second one is on the glass cantilever, which is landed to the

NiFe stripe at approx. 15 µm distance from the on-sample CPW. The transmission parameters S_{21} and S_{12} [Fig. 6.9(b,e)] show almost identical signals with a spin-wave band from approx. 5 GHz at the zero magnetic field. While the spin-wave signal is detectable in transmission, we did not manage to improve it, and it is substantially worse than the quality required for analysis, e.g., the dispersion extraction. The reflection parameters, shown in Fig. 6.9(c,d), also present the difference, where (c) the antenna on the sample with a very distinct signal showing two spin-wave bands (attributed to the first two maxima of the CPW excitation), and (d) the antenna on glass, where no reflection is detected whatsoever.

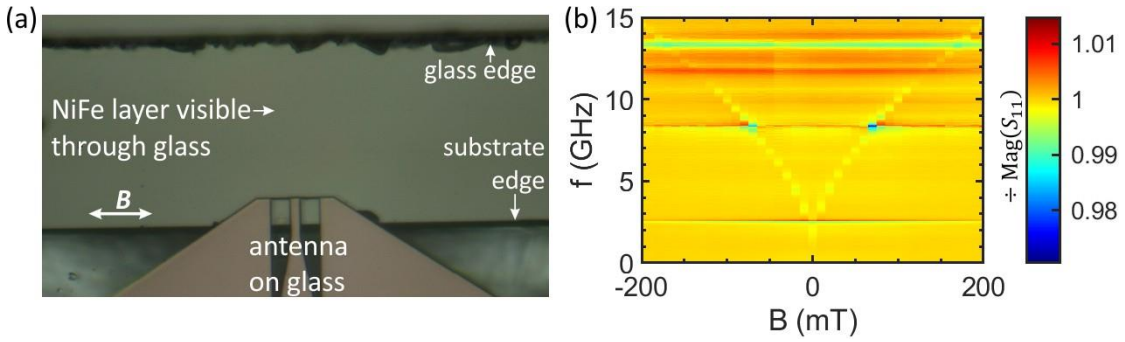

Fig. 6.8: FMR experiment using the antenna device. (a) Navigation microscope image of the antenna ending on the sample, with the excitation striplines nearby the sample edge (free space below the glass cantilever). (b) VNA reflection data showing a weak but detectable signal.

6.5 Summary of the antenna device results

The approach of separating the antenna from the sample proved to be successful and useful, in some cases even enabling the otherwise almost impossible experiment (BLS detection on YIG) or providing significant simplification (injection locking experiment). One of the arguments for this approach is the lower time investment into the antenna fabrication on the sample, here we should note that the fabrication of the antenna device is even more time demanding, but the reusability beats the time investment. Despite good results, summarized in [126], we acknowledge the yet unresolved problems of the antenna device of the stage mechanical instability, limiting long (e.g., 24 hours) experiments, while improvements are under consideration.

The use of the antenna device in VNA-powered experiments is even more intriguing. In the thesis submission time, the imperfect RF design and the lack of calibration options of the antenna device rather disqualify this approach from valid experiments with a vast room for improvement.

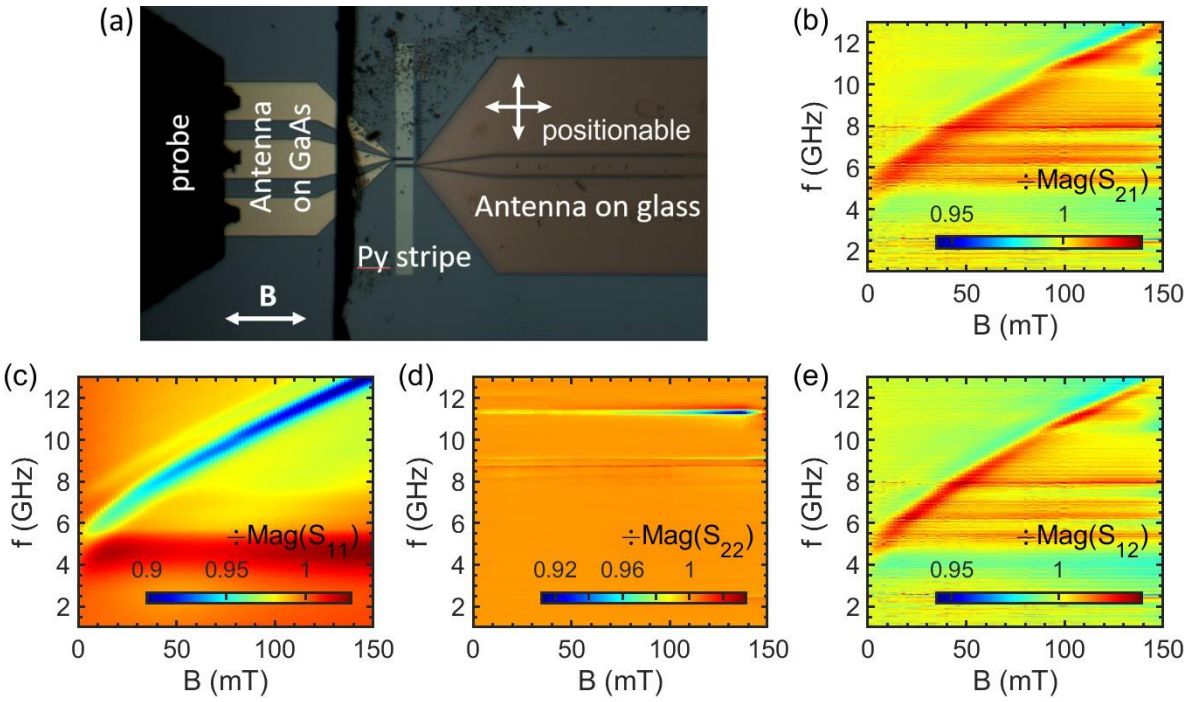

Fig. 6.9: PSWS experiment with one fixed antenna on the sample and the freestanding antenna device as the second antenna. (a) Navigation microscope image with the fixed antenna contacted with a probe on the left (VNA port 1) and the positionable antenna on the right (VNA port 2). Both antennas have a CPW excitation part overlaid on the NiFe stripe. (b-e) Magnitude plots of individual S-parameter signals. (c) The fixed antenna exhibits two spin-wave bands measured in the reflection signal S_{11}, opposed to (d) no reflection signal measured from the CPW antenna on the antenna device. (b,e) Weak but detectable spin-wave transmission signals, equally for (b) S_{21} and (e) S_{12} signals.

Conclusion

In the first part of this work, we probed and characterized the magnetic vortex nucleation states using micromagnetic simulations, magnetic imaging by Lorentz microscopy (LTEM), and Magnetic Transmission X-ray Microscopy (MTXM), and we correlated the results with electrical measurements via the anisotropic magnetoresistance (AMR) effect [92]. The advantage of the AMR measurements proved to be in a single disk sensitivity and overall simplicity of the characterization process. However, the pinning and subtle differences between samples proved problematic and made drawing conclusions rather uneasy. We were still able to classify the nucleation process by dividing the nucleation states into the C-state, vortex-pair state, and the buckling state. The characteristic features of the individual states in the AMR curves were also presented, allowing characterization of the nucleation process and, e.g., study the driving effects behind the individual nucleation states with a possibility for statistical studies unattainable by any other method. The acquired knowledge about the vortex nucleation can serve, e.g., for improving the reliability of the vortex switching, which is critical in data storage applications.

Besides the three mentioned states, the vortex-antivortex-vortex (VAV) triplet was a curious discovery with an unmistakable spin structure. However, while both the MTXM and AMR data convincingly verify its existence, it proved to be extremely hard to stabilize on purpose. Some preliminary simulations showed the VAV triplet's interesting properties, e.g., when exposed to high-frequency excitation leading to unusual spin-wave modes generated within the disk. Nonetheless, extensive time and effort were spent trying to achieve consistent stabilization of the triplets, but it was never successful.

The part of this work devoted to vortices was done still at the Faculty of Mechanical Engineering, and later in temporary CEITEC premises in the former FEI company building. But then our moving to new facilities after about two years brought unprecedented experimental options in both sample fabrication (in the new nanofabrication facility) and magnetic characterization (installation of new equipment such as vector network analyzer [VNA], Brillouin light scattering [BLS], or Kerr microscope), which allowed us for modern magnetization dynamics experiments without the limitations only to the static regime.

The mentioned improvements in our working environment shifted our interests more towards spin-waves [126–128]. We developed experimental processes to measure ferromagnetic resonance (FMR) and propagating spin-wave spectroscopy (PSWS) using the VNA and begun to use the BLS as a great, versatile tool for spin-wave detection. VNA proved to be extremely useful in probing the dynamic material properties, to which the whole Chapter 4 was devoted, describing the VNA basics (receiver operation, sample connection, calibration, excitation in magnetization dynamics experiments), followed by the description of FMR and PSWS experiments from all practical aspects. Chapter 5 then described the developments in the dispersion relation measurement using the PSWS experiment, showing good potential in high quality, detailed results. The dispersion measurements are in good agreement with the dipole-exchange model by Kalinikos and Slavin (presented in Section 1.9), providing room to extract the material parameters by fitting the dispersions.

The spin-wave dispersion extraction method presented in Chapter 5 was successfully implemented, and dispersion results were provided for NiFe, CoFeB, and YIG layers. It requires measuring multiple propagation distances, which (besides the dispersion extraction) allows for fitting of the propagation length from the transmission signal attenuation. The propagation distance can also be calculated using dispersion relations with used parameters

experimentally extracted for each material. Measurements of the thicker (100 nm) CoFeB layer also yielded hybridized dispersions for $n = 0$ and $n = 2$ modes because for the thicker samples, the modes start to cross within the detectable k-vector range. The hybridizations were described analytically in the last part of Chapter 1, providing interesting conclusions regarding the surface pinning. Most of the calculations presented in the literature are done with the boundary condition of so-called totally unpinned surface spins, which proved to be unusable because the predicted hybridization openings were not reflected in the experiment. We obtained matching theoretical calculations of the hybridized dispersions only after introducing the partially pinned boundary conditions to the calculation.

An example of PSWS measurement on a simple (FIB milled) magnonic crystal was also shown, where the phase development in space will no longer be linear. This is a possible future direction of this method, where modeling the phase and fitting it to the experiment will be necessary. Another possible future direction of the VNA-measured PSWS method is excitation and detection using high-k antennas, e.g., ladders or meanders, giving the possibility to probe the exchange interaction dominated part of the spin-wave dispersion.

In the last Chapter 6, we introduced a spin-wave measurement approach using our developed antenna device, discarding the necessity of fabricating the excitation antennas on the sample. The antenna device has a glass cantilever with the excitation antenna, which can be positioned anywhere on the sample. The excitation properties were calculated for increasing antenna distance to the surface, showing that imperfect placement (landing) of the cantilever on the sample still allows for successful data acquisition. The optical detection using BLS was seamless with a slight decrease of spatial resolution but allowing for more rapid experimental flow. The antenna device also proved to be useful in specific situations, e.g., measurement on YIG, which is a transparent material with a very poor thermal signal. The YIG's thermal signal is typically undetectable within a reasonable time, but the added excitation from the antenna device enhances the signal by a factor in order of hundreds without any sample modifications. The injection-locking of an SHNO is another great example, where the experimental flow is greatly simplified as the lack of space around the nano-oscillator body complicates fabricating the antenna on the sample itself. The use of the antenna device in VNA-powered experiments is still mostly opened for development, but electrical measurements' functionality was proven.

Despite the COVID 19 pandemic that we faced in 2020 during the finishing of this work, society has the most advanced technology in possession, providing unprecedented possibilities in all directions. Humanity's deep commitment to progress through science was proven by the development and approval of COVID 19 vaccines by multiple companies [135] in record sub-one year time (the pandemic reached Europe at the beginning of 2020 while western authorities approved the first vaccines for wide use in December 2020). The results presented in this work impact only a tiny area of science, yet we should be optimistic about our future perspective in both our personal lives and in the field of magnetism [136].

List of abbreviations

AFM	atomic force microscopy
ALS	Advanced Light Source (synchrotron facility)
AMR	anisotropic magnetoresistance
BLS	Brillouin light scattering
BV	backward volume
BVMSW	backward volume magnetostatic waves
CPW	coplanar waveguide
DE	Damon-Eshbach (spin-wave mode)
DUT	device under test
EBL	electron beam lighography
FIB	focused ion beam
FMR	ferromagnetic resonance
FVMSW	forward volume magnetostatic waves
GS	ground-signal
LTEM	Lorentz transmission electron microscopy
MALTS	Micromagnetic Analysis to Lorentz TEM Simulation
MSSW	magnetostatic surface waves
MTXM	Magnetic Transmission X-ray Microscopy
OOMMF	Object Oriented Micromagnetic Framework
PCB	printed circuit board
PMMA	polymethyl methacrylate
PSSW	perpendicular standing spin-waves
PSWS	propagating spin-wave spectroscopy
SEM	scanning electron microscope
SMA	SubMiniature version A
SHNO	spin Hall nano-oscillator
TEM	transmission electron microscope
VAV	vortex-antivortex-vortex
VNA	vector network analyzer
VSM	vibrating sample magnetometer
XMCD	X-ray Magnetic Circular Dichroism
XRR	X-ray reflectometry
YIG	yttrium iron garnet $Y_3Fe_5O_{12}$

References

[1] C. Chappert, A. Fert, F.N. Van Dau, The emergence of spin electronics in data storage., Nat. Mater. 6 (2007) 813–23. https://doi.org/10.1038/nmat2024.

[2] A. Hubert, R. Schäfer, Magnetic Domains - The Analysis of Magnetic Microstructures, Springer, 1998. https://doi.org/10.1007/978-3-540-85054-0.

[3] B. Dieny, I.L. Prejbeanu, K. Garello, P. Gambardella, P. Freitas, R. Lehndorff, W. Raberg, U. Ebels, S.O. Demokritov, J. Akerman, A. Deac, P. Pirro, C. Adelmann, A. Anane, A. V. Chumak, A. Hirohata, S. Mangin, S.O. Valenzuela, M.C. Onbaşlı, M. d'Aquino, G. Prenat, G. Finocchio, L. Lopez-Diaz, R. Chantrell, O. Chubykalo-Fesenko, P. Bortolotti, Opportunities and challenges for spintronics in the microelectronics industry, Nat. Electron. 3 (2020) 446–459. https://doi.org/10.1038/s41928-020-0461-5.

[4] S.D. Bader, Colloquium: Opportunities in nanomagnetism, Rev. Mod. Phys. 78 (2006) 1. https://doi.org/10.1103/RevModPhys.78.1.

[5] R.P. Cowburn, D.K. Koltsov, A.O. Adeyeye, M.E. Welland, D.M. Tricker, Single-Domain Circular Nanomagnets, Phys. Rev. Lett. 83 (1999) 1042–1045. https://doi.org/10.1103/PhysRevLett.83.1042.

[6] T. Shinjo, T. Okuno, R. Hassdorf, K. Shigeto, T. Ono, Magnetic Vortex Core Observation in Circular Dots of Permalloy, Science (80-.). 289 (2000) 930–932. https://doi.org/10.1126/science.289.5481.930.

[7] S. Bohlens, B. Krüger, A. Drews, M. Bolte, G. Meier, D. Pfannkuche, Current controlled random-access memory based on magnetic vortex handedness, Appl. Phys. Lett. 93 (2008) 142508. https://doi.org/10.1063/1.2998584.

[8] S.-K. Kim, K.-S. Lee, Y.-S. Yu, Y.-S. Choi, Reliable low-power control of ultrafast vortex-core switching with the selectivity in an array of vortex states by in-plane circular-rotational magnetic fields and spin-polarized currents, Appl. Phys. Lett. 92 (2008) 022509. https://doi.org/10.1063/1.2807274.

[9] B. Van Waeyenberge, A. Puzic, H. Stoll, K.W. Chou, T. Tyliszczak, R. Hertel, M. Fähnle, H. Brückl, K. Rott, G. Reiss, I. Neudecker, D. Weiss, C.H. Back, G. Schütz, Magnetic vortex core reversal by excitation with short bursts of an alternating field., Nature. 444 (2006) 461–4. https://doi.org/10.1038/nature05240.

[10] M. Kammerer, M. Weigand, M. Curcic, M. Noske, M. Sproll, A. Vansteenkiste, B. Van Waeyenberge, H. Stoll, G. Woltersdorf, C.H. Back, G. Schuetz, Magnetic vortex core reversal by excitation of spin waves., Nat. Commun. 2 (2011) 279. https://doi.org/10.1038/ncomms1277.

[11] R. Hertel, S. Gliga, M. Fähnle, C. Schneider, Ultrafast Nanomagnetic Toggle Switching of Vortex Cores, Phys. Rev. Lett. 98 (2007) 117201. https://doi.org/10.1103/PhysRevLett.98.117201.

[12] V. Uhlíř, M. Urbánek, L. Hladík, J. Spousta, M.-Y. Im, P. Fischer, N. Eibagi, J.J. Kan, E.E. Fullerton, T. Šikola, Dynamic switching of the spin circulation in tapered magnetic nanodisks., Nat. Nanotechnol. 8 (2013) 341–6. https://doi.org/10.1038/nnano.2013.66.

[13] M. Urbánek, V. Uhlíř, C.-H. Lambert, J.J. Kan, N. Eibagi, M. Vaňatka, L. Flajšman, R. Kalousek, M.-Y. Im, P. Fischer, T. Šikola, E.E. Fullerton, Dynamics and efficiency of magnetic vortex circulation reversal, Phys. Rev. B. 91 (2015) 094415. https://doi.org/10.1103/PhysRevB.91.094415.

[14] M. Sushruth, J.P. Fried, A. Anane, S. Xavier, C. Deranlot, M. Kostylev, V. Cros, P.J. Metaxas, Electrical measurement of magnetic-field-impeded polarity switching of a ferromagnetic vortex core, Phys. Rev. B. 94 (2016) 100402. https://doi.org/10.1103/PhysRevB.94.100402.

[15] K. Guslienko, V. Novosad, Y. Otani, H. Shima, K. Fukamichi, Magnetization reversal due to vortex nucleation, displacement, and annihilation in submicron ferromagnetic dot arrays, Phys. Rev. B. 65 (2001) 024414. https://doi.org/10.1103/PhysRevB.65.024414.

[16] K.Y. Guslienko, V. Novosad, Y. Otani, H. Shima, K. Fukamichi, Field evolution of magnetic vortex state in ferromagnetic disks, Appl. Phys. Lett. 78 (2001) 3848–3850. https://doi.org/10.1063/1.1377850.

[17] V. Novosad, K.Y. Guslienko, H. Shima, Y. Otani, K. Fukamichi, N. Kikuchi, O. Kitakami, Y. Shimada, Nucleation and annihilation of magnetic vortices in sub-micron permalloy dots, IEEE Trans. Magn. 37 (2001) 2088–2090. https://doi.org/10.1109/20.951062.

[18] M. Rahm, M. Schneider, J. Biberger, R. Pulwey, J. Zweck, D. Weiss, Vortex nucleation in submicrometer

ferromagnetic disks, Appl. Phys. Lett. 82 (2003) 4110–4112. https://doi.org/10.1063/1.1581363.

[19] S.R. Bakaul, B.L. Wu, G.C. Han, Y.H. Wu, Probing magnetization reversal process in ferromagnetic disk by superconductor-ferromagnet junction, Appl. Phys. Lett. 97 (2010) 1–3. https://doi.org/10.1063/1.3463474.

[20] M.-Y. Im, K.-S. Lee, A. Vogel, J.-I. Hong, G. Meier, P. Fischer, Stochastic formation of magnetic vortex structures in asymmetric disks triggered by chaotic dynamics., Nat. Commun. 5 (2014) 5620. https://doi.org/10.1038/ncomms6620.

[21] S. Agramunt-Puig, N. Del-Valle, C. Navau, A. Sanchez, Controlling vortex chirality and polarity by geometry in magnetic nanodots, Appl. Phys. Lett. 104 (2014) 012407. https://doi.org/10.1063/1.4861423.

[22] G. Shimon, V. Ravichandar, A.O. Adeyeye, C.A. Ross, Simultaneous control of vortex polarity and chirality in thickness-modulated [Co/Pd] n /Ti/Ni 80 Fe 20 disks, Appl. Phys. Lett. 105 (2014) 152408. https://doi.org/10.1063/1.4897954.

[23] H. Jung, Y.S. Choi, K.S. Lee, D.S. Han, Y.S. Yu, M.Y. Im, P. Fischer, S.K. Kim, Logic operations based on magnetic-vortex-state networks, ACS Nano. 6 (2012) 3712–3717. https://doi.org/10.1021/nn3000143.

[24] V. Novosad, F. Fradin, P. Roy, K. Buchanan, K. Guslienko, S. Bader, Magnetic vortex resonance in patterned ferromagnetic dots, Phys. Rev. B. 72 (2005) 024455. https://doi.org/10.1103/PhysRevB.72.024455.

[25] N. Hasegawa, S. Sugimoto, H. Fujimori, K. Kondou, Y. Niimi, Y. Otani, Selective mode excitation in three-chained magnetic vortices, Appl. Phys. Express. 8 (2015) 063005. https://doi.org/10.7567/APEX.8.063005.

[26] S. Wintz, V. Tiberkevich, M. Weigand, J. Raabe, J. Lindner, A. Erbe, A. Slavin, J. Fassbender, Magnetic vortex cores as tunable spin-wave emitters, Nat. Nanotechnol. 11 (2016) 948–953. https://doi.org/10.1038/nnano.2016.117.

[27] A. Mahmoud, F. Ciubotaru, F. Vanderveken, A. V. Chumak, S. Hamdioui, C. Adelmann, S. Cotofana, Introduction to spin wave computing, J. Appl. Phys. 128 (2020) 161101. https://doi.org/10.1063/5.0019328.

[28] T. Kampfrath, A. Sell, G. Klatt, A. Pashkin, S. Mährlein, T. Dekorsy, M. Wolf, M. Fiebig, A. Leitenstorfer, R. Huber, Coherent terahertz control of antiferromagnetic spin waves, Nat. Photonics. 5 (2011) 31–34. https://doi.org/10.1038/nphoton.2010.259.

[29] a. V. Chumak, V.I. Vasyuchka, a. a. Serga, B. Hillebrands, Magnon spintronics, Nat. Phys. 11 (2015) 453–461. https://doi.org/10.1038/nphys3347.

[30] I.S. Maksymov, M. Kostylev, Broadband stripline ferromagnetic resonance spectroscopy of ferromagnetic films, multilayers and nanostructures, Phys. E Low-Dimensional Syst. Nanostructures. 69 (2015) 253–293. https://doi.org/10.1016/J.PHYSE.2014.12.027.

[31] M. Bailleul, D. Olligs, C. Fermon, S.O. Demokritov, Spin waves propagation and confinement in conducting films at the micrometer scale, Europhys. Lett. 56 (2001) 741–747. https://doi.org/10.1209/epl/i2001-00583-2.

[32] S. Blundell, Magnetism: a very short introduction, Oxford University Press, 2012. https://doi.org/10.1093/actrade/9780199601202.001.0001.

[33] J.M.D. Coey, Magnetism and Magnetic Materials, Cambridge University Press, Cambridge, 2010. https://doi.org/10.1017/CBO9780511845000.

[34] S. Blundell, D. Thouless, Magnetism in Condensed Matter, Oxford University Press, 2003. https://doi.org/10.1119/1.1522704.

[35] O. Wojewoda, Phase–resolved Brillouin light scattering: development and applications, Master's thesis, Faculty of Mechanical Engineering, Brno University of Technology, 2020.

[36] S.-H. Chung, R.D. McMichael, D.T. Pierce, J. Unguris, Phase diagram of magnetic nanodisks measured by scanning electron microscopy with polarization analysis, Phys. Rev. B. 81 (2010) 024410. https://doi.org/10.1103/PhysRevB.81.024410.

[37] N. a. Usov, S.E. Peschany, Magnetization curling in a fine cylindrical particle, J. Magn. Magn. Mater. 118 (1993) L290–L294. https://doi.org/10.1016/0304-8853(93)90428-5.

[38] K.Y. Guslienko, Low-frequency vortex dynamic susceptibility and relaxation in mesoscopic ferromagnetic dots, Appl. Phys. Lett. 89 (2006) 022510. https://doi.org/10.1063/1.2221904.

[39] P. Fischer, M.Y. Im, S. Kasai, K. Yamada, T. Ono, A. Thiaville, X-ray imaging of vortex cores in confined magnetic structures, Phys. Rev. B - Condens. Matter Mater. Phys. 83 (2011) 212402. https://doi.org/10.1103/PhysRevB.83.212402.

[40] M. Staňo, Characterization of magnetic nanostructures by magnetic force microscopy, Master's thesis, Faculty of Mechanical Engineering, Brno University of Technology, 2014.

[41] I. Turčan, Variable Field Magnetic Force Microscopy, Bachelor's thesis, Faculty of Mechanical Engineering, Brno University of Technology, 2015.

[42] M. Vaňatka, Spin vortex states in magnetostatically coupled magnetic nanodisks, Master's thesis, Faculty of Mechanical Engineering, Brno University of Technology, 2015.

[43] L. Landau, E. Lifshits, on the Theory of the Dispersion of Magnetic Permeability in Ferromagnetic Bodies, Phys. Zeitsch. Der Sow. 169 (1935) 14–22.

[44] T.L. Gilbert, Classics in Magnetics A Phenomenological Theory of Damping in Ferromagnetic Materials, IEEE Trans. Magn. 40 (2004) 3443–3449. https://doi.org/10.1109/TMAG.2004.836740.

[45] B. Hillebrands, K. Ounadjela, Spin dynamics in confined magnetic structures I, Springer, 2002. https://doi.org/10.1007/3-540-40907-6.

[46] M.J. Donahue, D.G. Porter, OOMMF user's guide, Interag. Rep. NISTIR 6376. (1999).

[47] A. Vansteenkiste, B. Van de Wiele, MuMax: A new high-performance micromagnetic simulation tool, J. Magn. Magn. Mater. 323 (2011) 2585–2591. https://doi.org/10.1016/j.jmmm.2011.05.037.

[48] A.A. Thiele, Steady-state motion of magnetic domains, Phys. Rev. Lett. 30 (1973) 230–233. https://doi.org/10.1103/PhysRevLett.30.230.

[49] K.Y. Guslienko, B.A. Ivanov, V. Novosad, Y. Otani, H. Shima, K. Fukamichi, Eigenfrequencies of vortex state excitations in magnetic submicron-size disks, J. Appl. Phys. 91 (2002) 8037–8039. https://doi.org/10.1063/1.1450816.

[50] T.Y. Chen, A.T. Galkiewicz, P.A. Crowell, Phase diagram of magnetic vortex dynamics, Phys. Rev. B - Condens. Matter Mater. Phys. 85 (2012) 180406. https://doi.org/10.1103/PhysRevB.85.180406.

[51] K.Y. Guslienko, K.S. Lee, S.K. Kim, Dynamic origin of vortex core switching in soft magnetic nanodots, Phys. Rev. Lett. 100 (2008) 027203. https://doi.org/10.1103/PhysRevLett.100.027203.

[52] K.S. Lee, S.K. Kim, Y.S. Yu, Y.S. Choi, K.Y. Guslienko, H. Jung, P. Fischer, Universal criterion and phase diagram for switching a magnetic vortex core in soft magnetic nanodots, Phys. Rev. Lett. 101 (2008) 267206. https://doi.org/10.1103/PhysRevLett.101.267206.

[53] M.-Y. Im, P. Fischer, K. Yamada, T. Sato, S. Kasai, Y. Nakatani, T. Ono, Symmetry breaking in the formation of magnetic vortex states in a permalloy nanodisk., Nat. Commun. 3 (2012) 983. https://doi.org/10.1038/ncomms1978.

[54] C. Kittel, On the Theory of Ferromagnetic Resonance Absorption, Phys. Rev. 73 (1948) 155–161. https://doi.org/10.1103/PhysRev.73.155.

[55] S.S. Kalarickal, P. Krivosik, M. Wu, C.E. Patton, M.L. Schneider, P. Kabos, T.J. Silva, J.P. Nibarger, Ferromagnetic resonance linewidth in metallic thin films: Comparison of measurement methods, J. Appl. Phys. 99 (2006) 093909. https://doi.org/10.1063/1.2197087.

[56] C. Herring, C. Kittel, On the Theory of Spin Waves in Ferromagnetic Media, Phys. Rev. 81 (1951) 869–880. https://doi.org/10.1103/PhysRev.81.869.

[57] A. Prabhakar, D.D. Stancil, Spin waves: Theory and applications, Springer US, 2009. https://doi.org/10.1007/978-0-387-77865-5.

[58] R.W. Damon, J.R. Eshbach, Magnetostatic Modes of a Ferromagnetic Slab, J. Appl. Phys. 31 (1960) S104–S105. https://doi.org/10.1063/1.1984622.

[59] T. Schneider, A.A. Serga, T. Neumann, B. Hillebrands, M.P. Kostylev, Phase reciprocity of spin-wave excitation by a microstrip antenna, Phys. Rev. B - Condens. Matter Mater. Phys. 77 (2008) 214411. https://doi.org/10.1103/PhysRevB.77.214411.

[60] K. Sekiguchi, K. Yamada, S.M. Seo, K.J. Lee, D. Chiba, K. Kobayashi, T. Ono, Nonreciprocal emission of

spin-wave packet in FeNi film, Appl. Phys. Lett. 97 (2010) 022508. https://doi.org/10.1063/1.3464569.

[61] L. Flajšman, Magneto-optical study of the dynamic properties of magnetic nanostructures and nanostructured metamaterials, Doctoral thesis, Central European Institute of Technology, Brno University of Technology, 2019.

[62] B.A. Kalinikos, A.N. Slavin, Theory of dipole-exchange spin wave spectrum for ferromagnetic films with mixed exchange boundary conditions, J. Phys. C Solid State Phys. 19 (1986) 7013–7033. https://doi.org/10.1088/0022-3719/19/35/014.

[63] A. Kreisel, F. Sauli, L. Bartosch, P. Kopietz, Microscopic spin-wave theory for yttrium-iron garnet films, Eur. Phys. J. B. 71 (2009) 59–68. https://doi.org/10.1140/epjb/e2009-00279-y.

[64] M.G. Cottam, Linear and Nonlinear Spin Waves in Magnetic Films and Superlattices, WORLD SCIENTIFIC, 1994. https://doi.org/10.1142/1687.

[65] D.B. Williams, C.B. Carter, Transmission electron microscopy: a textbook for materials science, Springer, 2009. https://doi.org/10.1007/978-0-387-76501-3.

[66] J.N. Chapman, The investigation of magnetic domain structures in thin foils by electron microscopy, J. Phys. D. Appl. Phys. 17 (1984) 623–647. https://doi.org/10.1088/0022-3727/17/4/003.

[67] M. De Graef, Y. Zhu, Magnetic imaging and its applications to materials, Academic Press, 2001.

[68] D.T. Ngo, L.T. Kuhn, In situ transmission electron microscopy for magnetic nanostructures, Adv. Nat. Sci. Nanosci. Nanotechnol. 7 (2016) 045001. https://doi.org/10.1088/2043-6262/7/4/045001.

[69] M. Krajnak, Advanced detection in Lorentz microscopy: pixelated detection in differential phase contrast scanning transmission electron microscopy, Ph.D. thesis, University of Glasgow, 2017.

[70] H. Hopster, H.P. Oepen, eds., Magnetic Microscopy of Nanostructures, Springer Berlin Heidelberg, Berlin, Heidelberg, 2005. https://doi.org/10.1007/b137837.

[71] C. Phatak, M. Tanase, A.K. Petford-Long, M. De Graef, Determination of magnetic vortex polarity from a single Lorentz Fresnel image, Ultramicroscopy. 109 (2009) 264–267. https://doi.org/10.1016/j.ultramic.2008.11.003.

[72] S.K. Walton, K. Zeissler, W.R. Branford, S. Felton, MALTS: A Tool to Simulate Lorentz Transmission Electron Microscopy From Micromagnetic Simulations, IEEE Trans. Magn. 49 (2013) 4795–4800. https://doi.org/10.1109/TMAG.2013.2247410.

[73] S. McVitie, D. McGrouther, S. McFadzean, D.A. MacLaren, K.J. O'Shea, M.J. Benitez, Aberration corrected Lorentz scanning transmission electron microscopy, Ultramicroscopy. 152 (2015) 57–62. https://doi.org/10.1016/j.ultramic.2015.01.003.

[74] M. Krajnak, D. McGrouther, D. Maneuski, V.O. Shea, S. McVitie, Pixelated detectors and improved efficiency for magnetic imaging in STEM differential phase contrast, Ultramicroscopy. 165 (2016) 42–50. https://doi.org/10.1016/j.ultramic.2016.03.006.

[75] N. Shibata, T. Seki, G. Sánchez-Santolino, S.D. Findlay, Y. Kohno, T. Matsumoto, R. Ishikawa, Y. Ikuhara, Electric field imaging of single atoms, Nat. Commun. 8 (2017) 1–7. https://doi.org/10.1038/ncomms15631.

[76] F. Krizek, S. Reimers, Z. Kašpar, A. Marmodoro, J. Michalička, O. Man, A. Edstrom, O.J. Amin, K.W. Edmonds, R.P. Campion, F. Maccherozzi, S.S. Dnes, J. Zubáč, J. Železný, K. Výborný, K. Olejník, V. Novák, J. Rusz, J.C. Idrobo, P. Wadley, T. Jungwirth, Atomically sharp domain walls in an antiferromagnet, (2020). http://arxiv.org/abs/2012.00894 (accessed December 16, 2020).

[77] P. Fischer, D.-H. Kim, W. Chao, J.A. Liddle, E.H. Anderson, D.T. Attwood, Soft X-ray microscopy of nanomagnetism, Mater. Today. 9 (2006) 26–33. https://doi.org/10.1016/S1369-7021(05)71335-3.

[78] P. Fischer, Viewing spin structures with soft X-ray microscopy, Mater. Today. 13 (2010) 14–22. https://doi.org/10.1016/S1369-7021(10)70161-9.

[79] J. Thieme, G. Schmahl, D. Rudolph, E. Umbach, eds., X-Ray Microscopy and Spectromicroscopy, Springer Berlin Heidelberg, 1998. https://doi.org/10.1007/978-3-642-72106-9.

[80] D.T. Attwood, Soft X-rays and Extreme Ultraviolet Radiation: Principles and Applications, Cambridge University Press, 1999. https://doi.org/10.1017/CBO9781107477629.

[81] M.-Y. Im, L. Bocklage, G. Meier, P. Fischer, Magnetic soft x-ray microscopy of the domain wall depinning

process in permalloy magnetic nanowires, J. Phys. Condens. Matter. 24 (2012) 024203. https://doi.org/10.1088/0953-8984/24/2/024203.

[82] T. McGuire, R. Potter, Anisotropic magnetoresistance in ferromagnetic 3d alloys, IEEE Trans. Magn. 11 (1975) 1018–1038. https://doi.org/10.1109/TMAG.1975.1058782.

[83] M.N. Baibich, J.M. Broto, A. Fert, F.N. Van Dau, F. Petroff, P. Etienne, G. Creuzet, A. Friederich, J. Chazelas, Giant Magnetoresistance of (001)Fe/(001)Cr Magnetic Superlattices, Phys. Rev. Lett. 61 (1988) 2472–2475. https://doi.org/10.1103/PhysRevLett.61.2472.

[84] T. Miyazaki, N. Tezuka, Giant magnetic tunneling effect in Fe/Al2O3/Fe junction, J. Magn. Magn. Mater. 139 (1995) L231–L234. https://doi.org/10.1016/0304-8853(95)90001-2.

[85] M. Vaňatka, Magnetic multilayers for spintronics applications, Bachelor's thesis, Faculty of Mechanical Engineering, Brno University of Technology, 2013.

[86] T. Sebastian, K. Schultheiss, B. Obry, B. Hillebrands, H. Schultheiss, Micro-focused Brillouin light scattering: imaging spin waves at the nanoscale, Front. Phys. 3 (2015) 1–23. https://doi.org/10.3389/fphy.2015.00035.

[87] W. Zhou, Z.L. Wang, Scanning microscopy for nanotechnology: techniques and applications, Springer, 2007. https://doi.org/10.1007/978-0-387-39620-0.

[88] P. Rai-Choudhury, Handbook of Microlithography, Micromachining, and Microfabrication: Microlithography, 1997. https://doi.org/10.1117/3.2265070.

[89] M. Dhankhar, M. Vaňatka, M. Urbanek, Fabrication of magnetic nanostructures on silicon nitride membranes for magnetic vortex studies using transmission microscopy techniques, J. Vis. Exp. 2018 (2018) 57817. https://doi.org/10.3791/57817.

[90] K.S. Buchanan, P.E. Roy, M. Grimsditch, F.Y. Fradin, K.Y. Guslienko, S.D. Bader, V. Novosad, Soliton-pair dynamics in patterned ferromagnetic ellipses, Nat. Phys. 1 (2005) 172–176. https://doi.org/10.1038/nphys173.

[91] T. Wren, O. Kazakova, Anisotropic magnetoresistance effect in sub-micron nickel disks, J. Appl. Phys. 117 (2015) 17E134. https://doi.org/10.1063/1.4918967.

[92] M. Vaňatka, M. Urbánek, R. Jíra, L. Flajšman, M. Dhankhar, M.-Y. Im, J. Michalička, V. Uhlíř, T. Šikola, Magnetic vortex nucleation modes in static magnetic fields, AIP Adv. 7 (2017) 105103. https://doi.org/10.1063/1.5006235.

[93] M. Goto, H. Hata, A. Yamaguchi, Y. Nakatani, T. Yamaoka, Y. Nozaki, H. Miyajima, Electric spectroscopy of vortex states and dynamics in magnetic disks, Phys. Rev. B. 84 (2011) 1–9. https://doi.org/10.1103/PhysRevB.84.064406.

[94] M. Hiebel, Fundamentals of vector network analysis, Rohde & Schwarz, 2016.

[95] T.R. Kuphaldt, Lessons in Electric Circuits Vol. 2 Alternate Current, First Edit, Koros Press, 2012.

[96] TX-LINE: A free and interactive calculator for the analysis and synthesis of transmission-line structures available for free from AWR Software, (n.d.). https://www.awr.com/awr-software/options/tx-line.

[97] V. Vlaminck, M. Bailleul, Spin-wave transduction at the submicrometer scale: Experiment and modeling, Phys. Rev. B. 81 (2010) 014425. https://doi.org/10.1103/PhysRevB.81.014425.

[98] W. Bang, M.B. Jungfleisch, J. Lim, J. Trossman, C.C. Tsai, A. Hoffmann, J.B. Ketterson, Excitation of the three principal spin waves in yttrium iron garnet using a wavelength-specific multi-element antenna, AIP Adv. 8 (2018) 1–6. https://doi.org/10.1063/1.5007101.

[99] J. Lucassen, C.F. Schippers, L. Rutten, R.A. Duine, H.J.M. Swagten, B. Koopmans, R. Lavrijsen, Optimizing propagating spin wave spectroscopy, Appl. Phys. Lett. 115 (2019) 012403. https://doi.org/10.1063/1.5090892.

[100] V. Roučka, Návrh zařízení pro měření magnetodynamických vlastností magnetických materiálů a nanostruktur, Bachelor's thesis, Faculty of Mechanical Engineering, Brno University of Technology, 2019.

[101] C. Bilzer, T. Devolder, P. Crozat, C. Chappert, S. Cardoso, P.P. Freitas, Vector network analyzer ferromagnetic resonance of thin films on coplanar waveguides: Comparison of different evaluation methods, J. Appl. Phys. 101 (2007) 074505. https://doi.org/10.1063/1.2716995.

[102] T. Usami, M. Itoh, T. Taniyama, Compositional dependence of Gilbert damping constant of epitaxial Fe100-xRhx thin films, Appl. Phys. Lett. 115 (2019) 142403. https://doi.org/10.1063/1.5120597.

[103] A. V Chumak, A.A. Serga, B. Hillebrands, Magnonic crystals for data processing, J. Phys. D. Appl. Phys. 50 (2017) 244001. https://doi.org/10.1088/1361-6463/aa6a65.

[104] S. Jiang, L. Sun, Y. Yin, Y. Fu, C. Luo, Y. Zhai, H. Zhai, Ferromagnetic resonance linewidth and two-magnon scattering in Fe1-xGdx thin films, AIP Adv. 7 (2017) 056029. https://doi.org/10.1063/1.4978004.

[105] S. Azzawi, A.T. Hindmarch, D. Atkinson, Magnetic damping phenomena in ferromagnetic thin-films and multilayers, J. Phys. D. Appl. Phys. 50 (2017). https://doi.org/10.1088/1361-6463/aa8dad.

[106] J. Ding, P. Lapa, S. Jain, T. Khaire, S. Lendinez, W. Zhang, M.B. Jungfleisch, C.M. Posada, V.G. Yefremenko, J.E. Pearson, A. Hoffmann, V. Novosad, Spin Vortex Resonance in Non-planar Ferromagnetic Dots, Sci. Rep. 6 (2016) 25196. https://doi.org/10.1038/srep25196.

[107] N. Hasegawa, K. Kondou, M. Kimata, Y.C. Otani, Spin pumping due to spin waves in magnetic vortex structure, Appl. Phys. Express. 10 (2017). https://doi.org/10.7567/APEX.10.053002.

[108] M.E. Stebliy, S. Jain, A.G. Kolesnikov, A. V. Ognev, A.S. Samardak, A. V. Davydenko, E. V. Sukovatitcina, L.A. Chebotkevich, J. Ding, J. Pearson, V. Khovaylo, V. Novosad, Vortex dynamics and frequency splitting in vertically coupled nanomagnets, Sci. Rep. 7 (2017) 1–7. https://doi.org/10.1038/s41598-017-01222-4.

[109] F.G. Aliev, J.F. Sierra, A.A. Awad, G.N. Kakazei, D.S. Han, S.K. Kim, V. Metlushko, B. Ilic, K.Y. Guslienko, Spin waves in circular soft magnetic dots at the crossover between vortex and single domain state, Phys. Rev. B - Condens. Matter Mater. Phys. 79 (2009) 1–7. https://doi.org/10.1103/PhysRevB.79.174433.

[110] P.R. Emtage, Interaction of magnetostatic waves with a current, J. Appl. Phys. 49 (1978) 4475–4484. https://doi.org/10.1063/1.325452.

[111] F. Ciubotaru, T. Devolder, M. Manfrini, C. Adelmann, I.P. Radu, All electrical propagating spin wave spectroscopy with broadband wavevector capability, Appl. Phys. Lett. 109 (2016) 012403. https://doi.org/10.1063/1.4955030.

[112] K. Yamanoi, S. Yakata, T. Kimura, T. Manago, Spin Wave Excitation and Propagation Properties in a Permalloy Film, Jpn. J. Appl. Phys. 52 (2013) 083001. https://doi.org/10.7567/JJAP.52.083001.

[113] U.K. Bhaskar, G. Talmelli, F. Ciubotaru, C. Adelmann, T. Devolder, Backward volume vs Damon-Eshbach: A traveling spin wave spectroscopy comparison, J. Appl. Phys. 127 (2020) 033902. https://doi.org/10.1063/1.5125751.

[114] M. Bailleul, D. Olligs, C. Fermon, Propagating spin wave spectroscopy in a permalloy film: A quantitative analysis, Appl. Phys. Lett. 83 (2003) 972–974. https://doi.org/10.1063/1.1597745.

[115] H. Qin, S.J. Hämäläinen, K. Arjas, J. Witteveen, S. van Dijken, Propagating spin waves in nanometer-thick yttrium iron garnet films: Dependence on wave vector, magnetic field strength, and angle, Phys. Rev. B. 98 (2018) 224422. https://doi.org/10.1103/PhysRevB.98.224422.

[116] H. Yu, O. D'Allivy Kelly, V. Cros, R. Bernard, P. Bortolotti, A. Anane, F. Brandl, R. Huber, I. Stasinopoulos, D. Grundler, Magnetic thin-film insulator with ultra-low spin wave damping for coherent nanomagnonics, Sci. Rep. 4 (2014) 1–5. https://doi.org/10.1038/srep06848.

[117] M. Collet, O. Gladii, M. Evelt, V. Bessonov, L. Soumah, P. Bortolotti, S.O. Demokritov, Y. Henry, V. Cros, M. Bailleul, V.E. Demidov, A. Anane, Spin-wave propagation in ultra-thin YIG based waveguides, Appl. Phys. Lett. 110 (2017) 092408. https://doi.org/10.1063/1.4976708.

[118] A. Krysztofik, H. Głowiński, P. Kuświk, S. Ziętek, L.E. Coy, J.N. Rychły, S. Jurga, T.W. Stobiecki, J. Dubowik, Characterization of spin wave propagation in (1 1 1) YIG thin films with large anisotropy, J. Phys. D. Appl. Phys. 50 (2017) 235004. https://doi.org/10.1088/1361-6463/aa6df0.

[119] M. Sushruth, M. Grassi, K. Ait-Oukaci, D. Stoeffler, Y. Henry, D. Lacour, M. Hehn, U. Bhaskar, M. Bailleul, T. Devolder, J.-P. Adam, Electrical spectroscopy of forward volume spin waves in perpendicularly magnetized materials, Phys. Rev. Res. 2 (2020) 043203. https://doi.org/10.1103/PhysRevResearch.2.043203.

[120] T. Schneider, A.A. Serga, A. V. Chumak, C.W. Sandweg, S. Trudel, S. Wolff, M.P. Kostylev, V.S.

Tiberkevich, A.N. Slavin, B. Hillebrands, Nondiffractive subwavelength wave beams in a medium with externally controlled anisotropy, Phys. Rev. Lett. 104 (2010) 1–4. https://doi.org/10.1103/PhysRevLett.104.197203.

[121] I. Bertelli, J.J. Carmiggelt, T. Yu, B.G. Simon, C.C. Pothoven, G.E.W. Bauer, Y.M. Blanter, J. Aarts, T. van der Sar, Magnetic resonance imaging of spin-wave transport and interference in a magnetic insulator, ArXiv. (2020) 1–8. https://doi.org/10.1126/sciadv.abd3556.

[122] J. Chen, F. Heimbach, T. Liu, H. Yu, C. Liu, H. Chang, T. Stückler, J. Hu, L. Zeng, Y. Zhang, Z. Liao, D. Yu, W. Zhao, M. Wu, Spin wave propagation in perpendicularly magnetized nm-thick yttrium iron garnet films, J. Magn. Magn. Mater. 450 (2018) 3–6. https://doi.org/10.1016/j.jmmm.2017.04.045.

[123] Y. V. Khivintsev, Y.A. Filimonov, S.A. Nikitov, Spin wave excitation in yttrium iron garnet films with micron-sized antennas, Appl. Phys. Lett. 106 (2015) 052407. https://doi.org/10.1063/1.4907626.

[124] S.A. Nikitov, D. V Kalyabin, I. V Lisenkov, A. Slavin, Y.N. Barabanenkov, S.A. Osokin, A. V Sadovnikov, E.N. Beginin, M.A. Morozova, Y.A. Filimonov, Y. V Khivintsev, S.L. Vysotsky, V.K. Sakharov, E.S. Pavlov, Magnonics: a new research area in spintronics and spin wave electronics, Physics-Uspekhi. 58 (2015) 1002–1028. https://doi.org/10.3367/ufne.0185.201510m.1099.

[125] G. Schmidt, C. Hauser, P. Trempler, M. Paleschke, E.T. Papaioannou, Ultra Thin Films of Yttrium Iron Garnet with Very Low Damping: A Review, Phys. Status Solidi. 257 (2020) 1900644. https://doi.org/10.1002/pssb.201900644.

[126] T. Hache, M. Vaňatka, L. Flajšman, T. Weinhold, T. Hula, O. Ciubotariu, M. Albrecht, B. Arkook, I. Barsukov, L. Fallarino, O. Hellwig, J. Fassbender, M. Urbánek, H. Schultheiss, Freestanding Positionable Microwave-Antenna Device for Magneto-Optical Spectroscopy Experiments, Phys. Rev. Appl. 13 (2020) 054009. https://doi.org/10.1103/PhysRevApplied.13.054009.

[127] L. Flajšman, K. Wagner, M. Vaňatka, J. Gloss, V. KřižÁková, M. Schmid, H. Schultheiss, M. Urbánek, Zero-field propagation of spin waves in waveguides prepared by focused ion beam direct writing, Phys. Rev. B. 101 (2020) 014436. https://doi.org/10.1103/PhysRevB.101.014436.

[128] O. Wojewoda, T. Hula, L. Flajšman, M. Vaňatka, J. Gloss, J. Holobrádek, M. Staňo, S. Stienen, L. Körber, K. Schultheiss, M. Schmid, H. Schultheiss, M. Urbánek, Propagation of spin waves through a Néel domain wall, Appl. Phys. Lett. 117 (2020) 022405. https://doi.org/10.1063/5.0013692.

[129] T.M. Spicer, P.S. Keatley, M. Dvornik, T.H.J. Loughran, A.A. Awad, P. Dürrenfeld, A. Houshang, M. Ranjbar, J. Åkerman, V. V. Kruglyak, R.J. Hicken, Time resolved imaging of the non-linear bullet mode within an injection-locked nano-contact spin Hall nano-oscillator, Appl. Phys. Lett. 113 (2018). https://doi.org/10.1063/1.5047148.

[130] T. Hache, T. Weinhold, K. Schultheiss, J. Stigloher, F. Vilsmeier, C. Back, S.S.P.K. Arekapudi, O. Hellwig, J. Fassbender, H. Schultheiss, Combined frequency and time domain measurements on injection-locked, constriction-based spin Hall nano-oscillators, Appl. Phys. Lett. 114 (2019). https://doi.org/10.1063/1.5082692.

[131] J.E. Hirsch, Spin hall effect, Phys. Rev. Lett. 83 (1999) 1834–1837. https://doi.org/10.1103/PhysRevLett.83.1834.

[132] K. Ando, S. Takahashi, K. Harii, K. Sasage, J. Ieda, S. Maekawa, E. Saitoh, Electric manipulation of spin relaxation using the spin hall effect, Phys. Rev. Lett. 101 (2008) 1–4. https://doi.org/10.1103/PhysRevLett.101.036601.

[133] A. Hoffmann, Spin hall effects in metals, IEEE Trans. Magn. 49 (2013) 5172–5193. https://doi.org/10.1109/TMAG.2013.2262947.

[134] O. V. Dobrovolskiy, S.A. Bunyaev, N.R. Vovk, D. Navas, P. Gruszecki, M. Krawczyk, R. Sachser, M. Huth, A. V. Chumak, K.Y. Guslienko, G.N. Kakazei, Spin-wave spectroscopy of individual ferromagnetic nanodisks, Nanoscale. 12 (2020) 21207–21217. https://doi.org/10.1039/d0nr07015g.

[135] V.M. Vashishtha, P. Kumar, Development of SARS-CoV-2 vaccines: challenges, risks, and the way forward, Hum. Vaccines Immunother. (2020). https://doi.org/10.1080/21645515.2020.1845524.

[136] A. Barman, S. Mondal, S. Sahoo, A. De, Magnetization dynamics of nanoscale magnetic materials: A perspective, J. Appl. Phys. 128 (2020) 170901. https://doi.org/10.1063/5.0023993.

Author's publications and other outputs

Journal contributions:

1. P. Procházka, J. Mach, D. Bischoff, Z. Lišková, P. Dvořák, M. Vaňatka, P. Simonet, A. Varlet, D. Hemzal, M. Petrenec, L. Kalina, M. Bartošík, K. Ensslin, P. Varga, J. Čechal, T. Šikola, Ultrasmooth metallic foils for growth of high quality graphene by chemical vapor deposition., Nanotechnology. 25 (2014) 185601. doi:10.1088/0957-4484/25/18/185601.
2. M. Urbánek, V. Uhlíř, C.-H. Lambert, J.J. Kan, N. Eibagi, M. Vaňatka, L. Flajšman, R. Kalousek, M.-Y. Im, P. Fischer, T. Šikola, E.E. Fullerton, Dynamics and efficiency of magnetic vortex circulation reversal, Phys. Rev. B. 91 (2015) 94415. doi:10.1103/PhysRevB.91.094415.
3. M. Vaňatka, J.-C. Rojas-Sánchez, J. Vogel, M. Bonfim, M. Belmeguenai, Y. Roussigné, A. Stashkevich, A. Thiaville, S. Pizzini, Velocity asymmetry of Dzyaloshinskii domain walls in the creep and flow regimes, J. Phys. Condens. Matter. 27 (2015) 326002. doi:10.1088/0953-8984/27/32/326002.
4. L. Flajšman, M. Urbánek, V. Křižáková, M. Vaňatka, I. Turčan, T. Šikola, High-resolution fully vectorial scanning Kerr magnetometer, Rev. Sci. Instrum. 87 (2016) 53704. doi:10.1063/1.4948595.
5. T. Ha Pham, J. Vogel, J. Sampaio, M. Vaňatka, J.-C. Rojas-Sánchez, M. Bonfim, D.S. Chaves, F. Choueikani, P. Ohresser, E. Otero, A. Thiaville, S. Pizzini, Very large domain wall velocities in Pt/Co/GdOx and Pt/Co/Gd trilayers with Dzyaloshinskii-Moriya interaction, EPL 113 (2016) 67001. doi:10.1209/0295-5075/113/67001.
6. K.K. Tikuišis, L. Beran, P. Cejpek, K. Uhlířová, J. Hamrle, M. Vaňatka, M. Urbánek, M. Veis, Optical and magneto-optical properties of Permalloy thin films in 0.7–6.4 eV photon energy range, Mater. Des. 114 (2017) 31–39. doi:10.1016/j.matdes.2016.10.036.
7. M. Vaňatka, M. Urbánek, R. Jíra, L. Flajšman, M. Dhankhar, M.-Y. Im, J. Michalička, V. Uhlíř, T. Šikola, Magnetic vortex nucleation modes in static magnetic fields, AIP Adv. 7 (2017) 105103. https://doi.org/10.1063/1.5006235.
8. M. Dhankhar, M. Vaňatka, M. Urbanek, Fabrication of magnetic nanostructures on silicon nitride membranes for magnetic vortex studies using transmission microscopy techniques, J. Vis. Exp. 2018 (2018) 57817. https://doi.org/10.3791/57817.
9. L. Flajšman, K. Wagner, M. Vaňatka, J. Gloss, V. KřiŽáková, M. Schmid, H. Schultheiss, M. Urbánek, Zero-field propagation of spin waves in waveguides prepared by focused ion beam direct writing, Phys. Rev. B. 101 (2020) 014436. https://doi.org/10.1103/PhysRevB.101.014436.
10. T. Hache, M. Vaňatka, L. Flajšman, T. Weinhold, T. Hula, O. Ciubotariu, M. Albrecht, B. Arkook, I. Barsukov, L. Fallarino, O. Hellwig, J. Fassbender, M. Urbánek, H. Schultheiss, Freestanding Positionable Microwave-Antenna Device for Magneto-Optical Spectroscopy Experiments, Phys. Rev. Appl. 13 (2020) 054009. https://doi.org/10.1103/PhysRevApplied.13.054009.
11. O. Wojewoda, T. Hula, L. Flajšman, M. Vaňatka, J. Gloss, J. Holobrádek, M. Staňo, S. Stienen, L. Körber, K. Schultheiss, M. Schmid, H. Schultheiss, M. Urbánek,

Propagation of spin waves through a Néel domain wall, Appl. Phys. Lett. 117 (2020) 022405. https://doi.org/10.1063/5.0013692.

12. M. Heigl, S. Koraltan, M. Vaňatka, R. Kraft, C. Abert, C. Vogler, A. Semisalova, P. Che, A. Ullrich, T. Schmidt, J. Hintermayr, D. Grundler, M. Farle, M. Urbánek, D. Suess, M. Albrecht, Dipolar-stabilized first and second-order antiskyrmions in ferrimagnetic multilayers, (2020). http://arxiv.org/abs/2010.06555.
13. M. Vaňatka, et al., Spin-wave dispersion relations of magnetic thin films measured by VNA, manuscript in preparation to be submitted by Jan 2021.

Conference and workshop contributions:

1. M. Vaňatka, M. Urbánek, R. Jíra, L. Flajšman, M. Dhankhar, V. Uhlíř, M.-Y. Im and T. Šikola, Magnetic vortex nucleation modes studied by anisotropic magnetoresistance and magnetic transmission X-ray microscopy (oral presentation), Czech and Slovak Conference on Magnetism, June 2016, Košice, Slovakia.
2. M. Vaňatka, M. Urbánek, R. Jíra, L. Flajšman, M. Dhankhar, V. Uhlíř, M.-Y. Im and T. Šikola, Vortex nucleation modes in Permalloy nanodisks studied by anisotropic magnetoresistance and by magnetic imaging (poster presentation), Joint European Magnetic Symposia, August 2016, Glasgow, UK.
3. M. Vaňatka, M. Urbánek, L. Flajšman, V. Uhlíř, and T. Šikola, Excitation modes of nucleation-controlled spin structures in permalloy nanodisks (poster presentation), Intermag, April 2017, Dublin, Ireland.
4. M. Vaňatka, M. Urbánek, L. Flajšman, V. Uhlíř, and T. Šikola, Lorentz TEM: study of the spin configurations in NiFe magnetic disks upon the vortex nucleation (poster presentation), Meeting on TEM in Materials Sciences, April 2018, Brno, Czech Republic.
5. M. Vaňatka, M. Urbánek, L. Flajšman, V. Uhlíř, and T. Šikola, Excitation modes of nucleation-controlled spin structures in permalloy nanodisks (poster presentation), ICN+T, July 2018, Brno, Czech Republic.
6. M. Vaňatka, T. Hache, L. Flajšman, H. Schultheiss, M. Urbánek, Levitating antennas for spin wave excitation and detection (poster presentation), Joint European Magnetic Symposia, August 2019, Uppsala, Sweden.
7. M. Vaňatka, O. Wojewoda, K. Davídková, M. Urbánek, Spin-wave dispersion of magnetic materials measured by the propagating spin-wave spectroscopy technique using variable gap antennas, Joint European Magnetic Symposia, December 2020, Lisabon, Portugal (fully online due to the pandemic situation)